



UNIVERSIDAD DE CASTILLA-LA MANCHA

**INSTITUTO DE NANOCIENCIA, NANOTECNOLOGÍA
Y MATERIALES MOLECULARES (INAMOL)**

*Facultad de Ciencias Ambientales y Bioquímica
Departamento de Química Inorgánica, Orgánica y Bioquímica*

**NANOARCHITECTURES BASED ON
GRAPHENE AND CARBON NANOTUBES:
DESIGN, SYNTHESIS AND PROPERTIES**

Miriam Barrejón Araque

Toledo, 2015



UNIVERSIDAD DE CASTILLA-LA MANCHA

**INSTITUTO DE NANOCIENCIA, NANOTECNOLOGÍA
Y MATERIALES MOLECULARES (INAMOL)**

*Facultad de Ciencias Ambientales y Bioquímica
Departamento de Química Inorgánica, Orgánica y Bioquímica*

**NANOARCHITECTURES BASED ON
GRAPHENE AND CARBON NANOTUBES:
DESIGN, SYNTHESIS AND PROPERTIES**

Directores: Fernando Langa de la Puente y
M^a José Gómez-Escalonilla Romojaro

Memoria presentada por Miriam Barrejón Araque para
optar al grado de Doctor Internacional en Ciencias
Químicas por la Universidad de Castilla-La Mancha.

Toledo, 2015



UNIVERSIDAD DE CASTILLA-LA MANCHA

INSTITUTO DE NANOCIENCIA, NANOTECNOLOGÍA Y MATERIALES MOLECULARES (INAMOL)

*Facultad de Ciencias Ambientales y Bioquímica
Departamento de Química Inorgánica, Orgánica y Bioquímica*

D. Fernando Langa de la Puente, Catedrático de Química Orgánica de la Universidad de Castilla-La Mancha, y Dña. M^a José Gómez-Escalonilla Romojaro, Profesora Titular de la Universidad de Castilla-La Mancha, **CERTIFICAN** que el presente trabajo titulado “**NANOARCHITECTURES BASED ON GRAPHENE AND CARBON NANOTUBES: DESIGN, SYNTHESIS AND PROPERTIES**”, realizado por Miriam Barrejón Araque para optar al grado de Doctor Internacional en Ciencias Químicas por la Universidad de Castilla-La Mancha, ha sido realizado bajo su dirección y autorizan la presentación del mismo.

Toledo, 2015

Fdo.: Fernando Langa

Fdo.: M^a José Gómez-Escalonilla

ILMO. Sr. Director del Departamento de Química Inorgánica, Orgánica y Bioquímica

Acknowledgements/Agradecimientos

En primer lugar me gustaría expresar mis agradecimientos a toda la gente que me ha rodeado en el laboratorio durante estos 4 años de tesis.

A mis directores de Tesis Fernando y María José, por darme la oportunidad de realizar esta tesis doctoral, por todo lo que me han enseñado, por su apoyo y dedicación constante.

A Pilar, por su ayuda siempre que la he necesitado.

A las *inamoleras* más veteranas con las que empecé mi aventura en este laboratorio, Ana, Bea, María, Rocío, Susana...por ayudarme en todo lo que necesitaba, por hacerme la adaptación más amena, los ratos de café, las comidas y los picnics por el campus...pero en especial a María, por ser la primera que me enseñó cómo trabajar en el mundo de las nanoformas de carbono, ¡Parece que lo hiciste bien porque al final voy a ser doctora! ☺

A Rubén, el chico grande del que muchos hablaban en Ciudad Real y al que conocí tras su estancia en Estrasburgo. Gracias por ayudarme siempre que te lo he pedido y por esos gritos y portazos que nos despiertan a todos cuando estamos adormiscados... Es broma, jeje, espero que todo te vaya genial.

A Gabi, con la que compartí poco tiempo pero me demostró ser una gran persona, aunque nos haya cambiado por un francesito...

A los actuales trabajadores en las "nanocosas", Luisimi, Virginia, Fernando, Max, Juliana, Maida, Pablo, con los que he vivido muchos buenos momentos, principalmente comidas en el Foster, el Wok, el Tempieto, los Mcflurry y las hamburguesas del Mcdonald, los cafés en la salita y en la cafetería...parece que solo sabemos comer??? Espero que sigamos compartiendo todos esos momentos que nos ayudan a que los largos días de laboratorio sean mas llevaderos y a engordar un poquito...

A las inorgánicas, María José, Rosa, Carol, que siempre tienen una sonrisa cuando te encuentras con ellas.

A los químicos, Cris, Noemí, Mario, Juan Ángel, Boiko, porque siempre están dispuestos a echarte una mano, o a prestarnos todo lo que les pedimos (algo continuo). Espero que os vaya a todos genial y que nos sigamos viendo.

Finally, thanks to all the guys from the group of Dr. D'Souza, Gary, Venu, Habtom, Sherard, Hannah... for helping me during my stay there, for being so friendly and facilitating me everything while I was in the USA.

A continuación me gustaría agradecer a todas aquellas personas que aunque no hayan estado a mi lado físicamente, me han dado siempre todo su apoyo en todos los sentidos, en los buenos y malos momentos.

A mi marido, Jose, por apoyarme, ayudarme, estar ahí cuando le necesito...y porque siempre me hace reír con sus grandísimas tonterías. Sin ti nada hubiera sido igual.

A mis padres, Ángel y Josefina, porque sin ellos nada de esto hubiera sido posible, por apoyarme en todo en la vida y facilitarme que pudiera realizar todos mis sueños.

A mi hermana y mi cuñado, Cande y Fer, porque son la pareja mas feliz que he visto y me alegran cada rato que paso con ellos...a ver si me hacéis tía pronto...

A mis abuelos, tíos, primos, que siempre se acuerdan de mí y me apoyan aunque no los tenga cerca.

A mis amigos y amigas, Rocío, Jose, David, Carlitos, Cova, Mari Mar, Malu, Mari Carmen, Francés...por todos los momentos que hemos vivido juntos y los que nos quedan.

Por último y no por ello menos importante, a Noa y a Bizcocho, por sacarme una sonrisa cada vez que llego a casa...☺

Finalmente agradecer a toda la gente que ha colaborado en mi trabajo y sin cuya ayuda mi tesis no hubiera resultado igual de bien.

Al Prof. José Luis García Fierro, por los análisis de espectroscopia fotoelectrónica de rayos X de todos los compuestos de esta tesis.

A la Prof. Masako Yudasaka, por las imágenes de microscopía electrónica de transmisión de los nanotubos de carbono.

Al Prof. Hermenegildo García, y a su grupo de investigación, por los estudios fotofísicos del óxido de grafeno y la síntesis del grafeno dopado.

Al Prof. Francis D'Souza y su grupo de investigación, por los estudios fotofísicos de los nanotubos de carbono.

Al Dr. Gonzalo Abellan, por las imágenes de microscopía electrónica de transmisión de grafeno.

A la Dra. Pilar Prieto y el Dr. Antonio Manuel García por sus cálculos teóricos sobre grafeno.

Al Prof. Teodomiro López y la Dra. Mercedes Gabas, por los estudios realizados sobre la función de trabajo del grafeno.

Abbreviations and acronyms

With the aim of facilitating the understanding of this manuscript the abbreviations and acronyms that will be found throughout this manuscript are detailed below:

AFM	Atomic force microscopy
BNAH	1-benzyl-1,4-dihydronicotinamide
CCD	Charge-coupled device
CH	Classical heating
CNH	Carbon nanohorn
CNT	Carbon nanotubes
CuAAC	Copper catalyzed azide-alkyne cycloaddition
CVD	Chemical vapour deposition
DBU	1, 8-diazobicyclo[5,4,0]undecene
DFT	Density functional theory
DIPEA	N,N-diisopropylethylamine
DMF	Dimethylformamide
DOS	Density of states
DWCNT	Double-walled carbon nanotube
EG	Exfoliated graphene
FET	Field effect transistor
FTIR	Fourier transform infrared spectroscopy
GHz	Gigahertz
GIC	Graphite intercalated compound
GO	Graphene oxide
HiPco	High pressure carbon monoxide process
HOBt	1-hydroxybenzotriazole
HRTEM	High resolution transmission electron microscopy
IBM	International Business Machines

MALDI	Matrix-assisted laser desorption/ionization
MV	Methyl viologen
MW	Microwave irradiation
NCS	N-chlorosuccinimide
NMP	N-methylpyrrolidone
NMR	Nuclear magnetic resonance
o-DCB	ortho-Dichlorobenzene
OPV	Organic Photovoltaic
OSWV	Osteryoung square wave voltammetry
PDI	Perylenediimide
PET	Photoinduced electron transfer
PTFE	Polytetrafluoroethylene
Ps	Picosecond
RBM	Radial breathing mode
SAED	Selected area electron diffraction
SC	Sodium cholate
SDBS	Sodium dodecylbenzenesulfonate
SDS	Sodium dodecyl sulfate
SEM	Scanning electron microscopy
SLG	Single layer graphene
SWNT	Single-walled carbon nanotube
TAS	Transient-absorption spectroscopy
TBAF	Tetrabutylammonium fluoride
TEM	Transmission electron microscopy
TFT	Thin film transistor
TGA	Thermogravimetric analysis
THF	Tetrahydrofuran
TMS	Trimethylsilyl
TMSA	Trimethylsilylacetylene

TFT	Thin film transistor
TPa	Terapascal
UV-vis-NIR	Ultraviolet-visible-near infrared
VBM	Valence bands maximum
XPS	X-ray photoelectron spectroscopy
δ :	Chemical shift
ϵ :	Molar absorptivity
λ_{ex} :	Excitation wavelength
ν :	Frequency

Contents

A BRIEF OUTLOOK OF HISTORY	1
CHAPTER 1: CARBON NANOTUBES	2
1.1 Introduction	4
1.1.1. Types of carbon nanotubes	13
1.1.2. Preparation and purification	18
1.1.3. Properties and applications	21
1.1.4. Chemical functionalization.....	26
1.2 Objectives	47
1.3 Results and discussion	51
1.3.1 Synthesis of nanohybrids SWCNT-C ₆₀	53
1.3.2 Synthesis of nanohybrids DWCNT-perylenediimides	67
1.4 Conclusions	93
1.5 Experimental section	97
1.4.2 Synthesis of nanohybrids.....	108
CHAPTER 2: GRAPHENE	117
2.1 Introduction	119
2.1.1 Graphene structure	121
2.1.2 Synthesis of graphene.....	124
2.1.3 Properties and applications	129
2.1.4 Chemical reactivity	135
2.2 Objectives	149
2.3 Results and discussion	155
2.3.1 Synthesis of a nanoconjugate combining GO and C ₆₀	157
2.3.2 Cycloaddition of nitrile imines to graphene.	171
2.3.3 N-functionalization of N-doped graphene (N)G.....	202
2.4 Conclusions	221
2.5 Experimental section	225

2.4.1 Synthesis of organic compounds	231
2.4.2 Synthesis of nanoconjugates.....	232
ANNEXE: EXPERIMENTAL TECHNIQUES	241
Fourier transform infrared spectroscopy (FTIR).....	243
Raman spectroscopy	243
Thermogravimetric Analysis (TGA).....	247
X-Ray photoelectron spectroscopy (XPS)	248
Atomic force microscopy (AFM).....	250
Transmission electron microscopy (TEM)	251
UV-vis-NIR absorption spectroscopy.....	252
Fluorescence spectroscopy	254
Transient-absorption spectroscopy (TAS)	255
Ultraviolet photoelectron spectroscopy (UPS).....	257
List of publications arising from this thesis	259

Abstract

Over the past 20 years, a great interest has been developed in the potential use of carbon nanostructures in optoelectronics. Due to their unusual and wondrous properties, carbon nanostructures appear as ideal materials for exploring their optical, mechanical and electrical properties, and carbon nanostructures are expected to play an important role in the fabrication of nanoscale electronic and optoelectronic devices.

This thesis deal with the synthesis and development of new nanoarchitectures based on carbon nanotubes and graphene. For this purpose, different synthetic methodologies such as Sonogashira cross coupling, “click” chemistry, cycloaddition reactions etc. have been employed.

To introduce the advent of carbon nanomaterials, a brief historical overview is set at the prologue. Thereafter, the work is divided in two chapters:

Chapter 1 provides an introduction to carbon nanotubes including their structure, properties and applications. The chemical reactivity is described as well in this introductory section. Next, the synthesis of different carbon nanotube hybrids, through modification on the sidewall thereof, is described. To this end, single-walled and double-walled carbon nanotubes derivatives have been used and the functionalization is performed *via* Tour reaction with aryl addends on the nanotube sidewall, and subsequent derivatization of the aryl group. The main characterization techniques, employed to confirm the successful formation of the desired nanoconjugates, are also reflected in this chapter. Finally, the electronic properties of the prepared nanohybrids are studied through different techniques such as electrochemistry and transient absorption spectroscopy.

Chapter 2 is related to graphene nanostructures. As in the previous chapter, an introductory section deals with the structure, properties, applications and chemical reactivity of graphene. Next, the synthesis of several graphene derivatives along with their characterization are showed. In this case, for the functionalization of graphene several approaches have been employed, such as Tour reaction, “Click” chemistry, 1,3-dipolar cycloaddition and alkylation reactions. Finally, the study of the electronic properties of the resulting hybrids through different techniques, such as the abovementioned transient absorption spectroscopy, and other new techniques, such as ultraviolet photoelectron spectroscopy, are showed.

A BRIEF OUTLOOK OF HISTORY

Nanoscience and nanotechnology are centered in the study and application of extremely small things and can be used across all the other science fields, such as chemistry, biology, physics, materials science, and engineering. Nanoscience and nanotechnology involve the ability to see and control individual atoms and molecules. The control and restructuring of matter takes place on the nanoscale in the size range about 1-100 nm, and is used to create materials, devices and systems with new properties and functions.¹ Everything on Earth is made up of atoms, the food we eat, the clothes we wear, the buildings and houses we live in, and our own bodies. The concepts that seeded nanotechnology were first discussed in 1959 by renowned physicist Richard Feynman in his talk *There's Plenty of Room at the Bottom*, in which he described the possibility of synthesis *via* direct manipulation of atoms. However, experimental nanotechnology did not come into its own until 1981, when International Business Machines (IBM) scientists in Zurich, Switzerland, built the first scanning tunneling microscope (STM). STM allows us to see single atoms by scanning a tiny probe over the surface of a silicon crystal. Other significant advances were made in 1985, when chemists discovered how to create a soccer-ball-shaped molecule of 60 carbon atoms, which they called buckminsterfullerene (also known as C₆₀ or buckyballs).²

Carbon, one of the most abundant elements in the universe, has been known since ancient times. Carbon has been a familiar and useful material since prehistory, in the form of charcoal and soot, although it was not until late in the eighteenth century that carbon actually came to be recognized as an element.³ The name carbon was actually conferred by Antoine Lavoisier, from the Latin *carbo* meaning charcoal. The Swedish chemist Carl Wihelm Scheele, in 1779, showed graphite, a familiar sooty material, consisting of pure carbon. A few years later it was demonstrated by Lavoisier that diamond was composed only of carbon as well. Thus, by the end of the 1700s, diamond and graphite were proven to be composed of atoms of the same element, carbon, except that they existed in physically different forms. Diamond is covalently bonded to four neighboring atoms forming a rigid three dimensional tetrahedral network while graphite is composed of atoms arranged in a repeating pattern in flat two

¹https://www.nano.gov/sites/default/files/pub_resource/nanotechnology_bigthingsfromatinyworld-print.pdf

² H. W. Kroto, J. R. Heath, S. C. O'Brien, R. F. Curl and R. E. Smalley, *Nature*, **1985**, 318, 162.

³ N. N. Greenwood, A. Earnshaw "*Chemistry of the elements*" Pergamon Press Oxford. **1984**.

dimensional sheets. These two materials with different appearance and properties but composed both of pure carbon are known as allotropes. Allotropes often have vastly different physical and chemical properties, even though they are composed of atoms of the same element.

In the two hundred years following the work of Lavoisier, the number of allotropic forms in which carbon was known to exist was only two.

In 1970, Eiji Osawa of Toyohashi University, predicted the existence of C_{60} molecules. He suggested that C_{60} should be a stable molecule and a short time later he and others published theoretical studies on what the properties of such a molecule might be. However, the first breakout in the discovery of the fullerenes came in 1985, when Kroto visited Professors Robert Curl and Richard Smalley at Rice University in Houston. At about that time Richard Smalley was developing an ingenious apparatus which enabled small clusters. Then, Smalley received a request from Harry Kroto, to use the apparatus from Smalley's laboratory at Rice University to study a special kind of carbon molecule. A year later, Smalley agreed to let Kroto use the cluster beam apparatus. Kroto, Smalley, and Curl conducted the study, with the assistance of three graduate students, James Heath, Sean O'Brien, and Yuan Liu. During the experiment, a variety of signals were obtained in the mass spectrum of the products with the strongest one appearing at $e/m = 720$. Later, after optimizing the experimental conditions, they obtained a spectrum consisting of only two peaks: one strong signal corresponding to $e/m = 720$, that is to C_{60} , and a weaker one corresponding to C_{70} .² The only structure which could offer a reasonable explanation for this behavior was a spherical one, a structure in which each carbon atom could have the full complement of electrons. These spherical structures were shown to be composed of a repeating geometric arrangement of 12 pentagons and 20 hexagons carbon ring. However, seeing a line in a mass spectrum did not convince all scientists of the discovery of a new allotrope of carbon. Full acceptance came when Krätschmer and Huffman were able to synthesize C_{60} in sufficient quantities to allow structural characterization.⁴

With this discovery, a new third allotrope of carbon was added to the two already known. Fullerenes have been shown to occur in nature as well, on the earth, in space etc.... While a number of varieties of buckyballs have now

⁴ W. Krätschmer, Lowell D. Lamb, K. Fostiropoulos and Donald R. Huffman, *Nature*, **1990**, 347, 354.

been shown to exist, C₆₀ and C₇₀ are generally the most abundant and readily isolated fullerenes.

In 1991 another allotrope of carbon was discovered, with properties similar to the buckyball, but in a tubular, rather than spherical shape. These filamentous structures were identified as carbon nanotubes (CNTs).⁵ The carbon nanotubes reported in the first report were composed of multi-tubes (multi-wall tubes).

There are some that hold the belief that in the 1950s there was an initial discovery of what could have possibly been seen as the first carbon nanotubes. Roger Bacon had the high powered electron microscope that would have been necessary. He got the first visual impression of the tubes of atoms that roll up, however, some state that his discovery just wasn't taken very seriously at that time because science did not know how this discovery could impact scientific research. Also in 1952, two Russian scientists, Radushkevich and Lukyanovich, published clear images showing MWCNT with a 50 nm diameter.⁶ Unfortunately, their paper was published in a Russian journal (Journal of Physical Chemistry of Russia), and Western scientists' access to Soviet press was limited during the Cold War. Some years later in 1976, Endo from Japan was interested in carbon fibres and was collaborating with Oberlin in France, when they reported on the observation of carbon nanotubes by electron microscopy.⁷ Therefore, Suomo Iijima was not the unique discoverer of carbon nanotubes, already in the fifties there were reports on the existence of carbon nanotubes.

It would be in 1993 that Iijima and Donald Bethune found single-walled nanotubes known as buckytubes.^{8,9} The diameters of these "buckytubes" fall in the 1 to 10 nanometers. The continuation of research revealed three basic types of nanotubes (zigzag, armchair, and chiral) as well as single-walled and multi-walled nanotubes.

In the early 21st century, a new nanostructure was discovered which focused even a larger attention than the above mentioned. Geim and

⁵ S. Iijima, *Nature*, **1991**, 354, 56.

⁶ L. V. Radushkevich, V. M. Lukyanovich, *Zurn. Fisic. Chim.*, **1952**, 26, 88.

⁷ A. Oberlin, M. Endo and T. Koyama, *J. Cryst. Growth.*, **1976**, 32, 335.

⁸ S. Iijima, and T. Ichihashi, *Nature*, **1993**, 363, 603.

⁹ D. S. Bethune, C. H. Kiang, M. S. DeVries, G. Gorman, R. Savoy, R. Beyers and J. Vázquez, *Nature*, **1993**, 363, 605.

Novoselov¹⁰ discovered how to obtain isolated sheets from graphite, yielding a new allotrope of carbon named as graphene, which overcame the expectations of any other material (Figure 1).

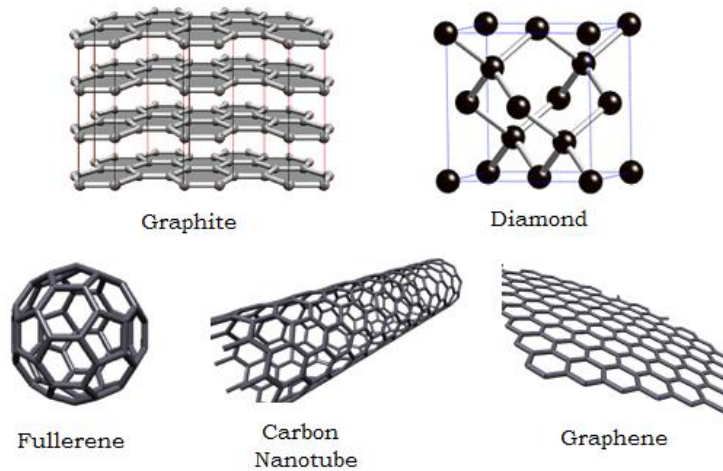


Figure 1. Structures of the main Carbon allotropes.

Historically, the word “*graphene*” comes from the Greek word *graphein*, which means to write, one of the earliest uses of this material.

The initial discovery of graphene was previously discussed by the Canadian physicist Philip Russel Wallace.¹¹ Wallace didn’t believe it was possible to make graphene; what he was interested in studying was graphite, the stuff in pencil lead. Graphite, a three-dimensional honeycomb structure of carbon atoms, was a bit too difficult to handle with the tools Wallace had available to him. Ever resourceful, Wallace invented a two-dimensional analog, graphene, from which he argued he could extract the properties of graphite. Graphene is a two-dimensional grid of carbon atoms arranged in hexagons. Wallace showed that, if you stack enough sheets of graphene on top of each other, you get graphite. So he used his calculations for graphene to extrapolate information about graphite. Later, in 2004, the physicists Andre Geim and

¹⁰ K. S. Novoselov, A. K. Geim, S. V. Morozov, D. Jiang, Y. Zhang, S. V. Dubonos, I. V. Grigorieva, and A. A. Firsov, *Science*, **2004**, 306, 666.

¹¹ P. R. Wallace, *Phys. Rev.*, **1947**, 71, 622.

Konstantin Novoselov were playing with graphite cubes and Scotch tape.¹² They would apply tape to a piece of graphite, then rip the tape off, pulling flakes of graphite with it. They did this again and again with the flaked-off graphite, separating it into thinner and thinner flakes, until they ended up with graphite flakes only one atom thick. Geim and Novoselov had discovered Wallace's graphene.

Publications on carbon nanostructures are on a continuously rising trend over the past decade, as illustrated in Figure 2.¹³ As observed, the youngest carbon allotrope, graphene, has shown a strong growth in the last decade.

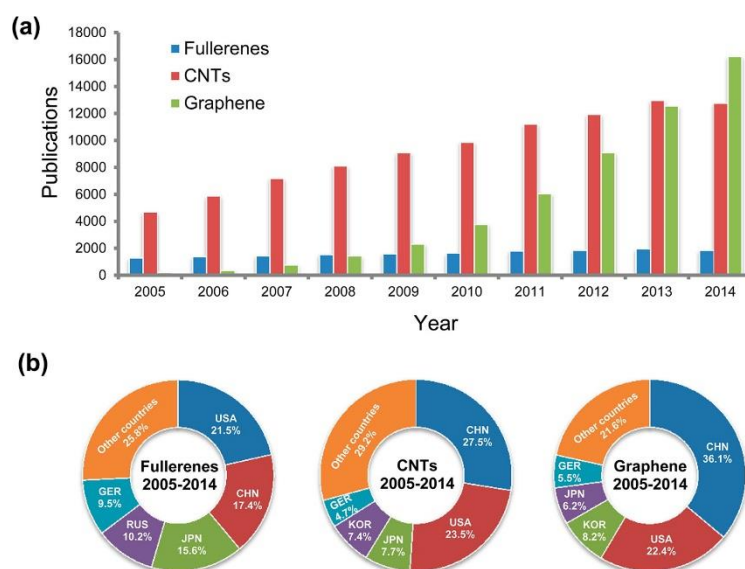


Figure 2. a) Timeline of scientific publications relating to nanocarbons in the past decade (2005–2014). (b) Regional distribution of publications on each topic. Publication analysis was completed using Web of Science.

Although there are many other carbon allotropes such as carbon nanohorns, nanofoams, nanobuds, nanodiamonds etc...that also present many interesting properties, their development cannot be compared to that of fullerene, carbon nanotubes and graphene.^{14,15}

¹² A.K. Geim and K.S. Novoselov, *Nature Mater.*, **2007**, 6, 183.

¹³ Z. Li, Z. Liu, H. Sun and C. Gao, *Chem. Rev.*, **2015**, 115, 7046.

¹⁴ A. Hirsch, *Nat. Mater.*, **2010**, 9, 868.

¹⁵ V. Georgakilas, J. A. Perman, J. Tucek and R. Zboril, *Chem. Rev.*, **2015**, 115, 4744.

CHAPTER 1: CARBON NANOTUBES

1.1 Introduction

1.1.1. Types of carbon nanotubes

In 1991, after the discovery and verification of the fullerenes, Sumio Iijima observed hollow tubes of carbon consisting of concentric shell structures containing from 2 to 50 layers of graphene (Figure 1-1) formed in a carbon arc discharge.⁵ These are nowadays known as multi-walled carbon nanotubes (MWCNTs) and their layers are separated by a distance of approximately the order of the interlayer distance of graphite (*ca.* 0.34 nm). Two years later, he and Donald Bethune independently observed single-walled nanotubes (SWCNTs), structures consisting of just one layer of graphene rolled up in the form of a cylinder with a diameter of around 1 nm.^{8,9}

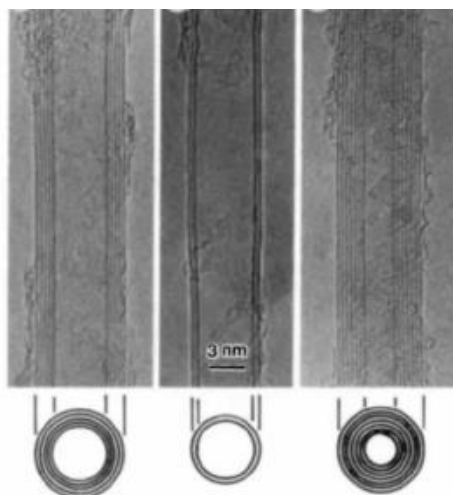


Figure 1-1. TEM image of MWCNTs observed by Iijima.

The discovery of SWCNTs gave rise to new insights in materials research because of their properties. They show unique mechanical, chemical and electronic properties which have prompted the development of potential applications. A special class of nanotubes were discovered in 2001 when C_{60} molecules inside SWCNTs (peapods) were heated at ~ 1200 °C inducing the coalescence between the C_{60} molecules, transforming them into tubular structures (Figure 1-2)¹⁶ and giving rise to double-walled carbon nanotubes (DWCNTs).

¹⁶ S. Bandow, M. Takizawa, K. Hirahara, M. Yudasaka and S. Iijima, *Chem. Phys. Lett.*, **2001**, 337, 48.

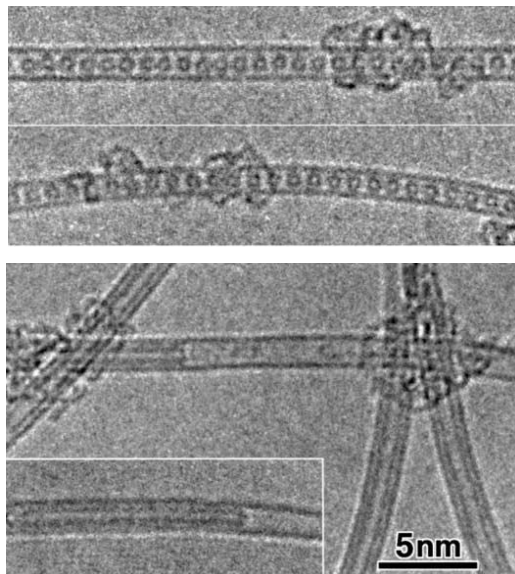


Figure 1-2. TEM images taken for $(C_{60})_n@SWCNTs$ (top) and $(C_{60})_n@SWCNTs$ heated at 1200 °C give rise to DWCNTs (bottom).

DWCNTs form a special class of nanotubes because their morphology and properties are similar to those of SWCNTs but their resistance to chemicals is significantly improved.¹⁷ This is especially important when functionalization is required. In the case of SWCNTs, covalent functionalization will break some C=C double bonds, leaving "holes" in the structure on the nanotube and, thus, modifying both its mechanical and electrical properties. In the case of DWCNTs, only the outer wall is modified, leaving the inner shell of the DWCNTs intact and maintaining its conductive behavior.^{18,19}

In summary, three different types of nanotubes are known nowadays depending on the number of walls that they present (Figure 1-3).

¹⁷ K. E. Moore, D. D. Tune and B. S. Flavel, *Adv. Mater.*, **2015**, 27, 3105.

¹⁸ A. H. Brozena, J. Moskowitz, B. Shao, S. Deng, H. Liao, K. J. Gaskell and Y. Wang, *J. Am. Chem. Soc.*, **2010**, 132, 3932.

¹⁹ Y. A. Kim, K-S. Yang, H. Muramatsu, T. Hayashi, M. Endo, M. Terrones and M. S. Dresselhaus, *Carbon Letters*, **2014**, 15, 77.

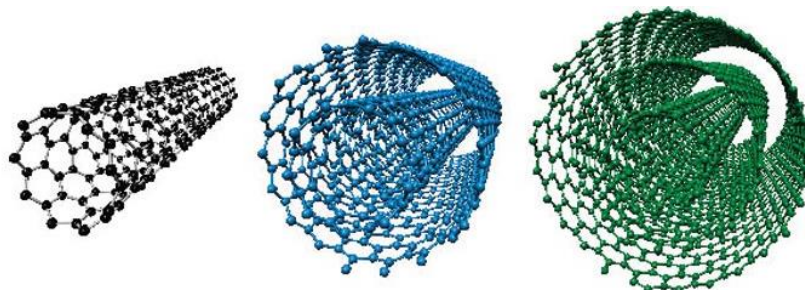


Figure 1-3. Schematic diagram of single, double and multi-walled carbon nanotubes.

CNTs consist of one or multiple rolled sheets of graphene. Another classification that is usually employed for SWNCTs depends on how the graphene sheet is folded. Accordingly, the structure of a SWCNT is given by the chiral vector, $C_h = na_1 + ma_2$ (Figure 1-4). In this equation a_1 and a_2 are the unit vectors of the graphene sheet, whereas (n, m) are the integers that define the number of unit vectors along the two directions of the graphene lattice. Once the integers are defined other parameters such as the diameter of the tube or the chiral angle (θ) can be determined.²⁰ The translation vector, T_a , is directed along the SWNT axis and perpendicular to C_h ; the magnitude of T_a corresponds to the length of the (n,m) SWCNT unit cell. Once (n,m) are specified, other structural properties, such as diameter (d_t) and θ can be determined (equations [1] and [2]).

$$d_t = (3^{1/2}/\pi) a_{cc} (m^2 + mn + n^2)^{1/2} \quad [1]$$

$$\theta = \tan^{-1} [3^{1/2}m/(2n + m)] \quad [2]$$

Where a_{cc} is the nearest-neighbour carbon atom distance of 0.142 nm.

In this way, depending on how the two-dimensional graphene sheet is “rolled up”, three types of nanotubes are possible (Figure 1-4): (i) arm chair ($n = m$ and chiral angle equal to 30°), (ii) zigzag ($n = 0$ or $m = 0$ and chiral angle equal to 0°), and (iii) chiral (other values of n and m and chiral angles lie between 0 and 30°).

²⁰ M. Ouyang, J. L. Huang and C. M. Lieber, *Acc. Chem. Res.*, **2002**, 35, 1018.

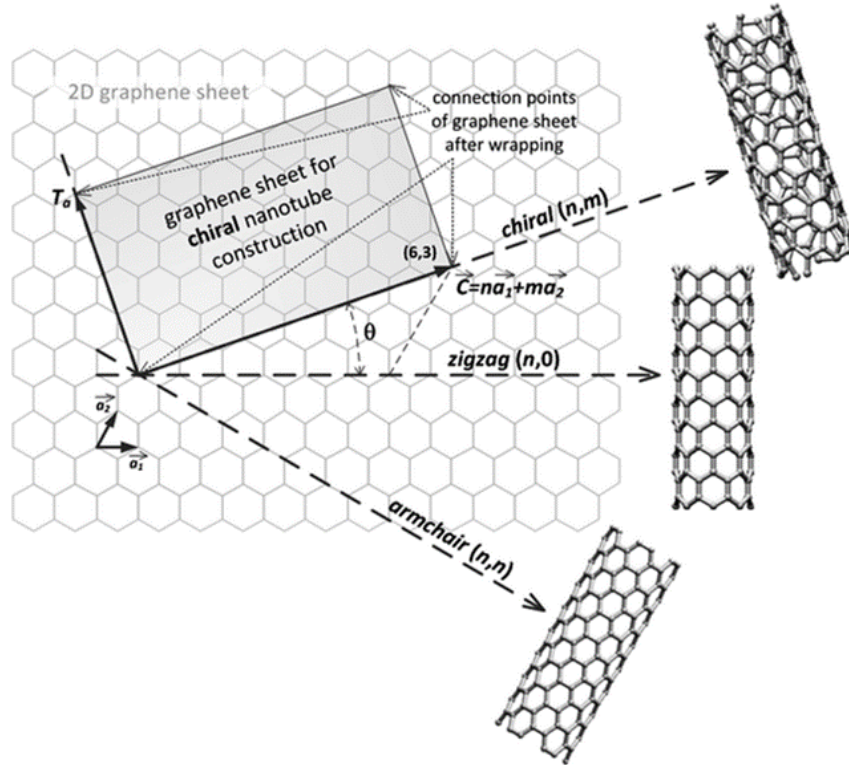


Figure 1-4. The principle of CNT construction from graphene sheet along the chiral vector.

The chirality of CNTs affects the material properties. Especially, the electronic conductivity is highly sensitive to a slight change of these parameters.^{21,22} The structural design has a direct effect on the nanotube's electrical properties. When $n - m$ is divisible by 3, then the nanotube is described as "metallic" (highly conducting), otherwise the nanotube is a semiconductor. For example, the tubes obtained by rolling graphene sheets in figure 1-5 would be $(12-0=12; \text{divisible by } 3 \rightarrow \text{metallic})$ and $(6-4=2; \text{not divisible by } 3 \rightarrow \text{semiconducting})$.

²¹ E. T. Thostenson, Z. F. Ren and T. W. Chou, *Compos. Sci. Technol.*, **2001**, 61, 1899.

²² D. Dass, R. Prasher and R. Vaid, *Afri. Rev. Phys.*, **2013**, 8, 5.

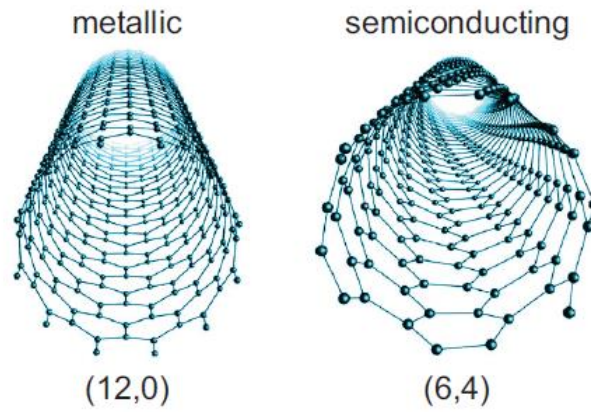


Figure 1-5. Carbon nanotubes with chirality vectors (n, m) assigned.

Therefore, the distinct electronic properties of SWCNT depend on their geometry and they are given by the electronic transitions within one-dimensional density of states (DOS) (Figure 1-6).

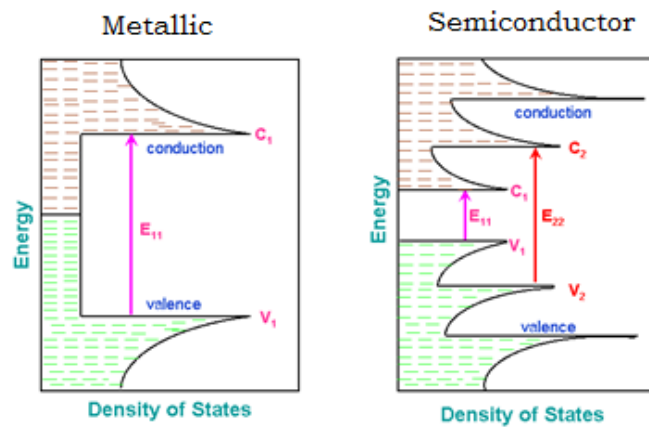


Figure 1-6. Typical densities of states as a function of energy for metallic (left) and semiconducting (right) SWCNTs.

1.1.2. Preparation and purification

Techniques like carbon arc-discharge,²³ laser ablation, high pressure carbon monoxide (HiPco),²⁴ and chemical vapor deposition (CVD)²⁵ have been employed to synthesize CNTs of sizeable quantities, although some other procedures can be found in the literature.^{14,26}

Arch-discharge

The arc-evaporation method was the one employed by Iijima in 1991 in which CNTs were observed for the first time.⁵ This method, which produces the best quality nanotubes, involves applying a current of about 50 A between two graphite electrodes in a helium atmosphere (Figure 1-7). This results in graphite evaporation, part of which condenses on the walls of the reactor vessel and part on the cathode. Deposit on the cathode usually contains the CNTs. SWCNTs are produced when Co and Ni or some other metal are added to the anode. The main drawback of this method is that, although it can be performed in such a way that one of the carbon compounds is favored, the result is always a mixture of SWCNTs, MWCNTs, metallic catalyst, fullerenes and other carbon nanostructures that should be purified afterwards, what inevitably hampers the process and rises the price of the final product.

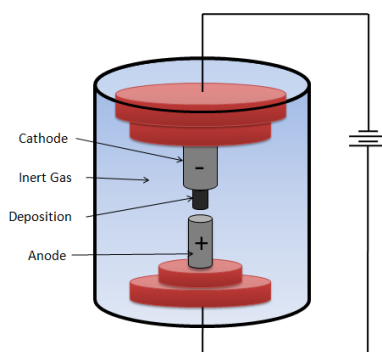


Figure 1-7. Representation of an arch discharge set up.

²³ N. Arora and N. N. Sharma, *Diamond Relat. Mater.*, **2014**, *50*, 135.

²⁴ P. Nivolaev, *J. Nanosci. Nanotechnol.*, **2004**, *4*, 307.

²⁵ M. Kumar and Y. Ando, *J. Nanosci. Nanotechnol.*, **2010**, *10*, 3739.

²⁶ J. Prasek, J. Drbohlavova, J. Chomoucka, J. Hubalek, O. Jasek, V. Adamc and R. Kizek, *J. Mater. Chem.*, **2011**, *21*, 15872.

Laser ablation

This technique was first developed by Smalley *et al.* in 1996,²⁷ following similar conditions to those employed for the production of fullerenes in 1992.²⁸ In this technique, intense laser pulses are used to ablate a carbon target (Figure 1-8). The pulsed laser-ablation of graphite in the presence of an inert gas and catalyst yields CNTs²⁷ in the form of ropes or bundles of 5 to 20 nm diameter and tens to hundreds of micrometers long. Despite this technique is not suitable for large scale production, it is very useful as the result are high quality SWCNTs with high reproducibility and a variety of diameters, which can be obtained by varying some parameters (furnace temperature, catalytic metals and flow rate). The laser induces the vaporization of the carbon target at high temperature, and the vaporized SWCNTs are transported by the inert gas to the water-cooled trap where they are finally collected.²⁹

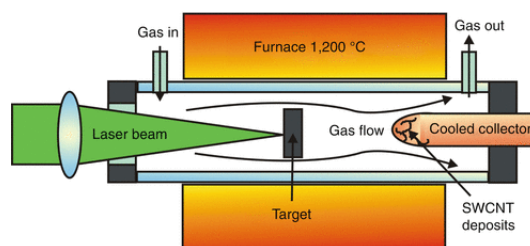


Figure 1-8. Schematic representation of a laser ablation apparatus.

Chemical vapor deposition (CVD)

The CVD method has shown the most promise in terms of its price/unit ratio. This utilizes hydrocarbon gases as sources for carbon atoms and metal catalyst particles as “seeds” for nanotube growth that takes place at relatively low temperatures (500-1000 °C) (Figure 1-9). That is, the substrate, normally quartz, is prepared with a layer of catalyst metal nanoparticles (iron, copper, nickel, or a combination of different metals) that would serve as seeds for the CNT growth. Afterwards a carbon-containing gas (acetylene, ethylene, ethanol

²⁷ A. Thess, R. Lee, P. Nikolaev, H. Dai, P. Petit, J. Robert, C. Xu, Y. H. Lee, S. G. Kim, A. G. Rinzler, D. T. Colbert, G. E. Scuseria, D. Tomalnek, J. E. Fischer and R. E. Smalley, *Science*, **1996**, 273, 483.

²⁸ T. Guo, M. D. Diener, Y. Chai, M. J. Alford, R. E. Haufler, S. M. McClure, T. Ohno, J. H. Weaver, G. E. Scuseria and R. E. Smalley, *Science*, **1992**, 257, 1661.

²⁹ Z. F. Ren, Z. P. Huang, J. W. Xu, J. H. Wang, P. Bush, M. P. Siegal and P. N. Provencio, *Science*, **1998**, 282, 1105.

or methane) is introduced in the reactor chamber. Due to the high temperature inside the reactor those gases decompose and the CNT grows at the sites of the metal nanoparticles.³⁰ Compared with the arc discharge and the laser ablation techniques, CVD is the most versatile way of synthesizing CNTs. The low temperatures required, its performance carried out at ambient pressure, and the possibility of employing various substrates at once, make of this technique the most suitable for the production of CNTs.

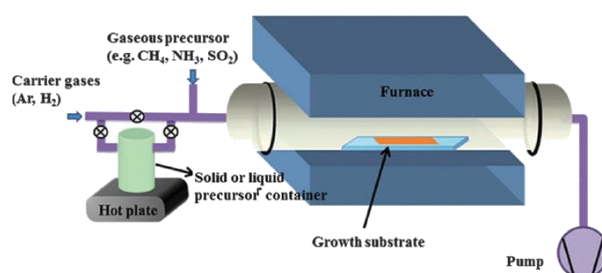


Figure 1-9. Experimental setup for CVD technique.

Most CNTs samples contain carbonaceous impurities such as amorphous carbon, fullerenes, nanoparticles, and transition metals introduced as catalysts during the synthesis of CNTs. The most common purification method implies the treatment of the carbon soot with acids, typically nitric acid or a mixture HNO₃/H₂SO₄, in order to dissolve the metallic nanoparticles. This acidic treatment partially oxidizes the wall of the nanotubes introducing some oxygen functionalities on it, and totally oxidizes the amorphous carbon removing it from the final product.^{31,32} Although purification based on an initial selective oxidation to remove amorphous carbon followed by a reflux in concentrated nitric acid is effective in removing metal from the reaction products, the refluxing in nitric acid induces wall damage in the nanotubes.

SWCNTs with a purity higher than 90% have been produced using ultrasonically assisted microfiltration from amorphous and crystalline carbon impurities and metal particle.³³ Micro-filtration is based on particle size. Usually CNTs and a small amount of carbon nanoparticles are trapped in a filter. The

³⁰ N. M. Rodriguez, A. Chambers, C. Bielawski and R. T. K. Baker, *Langmuir*, **1995**, *11*, 3862.

³¹ A. F. Ismail, P. S. Goh, J. C. Tee and S. M. Sanip, *Nano Brief Rep. Rev.*, **2008**, *3*, 127.

³² K.A. Worsley, I. Kalinina, E. Bekyarova and R. C. Haddon, *J. Am. Chem. Soc.*, **2009**, *131*, 18153.

³³ K. B. Shelimov, R. O. Esenaliev, A. G. Rinzler, C. B. Huffman and R E. Smalley, *Chem. Phys. Lett.*, **1998**, *282*, 429.

other nanoparticles (catalyst metal, fullerenes and carbon nanoparticles) are passing through the filter.^{34,35}

Annealing and thermal treatment is another method used to purify carbon nanotubes. High temperature has effect on the productions and paralyzes the graphitic carbon and the short fullerenes. When high temperature is used, the metal will be melted and can also be removed.³⁵

The purity of the CNTs can be evaluated by Raman spectroscopy, transmission electron microscopy (TEM), scanning electron microscopy (SEM), atomic force microscopy (AFM) and UV-visible-near-infrared (UV-vis-NIR).

1.1.3. Properties and applications

Vital to the applications of CNTs are their unusual mechanical and thermal properties.³⁶ The graphitic sp^2 bond is 33% stronger than the sp^3 bond of diamond, the hardest substance in nature. The Young's modulus of nanotube bundles, exceeds 1 TPa.³⁷ This is particularly beneficial for the high strength properties of composites based on nanotubes. Since defects strongly influence the mechanical properties of nanotubes, researchers come back continuously to face the challenges of controlling the synthesis process.

Thermal conductivity is also an important property when talking about carbon nanotubes.³⁸ It is superior to that of all materials, including diamond, due to the benefits derived from the strength and toughness of the sp^2 bond and from the 1D character of nanotubes. When compared to copper wires, which are commonly used as thermal conductors, the carbon nanotubes can transmit over 15 times the amount of watts per meter per Kelvin. Due to their relationship to graphene, carbon nanotubes remain stable up to very high temperatures, close to the melting point of graphite near 4000 K.

Something important to mention here is that the wider the nanotube, the more stable it is. Since DWCNTs are normally wider than SWCNTs, we can expect that the former will be generally the more stable of both. We can thus

³⁴ R. C. Haddon, J. Sippel, A. G. Rinzler and F. Papadimitrakopoulos, *MRS Bull.*, **2004**, 29, 252.

³⁵ H. Kajiura, S. Tsutsui, H. J. Huang and Y. Murakami, *Chem. Phys. Lett.*, **2002**, 364, 586.

³⁶ R. S. Ruoff and D. C. Lorents, *Carbon*, **1995**, 33, 925.

³⁷ C. Q. Sun, H. L. Bai, B. K. Tay, S. Li and E. Y. Jiang, *J. Phys. Chem B*, **2003**, 107, 7544.

³⁸ S. Berber, Y. K. Kwon and D. Tománek, *Phys. Rev Lett.* **2000**, 84, 4613.

foresee the following hierarchy of stability in carbon nanoscaled objects: graphite > DWCNTs > SWCNTs > fullerenes.

The transport properties of carbon nanotubes have also attracted great interest. The structure of a carbon nanotube determines how conductive the nanotube is. SWCNTs normally contains a mixture of both semiconducting and metallic nanotubes. Both, metallic and semiconducting SWCNTs are found to possess electrical characteristics that compare favorably with the best electronic materials presently available, however, the electric transport property of the arrays is dominated by the metallic pathways. Due to the low defect density and the absence of backscattering, metallic SWCNTs are ballistic conductors with an exceptionally long electron mean free path. The experimental evidence of ballistic transport through a SWCNT was first observed by Tans *et al.*^{39,40} This ballistic regime refers to the transport of electrons in a medium where the electrical resistivity due to the scattering, by the atoms, molecules or impurities in the medium itself, is negligible or absent.

A wide number of applications are derived from the outstanding properties of CNTs (Figure 1-10).¹⁴

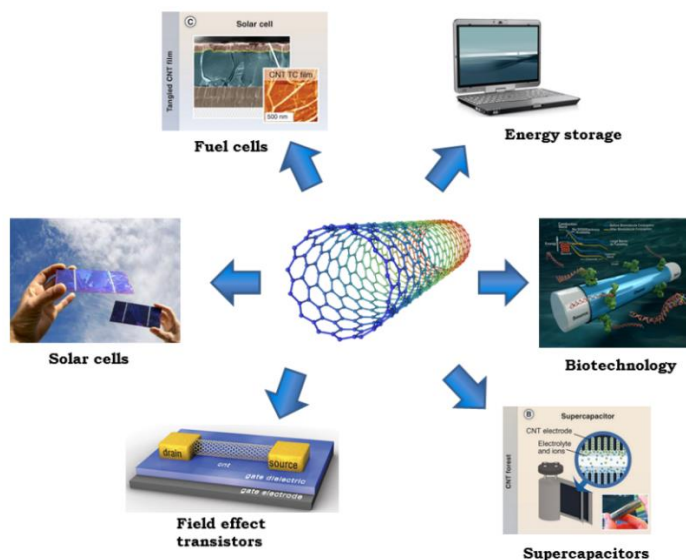


Figure 1-10. Overview of Applications of carbon nanotubes in different sectors.

³⁹ S. J. Tans, M. H. Devoret, H. J. Dai, A. Thess, R. E. Smalley, L. J. Geerligs, and C. Dekker, *Nature*, **1997**, 386, 474.

⁴⁰ C. Dekker, *Phys. Today*, **1999**, 52, 22.

One of the most significant potential applications of single-walled nanotubes is believed to be in the domain of nanoelectronics. This is as a result of SWCNT's being highly-conductive. In fact, SWCNTs ropes are the most conductive carbon fibers known. Alternative configurations of a carbon nanotube can result in the resultant material being semi-conductive like silicon. As previously mentioned, conductivity in nanotubes is based on the degree of chirality - *i.e.* the degree of twist and size of the diameter of the actual nanotube which results in a nanotube that is actually extremely conductive (making it suitable as an interconnect on an integrated circuit) or non-conductive (making it suitable as the basis for semi-conductors).

Interconnect

With high conductivity and small dimensions, carbon nanotubes may provide an alternative interconnect option to copper. Toshiba and Stanford University recently published a CNT-based interconnect operating at 1 GHz on a chip containing 11000 transistors on a chip.⁴¹ This research demonstrates that carbon nanotubes are not just a viable alternative to copper, but that they can also be used in manufacturing processes.

Field effect transistors

Field-effect transistors (FETs) are the basic building blocks of modern electronics. For decades, FETs have been built using semiconductors like silicon and gallium arsenide as active channel materials. These materials, however, are subject to well-established performance and processing limitations. Semiconducting carbon nanotubes are ideally suited to replace or complement traditional semiconductors in both high-performance and low-cost FET devices.⁴² A SWCNT, or an array of CNTs, are used as the channel material instead of bulk silicon. Alternative configurations of carbon-nanotubes result in defects being present that allow single-walled nanotubes to act as transistors. In such a switch, a molecule is positioned inside a carbon nanotube to affect the electronic current flowing across it. The result is a molecular gate in which the position of the molecule controls the flow of the electrical current. Thin film

⁴¹ G. F. Close, S. Yasuda, B. Paul, S. Fujita and H. S. P. Wong, *Nano Lett.*, **2008**, 8, 706.

⁴² J. M. Salazar-Rios, W. Gomulya, V. Derenskiy, J. Yang, S. Z. Bisri, Z. Chen, A. Facchetti and M. A. Loi, *Adv. Electron. Mat.*, **2015**, 8, 2015.

transistors (TFETs) with the best concurrent on/off ratios and on-drive currents have been reported in the literature.^{43,44}

Batteries

Most portable electronic devices use rechargeable lithium-ion batteries. These batteries release charge when lithium ions move between two electrodes, one of which is graphite and the other is metal oxide. Electrodes made of carbon nanotubes can be ten times thinner and lighter than amorphous carbon electrodes and their conductivity is more than one thousand times greater. Ultra-thin flexible batteries have been already made with CNT infused paper.^{45,46} These batteries can be rolled, folded, or cut without loss of efficiency.

Solar Cells

An organic solar cell is a type of polymer solar cell that uses organic electronics for light absorption and charge transport to produce electricity from sunlight by the photovoltaic effect. In the field of Organic Photovoltaics (OPVs), CNTs have been identified as promising candidates for numerous usages in solar cells, since SWCNTs possess a wide range of direct bandgaps matching the solar spectrum, strong photoabsorption, from infrared to ultraviolet, and high carrier mobility and reduced carrier transport scattering, which make themselves ideal photovoltaic materials.⁴⁷

An all carbon solar cell device is observed in Figure 1-11 in which the active layer is composed of a bilayer structure with semiconducting SWCNTs as the donor layer, and C₆₀ as the acceptor layer which separates hole-electron pairs (excitons) produced when light is absorbed by the SWNTs.⁴⁸

⁴³ M. Steiner, M. Engel, Y.-M. Lin, Y. Wu, K. Jenkins, D. B. Farmer, J. J. Humes, N. L. Yoder, J.-W. T. Seo, A. A. Green, M. C. Hersam, R. Krupke and P. Avouris, *Appl. Phys. Lett.*, **2012**, *101*, 053123.

⁴⁴ C. Wang, J. Zhang, K. Ryu, A. Badmaev, L. Gómez De Arco and C. Zhou, *Nano Lett.*, **2009**, *9*, 4285.

⁴⁵ L. F. Cui, L. Hu, J. W. Choi and Y. Cui, *ACS Nano*, **2010**, *4*, 3671.

⁴⁶ Z. Xiong, Y. S. Yun and H.-J. Jin, *Materials*, **2013**, *6*, 1138.

⁴⁷ G. Dinesha M. R. Dabera, M. R. Ranga Prabhath, K. T. Lai, K. D. G. Imalka Jayawardena, F. Laurent, M. Sam, Lynn J. Rozanski, A. A. Damitha, T. Adikaari, P. D. Jarowski, T. Pichler and S. R. P. Silva, *ACS Nano*, **2013**, *7*, 556.

⁴⁸ M. P. Ramuz, M. Vosgueritchian, P. Wei, C. Wang, Y. Gao, Z. Bao, *ACS Nano*, **2012**, *6*, 10384.

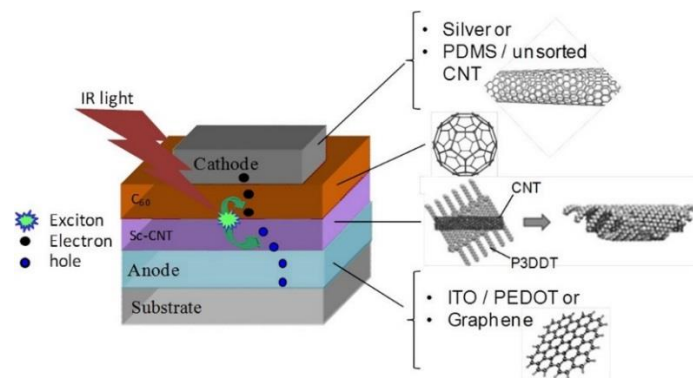


Figure 1-11. Structure of a carbon based solar cell, showing the components of each layer and the process of electron-hole pair generation and separation when light is absorbed.⁴⁸

A dye-sensitized solar cell, also called the Grätzel cell, is a low cost thin film solar cell that harnesses sunlight for photoexcitation of electrons to create an electrical current. Nanotubes have attracted a great deal of attention in this field of research to serve as potential replacements for expensive materials, reduce chemical stability problems, and increase conversion efficiency.⁴⁹

Drug delivery

In the last few years, many studies have suggested potential applications of CNTs in biomedical applications.^{50,51} Anti-cancer drugs may be delivered more efficaciously and with fewer systemic side-effects using a "smart" nanotechnology platform than by conventional methods. Small-diameter semiconducting SWCNTs represent one such promising platform, due to their strong absorbance in the so-called therapeutic infrared window (between 700-1100 nm, depending on body tissue type). Functionalization of SWCNTs has proven to enhance solubility and allow for efficient tumor targeting/drug delivery. Cancer, a group of diseases in which cells grow and divide abnormally, is one of the primary diseases being looked at with regards to how it responds to CNT drug delivery. Current cancer therapy primarily involves surgery, radiation therapy, and chemotherapy. These methods of treatment are usually

⁴⁹ X. Dang, H. Yi, M-H Ham, J. Qi, D. S. Yun, R. Ladewski, M. S. Strano, P. T. Hammon and A. M. Belcher, *Nat. Nanotech.*, **2011**, 6, 377.

⁵⁰ A. Eatemadi, H. Daraee, H. Karimkhanloo, M. Kouhi, N. Zarghami, A. Akbarzadeh, A. Mozhgan, Y. Hanifepour and S. W. Joo, *Nanoscale Res. Lett.*, **2014**, 9, 393.

⁵¹ G. Hong, S. Diao, A. L. Antaris and H. Dai, *Chem. Rev.*, **2015**, 115, 4823.

painful and kill normal cells in addition to producing adverse side effects. CNTs as drug delivery vehicles have shown potential in targeting specific cancer cells with a dosage lower than conventional drugs used,⁵² that is just as effective in killing the cells, however does not harm healthy cells and significantly reduces side effects.

1.1.4. Chemical functionalization

The chemical functionalization of CNTs has been one of the most studied topics from the beginning of the carbon nanostructures era.^{53,54,55,56,57} Due to the strong van der Waals forces that occur for such atomically flat structures, pristine carbon nanotubes tend to form insoluble bundles that limit their potential applications.⁵⁸ The addition of functional groups to the nanotube sidewalls disrupts these forces and enables good dispersion in a variety of solvents, including water, increasing the potential of this materials for several applications.⁵⁹

Among the methods known to modify the surface properties of CNTs are included defect functionalization, covalent functionalization of the sidewalls, non-covalent functionalization and endohedral functionalization (Figure 1-12).⁶⁰

⁵² C. Srinivasan, *Curr. Sci.*, **2008**, *94*, 300.

⁵³ N. Karousis, N. Tagmatarchis and D. Tasis, *Chem. Rev.*, **2010**, *110*, 5366.

⁵⁴ a) F. Langa and J.F Nierengarten, "Fullerenes: Principles and applications", RSC Publishing, **2012**; b) D.M. Guldi and N. Martín, *Carbon Nanotubes and related structures*, Wiley-VCH Verlag GmbH & Co. KGaA, **2010**.

⁵⁵ S. Basu-Dutt, M. L. Minus, R. Jain, D. Nepal and S. Kumar, *J. Chem. Edu.* **2012**, *89*, 221.

⁵⁶ T. Akasaka, F. Wudl and S. Nagase, "Chemistry of Nanocarbons", Ed. John Wiley & Sons, Chichester, UK, **2010**.

⁵⁷ D. Tasis, N Tagmatarchis, A. Bianco and M. Prato, *Chem. Rev.*, **2006**, *106*, 1105.

⁵⁸ V. Sgobba and D. M. Guldi, *Chem. Soc. Rev.*, **2009**, *38*, 165.

⁵⁹ Z. Yang, J. Ren, Z. Zhang, X. Chen, G. Guan, L. Qiu, Y. Zhang and H. Peng, *Chem. Rev.*, **2015**, *115*, 5159.

⁶⁰ A. Hirsch, *Angew. Chem. Int. Ed.* **2002**, *41*, 1853.

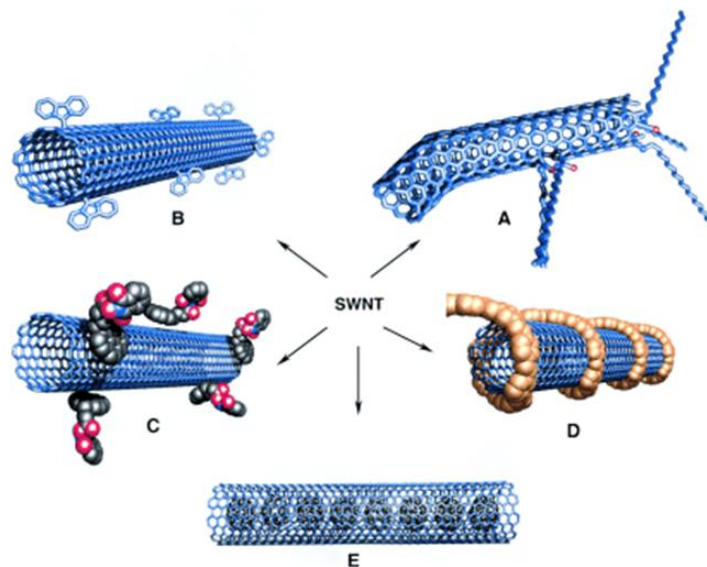


Figure 1-12. Functionalization possibilities for CNTs: A) defect-group functionalization, B) covalent sidewall functionalization, C) non-covalent functionalization with surfactants, D) non-covalent functionalization with polymers, and E) endohedral functionalization with, for example, C_{60} .⁶⁰

The covalent modification by different reactions on the walls or defects allows an improvement in dispersibility, at the time that different groups can be attached to the nanotube modifying the properties of the material. Concretely in the case of functionalization on the walls, when double bonds in the nanotube become saturated, the electronic properties are affected. The main inconvenient of this method is how to control the functionalization degree. A large excess of functionalization could involve a severe degradation in mechanical properties of CNTs as well as disruption of π electron system in nanotubes.

From a practical point of view, supramolecular solubilization of CNTs is more attractive, because the intrinsic properties remain intact, without altering its electronic structure.⁶¹ The interactions that stabilize these kind of complexes are usually weak and depending on several parameters, such as, temperature, pH, etc...which is an important drawback of this kind of functionalization.⁶²

⁶¹ R. Martel, *ACS Nano*, **2008**, *2*, 2195.

⁶² M. Melchionna and M. Prato, *J. Solid State Sci. Technol.*, **2013**, *2*, 3040.

The chemical reactivity of carbon nanotubes strongly depends also on the lengths, chiralities or diameters of the materials.^{63,64} Although graphene, fullerene and carbon nanotubes are built from the same basic element, the chemical reactivity is substantially different among them. In a nanotube, orbitals have an orientation which is different from that of the s- and p-orbitals in graphite and fullerene. This distortion can be described by the pyramidalization angle (θ_p) (Figure 1-13).^{65,66} θ_p is defined by the angle between the π orbital and σ bond minus 90° . A large pyramidalization angle of the carbon atom indicates higher reactivity towards addition reactions. In this aspect, graphene with a planar structure is the less reactive with a pyramidalization angle of $\theta_p = 0^\circ$. However the rolling of graphene sheet into a CNT induces strain, and the increase of strain will be related with the deviation from planarity. The strain is inversely related to the degree of curvature, thus they exhibit varying degrees of pyramidalization depending on the tube diameter. Therefore it can be inferred that chemical reactivity is directly related to the nanotube diameter, being more reactive those with smaller diameters. However their curvature will be always lower than that of C_{60} , consequently being less reactive than C_{60} molecules and more reactive than a graphene sheet. The angle between the π orbital of a carbon atom in C_{60} and the σ -skeleton forming the curved surface is 101.6° , and hence all the carbon atoms in C_{60} have a pyramidalization angle of $\theta_p = 11.6^\circ$, being the most reactive as abovementioned.

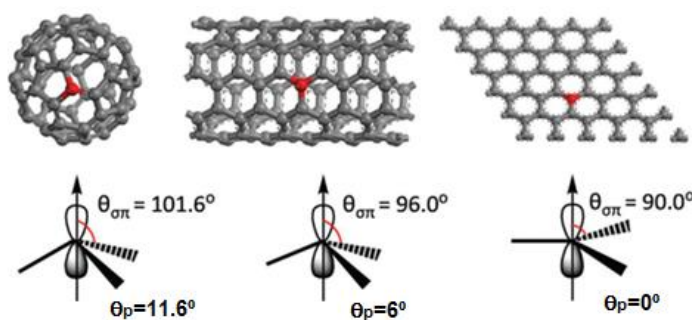


Figure 1-13. Pyramidalization angles for C_{60} , carbon nanotube and graphene. Pyramidal angle (θ_p) is defined by the angle between π orbital and σ bond minus 90° .

⁶³ A. Hirsch and O. Vostrowsky, *Top. Curr. Chem.*, **2005**, 245, 193.

⁶⁴ Z. Chen, W. Thiel and A. Hirsch, *ChemPhysChem*, **2003**, 4, 93.

⁶⁵ R. C. Haddon, *Science*, **1993**, 261, 1545.

⁶⁶ A. Hirsch, *Top. Curr. Chem.*, **1998**, 198, 1.

The other factor that governs reactivity in conjugated nonplanar molecules is the π -orbital misalignment (Φ), between adjacent pairs of conjugated carbon atoms (Figure 1-14).⁶⁷ There is very little π -orbital misalignment in the fullerenes, and in the case of C_{60} the π -orbital alignment is perfect because of the quasi-spheroidal geometry, so the reactivity is governed essentially by the pyramidalization factor.

In the case of carbon nanotubes, there are two types of carbon-carbon bonds in the sidewall: one is parallel to the circumference plane, whereas the other lies at an angle to the circumference plane. The first one shows a perfect alignment of the lobes of the p-orbitals, whereas the second bonding geometry requires a twist of the π -bond. In the last case, the angle between the lobes of the p-orbitals of the adjacent carbon atoms will differ from zero and this is a source of strain in the carbon nanotubes that is almost totally absent in the fullerenes. This strain due to orbital misalignment leads to a differentiation between the bonds in the CNTs that may be reflected in their relative reactivity.

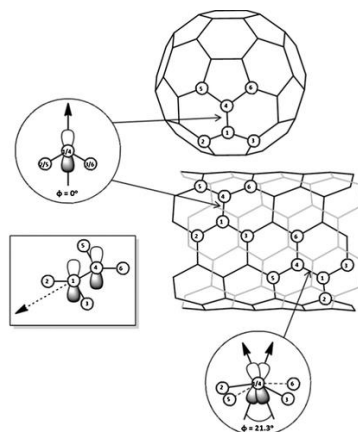


Figure 1-14. The π -orbital misalignment angles in the (5, 5) SWCNT and fullerene.

Covalent functionalization on the defects

The introduction of covalently linked groups over the wall of CNTs produces a disruption of the sp^2 conjugation of the tubes altering its electronic properties. Although those new functionalities create defects and tend to diminish the conducting properties of the tubes, they open many opportunities

⁶⁷ R. C. Haddon, *J. Am. Chem. Soc.* **1990**, *112*, 3385.

towards the dissolution and implementation of new functionalities with new properties.

Covalent functionalization is based on the covalent bond of functional groups onto CNTs, which can be performed on the defects of nanotubes or at their sidewalls. The sidewalls themselves contain defect sites such as pentagon-heptagon pairs called Stone-Walls defects, sp^3 -hybridized defects, and vacancies in the nanotube lattice⁶⁰ (Figure 1-15). These intrinsic defects are supplemented by oxidative damage to the nanotube framework by strong acids which leave holes functionalized with oxygenated functional groups.^{68,69} In particular, treatment of CNTs with strong acid such as HNO_3 , H_2SO_4 or a mixture of them,^{70,71} or with strong oxidants such as $KMnO_4$,⁷² tend to open these tubes and to subsequently generate oxygenated functional groups such as carboxylic acid, ketone, alcohol and ester groups, that serve to link many different types of chemical moieties onto the ends and defect sites of these tubes. These functional groups present a rich chemistry and the CNTs can be used as precursors for further chemical reactions.

⁶⁸ J. Chen, M. A. Hamon, H. Hu, Y. Chen, A. M. Rao, P. C. Eklund and R. C. Haddon, *Science*, **1998**, 282, 95.

⁶⁹ J. Zhang, H. Zou, Q. Qing, Y. Yang, Q. Li, Z. Liu, X. Guo and Z. Du, *J. Phys. Chem. B*, **2003**, 107, 3712.

⁷⁰ A. G. Rinzler, J. Liu, H. Dai, P. Nikolaev, C. B. Huffman, F. J. Rodríguez-Macías, P. J. Boul, A. H. Lu, D. Heymann, D. T. Colbert, R. S. Lee, J. E. Fischer, A. M. Rao, P. C. Eklund and R. E. Smalley, *Applied Physics A*, **1998**, 67, 29.

⁷¹ F. Langa and P. de la Cruz, *Comb. Chem. High Throughput Screen*, **2007**, 10, 766.

⁷² R. Yu, L. Chen, Q. Liu, J. Lin, K. L. Tan, S. Chon, H. Chang, G. Xu and T. S. Andy, *Chem Mater.*, **1998**, 10, 718.

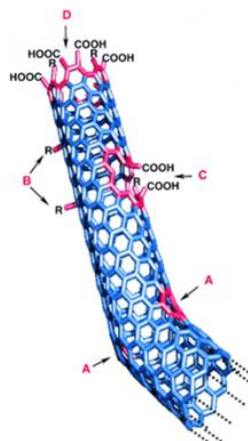


Figure 1-15. Typical defects in SWCNTs. A) Five or six-membered rings in the carbon lattice, B) sp^3 -hybridized defects, C) Carbon lattice damaged by oxidative conditions and D) open end of the SWCNT, terminated with COOH groups.⁶⁰

The presence of carboxyl groups leads to a reduction of van der Waals interactions between the CNTs, which strongly facilitates the separation of nanotube bundles into individual tubes. Carboxyl groups on the surface of acid-treated CNTs are often used for the creation of ester⁷³ or amide bonds.⁷⁴ Normally, this kind of functionalization takes place after replacing the carboxyl groups by acyl chlorides after SOCl_2 treatment (Figure 1-16).

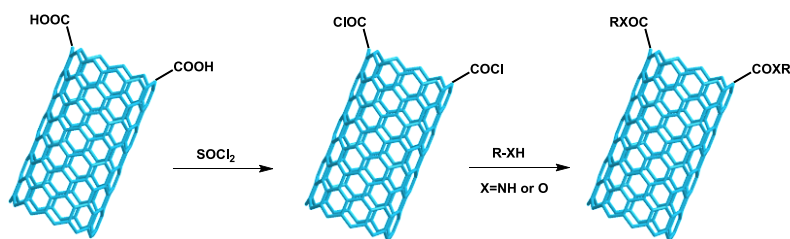


Figure 1-16. Ester or amide bonds formation from the acyl chloride derivatives.

As mentioned above, further chemical reactions can be performed onto the defects to build the desired functionality, such as silanization,⁷⁵ polymer

⁷³ M. Hamon, H. Hui, P. Bhowmik, M. E. Itkis and R. C. Haddon, *Appl. Phys. A: Mater. Sci. Process.*, **2002**, 74, 333.

⁷⁴ C. H. Andersson and H. Grennberg, *Eur. J. Org. Chem.*, **2009**, 26, 4421.

⁷⁵ P. C. Ma, J. K. Kim and B. Z. Tang, *Carbon*, **2006**, 44, 3232.

grafting,⁷⁶ esterification,^{68,77} thiolation,⁷⁸ alkylation and arylation,⁷⁹ and even some biomolecules⁸⁰ (Figure 1-17). The CNTs functionalized in this way are soluble in many organic solvents because the hydrophobic nature of CNTs is changed to hydrophilic one, due to the attachment of polar groups. However this method have an important drawback. During the functionalization reaction, a large number of defects are inevitably created on the CNT sidewalls and new defects are induced, disrupting the structural integrity of the nanotube.⁸¹

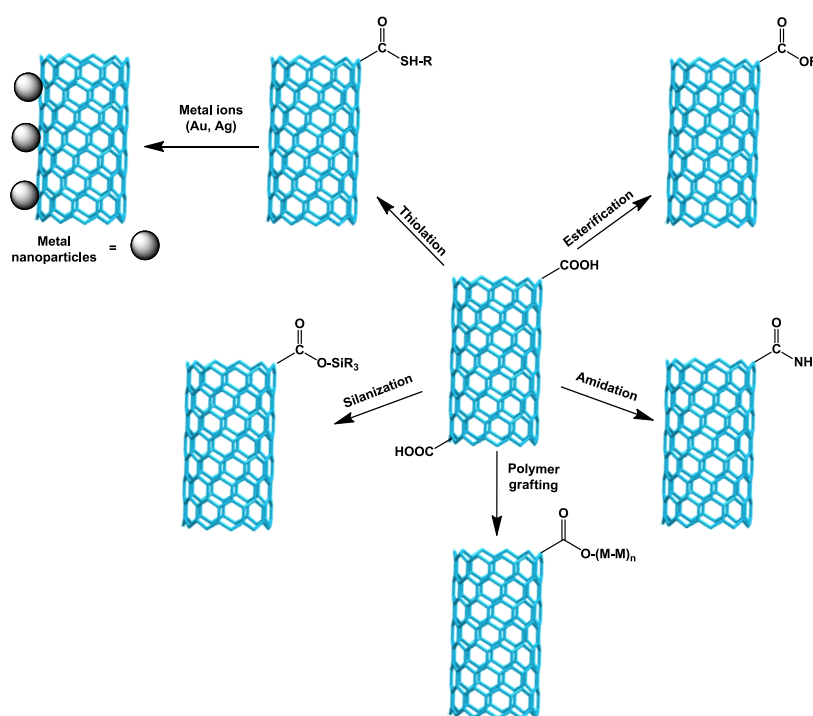


Figure 1-17. Strategies for covalent functionalization on the defects.

⁷⁶ P. Liu, *Eur. Polym. J.*, **2005**, *41*, 2693.

⁷⁷ M. Álvaro, P. Atienzar, P. De la Cruz, J. L. Delgado, V. Troiani, H. García, F. Langa, A. Palkar and L. Echegoyen, *J. Am. Chem. Soc.*, **2006**, *128*, 6626.

⁷⁸ J. Liu J, A. G. Rinzler, H. J. Dai, J. F. Hafner, R. K. Bradley, P. J. Boul, A. Lu, T. Iverson, K. Shelimov, C. B. Huffman, F. Rodriguez-Macias, Y. S. Shon, T. R. Lee, D. T. Colbert, and R. E. Smalley, *Science*, **1998**, *280*, 1253.

⁷⁹ J. J. Stephenson, A. K. Sadana, A. L. Higginbotham and J. M. Tour, *Chem. Mater.*, **2006**, *18*, 4658.

⁸⁰ J. N. Coleman, U. Khan and Y. K. Gunko, *Adv. Mater.*, **2006**, *18*, 689.

⁸¹ M. Monthieux, B.W. Smith, B. Burtiaux, A. Claye, J. E. Fischer and D.E. Luzzi, *Carbon*, **2001**, *39*, 1251.

Covalent functionalization on the wall

While the two-step functionalization of nanotubes through the oxidative introduction of carboxyl groups followed by the formation of amide or ester linkages does allow the chemical modification, it has only a relatively weak influence on the electrical and mechanical properties of the nanotubes. By comparison, the direct coupling of functional groups onto the π -conjugated carbon framework of the tubes, opens the possibility of further modification on the aforementioned properties.

Because of the low reactivity of CNTs, fluorination was taken into consideration as one of the first sidewall functionalization reactions in 1996.⁸² The fluorine atoms in fluorinated carbon nanotubes can be replaced through nucleophilic substitution reactions with relative ease, thus opening a flexible approach for providing the sidewalls with various types of functional groups.

Upon the large quantity of chemical procedures described in the literature, the 1,3-dipolar cycloaddition of azomethine ylides (*Prato reaction*) and the treatment of CNTs with aryldiazonium salts are probably the most employed ones (Figure 1-18). The Prato reaction was first described for the functionalization of fullerenes^{83,84} and some years later it was extended to carbon nanotubes.⁸⁵ The functionalization methodology is based on the 1,3-dipolar cycloaddition of azomethine ylides, generated by condensation of an α -amino acid and an aldehyde.

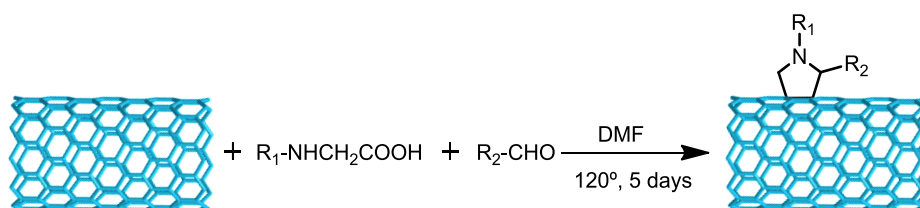


Figure 1-18. 1,3-dipolar cycloaddition on carbon nanotubes (Prato reaction).

As observed, the surface of the nanotube is functionalized with pyrrolidine rings, which permits the introduction of two different functionalities

⁸² T. Nakajima, S. Kasamatsu and Y. Matsuo, *Eur. J. Solid State Inorg. Chem.*, **1996**, 33, 831.

⁸³ M. Maggini, G. Scorrano and M. Prato, *J. Am. Chem. Soc.*, **1993**, 115, 9798.

⁸⁴ M. Prato and M. Maggini, *Acc. Chem. Res.*, **1998**, 31, 519.

⁸⁵ V. Georgakilas, K. Kordatos, M. Prato, D. M. Guldi, M. Holzinger, and A. Hirsch, *J. Am. Chem. Soc.*, **2002**, 124, 760.

allowing the modification of the properties. A great number of functional groups including, for example, porphyrins,⁸⁶ phthalocyanines⁸⁷ or ferrocene derivatives,⁸⁸ have been attached through this method to the CNT (Figure 1-19).

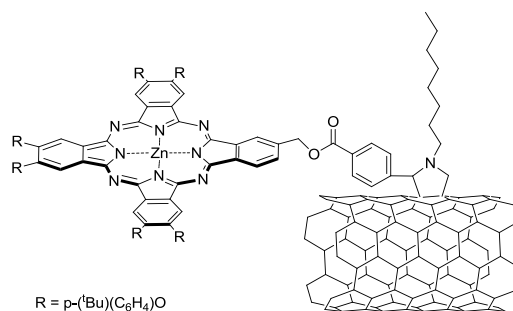


Figure 1-19. Porphyrin derivative attached through 1,3-dipolar cycloaddition of an azomethine ylide.⁸⁷

Apart from the abovementioned 1,3-dipolar cycloaddition, many other different cycloaddition reactions have been tried on CNTs during the last decade. Langa *et al.* reported a new method for CNT modification by thermal 1,3-dipolar cycloaddition of nitrile imines under microwave conditions (Figure 1-20).⁸⁹ Laser flash photolysis in dynamic flow of these carbon nanotubes in acetonitrile revealed the formation of several transient species decaying in the microsecond time scale.

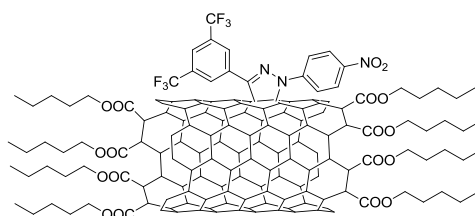


Figure 1-20. Modification of SWCNTs through 1,3-dipolar cycloaddition of nitrile imines.⁸⁹

⁸⁶ S. Campidelli, C. Sooambar, E. Lozano Diz, C. Ehli, D. M. Guldi, M. Prato, *J. Am. Chem. Soc.*, **2006**, *128*, 12544.

⁸⁷ B. Ballesteros, G. de la Torre, C. Ehli, G. M. A. Rahman, F. Agulló-Rueda, D.M. Guldi, and T. Torres, *J. Am. Chem. Soc.*, **2007**, *129*, 5061.

⁸⁸ N. Tagmatarchis, M. Prato and D. M. Guldi, *Physica E.*, **2005**, *29*, 546.

⁸⁹ M. Alvaro, P. Atienzar, P. de la Cruz, J. L. Delgado, H. García and F. Langa, *J. Phys. Chem. B*, **2004**, *108*, 12691.

Two years later, the 1,3-dipolar cycloaddition of a nitrile oxide on the SWCNT walls was reported also by Langa *et al.*⁹⁰ Now, pyridyl isoxazoline groups were attached to the sidewall of the nanotubes through the mentioned approach. Thereafter, a metal-ligand complex with zinc porphyrin was obtained and photochemical studies were performed.

[2+1] nitrene addition was studied by Takagaki *et al.*, where substituted $C_{2}B_{10}$ carborane cages were successfully attached to the side walls of SWCNTs (Figure 1-21).⁹¹ This hybrid revealed to show a high affinity for tumoral cells in the treatment of cancer. Another widely used [2+1] cycloaddition is the Bingel cyclopropanation reaction (Figure 1-21), in which a bromomalonate serves as a formal precursor of carbene and reacts with CNTs leading to a cyclopropane ring formation.

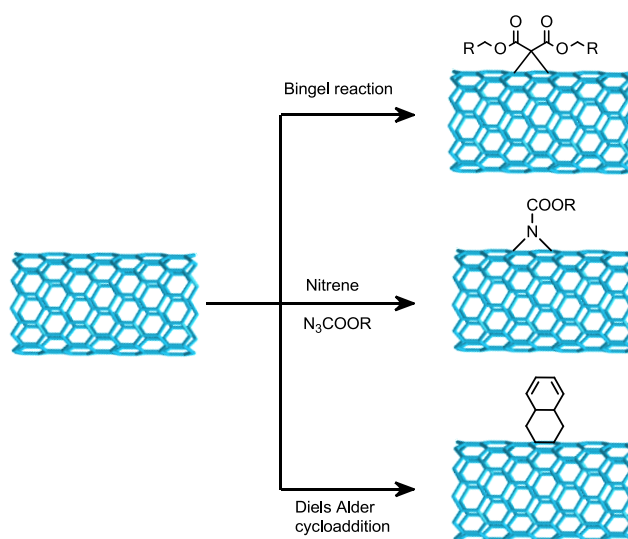


Figure 1-21. Functionalization of carbon nanotubes by cycloaddition reactions.

The Bingel reaction has been widely employed for the functionalization of fullerenes and was described for the first time on CNTs by Green *et al.*⁹² The

⁹⁰ M. Alvaro, P. Atienzar, P. de la Cruz, J. L. Delgado, V. Troiani, H. García, F. Langa, A. Palkar and L. Echegoyen, *J. Am. Chem. Soc.*, **2006**, *128*, 6626.

⁹¹ Z. Yinghuai, A. T. Peng, K. Carpenter, J. A. Maguire, N. S. Hosmane and M. Takagaki, *J. Am. Chem. Soc.*, **2005**, *127*, 9875.

⁹² K. S. Coleman, S. R. Bailey, S. Fogden and M. L. H. Green, *J. Am. Chem. Sci.*, **2003**, *125*, 8722.

carboxylate groups attached on the CNTs can be further derivatized for other applications.

Another cycloaddition reaction that have also been reported for the functionalization of CNTs is the Diels–Alder cycloaddition [4 +2] cycloaddition (Figure 1-21). A molecular modeling approach predicted this cycloaddition by observing the possible aromaticity stabilization at the corresponding transition states and products.

In this sense, our group performed the Diels–Alder cycloaddition of *o*-quinodimethane to SWCNT under microwave irradiation,⁹³ confirming the viability of Diels–Alder cycloaddition on the sidewall of carbon nanotubes. More recently, the cycloaddition of benzyne to SWCNT has been developed also in our group.^{94,95} Cycloaddition of benzyne to SWCNT can form the [2+2] or [4+2] adduct. Theoretical calculations suggested that both approaches were possible in this case, being the [4+2] product more stable (Figure 1-22).

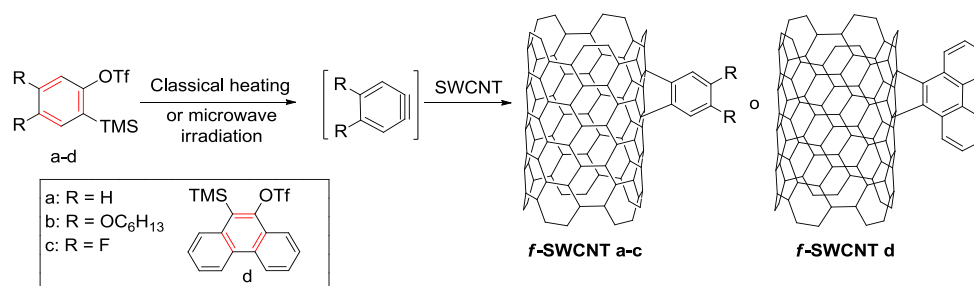


Figure 1-22. Modification of SWCNTs through the [4+2] cycloaddition of benzyne.⁹⁴

The other widely used approach to functionalize carbon nanotubes, the Tour reaction, consist in the chemical addition of aryl diazonium salts *via* highly reactive aryl radicals. The functionalization with diazonium salts⁹⁶ can be

⁹³ J. L. Delgado, P. Cruz, F. Langa, A. Urbina, J. Casado and J. T. L. Navarrete, *Chem. Commun.*, **2004**, 1734.

⁹⁴ A. Criado, M. Vizuete, M. J. Gómez-Escalonilla, S. García-Rodríguez, J. L. G. Fierro, A. Cobas, D. Peña, E. Guitián and F. Langa, *Carbon*, **2013**, 63, 140.

⁹⁵ A. Criado, M. J. Gómez-Escalonilla, J. L. G. Fierro, A. Urbina, D. Peña, E. Guitián and F. Langa, *Chem. Commun.*, **2010**, 46, 7028.

⁹⁶ (a) J. L. Bahr and J. M. Tour, *Chem. Mater.*, **2001**, 13, 3823; (b) S. M. Chergui, A. Ledebt, F. Mammeri, F. Herbst, B. Carbonnier, H. B. Romdhane, M. Delamar and M. M. Chehimi, *Langmuir*, **2010**, 26, 16115.

performed either by the reaction between a diazonium salt previously prepared and a CNT, or by the *in situ* generation of the desired diazonium salt in the presence of isoamyl nitrite (Figure 1-23). In both cases, a free radical species is obtained through the reduction of the diazonium salt. This method allows the functionalization of the sp^2 -carbon lattice with a wide variety of functional groups and it is the most widely used method for CNTs functionalization to increase their processability and add new functionalities. Examples of reactions performed on the aryl addend after functionalization with diazonium salts have been the Heck cross coupling reaction⁹⁷ and Suzuki coupling reactions.⁹⁸

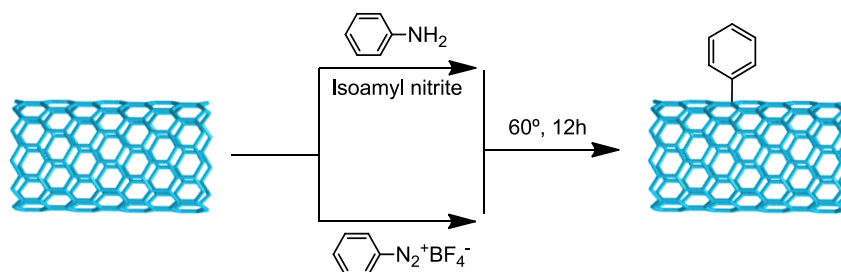


Figure 1-23. Functionalization of carbon nanotubes with diazonium salts (*Tour* reaction).

As an example, in Figure 1-24 is showed the functionalization of single-walled carbon nanotubes (SWNTs) *via* the Heck cross-coupling reaction of pre-functionalized *p*-iodophenyl SWNTs.

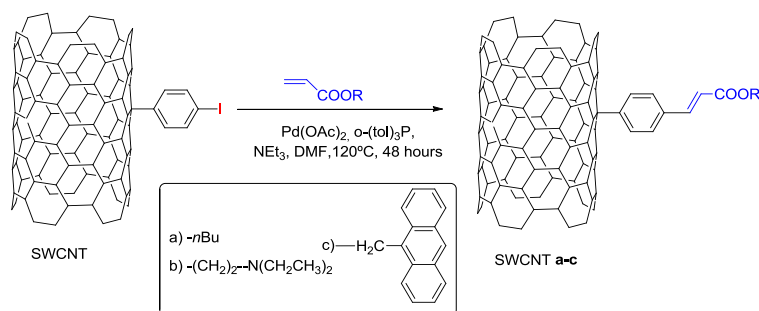


Figure 1-24. Modification of SWCNTs through Heck reaction onto an aryl addend previously attached to the nanotube through *Tour* reaction.⁹⁷

⁹⁷ M. J. Gómez-Escalonilla, P. Atienzar, J. L. García Fierro, H. García and F. Langa, *J. Mater. Chem.* **2008**, *18*, 1592.

⁹⁸ F. Cheng and A. Adronov, *Chem. Mater.*, **2006**, *18*, 5389.

Recently, Imahori *et al.* reported a iodophenyl functionalized SWCNT which was allowed to react through Suzuki coupling reaction with a pyrene boronic ester (Figure 1-25).⁹⁹

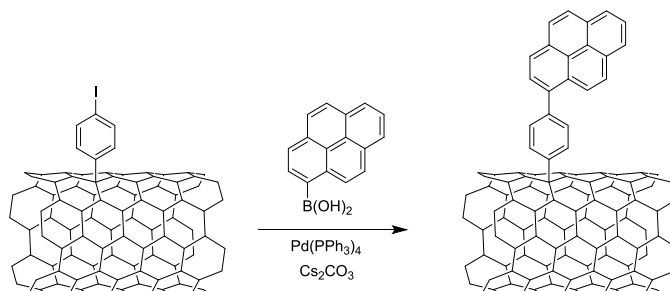


Figure 1-25: Modification of SWCNTs through Suzuki coupling onto an aryl addend previously attached to the nanotube through *Tour* reaction.⁹⁹

Among the wide number of substituents that can be introduced *via* Tour reaction, the attachment of acetylene derivatives is probably the most widely employed, since, as aforementioned, it opens the way to further functionalization of the nanotube *via* “click” chemistry.^{100,101,102,103} “Click” Chemistry is a term that was introduced by K. B. Sharpless in 2001¹⁰⁴ to describe a pair of functional groups that rapidly and selectively react (“click”) with each other under mild conditions. One of the most popular reactions within the *Click* chemistry concept is the azide alkyne Huisgen cycloaddition using a Copper (Cu) catalyst at room temperature (CuAAC) (Figure 1-26). The use of a copper catalyst permits the selective access to the 1, 4- regioisomer of the triazole. In 2005 the group of Adronov reported for the first time the fabrication of SWCNT-polystyrene (PS) hybrids using the CuAAC reaction.¹⁰⁵

⁹⁹ T. Umeyama¹, J. Baek, Y. Sato, K. Suenaga, F. Abou-Chahine, N. V. Tkachenko, H. Lemmetyinen and H. Imahori, *Nat. Commun.* **2015**, *6*, 7732.

¹⁰⁰ T. Palacin, H. L. Khanh, B. Jousseleme, P. Jegou, A. Filoramo, C. Ehli, D. M. Guldi and S. Campidelli, *J. Am. Chem. Soc.*, **2009**, *131*, 1534.

¹⁰¹ S. Campidelli, B. Ballesteros, A. Filoramo, D.D. Díaz, G. de la Torre, T. Torres, G. M. Aminur Rahman, C. Ehli, D. Kiessling, F. Werner, V. Sgobba, D. M. Guldi, C. Cioffi, M. Prato and J.-P. Bourgoïn, *J. Am. Chem. Soc.*, **2008**, *130*, 11503.

¹⁰² G. Clavéa and S. Campidelli, *Chem. Sci.*, **2011**, *2*, 1887.

¹⁰³ G. Tuci, C. Vinattieri, L. Luconi, M. Ceppatelli, S. Cicchi, A. Brandi, J. Filippi, M. Melucci and G. Giambastiani, *Chem. Eur.* **2012**, *18*, 8454.

¹⁰⁴ C. Hartmuth, M. G. Kolb, K. Finn and B. Sharpless, *Angew. Chem. Int. Ed.*, **2001**, *40*, 2004.

¹⁰⁵ H. Li, F. Cheng, A. M. Duft and A. Adronov, *J. Am. Chem. Soc.*, **2005**, *127*, 14518.

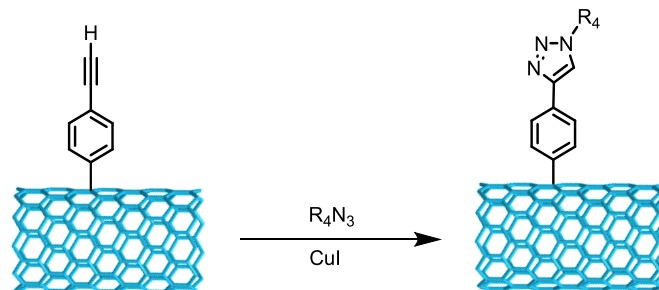


Figure 1-26. Schematic representation of the *click* reaction on carbon nanotubes.

This method has been also used, for example, by Campidelli *et al.* to decorate SWCNTs with phthalocyanines in order to construct interesting devices oriented to photovoltaics (Figure 1-27),¹⁰¹ or by Zheng *et al.* which employed it for the chemical modification of SWCNTs with β -cyclodextrin thus creating an useful hybrid oriented to drug delivery.¹⁰⁶

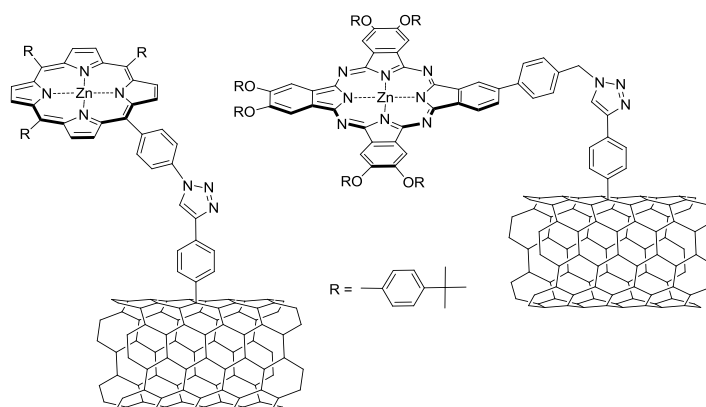


Figure 1-27. Modification of SWCNTs through CuAAC reaction onto aryl addend previously attached to the nanotube through *Tour* Reaction.

Nucleophilic and electrophilic additions onto the sidewall of the nanotubes have been also reported in the last decade (Figure 1-28). Prato *et al.* reported electrophilic addition of chloroform to SWCNTs in the presence of Lewis acid followed by hydrolysis resulting in the addition of hydroxyl groups to the surface of CNTs.¹⁰⁷ Further esterification with propionyl chloride to the corresponding ester derivatives, which greatly increased the solubility of

¹⁰⁶ Z. Guo, L. Liang, J. J. Liang, Y. F. Ma, X. Y. Yang, D. M. Ren, Y. S. Chen, J. Y. Zheng, *J. Nanopart. Res.*, **2008**, *10*, 1077.

¹⁰⁷ N. Tagmatarchis, V. Georgakilas, M. Prato and H. Shinohara, *Chem. Commun.*, **2002**, 2010.

SWCNTs. Another versatile electronic addition to SWCNTs was carried out by Balaban *et al.* under Friedel–Crafts conditions (Figure 1-28) to afford polyacylate nanotubes.¹⁰⁸ This renders CNTs highly dispersible in organic solvents. The first nucleophilic addition to CNTs was reported by Hirsh *et al.*¹⁰⁹ The addition of nucleophilic carbenes to the sidewall of CNTs was carried out. A few years later they reported the nucleophilic addition of organolithium and organomagnesium derivatives to SWCNT (Figure 1-28).¹¹⁰

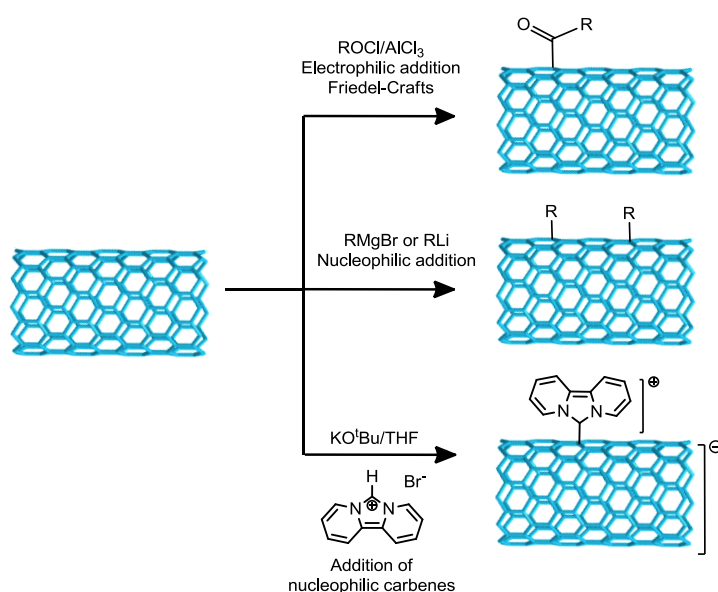


Figure 1-28. Sidewall functionalization by nucleophilic and electrophilic additions.

Covalent functionalization on Double-Walled Carbon Nanotubes

Similar to SWCNTs, DWCNTs are uniquely characterized by the chiral indices of the constituent inner and outer walls $(n_i, m_i)@(n_o, m_o)$, where each wall can be either semiconducting (S) or metallic (M). This gives rise to four possible combinations of inner@outer wall; namely, M@M, M@S, S@M, and S@S.¹⁷

¹⁰⁸ T. S. Balaban, M. C. Balaban, S. Malik, F. Hennrich, R. Fischer, H. Rosner and M. M. Kappes, *Adv. Mater.*, **2006**, *18*, 2763.

¹⁰⁹ M. Holzinger, O. Vostrowsky, A. Hirsch, F. Hennrich, M. Kappes, R. Weiss and F. Jellen, *Angew. Chem. Int. Ed.*, **2001**, *40*, 4002.

¹¹⁰ D. Wunderlich, F. Hauke and A. Hirsch, *Chem. Eur. J.*, **2008**, *14*, 1607.

As mentioned before, covalent functionalization has the unfortunate consequence of disturbing the electronic and optical properties that make carbon nanotubes an attractive material in the first place. Utilizing double-walled carbon nanotubes (two nested single-walled carbon nanotubes) provides an outer wall on which to tailor the surface properties, protecting the inner wall from covalent functionalization, thus preserving the conductivity (Figure 1-29).^{18,19,111,112,113,114}

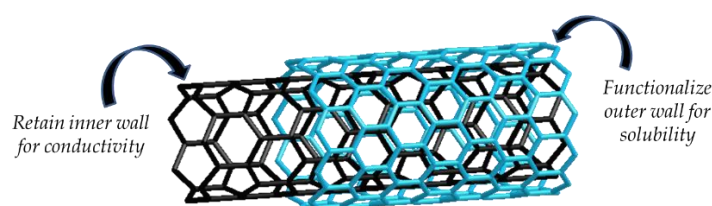


Figure 1-29. Covalent outer wall functionalization on DWCNTs.

Furthermore, changes to the chemical or electrochemical environment at the surface of the outer wall have been shown to induce electrical changes to the inner wall of the nanotube, suggesting the possibility of sensitive chemical detection *via* charge transport through the protected inner wall.^{115,116}

Functionalization of DWCNTs have been performed for example with aryldiazonium salts,¹¹⁷ fluorine atoms,^{118,119} through covalent functionalization on the defects and π - π interactions with porphyrins.¹²⁰

¹¹¹ C. Shen, A. H. Brozena and Y. Wang, *Nanoscale*, **2011**, 3, 503.

¹¹² S. Deng, Y. Piao, A. H. Brozena and Y. Wang, *J. Mater. Chem.*, **2011**, 21, 18568.

¹¹³ M. Vizuete, M. J. Gómez-Escalonilla, J. L. G. Fierro, P. Atienzar, H. García and F. Langa, *ChemPhysChem* **2014**, 15, 100.

¹¹⁴ M. Vizuete, M. J. Gómez-Escalonilla, S. García-Rodríguez, J. G. Fierro, P. Atienzar, H. García and F. Langa, *Chem. Eur. J.*, **2012**, 18, 16922.

¹¹⁵ M. Kalbac, A. A. Green, M. C. Hersam and L. Kavan, *ACS Nano*, **2010**, 4, 459.

¹¹⁶ M. Kalbac, A. A. Green, M. C. Hersam and L. Kavan, *Chem. Eur. J.*, **2011**, 17, 9806.

¹¹⁷ D. Bouilly, J. Cabana, F. Meunier, M. Desjardins-Carriere, F. Lapointe, P. Gagnon, F. L. Larouche, E. Adam, M. Paillet and R. Martel, *ACS Nano*, **2011**, 5, 4927.

¹¹⁸ H. Muramatsu, Y. A. Kim, T. Hayashi, M. Endo, A. Yonemoto, H. Arikai, F. Okino and H. Touhara, *Chem. Commun*, **2005**, 2002.

¹¹⁹ R. Zbořil, F. Karlický, A. B. Bourlinos, T. A. Steriotis, A. K. Stubos, V. Georgakilas, K. Šafářová, D. Jančík, C. Trapalis and M. Otyepka, *Small*, **2010**, 6, 2885.

¹²⁰ C. Aurisicchio, R. Marega, V. Corvaglia, J. Mohanraj, R. Delamare, D. A. Vlad, C. Kusko, C. A. Dutu, A. Minoia, G. Deshayes, O. Coulembier, S. Melinte, P. Dubois, R. Lazzaroni, N. Armaroli and D. Bonifazi, *Adv. Funct. Mat.*, **2012**, 22, 3209.

Bouilly *et al.*¹²¹ introduced the use of covalent functionalization with aryldiazonium salts on the outer wall of DWCNTs, in order to study the electrical transport occurring in the resulting materials. For the sake of comparison, the study was also performed on individual SWNTs. They observed that functionalization on SWCNTs had a dramatic current reduction, however, for DWCNTs this reduction was considerably less than in the case of SWCNTs. This proved unambiguously that the inner wall in DWCNTs can transport electrical current.

Recently in our group has been reported the synthesis of DWCNTs functionalized with dimethylanilino groups (Figure 1-30).¹²² Nanosecond laser flash photolysis showed shorter lived transients when compared to SWCNTs because of the influence of the inner wall.

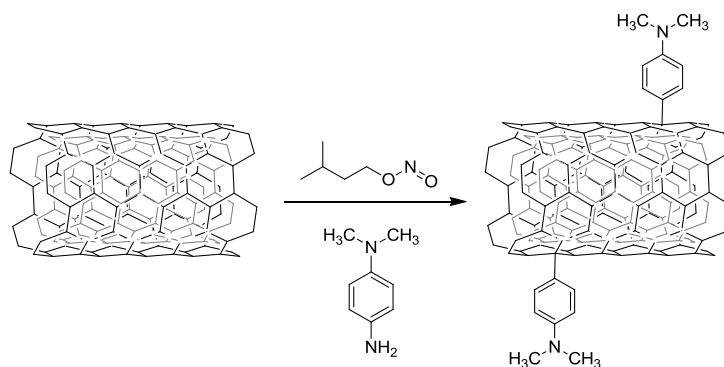


Figure 1-30: Modification of the outer wall of DWCNTs with dimethylanilino groups.¹²²

In summary, DWCNTs can be modified through the same reactions that SWCNTs, the only different being the preservation of the conductive properties after functionalization.

Non-Covalent Functionalization

Non-covalent functionalization appears as a very attractive method for the derivatization of CNTs preserving the extended π -network of the

¹²¹ D. Bouilly, J. Cabana, F. Meunier, M. Desjardins-Carriere, F. Lapointe, P. Gagnon, F. L. Larouche, E. Adam, M. Paillet and R. Martel, *ACS Nano*, **2011**, 5, 4927.

¹²² M. Vizueté, M. J. Gómez-Escalonilla, S. García-Rodríguez, J. L. G. Fierro, P. Atienzar, H. García and F. Langa, *Chem. Eur. J.*, **2012**, 21, 16922.

tubes.^{123,124,125} The non-covalent interactions are based either on van der Waals forces or π - π stacking. This kind of functionalization has been widely used towards the solubilization of the nanotubes (Figure 1-31).

In the search for non-destructive purification methods, it has been shown that nanotubes can be transferred to the aqueous phase through the non-covalent functionalization with surfactants such as sodium dodecyl sulfate, (SDS), sodium dodecylbenzene sulfonate (SDBS) and sodium cholate, (SC) (Figure 1-28).

Solubilization procedures are simple. CNTs are placed in a solution of surfactant and then sonicated with an ultrasonic sonicator. During sonication, the van der Waals interactions in the CNTs bundles are overcome leading to CNTs exfoliation, whereas at the same time surfactant molecules adsorb onto the surface of the CNTs. When using the surfactant, the surface changes from hydrophobic to hydrophilic facilitating their dispersion in aqueous media.

Another interesting approach is the use of biomolecules, such as proteins, DNA or polysaccharides (Figure 1-31). Immobilization of biomolecules on CNTs motivated the use of nanotubes as new types of biosensor materials.^{126,127} The electronic properties of nanotubes coupled with the specific recognition properties of the immobilized biosystems would lead to an ideal sensor. DNA/SWCNT systems have been utilized as sensors for different biomolecules as proteins, using the SWCNT structure to enhance the electric current response.¹²⁸

¹²³ G. Gavrel, B. Jousset, A. Filoramo and S. Campidelli, *Top. Curr. Chem.*, **2014**, 348, 95.

¹²⁴ E. M. Pérez and N. Martín, *Chem. Soc. Rev.*, **2015**, 44, 6425.

¹²⁵ A. D. Crescenzo, V. Ettore and A. Fontana, *Beilstein J. Nanotechnol.*, **2014**, 5, 1675.

¹²⁶ Z. Guo, P. J. Sadler, S. C. Tsang, *Adv. Mater.*, **1998**, 10, 701.

¹²⁷ F. Balavoine, P. Schultz, C. Richard, V. Mallouh, T. W. Ebbesen and C. Mioskowski, *Angew. Chem. Int. Ed.*, **1999**, 111, 2036.

¹²⁸ S. J. Wind, E. Penzo, M. Palma, R. Wang, T. Facio, D. Porath, D. Rotem, G. Livshits and A. Stern, *Self-Assem. Mol. Electron.*, **2013**, 1, 177.

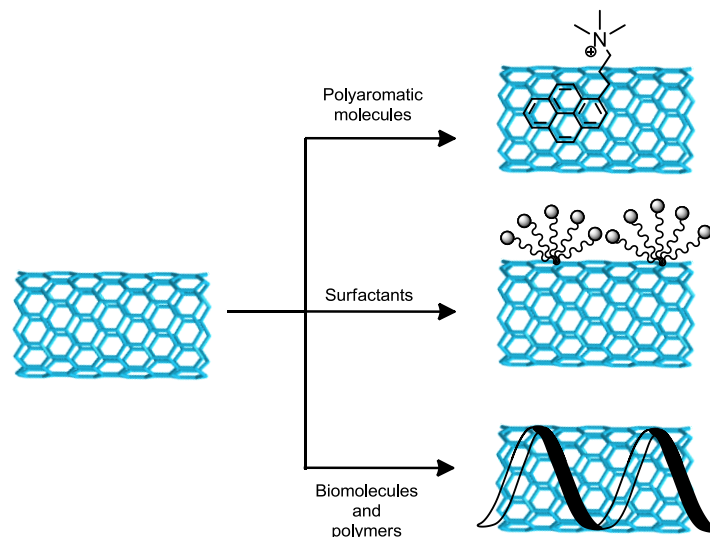


Figure 1-31. Functionalization of CNTs by noncovalent interactions.

Polymers have also been used in the formation of supramolecular complexes with CNTs (Figure 1-31). Thus, the suspension of SWCNTs in the presence of conjugated polymers in organic solvents led to hybrid systems, *via* polymer wrapping.^{129,130}

The non-covalent functionalization of CNTs by polyaromatic molecules have been also widely studied (Figure 1-31), since it could provide an efficient way to control the electronic properties of these materials without damaging the π network.⁵⁷⁻⁶³ In particular, it is known that pyrene derivatives interact strongly through π - π stacking.¹³¹ Guldi and Prato *et al.*^{132,133} reported the noncovalent association of SWCNTs with pyrene and porphyrin derivatives leading to novel electron donor-acceptor nanohybrids, which, upon photoexcitation, undergo fast electron transfer, followed by the generation of microsecond-lived charge-separated species. In this case, a charged pyrene

¹²⁹ S. A. Curran, P. M. Ajayan, W. J. Blau, D. L. Carroll, J. N. Coleman, A. B. Dalton, A. P. Davey, A. Drury, B. Mccarthy, S. Maier and A. Strevens, *Adv. Mater.*, **1998**, *10*, 1091.

¹³⁰ A. Start, J. F. Stoddart, D. Steuerman, M. Diehl, A. Boukai, E. W. Wong, A. Yang, S. W. Chung, H. Choi and J. R. Heath, *Angew. Chem.*, **2001**, *113*, 1771.

¹³¹ H. Jaegfeldt, T. Kuwana and G. Johansson, *J. Am. Chem. Soc.*, **1983**, *105*, 1805.

¹³² D. M. Guldi, G. M. A. Rahman, F. Zerbetto and M. Prato, *Acc. Chem. Res.*, **2005**, *38*, 871.

¹³³ C. Ehli, G. M. A. Rahman, N. Jux, D. Balbinot, D. M. Guldi, F. Paolucci, M. Marcaccio, D. Paolucci, M. Melle-Franco, F. Zerbetto, S. Campidelli and M. Prato, *J. Am. Chem. Soc.*, **2006**, *128*, 11222.

derivative, 1-(trimethylammonium acetyl) pyrene, (pyrene⁺), was used to solubilize SWCNTs through the formation of π - π interactions in aqueous solution. The electron-donor ability of semiconducting SWCNTs toward photoexcited fullerene attached through non-covalent interactions to the nanotube was demonstrated more recently by D'Souza *et al.* (Figure 1-32).¹³⁴

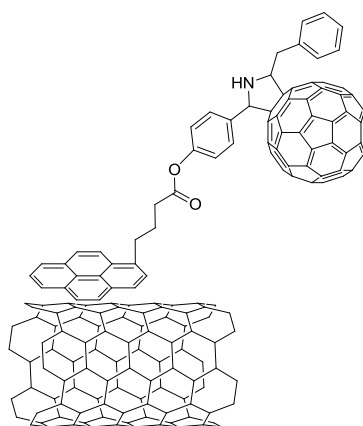


Figure 1-32: Non-covalent functionalization of carbon nanotubes with pyrene derivatives.¹³⁴

Upon this functionalization method the dispersibility of CNTs is improved and the discrimination by diameter and chirality is possible, which is crucial for further applications.¹³⁵

Endohedral functionalization

Another possibility of CNT functionalization is the filling of the inner cavity with molecules.^{136,137} The incorporation of fullerenes such as C₆₀^{138,139} or

¹³⁴ A. S. D. Sandanayaka, E. Maligaspe, T. Hasobe, O. Ito and F. D'Souza, *Chem. Commun.*, **2010**, 46, 8749.

¹³⁵ S. K. Samanta, M. Fritsch, U. Scherf, W. Gomulya, S. Z. Bisri and M. A. Loi, *Acc. Chem. Res.*, **2014**, 47, 2446.

¹³⁶ M. Vizuete, M. Barrejón, M. J. Gómez-Escalonilla and F. Langa, *Nanoscale*, **2012**, 4, 4370.

¹³⁷ M. Vizuete, M. Barrejón, M. J. Gómez-Escalonilla and F. Langa, *Handbook of Carbon Nanomaterials, Vol. 4: Materials and Fundamental Applications (Hybrids Involving Fullerenes and Carbon Nanotubes, Chapter 13)* Ed. D'Souza, F. & Kadish, M., World Scientific Publishing, New Jersey **2012**.

¹³⁸ B. W. Smith, M. Monthieux and D. E. Luzzi, *Chem. Phys. Lett*, **1999**, 315, 31.

¹³⁹ B. W. Smith and D. E. Luzzi, *Chem. Phys. Lett*, **2000**, 321, 169.

metallofullerenes are interesting examples of the endohedral chemistry of SWCNTs (Figure 1-33).

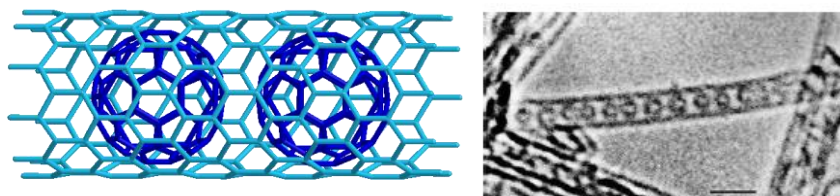


Figure 1-33. Encapsulated C₆₀ in carbon nanotubes.

This incorporation tends to form chains through van der Waals forces and are very often known as peapods.¹³⁹ In 1998, Smith *et al.*¹⁴⁰ accidentally observed for the first time the formation of SWCNTs containing a one-dimensional C₆₀ fullerene array (Figure 1-33 right) by means of high-resolution transmission electron microscopy (HR-TEM). These systems were later synthesized in high quantities by Burteaux *et al.*¹⁴¹ Since then, many other molecules have been encapsulated in CNTs.^{142,143,144} This method offers a new approach for tuning the electronic properties of these materials.

¹⁴⁰ B. W. Smith, M. Monthieux and D. E. Luzzi, *Nature*, **1998**, 396, 323.

¹⁴¹ B. Burteaux, A. Claye, B. W. Smith, M. Monthieux and D. E. Luzzi, *Carbon*, **2001**, 39, 1251.

¹⁴² D. A. Britz and A. N. Kholobystov, *Chem. Soc. Rev.*, **2006**, 35, 637.

¹⁴³ O. Vostrowsky and A. Hirsch, *Angew. Chem., Int. Ed.*, **2004**, 43, 2326.

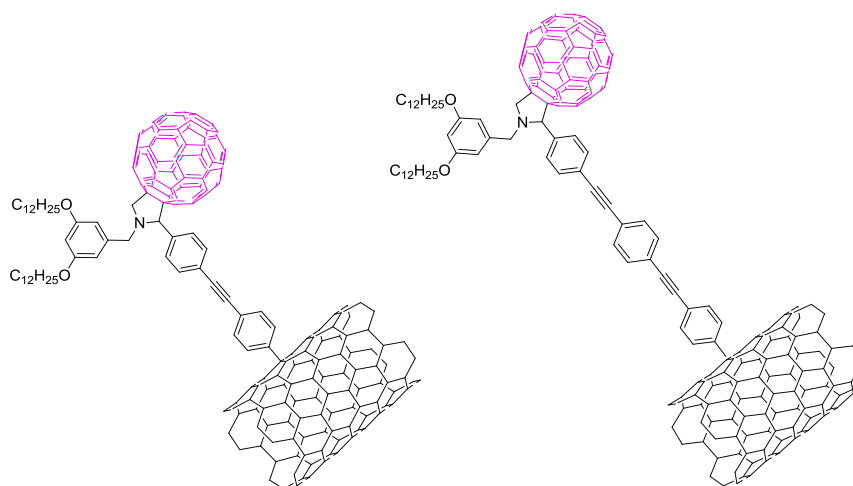
¹⁴⁴ R. Kitaura and H. Shinohara, *J. Appl. Phys.*, **2007**, 46, 881.

1.2 Objectives

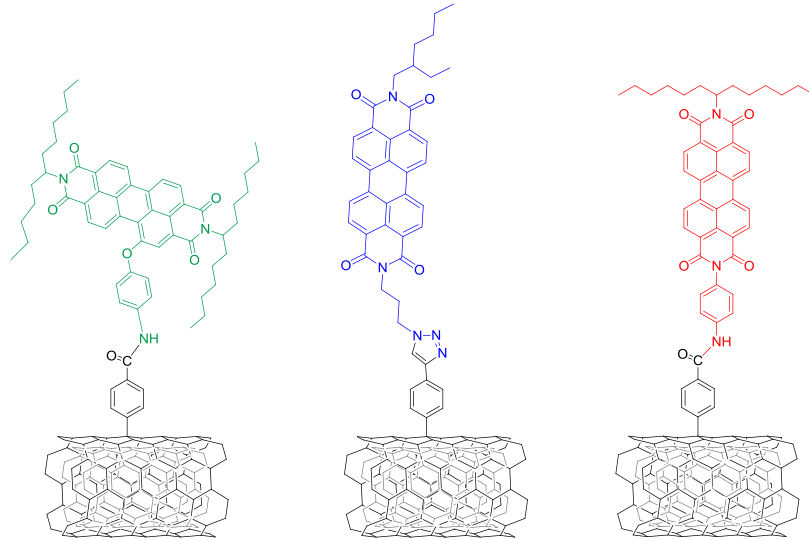
Based on the aforementioned unique properties of carbon nanotubes the following research was oriented towards the covalent functionalization of CNTs with electro-active moieties, with the aim of studying the modification of their electronic and chemical properties.

The specific aims in chapter 1 were as follows:

- a) Synthesis and comparative study of the photophysical behavior of two nano hybrid materials bearing fulleropyrrolidine derivatives, varying the length of the spacers between the nanotube and the fullerene cage.



- Full characterization of the nanoconjugates by analytical, spectroscopic, microscopic and electrochemical techniques (TGA, FTIR, Raman, XPS, AFM, HR-TEM and cyclic voltammetry).
 - Study of the electronic communication between the fullerene derivative moiety and the SWCNTs through transient absorption spectroscopy.
- b) Functionalization of the outer wall of DWCNTs with electron acceptor perylene diimides (PDIs) varying the spacers connecting both units.



- Verification of outer wall functionalization and the degree of PDI substitution on DWCNTs by TGA, XPS, FTIR, Raman and AFM techniques.
- Study of the presence of charge separation processes by steady-state, femtosecond transient absorption and photocatalytic electron pooling studies.

1.3 Results and discussion

1.3.1 Synthesis of nanohybrids SWCNT-C₆₀

Background

Although non-covalent functionalization of carbon nanotubes is a good strategy to avoid damaging the conjugated system of the sidewall, and therefore, maintain the properties of the material, this kind of interaction concerns weak forces between coupled molecules which may lower the electronic communication with the carbon nanotube as well as favors the desorption of the molecules from the nanotube sidewall. In this sense, covalent functionalization leads to more stable hybrids and a higher degree of functionalization; at the same time stronger electronic communications between the nanotube and the electroactive moiety are acquired. In this work, we have exclusively focused on this latter approach to attach different electroactive units to the surface of carbon nanostructures.

In recent years, hybrid structures combining two different forms of carbon nanostructures have been prepared with the aim of generating multifunctional nanomaterials with enhanced properties.^{136,145,146} The first synthesis of a conjugated hybrid consisting of C₆₀ and a SWCNT was reported by Langa *et al.* (Figure 1-34).¹⁴⁷ The new nanohybrid material was prepared by amidation of acid functionalized SWCNTs by an amine functionalized-fullerene derivative. Raman spectroscopy and HRTEM studies confirmed the presence of the C₆₀ cage attached to the sidewall of the SWCNT (Figure 1-34 right).

¹⁴⁵ G. Nasibulin, P. V. Pikhitsa, H. Jiang, D. P. Brown, A. V. Krasheninnikov, A. S. Anisimov, P. Queipo, A. Moisala, D. Gonzalez, G. Lientschnig, A. Hassanien, S. D. Shandakov, G. Lolli, D. E. Resasco, M. Choi, D. Tomanek and E. I. Kauppinen, *Nat. Nanotechnol.*, **2007**, 2, 156.

¹⁴⁶ M. Vizuete, M. J. Gómez-Escalonilla, J. L. G. Fierro, M. Yudasaka, S. Iijima, M. Vartanian, J. Iehl, J.-F. Nierengarten and F. Langa, *Chem. Commun.*, **2011**, 47, 12771.

¹⁴⁷ J. L. Delgado, P. de la Cruz, A. Urbina, J. T. López Navarrete, J. Casado and F. Langa, *Carbon*, **2007**, 45, 2250.

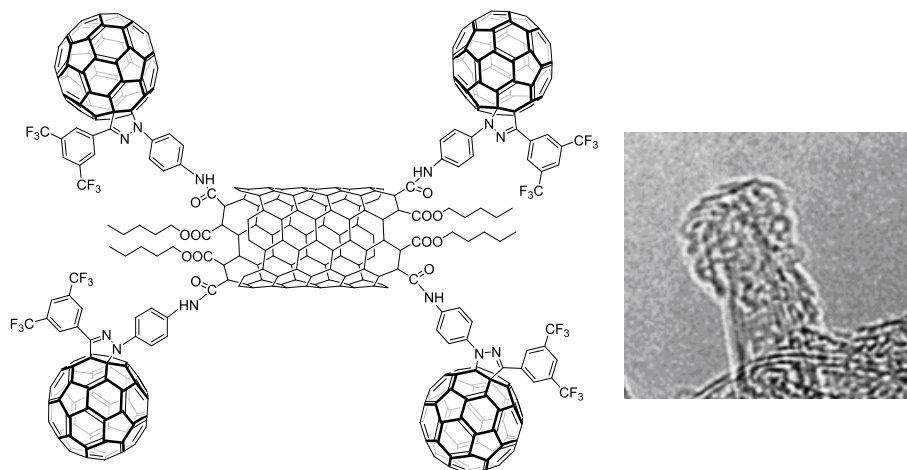


Figure 1-34. (Left) First hybrid SWCNT- C_{60} obtained; (right) HRTEM image of nano hybrid material (bar = 5 nm).

A grapevine nanostructure based on CNTs covalently functionalized with C_{60} was reported by Yang *et al.*¹⁴⁸ In this work, the amidation of SWCNT-COOH with an amino-functionalized fulleropyrrolidine was performed. Electron spin resonance (ESR) spectroscopy indicated a tendency for ground-state electron transfer from the SWCNT to the C_{60} moieties in the grapevine nanostructure.

Some other nanoconjugates that combine fullerenes covalently bonded to the sidewall of CNTs have been also reported.¹⁴⁹ However, in most of the cases, the resulting materials were completely insoluble thus making their characterization difficult and limiting the study of their electronic properties.

Recently in our group has been prepared a soluble hybrid nanomaterial which combines fullerenes and carbon nanohorns (CNHs) (Figure 1-35).¹⁴⁶ Electrochemical investigations revealed the existence of electronic communication between both kinds of carbon nanostructures. A similar

¹⁴⁸ W. Wu, H. Zhu, L. Fan and S. Yang, *Chem. Eur. J.*, **2008**, *14*, 5981;

¹⁴⁹ (a) S. Giordani, J.-F. Colomer, F. Cattaruzza, J. Alfonsi, M. Meneghetti, M. Prato and D. Bonifazi, *Carbon*, **2009**, *47*, 578; (b) Q. Wang and H. Moriyama, *Langmuir*, **2009**, *25*, 10834; (c) N. Mackiewicz, T. Bark, B. Cao, J. A. Delaire, D. Riehl, W. L. Ling, S. Foillard and E. Doris, *Carbon*, **2011**, *49*, 3998. (c) S. Giordani, J.-F. Colomer, F. Cattaruzza, J. Alfonsi, M. Meneghetti, M. Prato and D. Bonifazi, *Carbon*, **2009**, *47*, 578.

electrochemical behavior was found previously in an endohedral $C_{60}@SWCNT$,¹⁵⁰ although the distances calculated by molecular mechanic in both cases were very different (12 Å for CNH- C_{60} and 3.4 Å for $C_{60}@SWCNT$). This fact led us to study the electrochemical behavior of two hybrid materials with similar nanoenvironment, showing different length between both nanostructures.

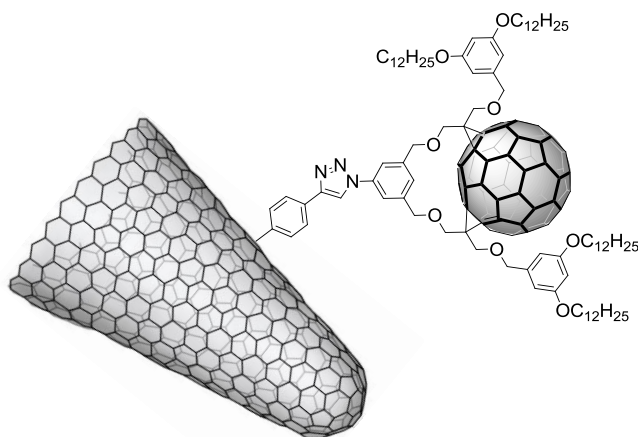
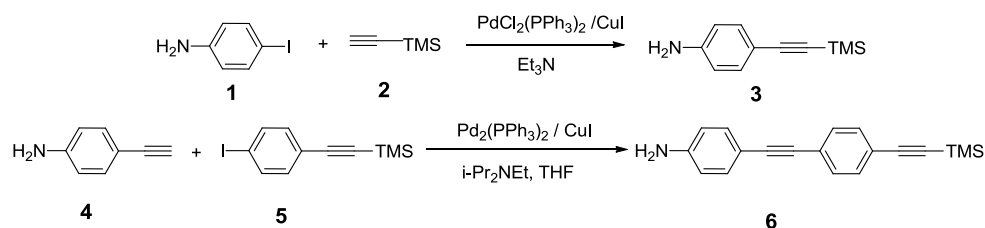


Figure 1-35. Modification of CNHs with a fullerene derivative.¹⁴⁶

In the first part of this chapter, the synthesis, characterization as well as the study of the photophysical properties of a soluble hybrid material which combines fullerenes and SWCNTs into a single structure is presented.

Synthesis

Previous to the covalent modification of SWCNTs, the synthesis of aminophenyl derivatives was accomplished (Scheme 1-1).

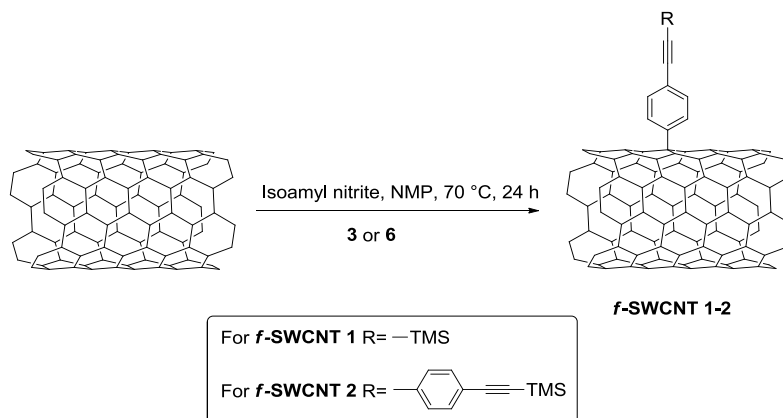


Scheme 1-1. Structures of the desired molecules 3 and 6.

¹⁵⁰ N. Karousis, S. P. Economopoulos, Y. Iizumi, T. Okazaki, Z. Liu, K. Suenaga and N. Tagmatarchis, *Chem. Commun.*, **2010**, 46, 9110.

The synthesis of **3** was achieved following the procedure described in the literature.¹⁵¹ For this purpose, Sonogashira coupling¹⁵² of iodoaniline with trimethylsilylacetylene (TMSA) in trimethylamine (Et₃N) gave high yield of the desired product. For the synthesis of **6** a slightly modified procedure was used. The same catalyst were employed, however the reaction was performed in tetrahydrofuran (THF) using *N,N*-diisopropylethylamine (DIPEA) as base, yielding the aminophenyl derivative **6**.

Thereafter, modification of pristine SWCNTs with *in-situ* generated diazonium salts was performed.⁹⁶ Aminophenyl derivatives **3** and **6**, previously described were employed. The reaction was accomplished in the presence of isoamyl nitrite using *N*-methyl pyrrolidinone (NMP) as solvent (Scheme 1-2).



Scheme 1-2. Synthetic procedure for the functionalization of SWCNTs with diazonium salts.

Successive cleavage of the TMS groups of **f-SWCNT 1** and **f-SWCNT 2** was performed *in situ* using TBAF (tetra-*n*-butylammonium fluoride), affording the corresponding deprotected alkyne groups; then, fullerene derivative **7**, previously reported by Nierengarten *et al.*,¹⁵³ was linked through copper-free Sonogashira C-C cross-coupling reaction under microwave irradiation¹⁵⁴ yielding the targeted hybrids **f-SWCNT 3** and **f-SWCNT 4**

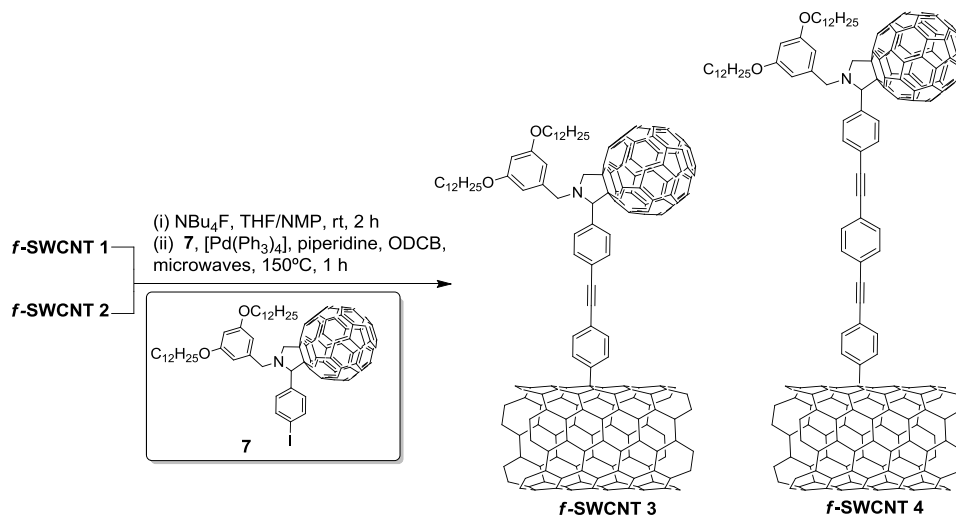
¹⁵¹ J. J. Hwang and J. M. Tour, *Tetrahedron*, **2002**, 58, 10387.

¹⁵² K. Sonogashira, Y. Tohda and N. Hagishara, *Tetrahedron Lett.* **1975**, 50, 4467.

¹⁵³ F. Ajama, T. M. Figueira, C. Bourgogne, M. Holler, P. W. Fowler and J. F. Nierengarten, *Eur. J. Org. Chem.*, **2005**, 3766.

¹⁵⁴ A. Gouloumis, F. Oswald, M. E. El-Khouly, F. Langa, Y. Araki and O. Ito, *Eur. J. Org. Chem.*, **2006**, 2344.

(Scheme 1-3). The presence of the two long alkyl chains per fullerene subunit improved significantly the nanotube's solubility after functionalization.

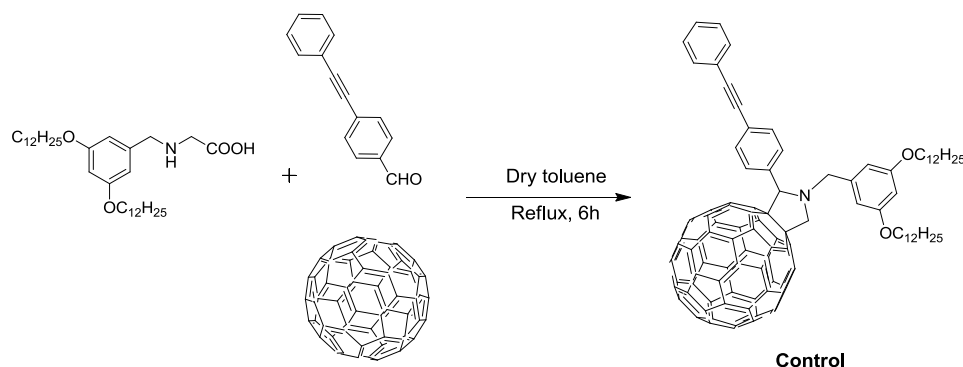


Scheme 1-3. Synthetic procedure for the Sonogashira cross-coupling.

Both nanoconjugates were fully characterized by analytical, spectroscopic, and microscopic techniques (TGA, XPS, FTIR, Raman, cyclic voltammetry, AFM and HRTEM), to obtain fully detailed information about the structural, electronic and chemical properties of the functionalized carbon nanotubes. A brief description of the fundamentals of these techniques can be found in the Annexe: *Experimental Techniques Section*.

To further compare the photophysical results obtained for the **f-SWCNT 3** and **f-SWCNT 4**, a **control** sample was also prepared (Scheme 1-4). For this purpose, the previously synthesized aldehyde¹⁵⁵ was allowed to react with the amino acid derivative¹⁵³ and C_{60} via 1,3-dipolar cycloaddition reaction to yield the **control** sample.

¹⁵⁵ K. Worm-Leonhard and M. Meldal, *Eur. J. Org. Chem.*, **2008**, 5244.



Scheme 1-4. Synthetic route for the preparation of the **control**.

Characterization

Fourier transform infrared spectroscopy (FTIR) spectra gave evidence of the covalent functionalization on SWCNT (Figure 1-36). The FTIR spectra of *f*-SWCNT 1 and *f*-SWCNT 2 is almost featureless with weak skeletal vibration of the aromatic domains between 1400-1600 cm^{-1} . In the spectra of *f*-SWCNT 3 and *f*-SWCNT 4, the C-H stretching vibrations due to the dodecyl chains of the pyrrolidine unit were identified at 2845–2918 cm^{-1} ; the appearance of strong peaks at around ~ 1450 and ~ 1600 cm^{-1} (attributed to the C-N bond of the pyrrolidine moiety and to the C=C aromatic stretches), provided significant support for the covalently attach of pyrrolidine derivative onto the surface of SWCNTs.

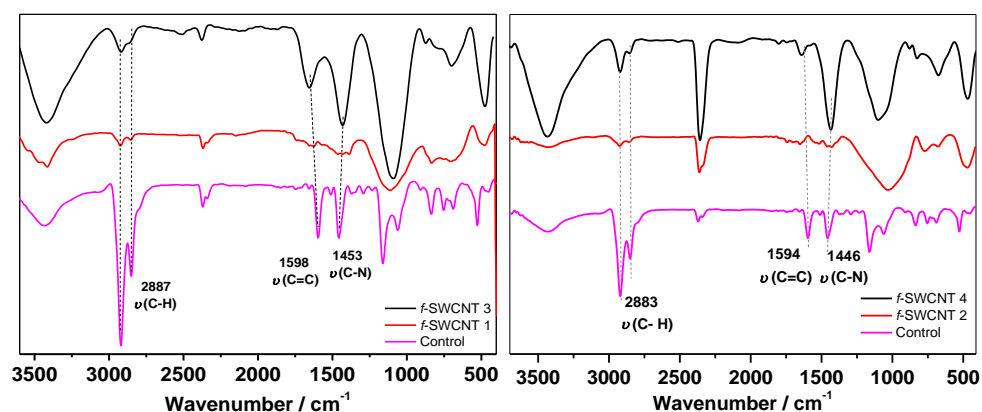


Figure 1-36. FTIR spectra of the functionalized samples *f*-SWCNT 3 and *f*-SWCNT 4 compared to the **control** sample.

Raman spectroscopy provided also efficient support for the successful covalent functionalization of SWCNTs (Figure 1-37). The ratio between the

intensities of the disorder-induced D band and the first-order graphite G band (I_D/I_G) (see Annex: *Experimental Techniques Section*) provides a parameter that can be used for quantifying the number of defects. As observed, the intensity of the I_D/I_G ratio was higher for *f*-SWCNT 1 (0.35) and *f*-SWCNT 2 (0.62) when compared to SWCNT (0.07) as a consequence of the increase of the structural defects of CNTs. No further increase was observed when going from *f*-SWCNT 1 to *f*-SWCNT 3 and *f*-SWCNT 2 to *f*-SWCNT 4 since the Sonogashira coupling take place onto the triple bonds rather than directly on the nanotube surface. In addition, the main [60]fullerene band, related to the vibrational mode $A_2(g)$ of the non-functionalized molecule, was observed in the spectra of *f*-SWCNT 3 and *f*-SWCNT 4 at 1462 cm^{-1} and 1420 cm^{-1} respectively, confirming the achievement of the cross coupling.

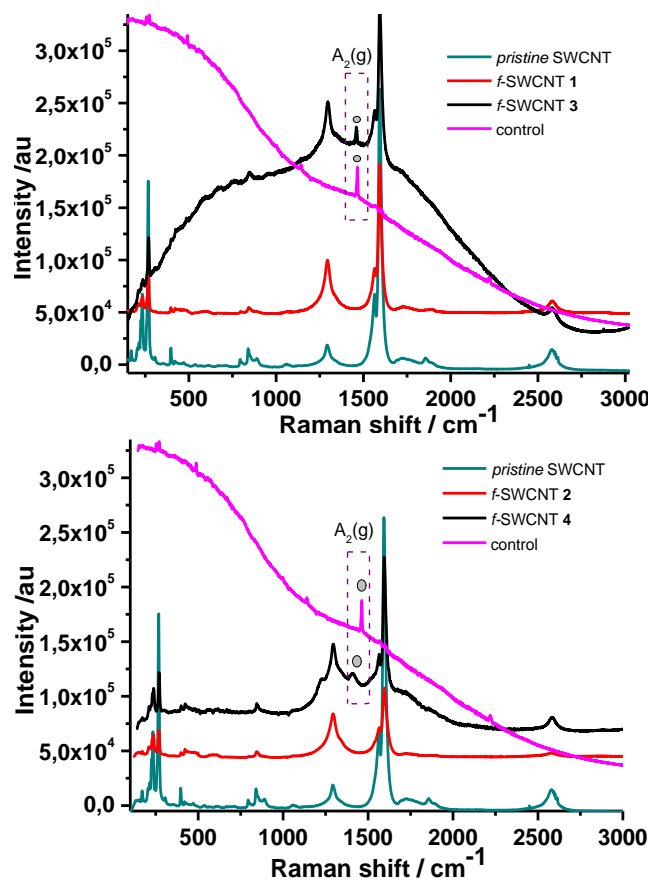


Figure 1-37. Raman spectra of pristine SWCNT compared to the functionalized samples *f*-SWCNT 3 (top panel) and *f*-SWCNT 4 (bottom panel) and the control sample, $\lambda_{\text{exc}} = 785\text{ nm}$.

Experiments for the calculation of functionalization degrees were performed by TGA under a nitrogen flow and consisted on heating ramps of 10°C/min up to 1000°C. Figure 1-38 shows the thermal behavior of the functionalized materials together with that of pristine SWCNT and **control** sample.

Pristine SWCNT shows a weight loss of 8% at 550 °C, attributed to impurities remaining in the sample after the production process. The thermogram of *f*-SWCNT 1 shows a weight loss of 6.6% at 550 °C, corrected by the respective weight loss of the pristine starting material. An additional 19% weight loss is observed for *f*-SWCNT 3 which is directly related to the decomposition of the fulleropyrrolidine derivative. Considering the thermogram of the **control** (39% at 550°C), the actual weight loss corresponding to the fulleropyrrolidine derivative attached to the nanotube is 48% at 550 °C, which is approximately one group each 241 carbon atoms.

For *f*-SWCNT 2 a weight loss of 9.7% is observed at 550 °C. *f*-SWCNT 4 shows an additional weight loss of 15.9%. The actual weight loss corresponding to the fulleropyrrolidine derivative is in this case of 38% at 550°C which is approximately one group each 310 carbon atoms.

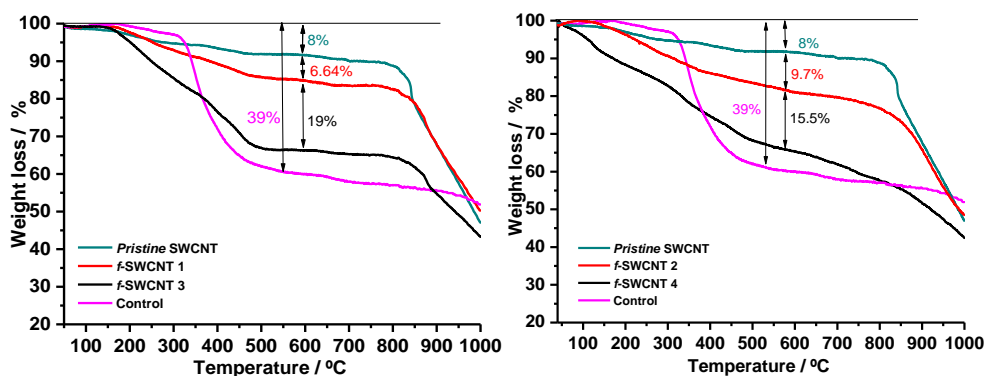


Figure 1-38. TGA graphs of *pristine* SWCNT compared to that of the functionalized samples *f*-SWCNT 3 and *f*-SWCNT 4, and the **control** fullerene derivative.

Further evidence on the anchoring of the fulleropyrrolidine derivative onto the surface of SWCNT was obtained by means of X-ray Photoelectron Spectroscopy (XPS). XPS measures the surface composition by determining the binding energy of photoelectrons ejected when the sample is irradiated with X-rays (see Annexe: *Experimental Techniques Section*).

Quantitative data for *f*-SWCNT 1-4 are presented in Table 1. It appears that the extent of Si incorporation is almost the same for *f*-SWCNT 1 (1.6% O atom) and *f*-SWCNT 2 (1.5% O atom). After Sonogashira cross coupling, as expected, *f*-SWCNTs 3 and *f*-SWCNTs 4 revealed the presence of nitrogen (N 1s, 399 eV) from the pyrrolidine unit. The N content for *f*-SWCNT 3 and *f*-SWCNT 4 is the same (1.1% atom) while the O content is slightly higher (5.4-5.5% atom) than that of the *f*-SWCNT 1 and *f*-SWCNT 2 counterparts, evidencing the anchorage of dodecyl alkyl chains from fullerenederivative. These findings also supports successful anchorage of fulleropyrrolidine on the CNT surface.

Table 1. Surface composition for *f*-SWCNT 1-4.

Sample	C (% at)	O (%at)	N (%at)	I (%at)	Si(%at)
<i>pristine</i> SWCNT	95.7	4.3	-	-	-
Control	90.6	4.7	2.4	2.3	-
<i>f</i> -SWCNT 1	94.3	4.1	-	-	1.6
<i>f</i> -SWCNT 2	94.7	3.8	-	-	1.5
<i>f</i> -SWCNT 3	93.4	5.5	1.1	-	-
<i>f</i> -SWCNT 4	93.5	5.4	1.1	-	-

The high resolution spectra for C1s and O1s of *pristine* SWCNT sample are displayed in Figure 1-39. Following the assignment by Boehm¹⁵⁶ and our previous works,⁹⁴ the C1s emission (Figure 1-39 (a)) was satisfactorily curve-resolved into five components that can be identified as follows: a main peak at 284.8 eV (generated by photoelectrons emitted from carbon atoms in graphite configuration); this peak, together with the weak π - π^* plasmon component at about 291.3 eV, is indicative of the C nanotube structure of SWCNT. The component at 286.3 eV is often assigned to C-OH, and the components at 287.7 and 289.2 eV to C=O and -COO- species, respectively. Similarly, the O1s (Figure 1-39 (b)) line was curve-resolved with two components: the minor component at 531.6 eV corresponds to O=C surface groups whereas the major one at 533.2 eV is often associated with the O-C bond.¹⁵⁷

¹⁵⁶ H.P. Boehm, *Carbon*, **2002**, *40*, 145.

¹⁵⁷ A. Jung, R. Graupner, L. Ley and A. Hirsch, *Phys. Status Solidi*, **2006**, *243*, 3217.

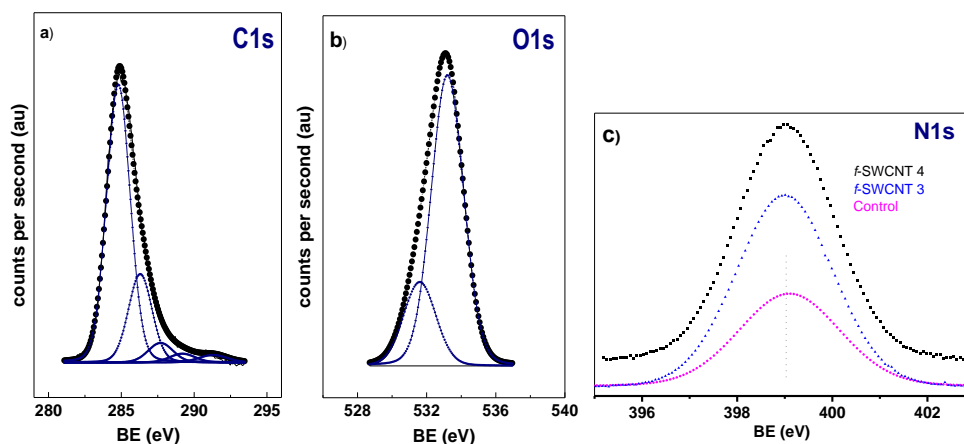


Figure1-39. Deconvolution at core level for C1s, O1s and N1s peaks of a) and b) *pristine* SWCNT and c) *f*-SWCNT 3, *f*-SWCNT 4 and **control** sample.

The high-resolution N1s core level spectrum (Figure 1-39 (c)) of **control** sample shows the component assigned to photoelectrons emitted from the N atom of tertiary amines centred at 399.0 eV (the N1s peak for the pyrrolidine ring). Similarly, the N1s peak at 399.0-399.1 eV was recorded for *f*-SWCNT 3 and *f*-SWCNT 4 (Figure 1-39 (c)) which fits very well with the BE of the fulleropyrrolidine precursor.

Atomic force microscopy (AFM) was used to further study the morphology of the hybrids. Dilute solutions of *pristine* SWCNTs in H₂O-SBDS were drop casted onto SiO₂ surfaces. The images suggested SWCNTs with an average height of 1.2 nm (Figure 1-40). After functionalization, the height was increased by approximately 2 nm for the *f*-SWCNT 3 and 2.5 nm for *f*-SWCNTs 4 (Figure 1-41). These heights were in concordance with the distance calculated for the skeleton structure of the organic addends by means of theoretical calculations using the semiempirical PM3 method implemented on HyperChem 8.0 program package (Figure 1-42); so the observed increase fitted quite well with that expected for these hybrids.

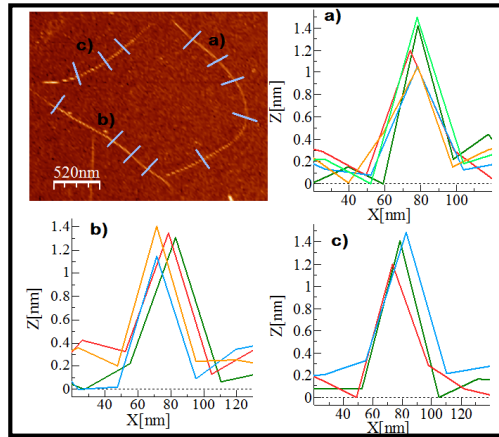


Figure1-40. AFM Images of HiPco SWCNTs.

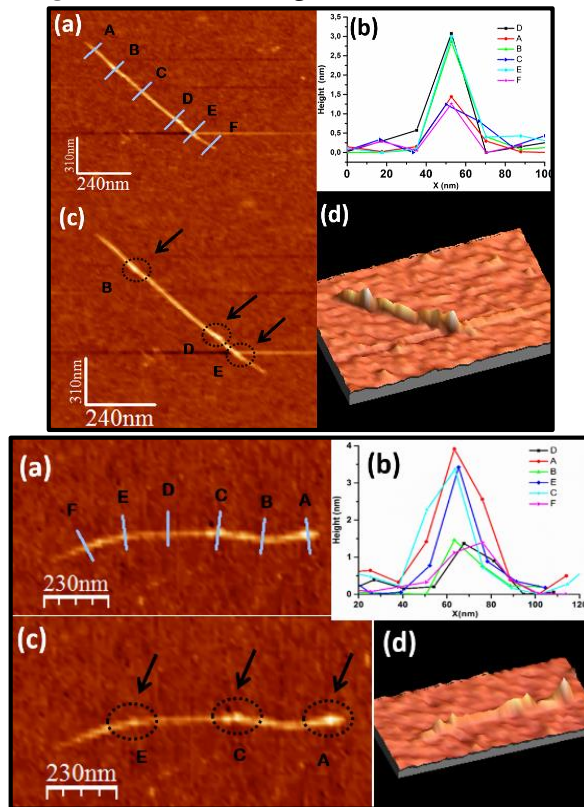


Figure1-41. AFM Images of *f*-SWCNT 3 and *f*-SWCNT 4(Top and Bottom respectively); the Z-profiles indicated with lines A-F are shown in the graph (b); (c) AFM images highlighting the functionalized zones; (d) 3-dimensional images of hybrids 3 and 4.

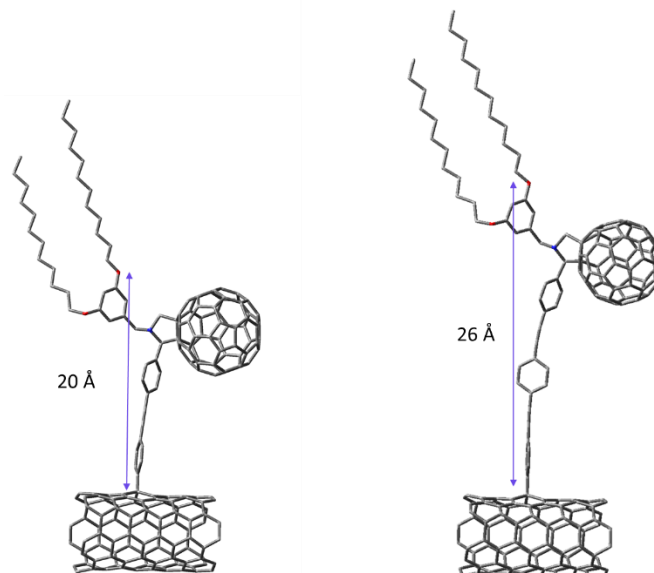


Figure 1-42: Modelling structures optimized using semiempirical PM3 method implemented on HyperChem 8.0 program package.

Transmission electron microscopy (TEM) was performed in order to obtain detailed views of the morphology. TEM observations showed that the carbon nanotubes maintained the tube-like structure after the chemical functionalization but with many defects (Figure 1-43). Spherical objects were found on the tube walls which can be attributed to the C_{60} cages (Figure 1-43 (b)). Some of them were seen having non-spherical forms (Figure 1-43 (a)), which could be the C_{60} damaged possibly by the electron beam during the TEM observation.

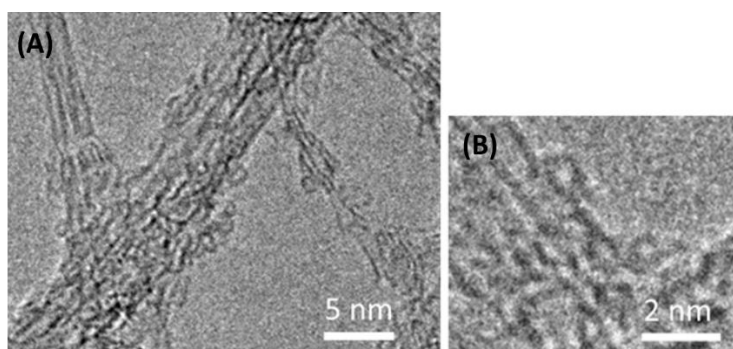


Figure 1-43. TEM images of *f*-SWCNT 3.

The electrochemical properties of both hybrids were investigated by Osteryoung square wave voltammetry (OSWV) (Figure 1-44). These studies were performed at room temperature in *o*-dichlorobenzene/acetonitrile 4:1 containing tetra-*n*-butylammonium hexafluorophosphate (TBAPF₆) (0.1 M) as electrolyte.

The reduction peaks of the **control** showed the first cathodic peak around -1.13 mV, which was cathodically shifted compared to the parent C₆₀ (-1.02 mV); this was expected as the saturation of a double bond in fullerene cage causes partial loss of conjugation. The characteristic reductions peaks of C₆₀ were also observed at -1.19, -1.54 and -2.09 for the modified *f*-SWCNT **3** and at -1.15, -1.51 and -2.04 for *f*-SWCNT **4** (see also Table 2). In addition, comparison of the redox potential of the **control** with that of the final hybrids showed a cathodic shift of 60 mV and 20 mV for *f*-SWCNT **3** and *f*-SWCNT **4** respectively. The observed shift was attributed to the existence of electronic interactions between the SWCNTs and the fullerene cages.

Something important to mention here is that a smaller cathodic shift was expected for *f*-SWCNT **4** when compared to *f*-SWCNT **3**, due to the lower proximity of the former between the C₆₀ cage and the nanotube (see Figure 1-45), which decrease the interactions between both units. This was in agreement with the obtained data.

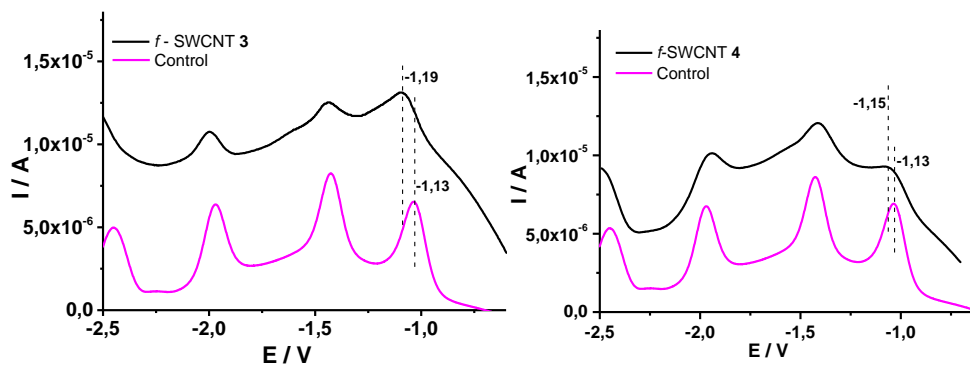


Figure1-44. OSWV (reduction run) of *f*-SWCNT **3** (left) and *f*-SWCNT **4** (right) compared to that of the **control**.

Table 2. Electrochemical data [V *vs.* Ag/AgNO₃] for the reduction process of functionalized *f*-SWCNT **3** and *f*-SWCNT **4**, and their reference compounds (**control** sample and C₆₀) determined by OSWV.^a

Sample	E ^{1red} (V)	E ^{2red} (V)	E ^{3red} (V)
C ₆₀	-1.02	-1.42	-1.90
Control	-1.13	-1.53	-2.07
<i>f</i> -SWCNT 3	-1.19	-1.54	-2.09
<i>f</i> -SWCNT 4	-1.15	-1.51	-2.04

^a In *o*-DCB/acetonitrile 4 : 1 solution (0.1 M TBAPF₆) at room temperature. Values referenced *versus* Fc/Fc⁺.

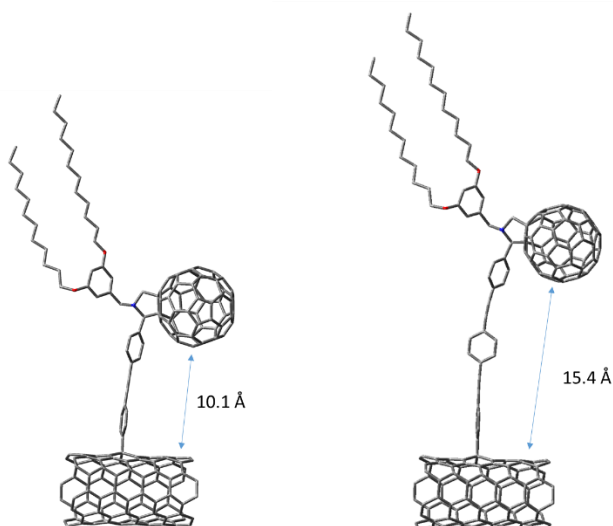


Figure 1-45: Modelling structures optimized using semiempirical PM3 method implemented on HyperChem 8.0 program package.

In order to study the photophysical behaviour of both hybrids, transient absorption studies are currently in progress.

1.3.2 Synthesis of nanohybrids DWCNT-perylenediimides

Background

As aforementioned, double-walled carbon nanotubes (DWCNTs) consist of two concentric SWCNTs with an inter-wall spacing of 0.33–0.42 nm,¹⁵⁸ and are emerging as promising SWCNT substitutes as they exhibit higher stability and improved performance for several applications (*e.g.*, field effect transistors or field emission).^{159,160} As previously mentioned, the covalent functionalization of DWCNTs occurs exclusively on the outer wall surface, while the inner tube remains unaltered¹⁶¹ encouraging a detailed understanding of functionalized-DWCNT electronic properties.

Perylenediimide (PDI)¹⁶² derivatives are a family of dyes that, due to synthetic versatility and easily tunable electronic character,¹⁶³ have become some of the most promising classes of molecular materials in organic optoelectronic applications.¹⁶⁴ These systems have been extensively used as electroactive counterparts in combination with different carbon nanomaterials, to obtain attractive molecular systems that undergo photoinduced electron

¹⁵⁸ Y. Li, K. Wang, J. Wei, Z. Gu, Z. Wang, J. Luo and D. Wu, *Carbon*, **2005**, *43*, 31.

¹⁵⁹ M. Kalbac, A. A. Green, M. C. Hersam and L. Kavan, *ACS Nano*, **2010**, *4*, 459.

¹⁶⁰ L. M. Arellano, L. Martín-Gomis, H. B. Gobeze, M. Barrejón, D. Molina, M. J. Gómez-Escalonilla, J. L. G. Fierro, M. Zhang, M. Yudasaka, S. Iijima, F. D'Souza, F. Langa and Á. Sastre-Santos, *J. Mater. Chem. C*, **2015**, *3*, 10215.

¹⁶¹ (a) G. Marcolongo, G. Ruaro, M. Gobbo and M. Meneghetti, *Chem. Commun.*, **2007**, 4925; (b) J. F. Colomer, R. Marega, H. Traboulsi, M. Meneghetti, G. van Tendeloo and D. Bonifazi, *Chem. Mater.*, **2009**, *21*, 4747; (c) T. Hayashi, D. Shimamoto, Y. A. Kim, H. Muramatsu, F. Okino, H. Touhara, T. Shimada, Y. Miyauchi, S. Maruyama, M. Terrones, M. S. Dresselhaus and M. Endo, *ACS Nano*, **2008**, *2*, 485; (d) L. G. Bulusheva, A. V. Okotrub, E. Flahaut, I. P. Asanov, P. N. Gevko, V. O. Koroteev, Yu. V. Fedoseeva, A. Yaya and C. P. Ewels, *Chem. Mater.*, **2012**, *24*, 2708; (e) N. Karousis, K. Kobayashi, H. Shinohara and N. Tagmatarchis, *Small*, **2010**, *6*, 2826.

¹⁶² F. Würthner, C. R. Saha-Möller, B. Fimmel, S. Ogi, P. Leowanawat and D. Schmidt, *Chem. Rev.*, **2015**, DOI: 10.1021/acs.chemrev.5b00188

¹⁶³ (a) F. Würthner, *Chem. Commun.*, **2004**, 1564; (b) H. Langhals, *Helv. Chim. Acta*, **2005**, *88*, 1309.

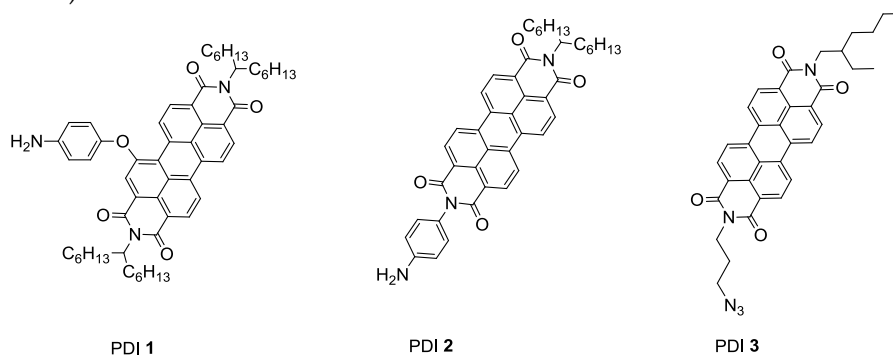
¹⁶⁴ (a) M. Guide, S. Pla, A. Sharenko, P. Zalar, F. Fernández-Lázaro, A. Sastre-Santos and T.-Q. Nguyen, *Phys. Chem. Chem. Phys.*, **2013**, *15*, 18894; (b) Q. Yan, Y. Zhou, Y.-Q. Zheng, J. Pei and D. Zhao, *Chem. Sci.*, **2013**, *4*, 4389; (c) X. Zhang, Z. Lu, L. Ye, C. Zhan, J. Hou, S. Zhang, B. Jiang, Y. Zhao, J. Huang, S. Zhang, Y. Liu, Q. Shi, Y. Liu and J. Yao, *Adv. Mater.*, **2013**, *25*, 5791; (d) R. Shivanna, S. Shoaee, S. Dimitrov, S. K. Kandappa, S. Rajaram, J. R. Durrant and K. S. Narayan, *Energy Environ. Sci.*, **2014**, *7*, 435.

transfer processes.¹⁶⁵

In this sense, in this second part of the chapter we have focused on the synthesis of three new hybrids combining perylenediimide units attached to DWCNTs.

Synthesis

Previous to the covalent modification of DWCNTs, perylenediimide derivatives (**PDI 1-3**) (Scheme 1-3) were synthesized in the group of Prof. Ángela Sastre, at the Instituto de Biongeniería at Universidad Miguel Hernández (Elche, Alicante).¹⁶⁶



Scheme 1-5. Structures of Perylenediimides (**PDI 1-3**).

Thereafter, covalent modification of DWCNTs through Tour reaction was performed (Scheme 1-6). For this purpose, a dispersion of ultrapure DWCNTs was reacted with 4-aminobenzoic acid (Scheme 1-6, top route) and 4-[(trimethylsilyl)ethynyl]aniline (Scheme 1-6, bottom route) in the presence of isoamyl nitrite to yield the modified **DWCNT-COOH** and **DWCNT-TMS**.

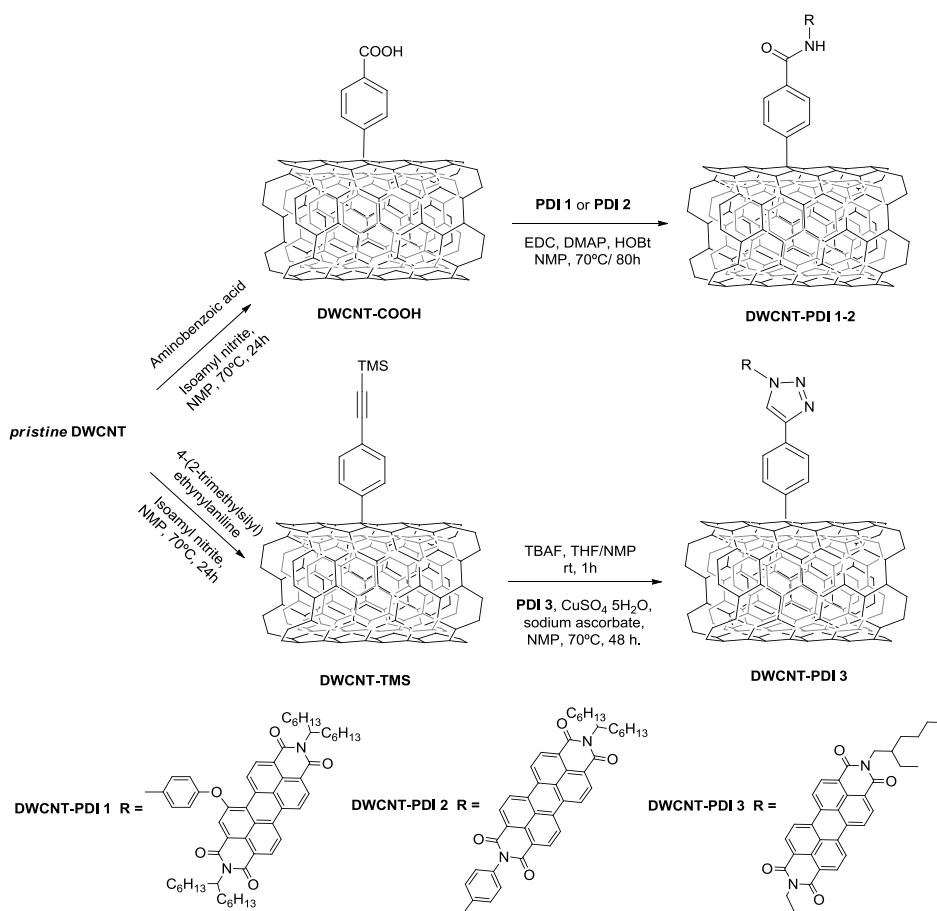
The covalent attachment of **PDI 1-3** to the sidewall of DWCNTs was

¹⁶⁵ (a) J. Baffreau, S. Leroy-Lhez, V. A. Nguyen, R. M. Williams and P. Hudhomme, *Chem. Eur. J.*, **2008**, *14*, 4974; (b) T. W. Chamberlain, E. S. Davies, A. N. Khlobystov and N. R. Champness, *Chem. Eur. J.*, **2011**, *17*, 3759; (c) U. Hahn, J.-F. Nierengarten, B. Delavaux-Nicot, F. Monti, C. Chiorboli and N. Armaroli, *New J. Chem.*, **2011**, *35*, 2234; (d) L. Feng, M. Rudolf, S. Wolfrum, A. Troeger, Z. Slanina, T. Akasaka, S. Nagase, N. Martín, T. Ameri, C. J. Brabec and D. M. Guldi, *J. Am. Chem. Soc.*, **2012**, *134*, 12190; (e) R. K. Dubey, M. Niemi, K. Kaunisto, A. Efimov, N. V. Tkachenko and H. Lemmetyinen, *Chem. Eur. J.*, **2013**, *19*, 6791; (f) S. Pla, L. Martín-Gomis, K. Ohkubo, S. Fukuzumi, F. Fernández-Lázaro and Á. Sastre-Santos, *Asian J. Org. Chem.*, **2014**, *3*, 185.

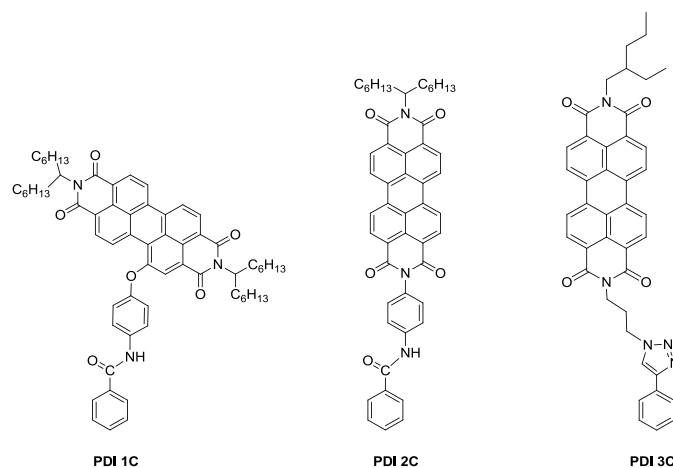
¹⁶⁶ M. Barrejón, S. Pla, I. Berlanga, M.J. Gómez-Escalonilla, L. Martín-Gómis, J.L.G. Fierro, M. Zhang, M. Yudasaka, S. Ijima, H. B. Gobeze, F. D'Souza, A. Sastre-Santos and F. Langa, *J. Mater. Chem. C*, **2015**, *3*, 4960.

accomplished by using two different approaches: by amidation of previously prepared **DWCNT-COOH**⁹⁶ with amine derivatives **PDI 1** and **PDI 2** in the presence of *N,N'*-dicyclohexylcarbodiimide (DCC) and 1-hydroxybenzotriazole (HOBT) to get **DWCNT-PDI 1** and **DWCNT-PDI 2** (Scheme 1-6, top route) and via “click” chemistry reaction between ethynylphenyl-functionalized DWCNTs, (formed by *in situ* removing of the TMS group from **DWCNT-TMS** with TBAF) and the azide derivative **PDI 3** to obtain **DWCNT-PDI 3** (Scheme 1-6, bottom route).

In order to study the photophysical behavior of the final hybrids compared with exactly the same moieties attached directly to the nanotubes, control compounds **PDI 1-3C** were also prepared (Scheme 1-7).



Scheme 1-6. Synthetic routes for the preparation of nanohybrids **DWCNT-PDIs 1-3**.



Scheme 1-7 Control compounds (**PDI 1-3C**) prepared to compare with the final hybrids.

As described in the next section, the new hybrids were characterized by common spectroscopic techniques.

Characterization

The first evidence of covalent functionalization was deduced from thermogravimetric analysis (TGA) experiments (Figure 1-46). In the 200-550 °C temperature range, we observe weight loss about 11.8% for **DWCNT-COOH**. Nanostructures **DWCNT-PDI 1** and **DWCNT-PDI 2**, showed an additional weight loss of 11.8% and 4.1% respectively, directly associated to the decomposition of the PDIs addends. Considering the weight losses of the **PDI 1** and **PDI 2** at 550 °C (51% and 59% respectively), the actual weight loss corresponding to the fulleropyrrolidine derivative attached to the nanotube is 15.5 % for **DWCNT-PDI 1** (one group each 347 carbon atoms) and 7% for **DWCNT-PDI 2** (one group each 875 carbon atoms).

In the case of **DWCNT-PDI 3**, TGA shows an additional weight loss around 7.9% at 550 °C, after subtracting the weight loss corresponding to **DWCNT-TMS** (11.3%). In this case, considering the thermogram of **PDI 3** (53% weight loss at 550 °C) the actual weight loss corresponding to the fulleropyrrolidine is 15%, which corresponds to one functional group every 363 carbon atoms.

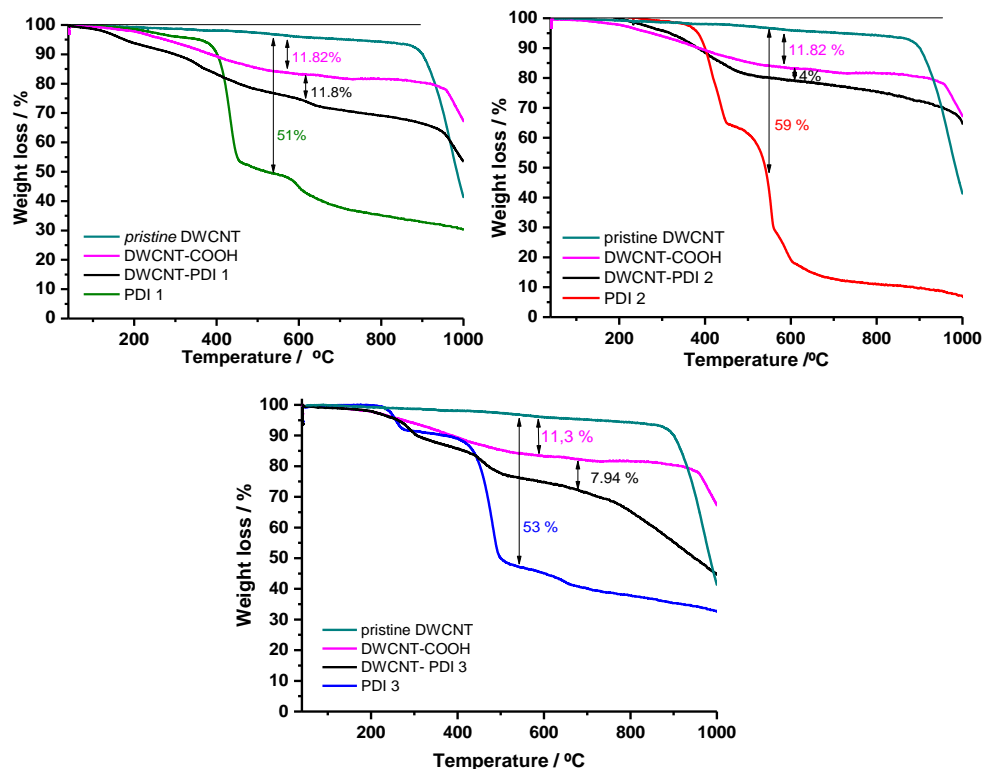


Figure 1-46. TGA curves recorded at 10 °C / min under N₂ of pristine DWCNT and functionalized **DWCNT-PDI 1-3**.

Raman spectroscopy provided also a wealth of information relevant to confirm the success in the functionalization process. The D band (defect induced mode), almost absent on the pristine sample ($I_D/I_G = 0.02$), became clear at 1306 cm^{-1} after functionalization by diazonium chemistry ($I_D/I_G = 0.25$ for **DWCNT-COOH** and $I_D/I_G = 0.35$ for **DWCNT-TMS**) (Figure 1-47). The introduction of disorder into the graphene network by the interaction of aryl moieties with the outer nanotube surface of the outer tube is the origin of this increasing of the I_D/I_G ratio. As expected, the introduction of the perylene groups by amidation (**DWCNT-PDI 1-2**) or “click” chemistry (**DWCNT-PDI 3**) does not modify the intensity of the D band. The appearance of a new band at around 1371 cm^{-1} in the final hybrids (**DWCNT-PDI 1-3**), (which overlaps with D-band), typical of the perylenes, demonstrates the presence of the perylene moieties in then hybrid.

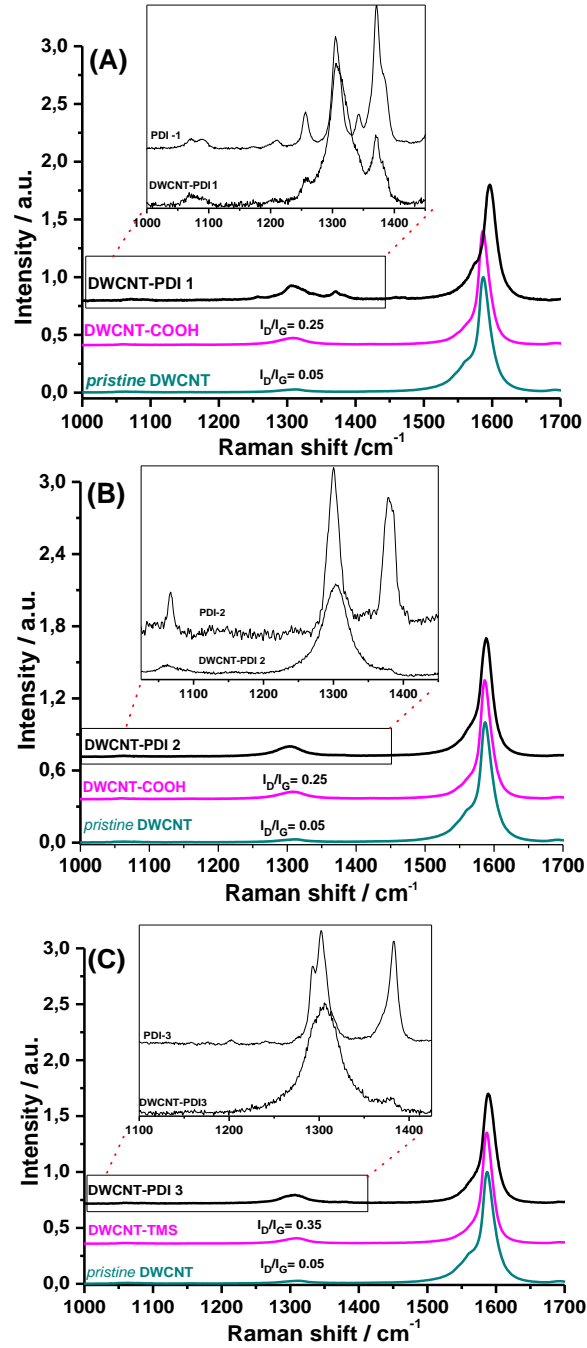


Figure 1-47. Raman spectra of pristine DWCNT and functionalized DWCNT-PDI 1 (Top) DWCNT-PDI 2 (centre) and DWCNT-PDI 3 (bottom) ($\lambda_{\text{exc}} = 785$ nm).

The G band is very sensitive to charge transfer processes (see Annexe: *Experimental Techniques Section*), showing a shift to higher frequencies (up-shift) with dopants or acceptor impurities or toward lower frequencies (down-shift) with electron donors. As observed in Figure 1-48, for **DWCNT-PDI 1-3**, the G⁺ component of the G band is shifted, by 2-9 cm⁻¹, to higher wavenumbers respecting to pristine DWCNTs due to p-doping effect^{167,168,169} of the electron-acceptor perylenes. The higher shift (9 cm⁻¹) observed in **DWCNT-PDI 1** respecting to that in **DWCNT-PDI 2-3** can be related to the parallel orientation of the perylene moiety in **DWCNT-PDI 1**, favouring the π - π interactions.

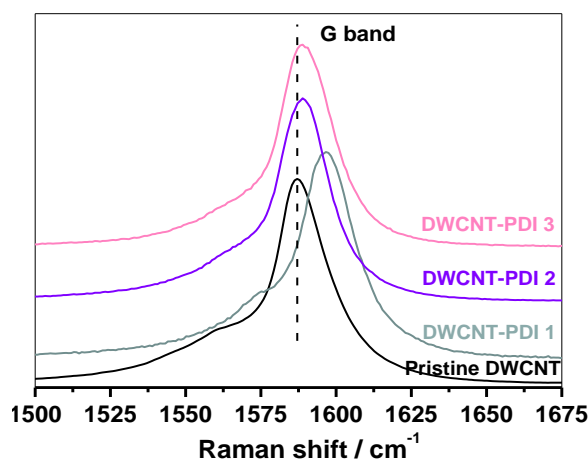


Figure 1-48. G-band region of pristine DWCNT (black) and functionalized samples **DWCNT-PDI 1** (grey), **DWCNT-PDI 2** (purple) and **DWCNT-PDI 3** (soft pink) at 785 nm laser excitation.

Something important to mention here is that the radial breathing modes (RBM) of DWCNTs changes after functionalization by phenylcarboxylic acid and phenylethynyl groups. The diameters of CNTs are related to their RBM frequencies (see Annexe: *Experimental Techniques Section*) (ω_{RBM}) by the equation [3]¹⁷⁰

¹⁶⁷ P. Puech, A. Ghandour, A. Sapelkin, C. Tinguely, E. Flahaut, D. J. Dunstan and W. Bacsa, *Phys. Rev. B*, **2008**, 78, 045413.

¹⁶⁸ R. Voggu, C. S. Rout, A. D. Franklin, T. S. Fisher and C. N. R. Rao, *J. Phys. Chem. C*, **2008**, 112, 13053.

¹⁶⁹ G. M. Do Nascimento, T. Hou, Y. A. Kim, H. Muramatsu, T. Hayashi, M. Endo, N. Akuzawa and M. S. Dresselhaus, *Carbon*, **2011**, 49, 3585.

¹⁷⁰ A. A. Green and M. C. Hersam, *Nature*, **2009**, 4, 64.

$$(\omega_{\text{RBM}}) = 218.2/dt + 19.6 \text{ cm}^{-1} \quad [3]$$

where dt is the diameter of the nanotube (in nm). Thus, the diameters of the outer and inner tubes were found to be ~ 1.00 - 1.81 nm and ~ 0.88 nm respectively. Comparison of the RBM intensity of the inner walls of pristine and *functionalized* DWCNTs showed no significant changes but the lower intensity of the outer walls of functionalized **DWCNT-COOH** and **DWCNT-TMS** respecting to pristine DWCNTs yielded further evidence of the success of functionalization of the outer walls (Figure 1-49).

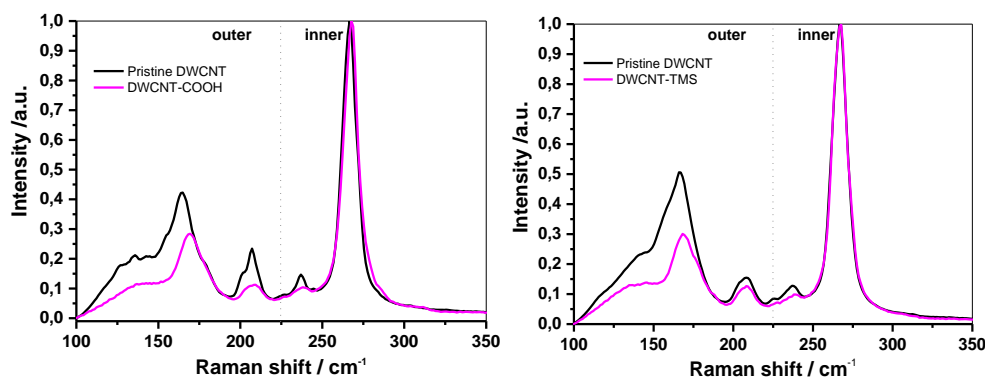


Figure 1-49. RBM zone of: (left) *pristine* DWCNT compared to **DWCNT-COOH** and (right) *pristine* DWCNT compared to **DWCNT-TMS** (red line) at excitation wavelength of 785 nm.

FTIR spectroscopy also provided information about the covalent attachment of perylenediimide to the surface of DWCNTs (see Figure 1-50). The appearance of the stretching band of the C-H around 2900 cm^{-1} from PDI moieties is clearly discernible in hybrids **1-3**. Also, as observed in Figure 1-50(C), the disappearance of the azide peak at 2098 cm^{-1} of **PDI 3** after the “click” coupling suggested that PDI moiety had been covalently bonded to DWCNT through the formation of the triazole ring.

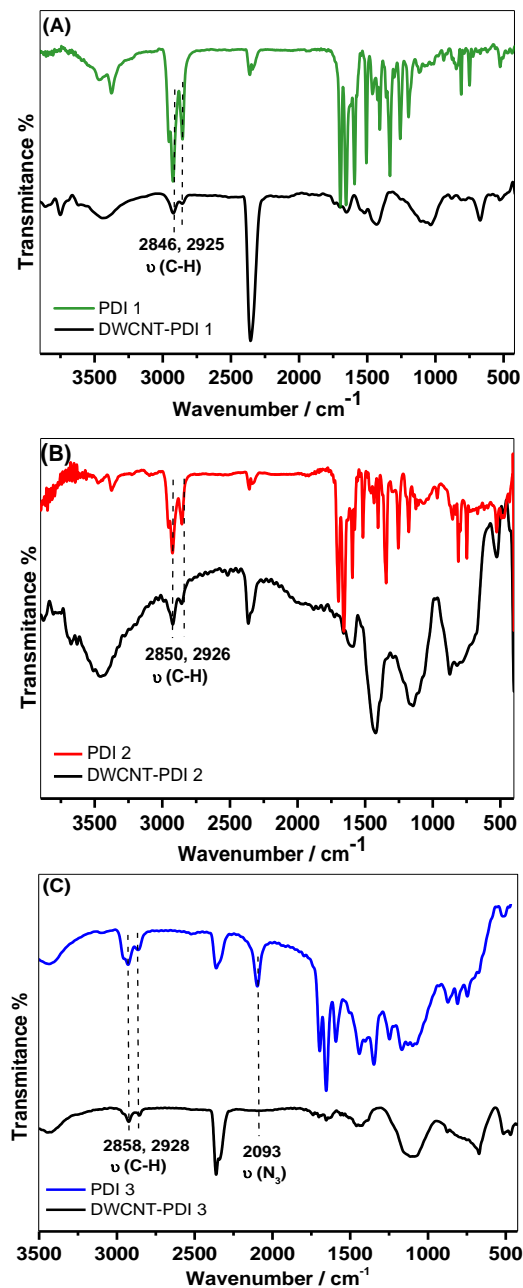


Figure 1-50. IR spectra (KBr) of DWCNT-PDI 1 (A), DWCNT-PDI 2 (B) and DWCNT-PDI 3 (C) compared with the corresponding PDIs.

XPS studies were also performed. The deconvoluted high resolution C1s spectrum of the pristine DWCNT (Figure 1-51), showed the main component at

284.8 eV, due to the binding energy of the sp^2 bonded carbon on DWCNTs, and other minor components at 286.2, 287.7 and 289.2 eV assigned to C-O, C=O and COO respectively.^{113,171} In addition, a broad component at about 291.4 eV, originated from the $\pi-\pi^*$ plasmon emission of C atoms in graphitic structures, was observed. Similarly, the high resolution O1s peak of DWCNT was resolved in two components at 531.8 and 533.3 eV of almost the same intensity.

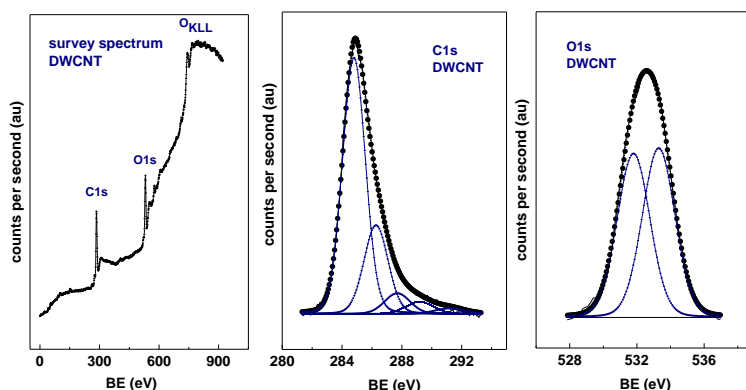


Figure 1-51. Survey, C1s and O1s core-level spectra of *pristine* DWCNT.

Compared with pristine DWCNT, for **DWCNT-COOH** an increase in the oxygen content occurs as expected (from 4.9% to 5.6%), confirming the anchorage of Ph-COOH groups (Figure 1-52).

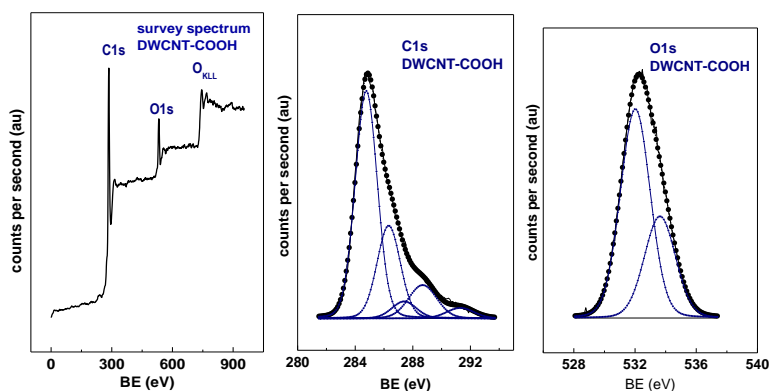


Figure 1-52. Survey, C1s and O1s core-level spectra of **DWCNT-COOH**.

The anchorage of the **PDI-1** on the **DWCNT-COOH** groups was also confirmed by XPS. The high resolution C1s, O1s and N1s peaks are displayed in

¹⁷¹ (a) E. Bekyarova, M. E. Itkis, P. Ramesh, C. Berger, M. Sprinkle, W.A. de Heer and R.C. Haddon, *J. Am. Chem. Soc.* **2009**, *131*, 1336.

Figure 1-53. The C1s spectrum of **DWCNT-PDI 1** showed substantial differences with respect that of **DWCNT-COOH** sample: (i), the π - π^* plasmon component disappeared and (ii), a new component at 285.4 eV assigned to the sp^3 carbon atoms, appeared. As this sp^3 component comes from alkyl chains, it is inferred that **PDI 1** has been successfully attached on the modified DWCNT substrate. Moreover, the N1s peak was satisfactorily fitted into two components at 399.2 and 400.3 eV, the intensity of the former being almost twice than the later. The bulk **PDI 1** showed the same two N1s components at very similar BEs (399.2 and 400.2 eV) and the respective peak areas were similar to that of functionalized **DWCNT-PDI 1** which indicated that the N-bearing groups of the **PDI 1** are present on functionalized DWCNT showing that the amidation reaction between carboxylic acid groups of functionalized DWCNT and terminal $-NH_2$ group of **PDI 1** had occurred.

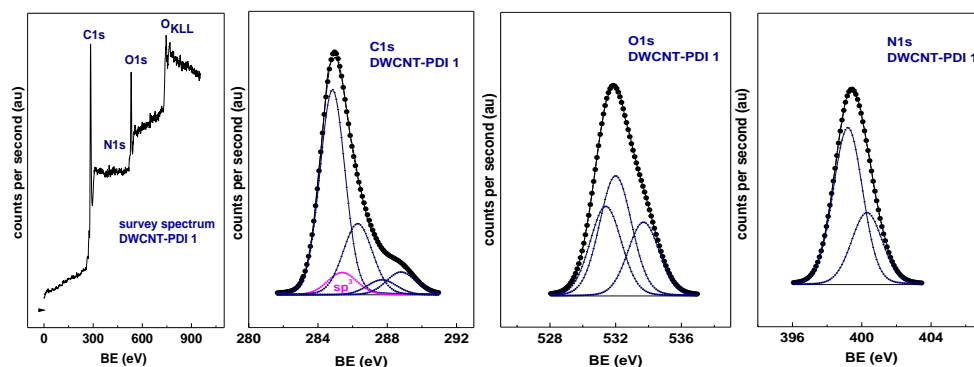


Figure 1-53. Survey, C1s, O1s and N1s core-level spectra of **DWCNT-PDI 1**.

Also the linkage of **PDI 2** onto the surface of carbon nanotube to yield **DWCNT-PDI 2** was monitored by XPS. The survey spectrum and the high resolution C1s, O1s y N1s spectra are displayed in Figure 1-54.

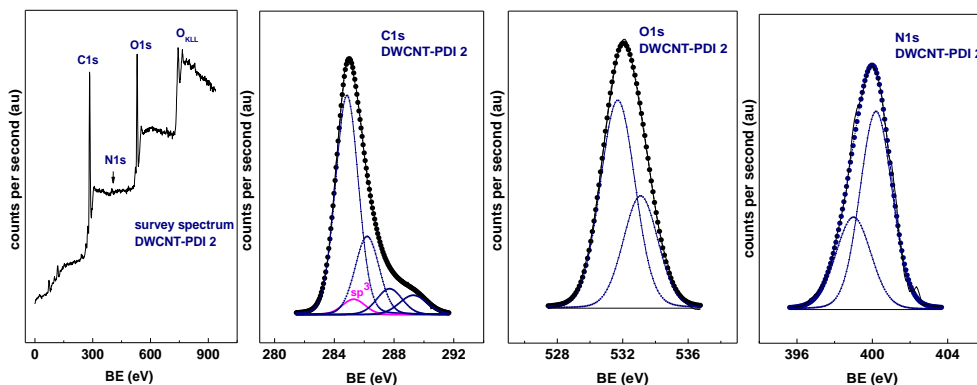


Figure 1-54. Survey, C1s, O1s and N1s core-level spectra of DWCNT-PDI 2.

Like in the previous case, the N1s spectrum of DWCNT-PDI 2 was adequately fitted with two components at binding energies of 399.0 and 400.2 eV, the intensity of the former being about one-half than the later as expected from the structure of PDI 2. The similarity of the binding energies of N1s components, together with their relative proportion in functionalized carbon nanotube indicates the introduction of PDI 2 onto the DWCNTs.

Finally, the reaction between DWCNT-TMS and PDI 3 was also followed by XPS. The DWCNT-TMS material showed the same elements of DWCNT-COOH sample at almost the same binding energies, although small changes in intensity were observed (Figure 1-55). In addition, it displayed the Si2p peak at a binding energy of 101.5 eV, due to the TMS group.

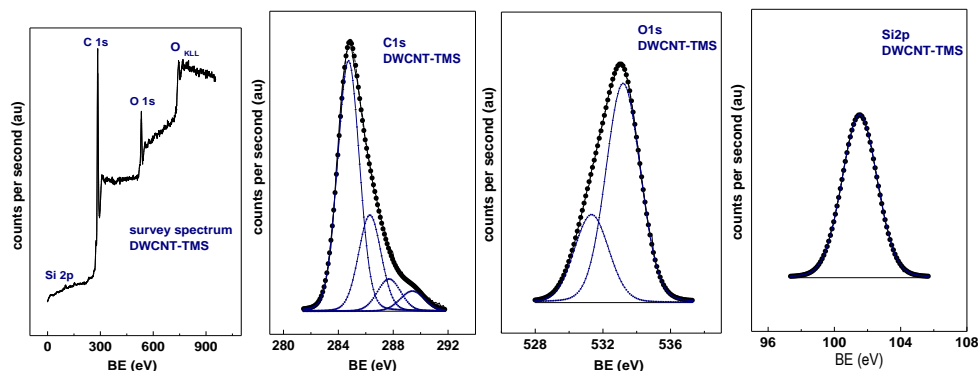


Figure 1-55. Survey, C1s, O1s and Si2p core-level spectra of DWCNT-TMS.

The survey spectrum and the high resolution C1s, O1s y N1s spectra of DWCNT-PDI 3 are displayed in Figure 1-56. If a comparison is made between the binding energies and atomic percentages of the elements in DWCNT-PDI 3

with that of **DWCNT-TMS**, the appearance of N and the relative increase in O-content with respect **DWCNT-TMS** provided evidence on the success in the “click” reaction between **PDI 3** and the **DWCNT-TMS** substrate.

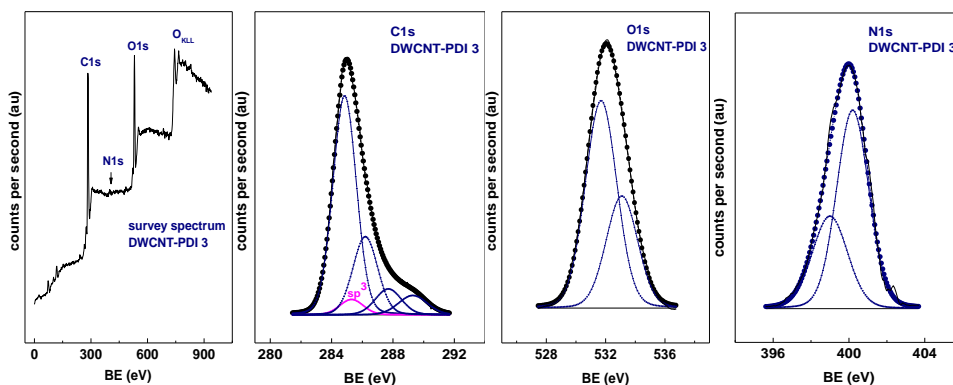


Figure 1-56. Survey, C1s, O1s and N1s core-level spectra of **DWCNT-PDI 3**

The heights of the nanoconjugates **DWCNT-PDI 1-3** were measured by Atomic Force Microscopy (AFM). AFM analyses were carried out by first depositing the samples on pre-exfoliated mica surfaces. Pristine **DWCNTs** resulted on a diameter distribution in the range of 1-3 nm, with an average diameter of ~ 1.5 nm (Figure 1-57).

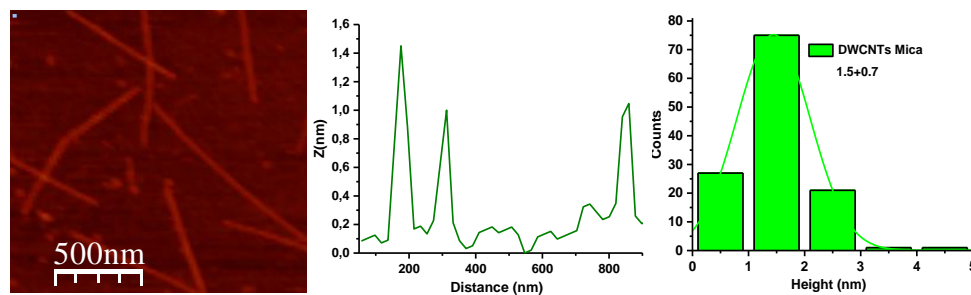


Figure 1-57. AFM images and height profile along the region indicated for pristine **DWCNT** on mica together with its height distribution histogram showing the diameter distribution of the sample.

In the case of the hybrid **DWCNT-PDI 1**, as shown in Figure 1-58, after incorporation of **PDI 1** on the surface of double-walled carbon nanotube, the observed average height was 3.2 ± 1 nm on a statistics of 125 nanotubes. According to these measurements, covalently attached perylene addend generates an average increase of around 2.2 nm. The length of the perylene moiety **1** was estimated for the most stable conformation, using the

semiempirical PM3 method implemented on HyperChem 8.0 program package (calculated length = 20 Å); so, the observed increase fitted quite well with that expected for this hybrid. Additionally, very thin bundles or individual tubes were observed at the edges corresponding to non-functionalized DWCNTs.

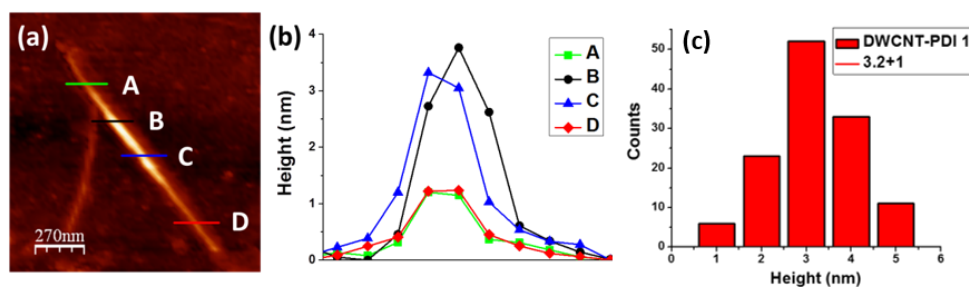


Figure 1-58. (a) AFM image of **DWCNT-PDI 1** on a mica substrate, (b) the Z-profiles indicated with lines A, B, C and D are shown in the graph, and (c) diameter distribution histogram of the **DWCNT-PDI 1**.

Similar results were obtained for the hybrids **2** and **3**. In these cases, the observed heights were a bit higher than that of **DWCNT-PDI 1** since the PDI units were oriented vertically to the DWCNT (Figure 1-59).

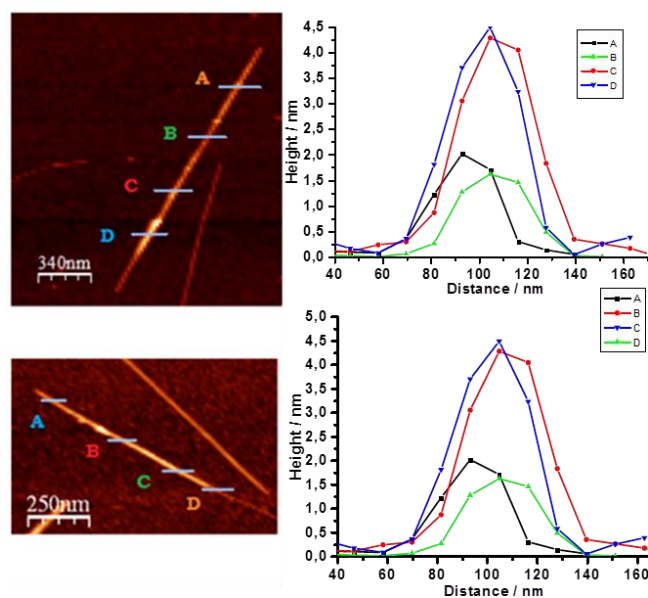


Figure 1-59. AFM image of **DWCNT-PDI 2** (top panel) and **DWCNT-PDI 3** (bottom panel) on a mica substrate.

As observed, for **DWCNT-PDI 2** the height was around 4.3 nm, that is, the height was increased by approximately 2.8 nm with respect to the *pristine* DWCNT. This was in concordance again with the length estimated by semiempirical methods for the **PDI 2** moiety (25.4 Å). Due to the similarity between both units, similar results were obtained in the case of **DWCNT-PDI 3** (observed height by AMF ~4.3 nm; estimated length = 24.3 Å).

The morphological characterization of functionalized hybrids materials **1-3** was investigated by HR-TEM as well. For example, TEM observation of nanoconjugate **DWCNT-PDI 2** (Figure 1-60) showed that the multi-layered structure of nanotubes were not degraded by the chemical processes and there were certain materials attaching to the nanotube wall, which could be attributed to perylene moieties.

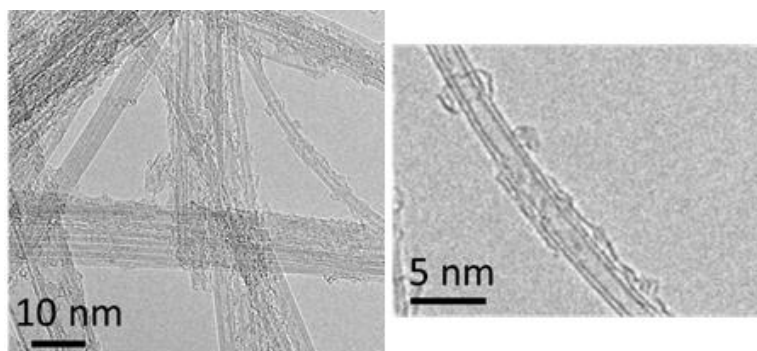


Figure 1-60. TEM image of **DWCNT-PDI 2** hybrid material.

The electrochemical behavior of **DWCNT-PDIs** and reference compounds **PDI 1-3C** was investigated by cyclic voltammetry (CV) and Osteryoung Square Wave Voltammetry (OSWV) at room temperature in a standard three-electrode cell, in dry *o*-DCB/acetonitrile 4:1 solution containing 0.1 M tetra-*n*-butylammonium hexafluorophosphate (TBAPF₆) as supporting electrolyte. Comparison between the reduction potential of **DWCNT-PDIs** and their respective reference compounds **PDICs** gave light on the electronic interactions between the carbon nanotube and the **PDI**. Table 3 shows a summary of the electrochemical data deduced from OSWV measurements. Reference perylenediimides **PDI 1-3C** are active in the cathodic zone showing two reduction potentials in the observation window. **PDI 2C** shows a lower first reduction potential (40-50 mV), than the other two perylenediimide derivatives indicating a better acceptor ability. Comparison of the first reduction potential of the hybrids and reference compounds indicate, in all cases, small shifts to

more negative values when the PDIs are covalently attached to the DWCNTs, evidencing electronic communication between both electroactive groups, the electron donor CNT and the electron acceptor PDI.

Table 3. Electrochemical data [V vs Fc/Fc⁺] for the reduction process of functionalized DWCNTs and its reference compounds (**PDI 1-3C**) detected by OSWV.^a

Sample	E ^{1red} (V)	E ^{2red} (V)
PDI 1C	-1.13	-1.33
DWCNT-PDI 1	-1.15	-1.36
PDI 2C	-1.07	-1.30
DWCNT-PDI 2	-1.10	-1.27
PDI 3C	-1.14	-1.26
DWCNT-PDI 3	-1.20 ^b	

^[a] In *o*-DCB/acetonitrile 4:1 solution (0.1 M TBAPF₆) at room temperature. ^[b] Broad reduction peak attributed to the overlapping of the first and second reduction processes.

The ground-state features of perylendiimides in the final nanohybrids were probed by steady-state absorption experiments. The UV-vis spectra of functionalized DWCNTs were recorded in comparison with its control perylendiimides **PDI 1-3C** using NMP as solvent (Figure 1-61).

In hybrids **2** and **3**, we observe a small red-shift in the absorption maxima corresponding to the PDI chromophore (450-550 nm), when compared with that of its PDIs references, suggesting the existence of electronic interactions between DWCNTs and PDIs in the ground state. Nevertheless, the most interesting feature in the absorption spectra of DWCNT-PDI hybrids is the appearance of a new band at around 550 nm.

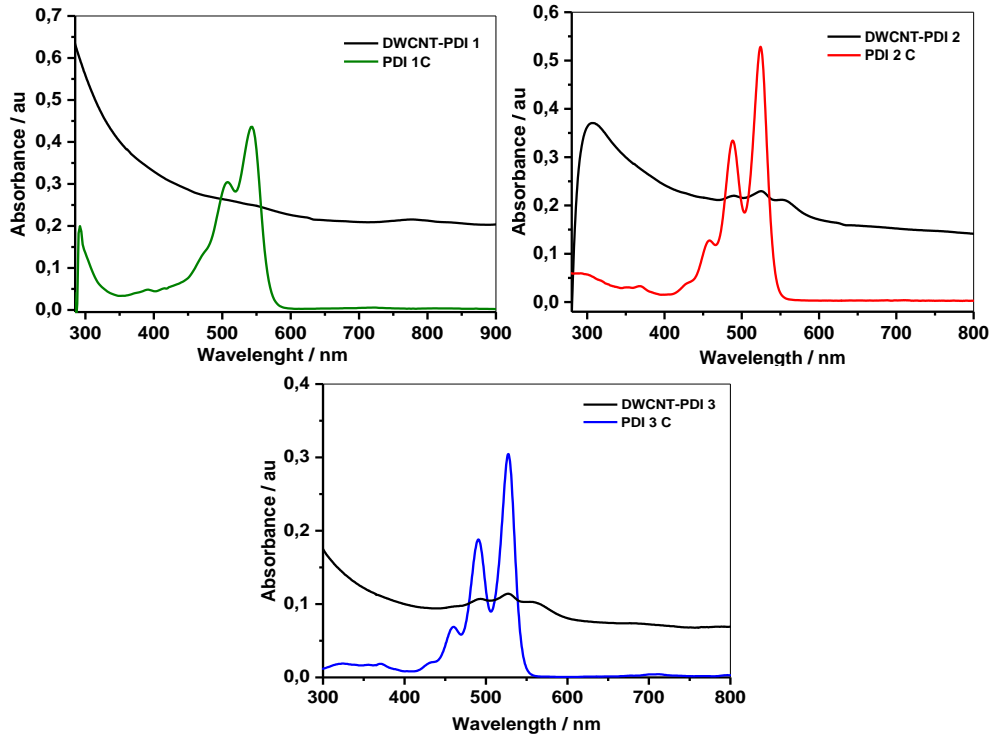


Figure 1-61. UV-vis absorption spectra of **DWCNT PDI 1-3** and its control **PDI 1C-3C** recorded in NMP.

To determine the origin of this band, the absorption spectra of **DWCNT-PDI 2-3** were registered in solvents with different polarity as chlorobenzene ($ET(30) = 36.8$ kcal/mol) and NMP ($ET(30) \text{ NMP} = 42.2$ kcal/mol) (Figure 1-62).

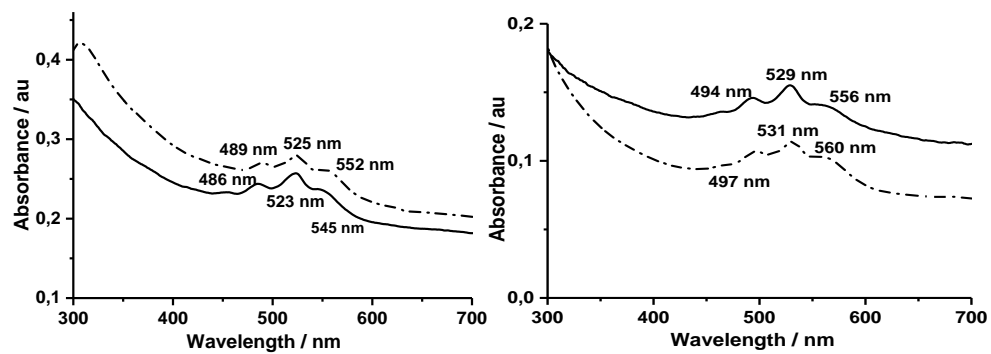


Figure 1-62. Absorption spectra of: (left) **DWCNT-PDI 2** in chlorobenzene (black line) and NMP (dotted line) and (right) **DWCNT-PDI 3** in chlorobenzene (black line) and NMP (dotted line).

Whilst the absorption bands corresponding to the PDI chromophore were shifted by 2-3 nm in chlorobenzene, when the more polar NMP was used as solvent, the shift of the new band was higher (4-7 nm), indicating higher influence of solvent's polarity and suggesting the existence of charge transfer. To confirm this hypothesis, a mixture of DWCNT and **PDI-3C** was prepared (Figure 1-63).

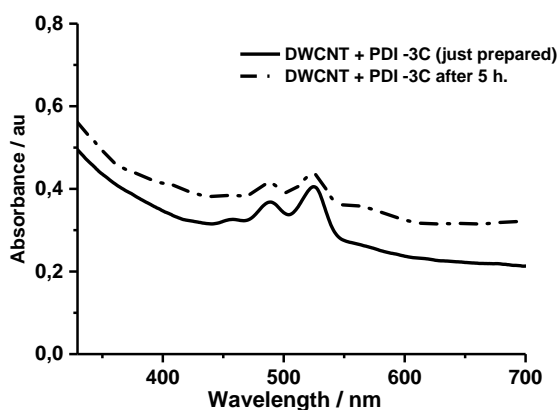


Figure 1-63. Absorption spectra of a mixture of DWCNT and **PDI-3C** in NMP, just prepared (black line) and after 5h (dotted line).

The absorption spectrum of the mixture (just prepared) do not show the presence of this band, but it can be observed after 5 hours, indicating a dynamic process, which can be assigned to charge transfer.

The existence of electronic interactions between PDI moieties and DWCNTs was also supported by emission spectroscopy by comparing the fluorescence of reference compounds **PDI 1-3C** with the fluorescence observed for **DWCNT-PDI 1-3** when excited at the maximum absorption wavelength of PDICs (Figure 1-64). In all cases, the fluorescence of PDI in the hybrids is weaker than those of the reference compounds (~ 60-70%) indicating that DWCNTs quench the emission of the attached PDI. These results suggest the existence of non-fluorescent static complex in the hybrids (*via* intra- or intermolecular association) or occurrence of electron transfer from DWCNT to the singlet excited PDI.

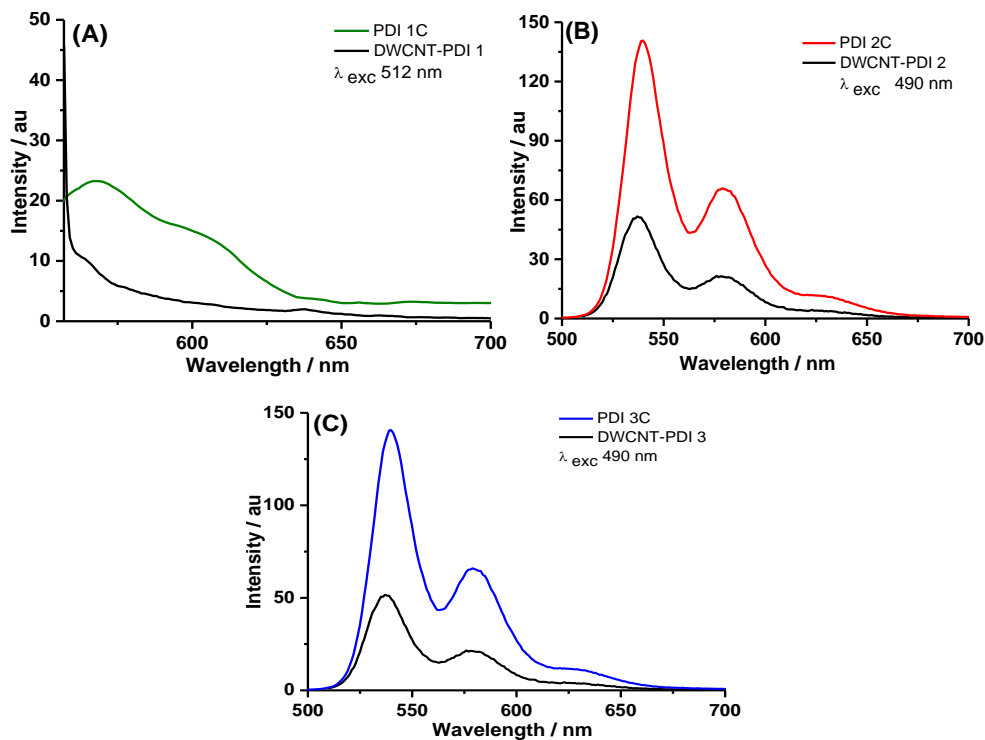


Figure 1-64. Fluorescence spectra of DWCNT-PDIs hybrid materials (black line) as compared with its control PDIs ((A) 1 (—), (B) 2 (—) and (C) 3 (—)), obtained in NMP. The excitation wavelength was indicated in each case, and the concentrations were adjusted showing the same optical density at the excitation wavelength.

Further, femtosecond transient absorption and electron pooling studies were performed to secure evidence for any electron transfer in these donor-acceptor hybrids. The studies were performed in the group of Prof. Francis D'Souza, at North Texas University.

First, photoluminescence behavior of pristine DWCNT utilized in the present study was examined in Sodium cholate hydrate solution (SC) since better exfoliation of nanotubes compared to that in organic solvents is generally observed in this media.¹⁷² As shown in Figure 1-65, although weak, DWCNTs revealed weak emission bands whose peak positions matched those of SWCNTs.

¹⁷² D. A. Tsybouski, J.-D. R. Rocha, S. M. Bachilo, L. Cagnet and R. B. Weisman, *Nano Lett.*, 2007, 7, 3080.

Earlier, Weisman and co-workers¹⁷³ attributed this to the presence of small percentage of SWCNTs trapped in commercial samples of DWCNTs, such as the one used in the present study.

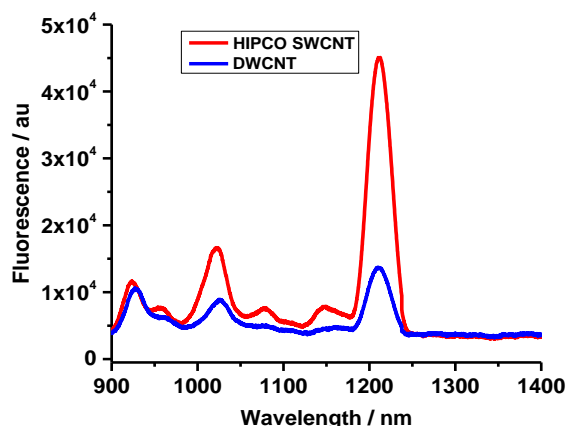


Figure 1-65. Emission spectra of both HiPco SWCNT and DWCNT dispersed in aqueous 2% sodium cholate hydrate (SC), exciting at 659nm.

Transient absorption studies on perylenediimide precursors used to derivatize DWCNTs were performed in Ar-saturated NMP (Figure 1-66). At the excitation wavelength of 400 nm, transient spectra revealed negative peaks in the 485, 528 and 580 nm range, opposite mimic of the ground state absorption and positive peaks in the 650-1000 nm range with peak maxima at 700 nm. The ground state recovery of the 528 nm band and decay of the 700 nm band (see Figure 1-66 d, e and f) for all three cases appeared to be mirror images. PDI-exhibited absorption bands close to ¹PDI* in the 700 nm range.

¹⁷³ D. A. Tsyboulski, Y. Hou, N. Fakhri, S. Ghosh, R. Zhang, S. M. Bachilo, M. Pasquali, L. Chen, J. Li and R. B. Weisman, *Nano Lett.*, **2009**, *9*, 3282.

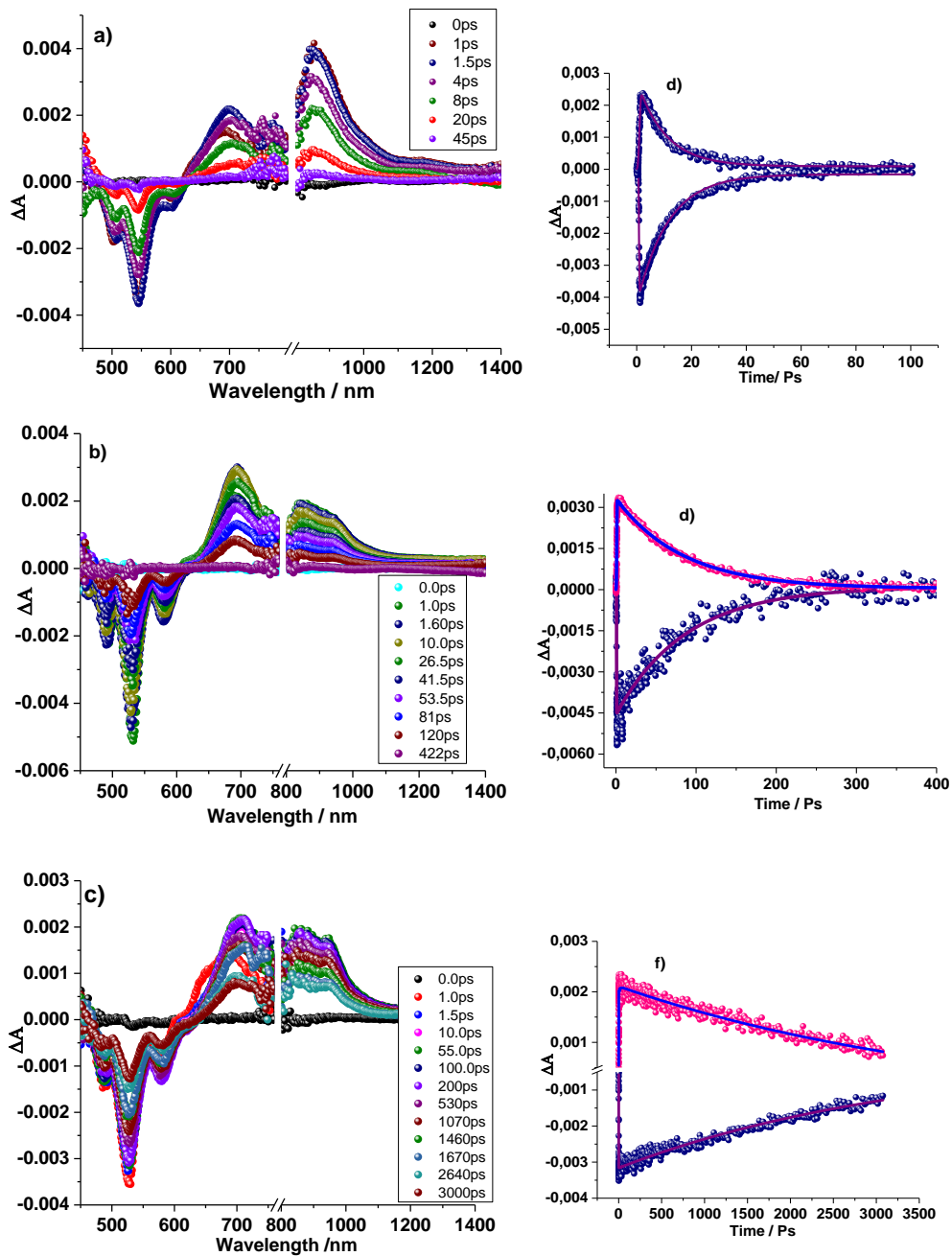


Figure 1-66. Femtosecond transient absorption spectra of (a) PDI 1C, (b) PDI 2C and (c) PDI 3C in Ar-saturated NMP at the excitation wavelength of 400 nm at the indicated time intervals. Figures d, e and f show the time profiles of the 528 and 700 nm bands of the respective PDI derivatives.

Figure 1-67 shows the transient absorption spectra of **DWCNT-PDI 1-3** in NMP. Immediately after excitation, strong exciton bands both in the visible and near-IR region within 1 ps were observed. At 1 ps, peak minima at 518, 551, 700, 1004, 1089, 1200 and 1337 nm were observed irrespective of the nature of the hybrids.

These peak positions matched that of pristine SWCNTs and the total recovery of these bands occurred within 3-4 ps (figure d, e and f), time constant reported earlier for SWCNT exciton recovery.¹⁷⁴ At higher time scales of over 4 ps, no new peaks corresponding to either 1PDI* or PDI⁻ or DWCNT^{·+} suggesting that the time scale for all these processes are much smaller and that any signal corresponding to these processes are buried within the exciton peaks originated from trace amounts of SWCNTs in the sample.

¹⁷⁴ Y. Shibono, T. Umeyama, Y. Matano, N. V. Tkachenko, H. Lemmetyinen and H. Imahori, *Org. Lett.*, **2006**, *8*, 4425.

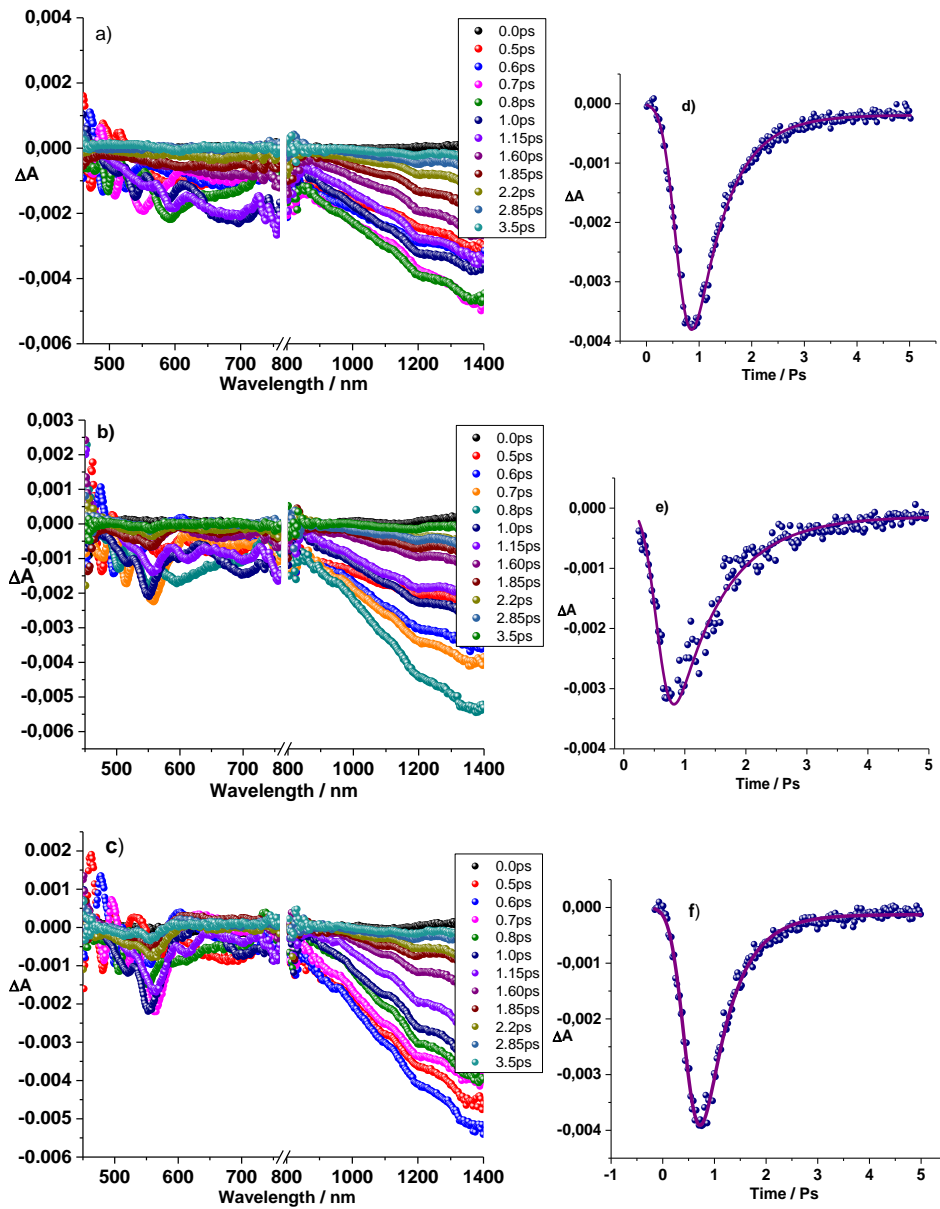


Figure 1-67. Femtosecond transient absorption spectra of (a) **DWCNT-PDI 1**, (b) **DWCNT-PDI 2** and (c) **DWCNT-PDI 3** in Ar-saturated NMP at the excitation wavelength of 400 nm at the indicated time intervals. Figs. d, e and f show the time profile of the 1200 nm peak attributed to exciton of trace amounts of SWCNT present in the sample.

Studies on the utilization of donor-acceptor nanohybrids as a photocatalysts to accumulate electron transfer products is highly useful not only to gather additional evidence of electron transfer in the nanohybrids especially when the spectroscopic evidence of electron transfer is bleak but also as functional materials for light driven catalytic processes such as solar fuel production.¹⁷⁵ In this regard, one of the well-established methods involves photocatalytic electron pooling using methyl viologen (MV^{2+}) as an electron acceptor, and 1-benzyl-1,4-dihydronicotinamide (BNAH) as a sacrificial electron donor.^{176,177}

Figure 1-68 (a) shows the spectrum of **DWCNT-PDI 1** in the presence of MV^{2+} and various amounts of BNAH. Similar spectra were obtained for other investigated hybrid systems. It could be seen that in the absence of BNAH, when the concentration of MV^{2+} is 0.5 mM in the hybrid solution, no peak at 608 nm corresponding to the formation of MV^+ was observed. However, MV^+ peak appears in the presence of BNAH which increase with the increase in concentration of BNAH. This suggests that the BNAH acts as a sacrificial hole-shifting component in the electron mediation experiment.

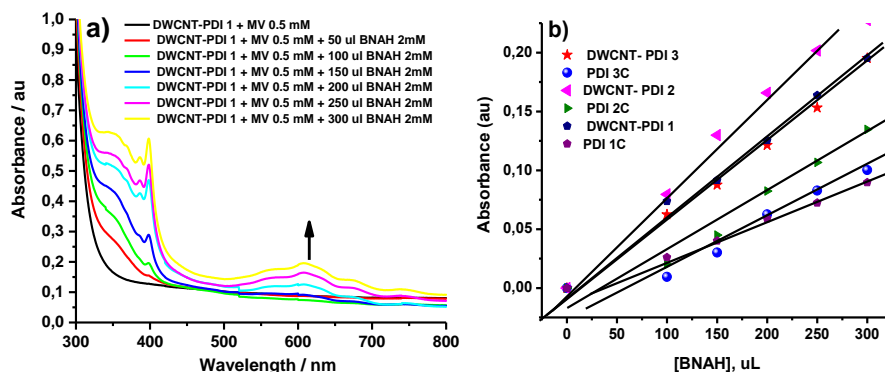


Figure 1-68. (a) Electron pooling experiment of **DWCNT-PDI 1** dissolved in DMF containing 0.5 mM MV^{2+} upon addition of increasing amounts of BNAH. (b) Extent of MV^+ formation for the hybrids **1-3** and control compounds **PDI 1-3C** revealing the effect of DWCNT in improving electron pooling ability.

¹⁷⁵ F. D'Souza and O. Ito, *Chem. Soc. Rev.*, **2012**, 41, 86.

¹⁷⁶ S. Fukuzumi, H. Imahori, K. Ohkubo, H. Yamada, M. Fujitsuka, O. Ito and D. M. Guldi, *J. Phys. Chem. A*, **2002**, 106, 1903.

¹⁷⁷ F. D'Souza, A. S. D. Sandanayaka and O. Ito, *J. Phys. Chem. Lett.*, **2010**, 1, 2586.

As depicted in figure 1-69 the photocatalytic process involves electron pooling into the added MV^{2+} in the presence of hole shifter BNAH by the continuous irradiation of the nano hybrids.

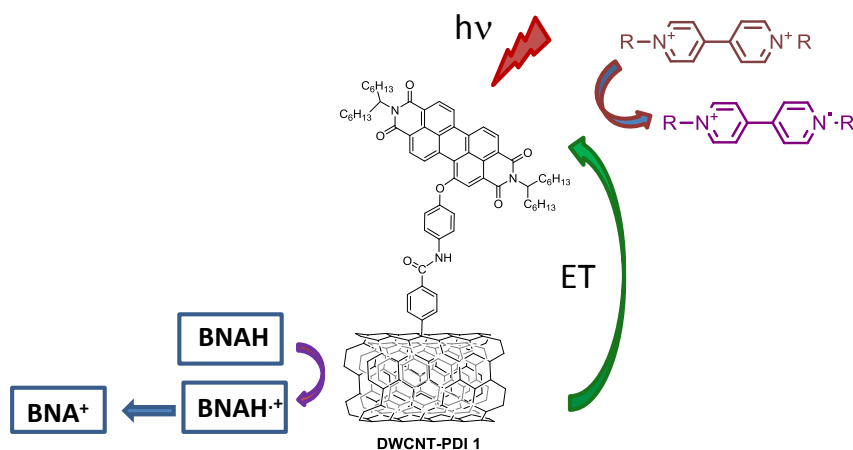


Figure 1-69. Mechanistic details of electron pooling in **DWCNT-PDI 1** hybrid catalyzed photochemical reaction.

Control experiments were also performed by utilizing perylene precursors without DWCNTs under similar experiments conditions. As shown in Figure 1-68 (b), efficiency of electron pooling for the donor-acceptor hybrids is at least twice as much as that of pristine perylene diimide precursors highlighting the importance of having both donor and acceptor in the photocatalytic cycle. However, the overall electron pooling efficiencies for DWCNT-PDI hybrids are much lower than that reported for fullerene or SWCNT based hybrids,¹⁷⁷ indicating poor electron transfer efficiencies as suggested by fluorescence and transient absorption studies. It may be mentioned here that in a study by Aurisicchio *et al.*,¹²⁰ the authors concluded lack of electron transfer in porphyrin-DWCNT hybrid materials wherein the utilized porphyrin was an electron donor unlike the electron acceptor, PDI used in the present study.

Despite the high purity of the starting DWCNTs (>98%), from the previous results we can remark that owing to the presence of a small amount of *pristine* SWCNTs, strong exciton peaks, associated with these SWCNTs impurities, are observed in the transient spectra. These exciton peaks could hamper the observation of the radical anion PDI⁻ generated during the electron-transfer process which could be buried by them.

1.4 Conclusions

In the context of the previous findings the next conclusions can be drawn from this chapter:

In the first part of the chapter, two nanoconjugates containing SWCNTs and fulleropyrrolidine derivatives have been successfully prepared and characterized by the common techniques for these kinds of materials (FTIR, Raman spectroscopy, TGA, XPS, as well as AFM and TEM microscopies).

The presence of the fulleropyrrolidine moiety attached to the nanotube was expected to induce electronic communication. In this sense, the electrochemical properties of both hybrids *f*-SWCNT **3** and *f*-SWCNT **4** were investigated by Osteryoung square wave voltammetry (OSWV). A cathodic shift was observed in both cases which is attributable to the existence of electronic interactions between the SWCNTs and the fullerene cages. Further, femtosecond transient absorption studies are in progress to study the photophysical properties of these materials.

In the second part of the chapter, three different DWCNT-PDI covalent nanoconjugates were synthesized and characterized also by the common spectroscopic and microscopic techniques above-mentioned. Functionalization of the outer wall leaving the inner walls intact was confirmed by Raman spectroscopy and TGA experiments.

The existence of electronic communication between the PDI moieties and the DWCNTs was confirmed by fluorescence studies. Hence, the fluorescence of PDI in the hybrids was found to be quenched (60-70%) due to interactions with DWCNT.

Further evidence of the existence of electronic communication between both electroactive units was obtained from the electrochemical studies, which showed small shifts of the first reduction potential to more negative values when the PDIs are covalently attached to the DWCNTs.

Finally, femtosecond transient absorption and electron pooling studies were performed to seek evidence of charge separation in these hybrids. However, evidence of photoinduced electron transfer from DWCNT to the singlet excited PDI from the femtosecond transient absorption and photocatalytic electron pooling studies were rather weak warranting additional tuning of energy levels in the hybrid.

1.5 Experimental section

- **Materials**

Organic solvents used in this work were purchased from Aldrich or Acros Organics and used as received, unless stated otherwise.

HiPco SWCNTs were purchased from NanoIntegris (purified grade, length = 100-1000 nm, diameter ~0.8-1.2 nm, < 15% remaining iron particles) and used without further purification treatment.

Ultra-Pure DWCNTs were purchased from XinNano Materials, Inc., (www.xinnanomaterials.com), (catalog number: XNM-UP-11050, purity > 98%). The diameters of the outer and inner tubes were found to be 1.00–1.81 nm and 0.88 nm respectively.

- **Instrumentation**

Microwave reactions were performed in a CEM Discover reactor, equipped with fiber optic temperature detector and pressure control.

Elmasonic P 300 H sonicator bath (37 kHz) was used to perform the sample sonication.

¹H NMR spectra were obtained on Bruker TopSpin AV-400 (400 MHz) spectrometer. Chemical shifts are reported in parts per million (ppm) relative to the solvent residual peak (CDCl₃, 7.27 ppm and CDCl₂CDCl₂, 6 ppm). **¹³C NMR** chemical shifts are reported relative to the solvent residual peak (CDCl₃, 77.00 ppm and CDCl₂CDCl₂, 44.00 ppm).

UV-vis measurements were carried out on a Shimadzu UV 3600 spectrophotometer.

FTIR spectra were obtained on a Fourier Transform IR spectrometer (Avatar 370), using pellets of dispersed samples of the corresponding compounds in dried KBr.

Fluorescence spectra were recorded with a Perkin Elmer LS 55 and on a Cary Eclipse fluorescence spectrophotometer.

TGA analysis were performed using a TGA/DSC Linea Excellent instrument by Mettler-Toledo, collected under inert atmosphere of nitrogen, with a rate of 10°C min⁻¹, and the weight changes were recorded as a function of temperature.

Raman spectra were obtained on Renishaw inVia Raman microscope at room temperature with an exciting laser source (785 cm⁻¹). Measurements were taken with 10 s of exposure times at varying numbers of accumulations. The laser spot

was focused on the sample surface using a long working distance 100× objective. Raman spectra were collected on numerous spots on the sample and recorded with a Peltier cooled CCD camera.

Mass spectra were obtained from a Bruker Microflex matrix-assisted laser desorption/ionization time of flight (MALDI-TOF) and from a VOYAGER DETM STR mass spectrometer (MALDI-TOF) using dithranol as matrix.

AFM images were acquired in tapping mode using a Multimode V8.10 (Veeco Instruments Inc., Santa Barbara, USA) with a NanoScope V controller (Digital Instruments, Santa Barbara, USA). The cantilevers (RTESP from Bruker Probes) were silicon cantilevers with a resonance frequency of 300 kHz and a nominal force constant of 40 Nm⁻¹.

TEM observations were carried out using TOPCON002B (Topcon CO.) at an acceleration voltage of 120 kV.

Photoelectron spectra (XPS) were obtained with a VG Escalab 200R spectrometer equipped with a hemispherical electron analyzer and an MgK α ($h\nu = 1253.6$ eV, 1 eV = 1.6302×10^{-19} J, X-ray source, powered at 100 W. The background pressure in the analysis chamber was kept below 7×10^{-9} mbar during data acquisition. The area under analysis was around 7.4 mm² and the pass energy of the analyzer was set at 50 eV, for which the resolution as measured by the full width at half maximum (FWHM) of the Au4f 7/2 core level was 0.86 eV. High resolution spectra were recorded in increments of 0.1 eV with dwell times of 50 ms. High-resolution spectra envelopes were obtained by curve fitting synthetic peak components using the software “XPS peak” after subtracting an S-shaped background. Symmetric Gaussian-Lorentzian product functions (90G/10L) were used to approximate the line shapes of the fitting components.

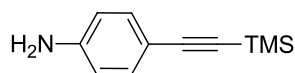
Osteryoung Square Wave voltammetry (OSWV) experiments were carried out on a potentiostat/galvanostat AUTOLAB in a one-compartment cell equipped with a platinum working microelectrode ($\varnothing = 2$ mm) and a platinum wire counter electrode. The measurements were performed in *o*-DCB/Acetonitrile 4:1 solution. Tetra-*n*-butylammonium hexafluorophosphate (TBAPF₆) (0.1 M as supporting electrolyte) was purchased from Aldrich-Sigma and used without purification.

Femtosecond transient absorption spectroscopy experiments were performed using an ultrafast femtosecond laser source (libra) by coherent incorporating

diode-pumped, mode locked ti:sapphire laser (vitesse) and diode-pumped intra cavity doubled Nd:YLF laser (evolution) to generate a compressed laser output of 1.45 W. For optical detection, a helios transient absorption spectrometer coupled with femtosecond harmonics generator both provided by ultrafast systems llc was used. The source for the pump and probe pulses were derived from the fundamental output of libra (compressed output 1.45 W, pulse width 100 fs) at a repetition rate of 1 khz. 95% of the fundamental output of the laser was introduced into harmonic generator, which produces second and third harmonics of 400 and 267 nm besides the fundamental 800 nm for excitation, while the rest of the output was used for generation of white light continuum.

1.4.1 Synthesis of organic compounds

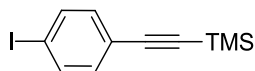
4-[(Trimethylsilyl)ethynyl]aniline (**3**)¹⁵¹



To a stirring solution of 4-iodoaniline (5 gr, 22.8 mmol) in triethylamine (40 mL) was added at room temperature bis(triphenylphosphine)palladium(II) dichloride (80 mg, 0.114 mmol), copper(I) iodide (43.4 mg, 0.2 mmol) and TMSA (3.5 mL, 1.1 equiv.). The mixture was stirred overnight. Then the mixture was filtered and the filtrate was washed with ether (100 mL). The combined organic phase was then washed with NH₄Cl (2 M) (2x 100 mL), brine and dried over Na₂SO₄ to give the desired product as a white solid (4.2 gr, 97%).

¹H-RMN (400 MHz, CDCl₃, δ/ppm): 7.30 (d, 2H, J=8.8 Hz), 6.40 (d, 2H, J=8.4 Hz), 3.65 (s, 2H), 0.15 (s, 9H).

(4-Iodo-phenylethynyl)trimethylsilane (**5**)¹⁵¹

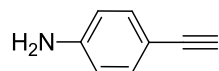


To a round-bottom flask fitted with an addition funnel and nitrogen inlet was added BF₃(O(C₂H₅)₂) (2.6 mL, 21.1 mmol, 4 equiv.) which was then chilled in a dry ice-acetone bath (-20°C). To the reaction flask was added dropwise over 5 minutes a solution of the aniline derivative **3** (1 gr, 5.28 mmol, 1 equiv.) in dry ether, followed by a solution of *tert*-butylnitrite (2.2 mL, 18.48 mmol, 3.5 equiv.) also in dry ether. The mixture was then stirred an additional 10 minutes, and the cold bath was allowed to warm to 5°C over 15 minutes. To the mixture was added diethyl ether, and the mixture was chilled in an ice-bath for 15 minutes.

The solid was collected by filtration, washed with diethyl ether, and dried to give the diazonium salt. After briefly air-drying, the diazonium salt was dissolved in CH₃CN and then added dropwise *via* cannula to a solution of NaI (870 mg, 5.8 mmol, 1.1 equiv.) and I₂ (134.5 mg, 0.5 mmol, 0.1 equiv.) in acetonitrile (CH₃CN). The mixture was stirred at room temperature for 1 hour, then Na₂S₂O₃ (aq) (2 M) was added to the mixture. The mixture was extracted with CH₂Cl₂ (3x 80mL), and the organic phase was washed with brine and dried over MgSO₄. The crude product was purified by column chromatography (silica gel), first with hexane and then mixtures of hexane/EtOAc to give the desired product (600 mg, 38%).

¹H-RMN (400 MHz, CDCl₃, δ/ppm): 7.64 (d, 2H, J=8.5 Hz), 7.19 (d, 2H, J=8.5 Hz), 0.25 (s, 9H).

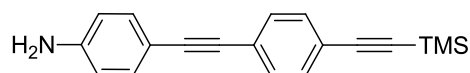
4-Ethynylaniline (**4**)



The silylated alkyne (1gr, 5.28 mmol, 1 equiv.) was dissolved in a mixture of CH₂Cl₂/MeOH (50:50). Potassium carbonate (1.45 gr, 10.6 mmol, 2 equiv.) was added, and the reaction was stirred overnight. Water was added and the reaction mixture was extracted with CH₂Cl₂, dried with MgSO₄, filtered, and then the solvent was removed under reduced pressure. The resulting product was used without further purification (700 mg, 5.06 mmol, 96%).

¹H-RMN (400 MHz, CDCl₃, δ/ppm): 7.31 (d, 2H, J=8.6 Hz), 6.61 (d, 2H, J=8.6 Hz), 2.97 (s, 1H).

1-trimethylsilylethynyl-4-((4-aminophenyl)-ethynyl)benzene (**6**)¹⁷⁸

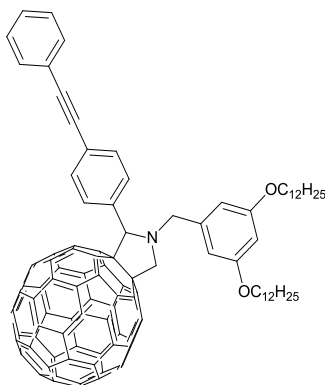


A slight excess of 4-ethynylaniline **4** (500 mg, 4.27 mmol, 1.2 equiv) was added to a solution of 4-Iodo-(phenylethynyl)trimethylsilane **5** (1.05 gr, 3.56 mmol, 1 equiv), *N,N*-diisopropylethylamine (2.5 mL, 14.2 mmol, 4 equiv), 2 mol% of PdCl₂(PPh₃)₂ and 4 mol% of CuI in THF (50 mL). After stirring 24 h under argon at room temperature, the solvent was evaporated, water was added and the

¹⁷⁸ G. Pera, S. Martín, L. M. Ballesteros, A. J. Hope, P. J. Low, R. J. Nichols and P. Cea, *Chem. Eur. J.* **2010**, *16*, 13398.

crude was extracted with CH_2Cl_2 . The organic layer was dried with MgSO_4 , filtered, and the solvent was removed under reduced pressure. The crude product was purified by column chromatography (silica gel) using hexane/EtOAc mixtures (8:2) as eluent to yield the desired product as a yellow solid (520 mg, 50%).

$^1\text{H-RMN}$ (400 MHz, CDCl_3 , δ /ppm): 7.42 (s, 4H), 7.35 (d, 2H, $J=8.4$ Hz), 6.67 (d, 2H, $J= 8.1$ Hz), 4.13 (br s, 2H, NH_2).

N-(3,5 didodecyloxybenzyl)-2-(4-phenylethynyl)phenylpyrrolidine (control)

A solution of C₆₀ (785 mg, 1.09 mmol), 3,5-bis(dodecyloxy)benzylglycine¹⁵³ (194.1 mg, 0.36 mmol) and 4-(Phenylethynyl)benzaldehyde¹⁷⁹ (75 mg, 0.36 mmol) in toluene was refluxed for 6 hours. The mixture was cooled, filtered and the solvent was evaporated under reduced pressure. Column chromatography (SiO₂, CH₂Cl₂/Hexane 2:8) yielded the desired **control** sample (40 mg, 8%) as a brown solid.

¹H NMR (400 MHz, CDCl₃, δ/ppm): 7.92 (br s, 2H, 2xH-ph), 7.64 (d, 2H, J=8 Hz, 2xH-ph), 7.51-7.54, (m, 2H, 2xH-ph), 7.33-7.36 (m, 3H, 3xH-ph), 6.82 (s, 2H, 2xH-ph), 6.50 (s, 1H, 1xH-ph), 4.92 (d, J= 9.0 Hz, 2H, CH₂N), 4.50 (d, J=13.2 Hz, 1H, 1xH-pyrrolidine), 4.20 (d, J=9.0 Hz, 1H, 1xH-pyrrolidine), 4.02-4.06 (m, 4H, 2xCH₂O), 3.65 (d, J=13.2 Hz, 1H, 1xH-pyrrolidine), 1.81-1.88 (m, 6H, 3xCH₂-alkyl chain), 1.56 (s, 6H, 3xCH₂-alkyl chain), 1.45-1.52 (m, 6H, 3xCH₂-alkyl chain), 1.28 (br s, 26H, 13xCH₂-alkyl chain), 0.87-0.90 (m, 6H, 2xCH₃-alkyl chains).

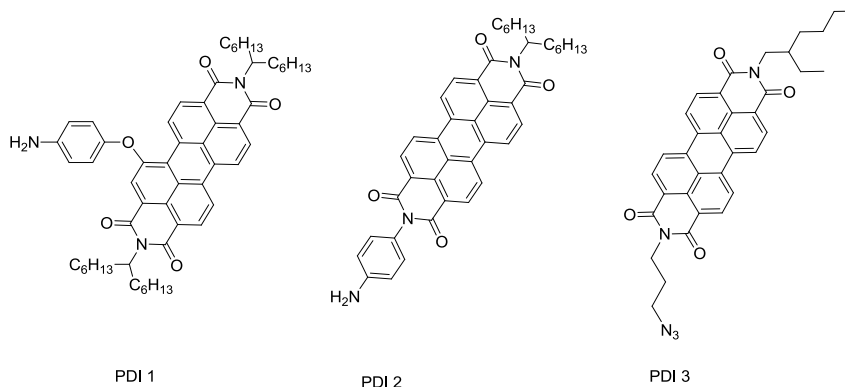
¹³C NMR (100 MHz, CDCl₃, δ/ppm):160.6, 156.3, 153.9, 153.1, 147.3, 146.7, 146.3, 146.2, 146.1, 146, 145.9, 145.7, 145.5, 145.3, 145.2, 145.1, 144.7, 144.6, 144.4, 142.5, 142.1, 142, 141.8, 141.6, 140.1, 139.7, 137.3, 136, 131.6, 128.4, 123.4, 107.3, 100.1, 90.1, 80.8, 68.7, 68.2, 66.5, 56.6, 31.9, 29.6, 29.5, 29.4, 26.1, 22.7, 14.1.

IR (KBr) ν , cm⁻¹: 3429, 2917 (CH aliphatic), 2851 (CH aliphatic) 1596 (C=C aromatic), 1453 (C=N pyrrolidine), 1161, 1058, 838, 756, 685, 521 (C₆₀).

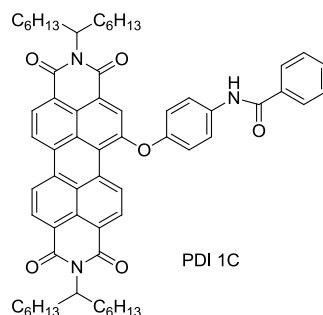
HR-MS (m/z) (MALDI-TOF): calculated for C₁₀₇H₆₇NO₂: 1397.52; found: 1397.69 (M⁺).

¹⁷⁹ K. Worm-Leonhard and M. Melda, *Eur. J. Org. Chem.*, **2008**, 31, 5244.

Synthesis of PDIs (1-3) was performed in the group of Prof. Ángela Sastre at the University of Miguel Hernandez, (Elche).¹⁶⁶



***N,N'*-di(1-hexylheptyl)-1-[4'-(benzoylamino)phenoxy]perylene-3,4,9,10-tetracarboxydiimide (PDI 1C):**



To a solution of **PDI 1** (15 mg, 0.018 mmol) in CH_2Cl_2 (30 mL) was added benzoyl chloride (1.16 mg, 0.008 mmol) dissolved in CH_2Cl_2 (30 mL). After stirring 48 h at room temperature, water (30 mL) and concentrated HCl (20 mL at 37%) were added. The mixture was filtered and the solid product washed with water and then with acetone affording 5 mg (65%) of **PDI 1C** as a red-orange colored solid.

¹H NMR (400 MHz, CDCl_3 , δ /ppm): 9.58 (d, 1H, $J=8.4$ Hz, 1xH-PDI), 8.72 -8.60 (m, 5H, 5xH-PDI), 8.30 (s, 1H, 1xH-PDI), 7.92-7.89 (m, 3H, 3xH-Ph), 7.78 (d, 2H, $J=8.6$ Hz, 2xH-Ph), 7.56-7.50 (m, 3H, 3xH-Ph), 7.24 (d, 1H, $J=8.6$ Hz, 1xH-Ph), 5.20-5.16 (m, 2H, 2xCH-alkyl chain), 2.21 (br. s, 1H, 1xNH), 1.87-1.80 (m, 4H, 2xN- $\text{CH}(\text{CH}_2-(\text{CH}_2)_4-\text{CH}_3)_2$), 1.60-1.56 (m, 4H, 2xN- $\text{CH}(\text{CH}_2-(\text{CH}_2)_4-\text{CH}_3)_2$), 1.35-1.25 (m, 32H, 16x CH_2 -alkyl chain), 0.82 (m, 12H, 4x CH_3 -alkyl chain).

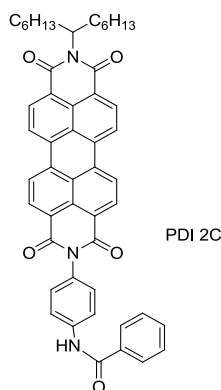
^{13}C NMR (100 MHz, CDCl_3 , δ /ppm): 165.7, 142.3, 135.4, 134.7, 134.4, 132.1, 129.3, 128.9, 128.6, 127.0, 125.9, 124.9, 123.7, 122.3, 120.6, 54.7, 53.4, 32.3, 31.7, 30.9, 29.7, 29.2, 29.1, 26.9, 22.5, 14.0.

IR (KBr) ν , cm^{-1} : 2926, 2857, 1697 (C=O imide), 1656 (C=O imide), 1594, 1510, 1440, 1337, 1249, 1198, 810.

UV/vis (benzonitrile), λ_{max} (log ϵ): 510 nm (5.70), 526 nm (5.83).

HR-MS (m/z) (MALDI-TOF): calculated for $\text{C}_{63}\text{H}_{71}\text{N}_3\text{O}_6$: 965.53 [M] $^-$; found: 965.55 [M] $^-$.

N-[4'-(benzoylamino)aminophenyl]-N'-(1-hexylheptyl)perylene-3,4,9,10-tetracarboxydiimide (PDI 2C):



To a solution of **PDI 2** (15mg, 0.023 mmol) in CH_2Cl_2 (30 mL) was added benzoyl chloride (1.6 mg, 0.011 mmol) dissolved in CH_2Cl_2 (30 mL). After 20 h stirring at room temperature, water (30 mL) and concentrated HCl (20 mL at 37%) were added. The mixture was filtered and the solid product washed with water and then with acetone yielding 6 mg (71%) of **PDI 2C** as a red-orange colored solid.

^1H NMR (400 MHz, CDCl_3 , δ /ppm): 8.88-8.81 (m, 8H, 8xH-PDI), 8.31 (br. s., 1H, 1xNH), 7.88- 7.86 (m, 4H, 4xH-Ph), 7.68 (t, 1H, $J=7.7$ Hz, 1xH-Ph), 7.59 (t, 2H, $J=7.9$ Hz, 2xH-Ph), 7.42 (d, 2H, $J=8.7$ Hz, 2xH-Ph), 5.25-5.21 (m, 1H, 1xCH-alkyl chain), 2.25-2.20 (m, 4H, 2x CH_2 -alkyl chain), 1.93-1.87 (m, 4H, 2x CH_2 -alkyl chain), 1.33-1.23 (m, 10H, 5x CH_2 - alkyl chain), 0.84 (m, 6H, 2x CH_3 -alkyl chain).

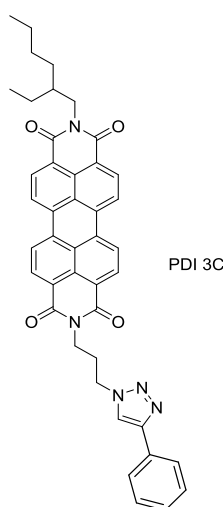
^{13}C NMR (100 MHz, CDCl_3 , δ /ppm):162.3, 161.8, 161.4, 160.9, 137.8, 136.2, 134.9, 133.3, 129.9, 129.5, 129.3, 127.2, 126.6, 126.3, 124.4, 123.9, 122.4, 122.2, 118.4, 115.5, 112.7, 109.9, 56.1, 53.5, 52.9, 52.7, 32.3, 31.6, 29.1, 26.8, 22.5, 13.9.

IR (KBr) ν , cm^{-1} : 2960, 2923, 2857, 1703 (C=O imide), 1656 (C=O imide), 1598, 1520, 1407, 1352, 1257, 1176, 1103, 813.

UV/vis (benzonitrile), λ_{max} ($\log \epsilon$): 463 nm (4.84), 494 nm (5.23), 532 nm (5.43).

HR-MS (m/z) (MALDI-TOF): calculated for $\text{C}_{50}\text{H}_{45}\text{N}_3\text{O}_5$: 767.33 [M] $^-$; found: 767.32 [M] $^-$.

N-[3'-(4''-phenyl-1'',2'',3''-triazol-1''-yl)propyl]-N'-(2-ethylhexyl)perylene-3,4,9,10-tetracarboxydiimide (PDI 3C):



To a solution of **PDI 3** (15 mg, 0.026 mmol) and phenylacetylene (2.62 mg, 0.026 mmol) in a mixture of CH_2Cl_2 (2 mL) and water (2 mL), was added $\text{CuSO}_4 \cdot 5\text{H}_2\text{O}$ (0.64 mg, 0.0026 mmol) and sodium ascorbate (0.77 mg, 0.0039 mmol). The oxygen was removed by several cycle of vacuum/argon. Finally, the solution was stirred at room temperature for 24 h. The organic layer was then diluted with CH_2Cl_2 , washed with water, dried on MgSO_4 , filtered and evaporated to dryness. Purification of the residue by column chromatography (SiO_2 , eluent: chloroform:acetone 8:2) gave pure **PDI 3C** (9 mg, 60%) as a red-orange colored solid.

$^1\text{H NMR}$ (300 MHz, $\text{CDCl}_2\text{CDCl}_2$, δ /ppm): 8.72-8.59 (m, 8H, 8xH-PDI), 7.93 (s, 1H, 1xH-triazole), 7.73 (d, 2H, $J=7.8$ S-12 Hz, 2xH-Ph), 7.36 (t, 2H, $J=7.8$ Hz, 2xH-Ph), 7.29-7.26 (m, 1H, 2xH-Ph), 4.59 (t, 2H, $J=6.8$ Hz, 1xN- $\text{CH}_2\text{-CH}_2\text{-CH}_2$ -triazole), 4.40 (t, 2H, $J=6.8$ Hz, 1xN- $\text{CH}_2\text{-CH}_2\text{-CH}_2$ -triazole), 4.24-4.12 (m, 2H, 2xN- $\text{CH}_2\text{-R}$), 2.60-2.51 (m, 2H, 1xN- $\text{CH}_2\text{-CH}_2\text{-CH}_2$ -triazole), 2.08-1.97 (m, 1H,

1xCH-alkyl chain), 1.47-1.36 (m, 8H, 4xCH₂-alkyl chain), 1.02-0.91 (m, 6H, 2xCH₃).

¹³C NMR (75 MHz, CDCl₂CDCl₂, δ/ppm): 163.5, 163.3, 135.1, 134.8, 134.3, 132.0, 131.5, 131.4, 131.3, 128.6, 125.6, 123.3, 123.2, 122.9, 122.7, 30.7, 29.5, 28.6, 24.1, 22.9, 13.9, 10.6.

IR (KBr) ν , cm⁻¹: 2962, 2929, 2857, 1696 (C=O imide), 1652 (C=O imide), 1589, 1437, 1344, 1248, 1173, 854, 807, 741.

UV/vis (benzonitrile), λ_{\max} (log ϵ): 462 nm (5.01), 494 nm (5.41), 532 nm (5.61).

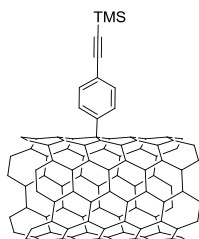
HR-MS (m/z) (MALDI-TOF): calculated for C₄₃H₃₇N₅O₄: 687.28 [M]⁻; found: 687.29 [M]⁻.

1.4.2 Synthesis of nanohybrids

General procedure for the modification of SWCNT with aryl diazonium salts.

Pristine HiPco SWCNTs (30 mg) were dispersed in NMP (250 mL) by means of an ultrasound bath sonicator for 10 minutes. Then, nitrogen was bubbled in the suspension for 2 minutes and the corresponding aniline (10 mmol) and isoamyl nitrite (10 mmol) were added. The mixture was allowed to react for 24 h at 70 °C. After cooling to room temperature, the suspension was filtered through a polytetrafluoroethylene (PTFE) (2 μ m) membrane and washed repeatedly with DMF, methanol and diethyl ether, until the filtrate solution remained colorless; finally, the material was dried overnight in a vacuum oven at 55 °C, thus affording functionalized materials **1** and **2**.

Preparation of *f*-SWCNT **1**



According to the general procedure, pristine SWCNTs (30 mg), aniline derivative **3** (1.89 gr, 10 mmol) and isoamyl nitrite (1.33 mL, 10 mmol) gave the desired product (35 mg).

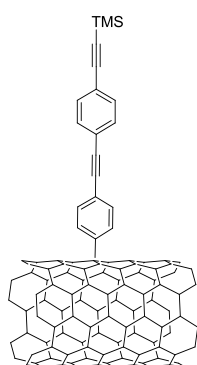
IR (KBr) ν , cm^{-1} : 2900 (C-H stretching mode), 1595 (C-H in plane stretching mode) and 2153 (C \equiv C stretching mode).

TGA: Weight loss and temperature of desorption: 6.64%, 550 °C.

Raman: $I_D/I_G = 0.35$.

XPS (% atomic): C = 94.3, O = 4.1, Si = 1.6.

Preparation of *f*-SWCNT 2



According to the general procedure, pristine SWCNTs (30 mg), aniline derivative **6** (2.89 gr, 10 mmol) and isoamyl nitrite (1.33 mL, 10 mmol) gave the desired product (32 mg).

IR (KBr) ν , cm^{-1} : 2900 (C-H stretching mode), 1598 (C-H in plane stretching mode).

TGA: Weight loss and temperature of desorption: 9.7%, 550 °C.

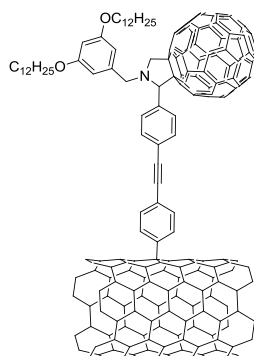
Raman: $I_D/I_G = 0.62$.

XPS (% atomic): C = 94.7, O = 3.8, Si = 1.5.

General procedure for the preparation of *f*-SWCNT 3 and *f*-SWCNT 4:

To a suspension of SWCNT (15 mg) in *o*-dichlorobenzene (40 mL) was added the fulleropyrrolidine derivative **7** (30 mg, 0.025 mmol), $[\text{Pd}(\text{Ph}_3)_4]$ (10% mol) and a large excess of piperidine (3 mL). The mixture was heated using microwave irradiation (50W) in a sealed tube for 60 minutes. After cooling to room temperature, the solid was then centrifuged followed by decanting of the solvent and the remaining solid washed several times with methanol and CH_2Cl_2 (sonicated, centrifuged, and filtered) until the filtrate solution remained colorless, thus affording functionalized SWCNTs **3** and **4**.

Preparation of *f*-SWCNT 3



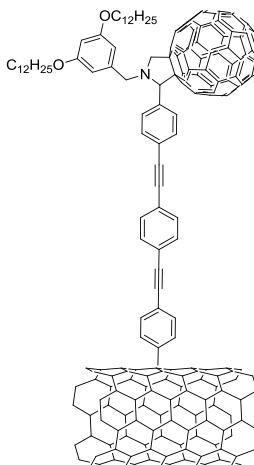
According to the general procedure, *f*-SWCNT 1 (15 mg), fulleropyrrolidine derivative 7 (30 mg, 0.025 mmol), [Pd(Ph₃)₄] (spatula tip), and piperidine (3 mL) gave the desired product (16 mg).

IR (KBr) ν , cm⁻¹: 2900 (C-H stretching mode), 1595 (C-H in plane stretching mode) and 1459 (C-N stretching mode).

TGA: Weight loss and temperature of desorption: 19%, 550 °C.

XPS (% atomic): C = 93.4, O = 5.5, N = 1.1.

Preparation of *f*-SWCNT 4



According to the general procedure, *f*-SWCNT 2 (15 mg), fulleropyrrolidine derivative 7 (30 mg, 0.025 mmol), [Pd(Ph₃)₄] (spatula tip), and piperidine (3 mL) gave the desired product (18 mg).

IR (KBr) ν , cm^{-1} : 2900 (C-H stretching mode), 1593 (C-H in plane stretching mode) and 1456 (C-N stretching mode).

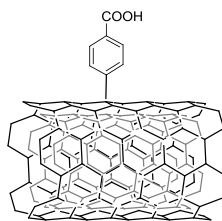
TGA: Weight loss and temperature of desorption: 15.5%, 550 °C.

XPS (% atomic): C = 93.5, O = 5.4, N = 1.1.

General procedure for the modification of DWCNT with aryl diazonium salts.

To a dispersion of ultrapure DWCNT (40 mg) (stirred for 48 hours + sonicated by tip sonicator for 6 hours) in NMP (70 mL) was added 2 equiv of the phenyl derivative and 2.4 equiv of isoamyl nitrite. The reaction mixture was stirred for 48 h at 70°C, and then filtered through a PTFE membrane with an average pore size of 0,2 μm . The black precipitate was washed with NMP and CH_2Cl_2 and then dried in the oven under reduce pressure obtaining the corresponding DWCNT-phenyl derivative.

Functionalization of DWCNT with 4-aminobenzoic acid (DWCNT-COOH)



According to the general procedure, to a dispersion of ultrapure DWCNT (40 mg) in NMP (70 mL) was added 4-aminobenzoic acid (915 mg , 6.66 mmol) and isoamyl nitrite (937 mg, 8 mmol) yielding 48 mg of the desired material.

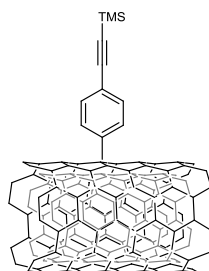
IR (KBr) ν , cm^{-1} : 2900 (C-H stretching mode), 1595 (C-H in plane stretching mode).

TGA: Weight loss and temperature of desorption: 12.7%, 600 °C.

Raman: $I_D/I_G = 0.25$.

XPS (% atomic): C = 94.3, O = 5.7.

Functionalization of DWCNT with 4-[(2-trimethylsilyl)ethynyl]aniline (DWCNT-TMS)



According to the general procedure, to a dispersion of ultrapure DWCNT (40 mg) in NMP (70 mL) was added 4-[(2-trimethylsilyl)ethynyl]aniline (1.2 gr, 6.66 mmol) and isoamyl nitrite (937 mg, 8 mmol) affording 56 mg of the functionalized material.

IR (KBr) ν , cm^{-1} : 2900 (C-H stretching mode), 1595 (C-H in plane stretching mode).

TGA: Weight loss and temperature of desorption: 12.3%, 600 °C.

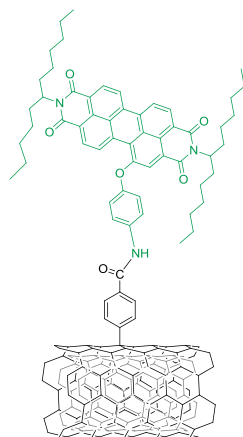
Raman: $I_D/I_G = 0.35$.

XPS (% atomic): C = 94.5, O = 4.8, Si = 0.7.

General procedure for the preparation of DWCNT-PDI 1 and DWCNT-PDI 2

DWCNT-COOH (4 mg) was dispersed in NMP (20 mL) and subsequently added to a stirred solution of the corresponding perylenediimide (10 mg), DCC (1 equiv), DMAP (1 equiv) and HOBt (1.2 equiv). The resulting mixture was stirred for 60 hours at 60 °C. The crude was then filtered on a PTFE membrane and washed with methanol and dichloromethane to afford the desired material.

Synthesis of DWCNT- PDI 1



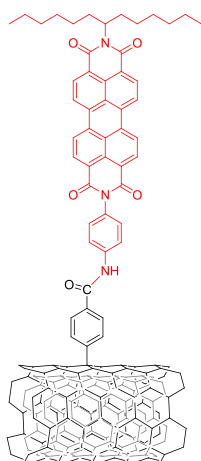
According to the general procedure, DWCNT-COOH (4 mg), PDI 1 (10 mg, 0.012 mmol), DCC (2.5 mg, 0.012 mmol), DMAP (1.5 mg, 0.012 mmol) and HOBt (1.9 mg, 0.014 mmol) in NMP (20 mL) gave the desired product (7 mg).

IR (KBr) ν , cm^{-1} : 2900 (C-H stretching mode), 1704 (C=O imide), 1649 (C=O imide), 1560 (C-H in plane stretching mode)

TGA: Weight loss and temperature of desorption: 21%, 600 °C.

XPS (% atomic): C = 89.6, O = 8.9, N = 1.5

Synthesis of DWCNT-PDI 2



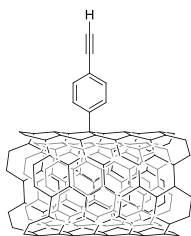
According to the general procedure, DWCNT-COOH (4 mg), PDI 2 (10 mg, 0.015 mmol), DCC (3.1 mg, 0.015 mmol), DMAP (1.9 mg, 0.015 mmol) and HOBt (2.4 mg, 0.018 mmol) in NMP (20 mL) gave the desired product (6 mg).

IR (KBr) ν , cm^{-1} : 2900 (C-H stretching mode), 1725 (C=O imide), 1659 (C=O imide), 1597 (C-H in plane stretching mode).

TGA: Weight loss and temperature of desorption: 16.6%, 600 °C.

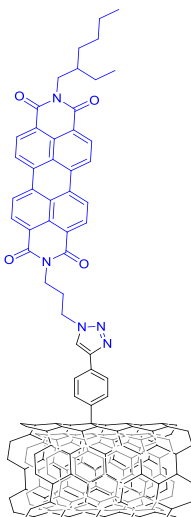
XPS (% atomic): C = 91.4, O = 6.8, N = 1.8

Deprotection of DWCNT-TMS



To a suspension of DWCNT-TMS (15 mg) in NMP (50 mL) at 0°C was added a solution of TBAF (1M in THF) (2mL). The reaction mixture was stirred at room temperature for 2 hours and then filtered on a PTFE membrane (0.2 μm). The nanotubes were washed several times with NMP and then with dichloromethane, redissolved in NMP and used directly for the next step.

Synthesis of DWCNT-PDI 3



To a suspension of deprotected DWCNT-TMS (10mL) in NMP (40 mL) were added PDI 3 (25 mg, 0.043 mmol), CuSO₄ · 5H₂O (11 mg, 0.043 mmol) and sodium ascorbate (8.5 mg, 0.043 mmol). The reaction mixture was stirred at 70°C for 48 hours and then filtered on a PTFE membrane (0.2µm). In order to remove sodium ascorbate, copper catalyst and free perylene, the black solid was washed with NMP and then with dichloromethane yielding the desired material (17 mg).

IR (KBr) ν , cm⁻¹: 2900 (C-H stretching mode), 1703 (C=O imide), 1655 (C=O imide), 1616 (C-H in plane stretching mode).

TGA: Weight loss and temperature of desorption: 16%, 600 °C.

XPS (% atomic): C = 88.3, O = 8.1, N = 3.6.

CHAPTER 2: GRAPHENE

2.1 Introduction

Graphene is a two-dimensional material which has unique mechanical, electrical and thermal properties^{59,180} arising from its strictly single atomic layers of sp^2 -bonded carbon atoms densely packed in a honeycomb crystal lattice. Graphene is considered to be the mother of all graphitic forms (Figure 2-1). It can be wrapped into zero dimensional fullerenes, rolled into a dimensional carbon nanotube or stacked into three-dimensional graphite.

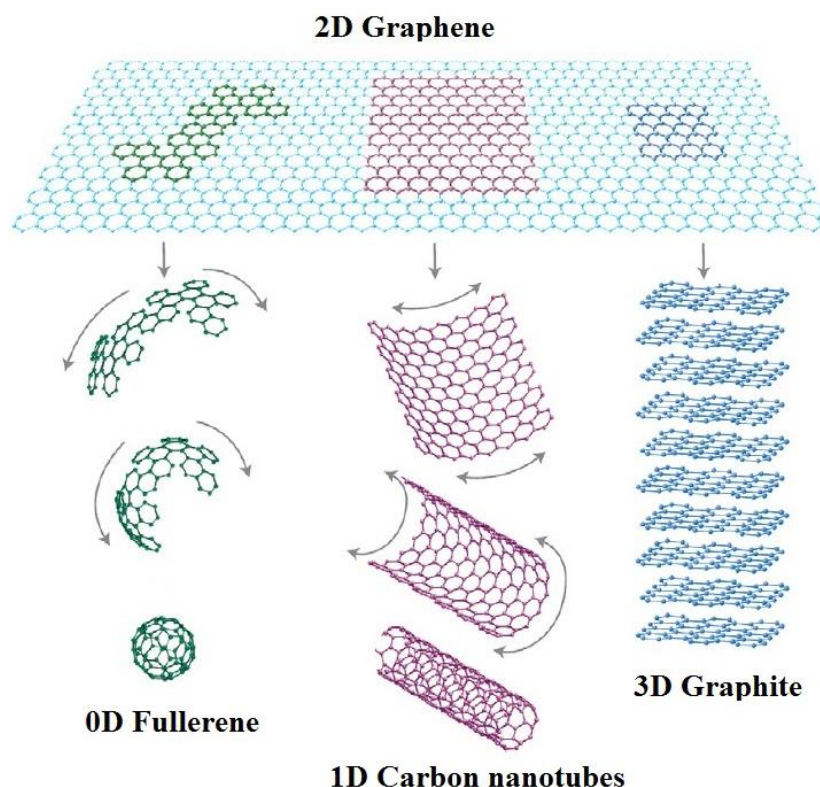


Figure 2-1: Schematic drawing of the relationship between graphene and other carbon materials. Graphene, a 2D building material, can be wrapped up into 0D buckyballs, rolled into 1D nanotubes or stacked into 3D graphite.¹²

2.1.1 Graphene structure

Graphene sheets are composed of carbon atoms linked in hexagonal shapes, as shown in Figure 2-2, with each carbon atom covalently bonded to

¹⁸⁰ N. Zhang, M.-Q. Yang, S. Liu, Y. Sun and Y.-J. Xu, *Chem. Rev.* **2015**, *115*, 10307.

three other carbon atoms.^{13,14,181} Each sheet of graphene is only one atom thick and each graphene sheet is considered a single molecule. It has the same structure than carbon nanotubes, but graphene is flat rather than cylindrical.

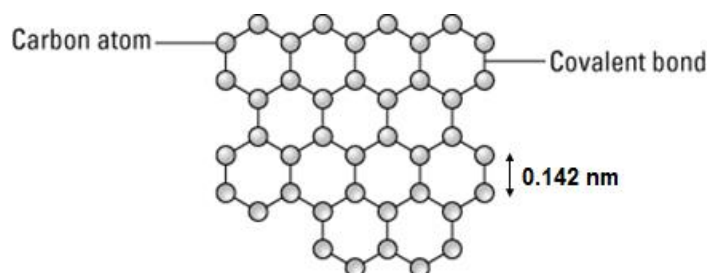


Figure 2-2. Schematic diagram of a graphene sheet.

Ideal graphene is an infinite perfectly planar sheet of C atoms, however, to create a device-like structure, the infinite sheet must be cut into finite systems. Cutting through an infinite graphene sheet, Figure 2-3, one first breaks C-C σ bonds and then obtains two semi-infinite graphene sheets, each with a one-dimensional edge. Depending on the cutting direction, two unique types of edges can be obtained: *zigzag* [Figure 2-3 (b)] and *armchair* [Figure 2-3 (c)],¹⁸² and both edge types have a different reactivity and different electronic and magnetic properties. In addition, depending on the crystallographic orientation of the edges, a semiconductor or metallic behavior is observed. The edges of the majority of synthesized graphene sheets consist of a mixture of both edges, which makes difficult to characterize the structural and electronic properties of this carbon allotrope.

¹⁸¹ A. C. Ferrari, F. Bonaccorso, V. Falco, K. S. Novoselov, S. Roche, P. Bøggild, S. Borini, F. H. L. Koppens, V. Palermo, N. Pugno, J. A. Garrido, R. Sordan, A. Bianco, L. Ballerini, M. Prato, E. Lidorikis, J. Kivioja, C. Marinelli, T. Ryhanen, A. Morpurgo, J. N. Coleman, V. Nicolosi, L. Colombo, A. Fert, M. G. Hernandez, A. Bachtold, G. F. Schneider, F. Guinea, C. Dekker, M. Barbone, Z. Sun, C. Galotias, A. N. Grigorenko, G. Konstantatos, A. Kis, M. Katsnelson, L. Vandersypen, A. Loiseau, V. Morandi, D. Neumaier, E. Treossi, V. Pellegrini, M. Polini, A. Tredicucci, G. M. Williams, B. H. Hong, J.-H. Ahn, J. M. Kim, H. Zirath, B. J. van Wees, H. van der Zant, L. Occhipinti, A. D. Matteo, I. A. Kinloch, T. Seyller, E. Quesnel, X. Feng, K. Teo, N. Rupesinghe, P. Hakonen, S. R. T. Neil, Q. Tannock, T. Lofwander and J. Kinaret, *Nanoscale*, **2015**, 7, 4598.

¹⁸² X. Jia, J. Campos-Delgado, M. Terrones, V. Meunier and M. S. Dresselhaus, *Nanoscale*, **2011**, 3, 86.

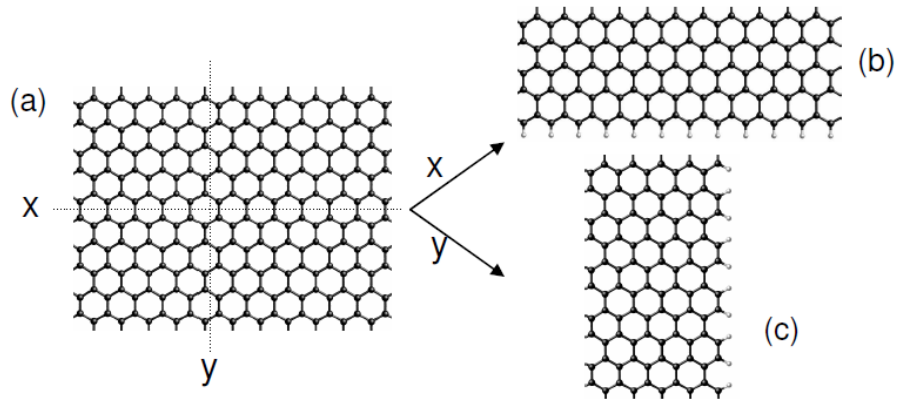


Figure 2-3. Infinite graphene sheet divided into two finites sheets.

The lattice of graphene has two carbon atoms, designated A and B, per unit cell. An *armchair* edge is formed by two different types (A and B) of carbon atoms of two-dimensional (2D) graphene lattice, whereas a *zigzag* boundary contains only one type of carbon atoms (Figure 2-4).

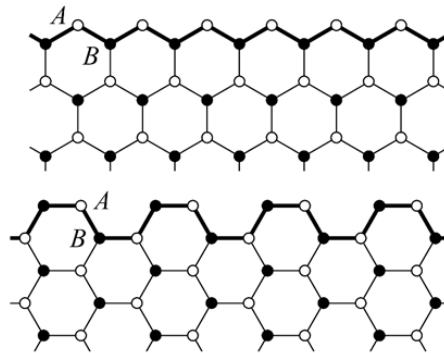


Figure 2-4. Two types of edges in single layer graphene: *zigzag* (top) and *armchair* (bottom).

2.1.2 Synthesis of graphene

Several production methodologies of graphene have been developed during the last decade (Figure 2-5).¹⁸³ These methodologies are generally classified in top-down and bottom-up approaches.

Top-down methods start from something large and proceeds to something smaller through the removal of material. In the particular case of graphene, the top-down method starts from graphite and separate the stacked sheets by overcoming the van der Waals interactions between the layers.

The bottom-up methods start with smaller entities and build them up to larger constructs. In the case of graphene, the starting material is a carbon source. The choice of the method to use is normally driven by the end application of the material.

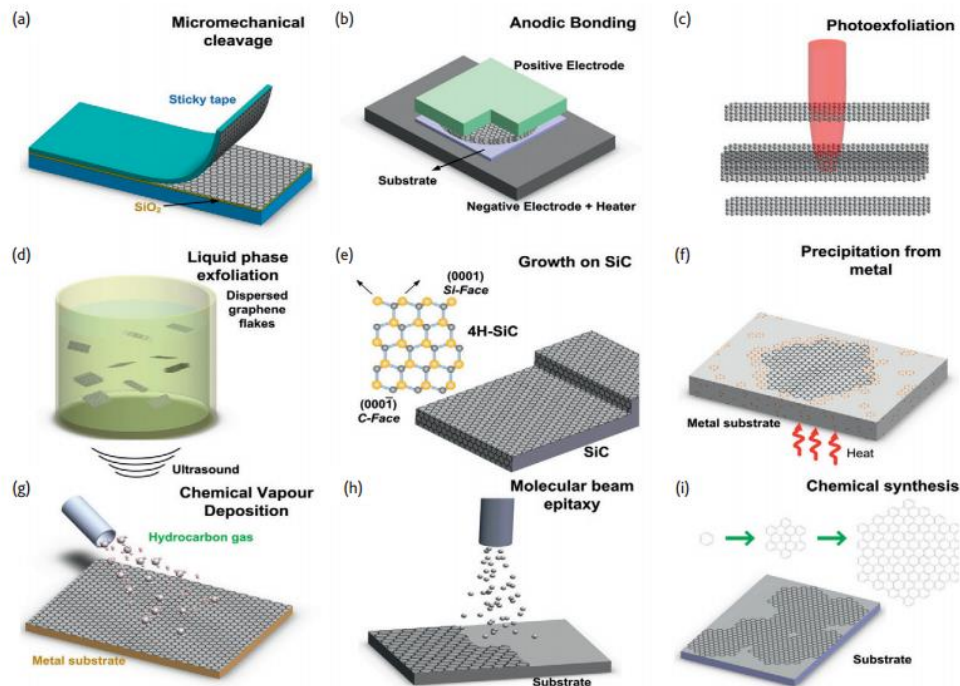


Figure 2-5. Schematic illustration of the main graphene production techniques.¹⁸³

¹⁸³ F. Bonaccorso, A. Lombardo, T. Hasana, Z. Suna, L. Colombb, A. C. Ferrari, *Mater. Today*, **2012**, *15*, 564.

TOP-DOWN METHODS:**Micromechanical cleavage**

Micromechanical cleavage (MC), usually known as “scotch tape”, has been used for decades by crystal growers and crystallographers (Figure 2-5 (a)).¹⁸⁴ In 1999, Lu *et al.* reported a controlled method of cleaving graphite,¹⁸⁵ yielding films consisting of several layers of graphene. They suggested that “more extensive rubbing of the graphite surface against other flat surfaces might be a way to get multiple or even single atomic layers of graphite plates.” It was then firstly demonstrated, achieving single layer graphene (SLG) using an adhesive tape, by Novoselov *et al.*¹² This method yields very high quality graphene, however very small amounts are obtained.

Laser ablation and photoexfoliation

Laser ablation is the use of a laser beam to remove material from a solid surface. If irradiation results in the detachment of an entire or partial layer, the process is called photoexfoliation (Figure 2-5 (c)). The ablation of a defined number of layers can be obtained exploiting the laser energy density required for ablating a SLG and N-layer graphene (NLGs).¹⁸⁶

Liquid-phase-exfoliation (LPE)

LPE of graphite is one of the most widely used methods for the preparation of single- or few-layer graphene (Figure 2-5 (d)).^{187,188,189,190} This method involves ultrasonic treatment of graphite in solvents such as NMP and DMF, since the energy required to exfoliate graphene is commonly provided by solvents whose surface energies match that of graphene. Among them, NMP has

¹⁸⁴ R. A. Schultz, M. C. Jensen and R. C. Bradt, *Int. Jour Fracture*, **1994**, 65, 291.

¹⁸⁵ X. Lu, M. F. Yu, H. Huang and R. S. Ruoff, *Nanotechnology*, **1999**, 10, 269.

¹⁸⁶ S. Dhar, A. Roy Barman, G. X. Ni, X. Wang, X. F. Xu, Y. Zheng,

S. Tripathy, Ariando, A. Russydi, K. P. Loh, M. Rubhausen, A. H.

Castro Neto, B. Ozyilmaz and T. Venkatesan, *AIP Adv*, **2011**, 1, 022109.

¹⁸⁷ (a) Y. Hernandez, V. Nicolosi, M. Lotya, F. M. Blighe, Z. Sun, S. De, I. T. McGovern, B. Holland, M. Byrne, Y. K. Gunko, J. J. Boland, P. Niraj, G. Duesberg, S. Krishnamurthy, R. Goodhue, J. Hutchison, V. Scardaci, A. C. Ferrari and J. N. Coleman, *Nat. Nanotechnol.*, **2008**, 3, 563. (b) J. N. Coleman, *Acc. Chem. Res.*, **2013**, 46, 14.

¹⁸⁸ M. Quintana, J. I. Tapia and M. Prato, *Beilstein J. Nanotechnol.*, **2014**, 5, 2328.

¹⁸⁹ A. Ciesielski and P. Samori, *Chem. Soc. Rev.* **2014**, 43, 381.

¹⁹⁰ M. Matsumoto, Y. Saito, C. Park, T. Fukushima and T. Aida, *Nat. Chem.*, **2015**, 7, 730.

been shown to be the most effective to overcome the interacting forces between graphene layers.

The LPE process generally involves three steps: 1) dispersion of graphite in a solvent, 2) exfoliation, and 3) “purification”. The third step is used to separate exfoliated from un-exfoliated flakes, and it is usually carried out *via* ultracentrifugation¹⁹¹ (Figure 2-6).

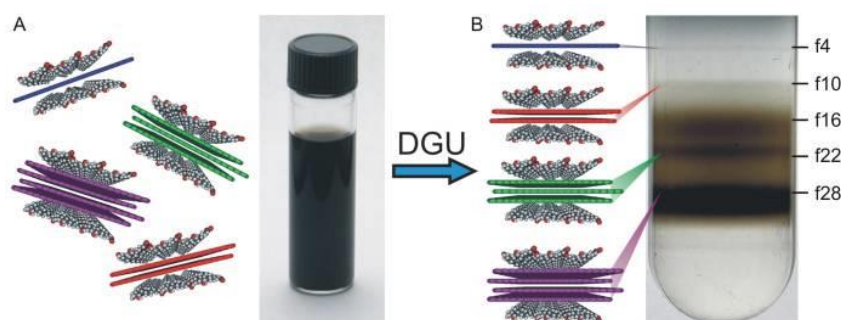


Figure 2-6. (A) Schematic illustration of ordered sodium cholate encapsulation of graphene sheets and photograph of an unsorted aqueous graphene suspension with a graphene loading of $\sim 0.1 \text{ mg mL}^{-1}$. (B) Photograph of a centrifuge tube following DGU marked with the main bands of monodisperse graphene.¹⁹²

To date, the exfoliation of graphite in dispersions has been obtained by a wide number of mechanochemical methods, which present advantages and disadvantages, however, liquid-phase exfoliation of graphite by ultrasonic techniques, is a straightforward process for the production of high quality graphene layers ready for organic functionalization. The primary physical phenomena associated with ultrasound are cavitation and nebulization. Acoustic cavitation consist in the formation, growth, and implosive collapse of bubbles in a liquid. Cavitation induces extreme conditions by collapsing air bubbles which initiates chemical reactions, while nebulization furthers the reaction within the heated droplets. Increasing the sonication time or the use of a sonication probe rather than a sonication bath have been shown to increase the

¹⁹¹ A. A. Green and M. C. Hersam, *Mater. Today*, **2007**, *10*, 59.

¹⁹² A. A. Green and M. C. Hersam, *J. Phys. Chem. Lett.*, **2010**, *1*, 544.

concentration of graphene in solution.¹⁹³ As aforementioned, after the ultrasonication process, graphene dispersions are normally centrifuged in order to eliminate graphite microcrystals (Figure 2-6). From the obtained dispersion it is possible to calculate the concentration of the graphene layers by obtaining the UV-vis absorption spectra.¹⁹⁴ This approach allows the quantification of graphene in the dispersion, enabling further organic functionalization by stoichiometric reactions.

LPE is a versatile technique and can be employed not only for the exfoliation of pristine graphite, but also for the exfoliation of graphite oxide and graphite intercalated compounds (GICs), which have different properties with respect to pristine graphite.

Oxidation of graphite

Chemically derived graphene oxide (GO) is an atomically thin sheet of graphite that has traditionally served as a precursor for graphene. The reduction of previously synthesized and exfoliated GO is probably one of the most employed methods to obtain graphene (Figure 2-7).^{195,196}

Graphite can be oxidized to graphite oxide that disperses readily in water as graphene oxide (Figure 2-7). In this method, graphene oxide is obtained by the Hummers approach using strong oxidants and concentrated acids.¹⁹⁷ This method allows graphene to be obtained in large amounts. Subsequent reduction of graphene oxide provides graphene-like structures, generally called reduced graphene oxide (rGO), since the complete reduction is not achieved.

¹⁹³ P. Blake, P. D. Brimicombe, R. R. Nair, T. J. Booth, D. Jiang, F. Schedin, L. A. Ponomarenko, S. V. Morozov, H. F. Gleeson, E. W. Hill, A. K. Geim and K. S. Novoselov, *Nano Lett.*, **2008**, *8*, 1704.

¹⁹⁴ M. Lotya, P. J. King, U. Khan, S. De and J. N. Coleman, *ACS Nano*, **2010**, *4*, 3155.

¹⁹⁵ Y. Zhu, S. Murali, W. Cai, X. Li, J. W. Suk, J. R. Potts and R. S. Ruoff, *Adv. Mat.*, **2010**, *22*, 5226.

¹⁹⁶ K. P. Loh, Q. Bao, G. Eda and M. Chhowalla, *Nat. Chem.*, **2010**, *2*, 1015.

¹⁹⁷ W. S. Hummers and R. E. Offeman, *J. Am. Chem. Soc.*, **1958**, *80*, 1339.

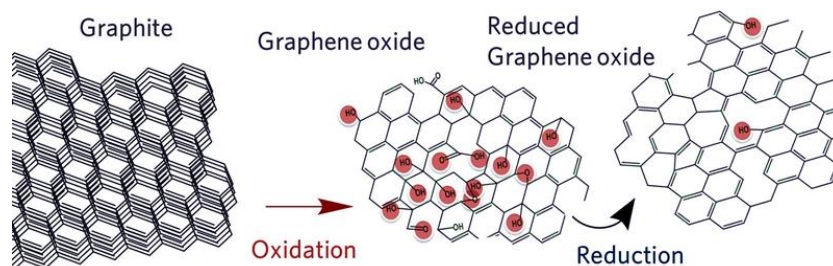


Figure 2-7: Graphite can be oxidized to give water dispersible Graphene Oxide (GO). Reduction of GO gives thick graphitic structures.

Ball milling

Mechanical activation by milling processes has been also applied to the exfoliation of graphite.¹⁹⁸ A ball mill consists of a hollow cylindrical rotor rotating about its axis, which contains balls and the material to be exfoliated. Reduction of the sized is achieved by collision between the balls and the material.

BOTTOM-UP METHODS:

Growth on SiC

The production of graphite from SiC has been investigated since the 1960s (Figure 2-5 (e)).¹⁹⁹ When SiC substrates are annealed at high temperatures, Si atoms selectively desorb from the surface and the C atoms left behind naturally form FLG. Because SiC is a wide-band-gap semiconductor, FLG on SiC can serve as a graphene substrate for electronics applications. Growth of graphene on SiC is usually referred to as “epitaxial graphene”.

Chemical vapor deposition (CVD)

CVD is a way of depositing gaseous reactants onto a substrate. (Figure 2-5(g)). The way CVD works is by combining gas molecules (often using carrier gases) in a reaction chamber which is typically set at ambient temperature. When the combined gases come into contact with the substrate within the reaction chamber (which is heated), a reaction occurs that create a thin film on the surface.¹⁴ The benefits of using CVD to deposit materials onto a substrate are that the quality of the resulting materials is usually very high. CVD graphene is

¹⁹⁸ E. Vázquez, F. Giacalone and M. Prato, *Chem. Soc. Rev.*, **2014**, 43, 58.

¹⁹⁹ D.V. Badami, *Nature*, **1962**, 193, 570.

created in two steps, the precursor pyrolysis of a material to form carbon, and the formation of the carbon structure of graphene using the disassociated carbon atoms. The main problem of this technique is that a high level of heat is required during the process, therefore metal catalysts must be used to reduce the reaction temperature, which introduce impurities in the final material.

Chemical synthesis

Graphene can also be chemically synthesized, assembling polycyclic aromatic hydrocarbons (PAHs),²⁰⁰ through surface-mediated reactions (Figure 2-5(i)). Two approaches can be used; the first exploits a dendritic precursor transformed by cyclodehydrogenation and planarization.²⁰¹ This produces small domains, called nanographene. The second relies on PAH pyrolysis.²⁰² Other benzene based precursors, such as poly-dispersed hyperbranched polyphenylene, give larger flakes.

2.1.3 Properties and applications

Graphene exhibits outstanding structural,²⁰³ electrical,²⁰⁴ and mechanical properties.²⁰⁵ It's strong but light, a million times thinner than paper, stronger than diamond, more conductive than copper (conducts both heat and electricity extremely well) and is nearly transparent in its purest form.¹⁸¹ The mechanical properties of graphene are very interesting in the design and control of graphene devices. Lee *et al.* studied the young's modulus of graphene by AFM.²⁰⁶ These studies revealed that single layer graphene is one of the strongest materials ever measured. The young's modulus has been also reported to increase with the number of layers.²⁰⁷

²⁰⁰ J. Wu, W. Pisula and K. A. Müllen, *Chem. Rev.*, **2007**, 107, 718.

²⁰¹ L. Zhi and K. A. Müllen, *J Mater Chem*, **2008**, 18, 1472.

²⁰² J. Cai, P. Ruffieux, R. Jaafar, M. Bieri, T. Braun, S. Blankenburg, M. Muoth, A. P. Seitsonen, M. Saleh, X. Feng, K. Müllen and R. Fasel, *Nature* **2010**, 466, 470.

²⁰³ J. C. Meyer, A. K. Geim, M. I. Katsnelson, K. S. Novoselov, T. J. Booth and S. Roth, *Nature*, **2007**, 446, 60.

²⁰⁴ N. Castro, F. Guinea, N. M. R. Peres, K. S. Novoselov and A. K. Geim, *Rev. Mod. Phys.*, **2009**, 81, 109.

²⁰⁵ I. W. Frank, D. M. Tanenbaum, A. M. van der Zande and P. L. J. McEuen, *Vac. Sci. Technol.*, **2007**, 25, 2558.

²⁰⁶ C. Lee, X. Wei, J. W. Kysar, and J. Hone, *Science*, **2008**, 321, 385.

²⁰⁷ Y. Zhang and C. Pan, *Diam. Relat. Mater.* **2012**, 24, 1.

Concerning the optical properties, single layer graphene has a high surface area with a negligible reflectance of the incident light in the visible region.

Noteworthy is that for pristine, the light absorbance of graphene is 2.3% per unit layer. The transparency of graphene thus decreases from single-layer to few-layer graphene. Adding another layer of graphene increases the amount of white light absorbed by approximately the same value (2.3%) (Figure 2-8).²⁰⁸

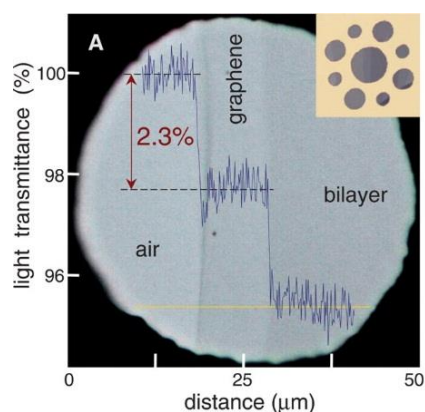


Figure 2-8. Image showing a thick metal support structure with several apertures partially covered by single-layer and few-layer graphene. The line scan profile shows the intensity of the transmitted white light.¹⁹⁵

Graphite exhibits a remarkable anisotropic behavior with respect to thermal and electrical conductivity. It is highly conductive in the direction parallel to the graphene layers because of the in-plane metallic character, whereas it exhibits poor conductivity in the direction perpendicular to the layers because of the weak van der Waals interactions between them.²⁰⁹ However the carbon atoms in the graphene layer form three σ bonds with neighboring carbon atoms by overlapping of sp^2 orbitals while the remaining p_z orbitals overlap to form a band of filled π orbitals – the valence band – and a band of empty π^* orbitals – the conduction band – which are responsible for the high in-plane conductivity.

²⁰⁸ C. Casiraghi, A. Hartschuh, E. Lidorikis, H. Qian, H. Harutyunyan, T. Gokus, K. S. Novoselov and A. C. Ferrari, *Nano. Lett.*, **2007**, 7, 2711.

²⁰⁹ D. D. L. Chung, *J. Mater. Sci.*, **2002**, 37, 1475.

Graphene is one, if not the most, promising candidates to replace silicon in electronic devices and boost their performance significantly.²¹⁰ As pure graphene is a zero band-gap semiconductor and a band gap is necessary for electronic devices, nanoribbons and few-layer graphene are of special interest because of their possibility to have a band gap. As mentioned above, graphene has two atoms per unit cell, giving rise to two conical points, K and K' per Brillouin zone, at which, the valence and the conduction bands cross (Figure 2-9). At room temperature, the mobilities are higher than that of modern Si transistors when the gate voltage is applied.

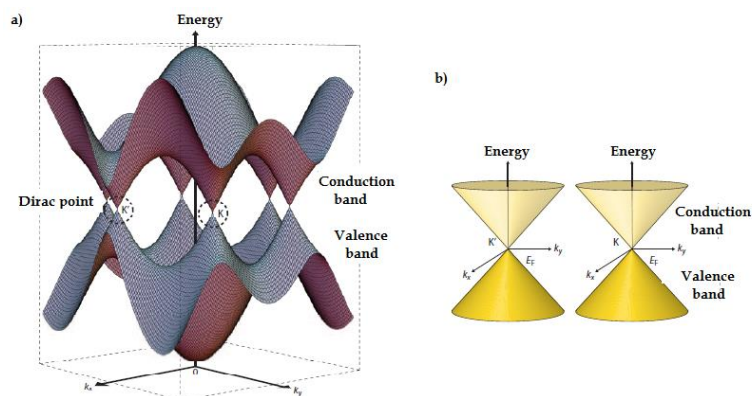


Figure 2-9. a) Energy bands near the Fermi level in single layer graphene. The conduction and valence bands cross at points K and K'. b) Conic energy bands in the proximity of the K and K' points.²¹¹

Based on the excellent properties described above a wide range of potential applications are known for graphene (Figure 2-10).^{212,213}

²¹⁰ Z. Liu, S. P. Lau and F. Yan, *Chem. Soc. Rev.*, **2015**, *44*, 5638.

²¹¹ T. Ando, *NPG Asia Mater.*, **2009**, *1*, 17.

²¹² E. P. Randviir, D. A. C. Brownson and C. E. Banks, *Mater. Today*, **2014**, *17*, 426.

²¹³ P. Avouris and C. Dimitrakopoulos, *Mater. Today*, **2012**, *15*, 86.

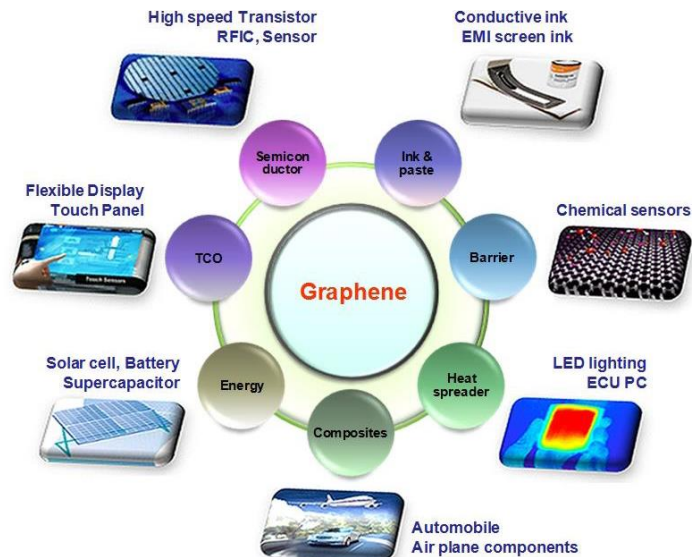


Figure 2-10: Overview of Applications of Graphene in different sectors ranging from conductive ink to chemical sensors, light emitting devices, composites, energy, touch panels and high frequency electronics.¹⁸¹

Optical Electronics

One particular area in which we will soon begin to see graphene used on a commercial scale is that in optoelectronics; specifically touchscreens, liquid crystal displays (LCD) and organic light emitting diodes (OLEDs). A useful material in optoelectronic applications must be able to transmit more than 90% of light and also offer electrical conductive properties exceeding $1 \times 10^6 \Omega\text{m}^{-1}$ and therefore low electrical resistance. Graphene is an almost completely transparent material and is able to optically transmit up to 97.7% of light. It is also highly conductive and so it would work very well in optoelectronic applications such as LCD touchscreens for smartphones, tablet and desktop computers and televisions.

Currently the most widely used material for this purpose is indium tin oxide (ITO). However, recent tests have shown that graphene is potentially able to match the properties of ITO. Also, it has recently been shown that the optical absorption of graphene can be changed by shifting the Fermi level. Although this does not sound like much of an improvement over ITO, the fact that high quality graphene has a very high tensile strength, and is flexible, makes it an interesting material for utilizing it in the aforementioned applications.

Photovoltaic Cells

Showing very low levels of light absorption whilst also offering high electron mobility means that graphene can be used as an alternative to silicon or ITO in photovoltaic cells. Silicon is currently widely used in the production of photovoltaic cells, however silicon cells are very expensive to produce. In this sense, graphene based cells are potentially much less expensive. Although the Si-based solar cells allow higher efficiencies to be obtained, the conductivity and transparency of graphene suggest that these efficiencies can be increased.²¹⁴ In addition, while silicon is able to generate electricity from certain wavelength bands of light, graphene is able to work on all wavelengths, which is another advantage to increase the mentioned efficiencies. Graphene can be used as window electrodes in inorganic (Figure 2-11 (a)), organic (Figure 2-11 (b)) and dye-sensitized solar cells devices (Figure 2-11 (c)).²¹⁵ Being flexible and thin means that graphene based photovoltaic cells could be used in clothing, to help recharge your mobile phone, or even used as photovoltaic curtains to help power our homes.

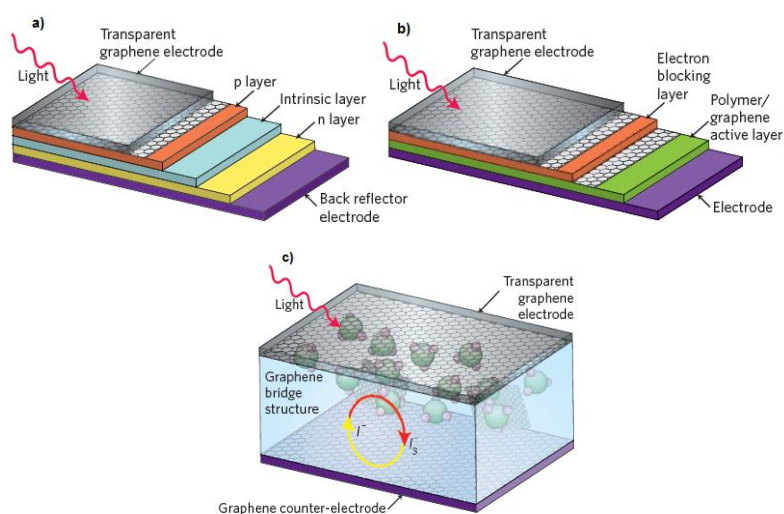


Figure 2-11: Schematics of inorganic (a), organic (b) and dye-sensitized (c) solar cells. I^- and I_3^- are iodide and tri-iodide, respectively.

²¹⁴ X. Li, H. Zhu, K. Wang, A. Cao, J. Wei, C. Li, Y. Jia, Z. Li, X. Li and D. Wu, *Adv. Mater.*, **2010**, *22*, 2743.

²¹⁵ F. Bonaccorso, Z. Sun, T. Hasan and A. C. Ferrari, *Nature Photon.*, **2010**, *4*, 611.

Energy Storage

The main problem in storing the energy in batteries and capacitors is that a battery can potentially hold a lot of energy, but it can take a long time to charge, while a capacitor, on the other hand, can be charged very quickly, but can't hold that much energy.

Graphene is being studied and developed to be used in the manufacture of supercapacitors which are able to be charged very quickly, yet also be able to store a large amount of electricity.^{216,217} Graphene based micro-supercapacitors will likely be employed in low energy applications such as smart phones and portable computing devices, while lithium ion batteries could be used in much higher energy usage applications such as electrically powered vehicles, or in smartphones, laptops and tablet PCs but presenting significantly lower size and weight.

Recent studies have shown that graphene could be used in portable electronic devices, such as energy storage in thin batteries of SLG.²¹⁸

Biological Engineering

Beyond the applications aforementioned, the biological application of graphene is a relative new area with significant potential. Since the reported use of graphene oxide (GO) as an efficient nanocarrier for drug delivery by Dai *et al.*²¹⁹ in 2008, the first study on graphene for biomedical applications, too many efforts have been made to explore the use of graphene for possible biomedical applications, such as drug/gene delivery, biological sensing and imaging, antibacterial materials and biocompatible scaffold for cell culture (Figure 2-12).²²⁰ With graphene offering a large surface area, high electrical conductivity, thinness and strength, it would be a good candidate for the development of fast and efficient biosensors, with the ability to monitor such things as glucose levels, hemoglobin levels, cholesterol and even DNA sequencing.²²¹ Eventually we may

²¹⁶ A. C. D. Brownson, K. D. Kampouris and C. E. Banks, *J. Pow. Sourc*, **2011**, 196, 4873.

²¹⁷ K. Chen, S. Song, F. Liua and D. Xue, *Chem. Soc. Rev.*, **2015**, 44, 6230.

²¹⁸ C. Casiraghi, A. Hartschuh, H. Qian, S. Piscanec, C. Georgi, A. Fasoli, K. S. Novoselov, D. M. Basko, and A. C. Ferrari, *Nano Lett.*, **2009**, 9, 1433.

²¹⁹ Z. Liu, J. T. Robinson, X. M. Sun and H. Dai, *J. Am. Chem. Soc.*, **2008**, 130, 10876.

²²⁰ J. A. Mann and William R. Dichtel, *ACS Nano* **2013**, 7, 7193.

²²¹ S. Daunert, P. Garrigues, G. Gauglitz, K. G. Heumann, K. Jinno, D. C. Muddiman, A. Roda, A. Sanz-Medel and S. A. Wise, *Anal. Bioanal. Chem.*, **2014**, 406, 6903.

even see engineered ‘toxic’ graphene that is able to be used as an antibiotic or even anticancer treatment.²²² Also, due to its molecular make-up and potential biocompatibility, it could be utilized in the process of tissue regeneration.²²³

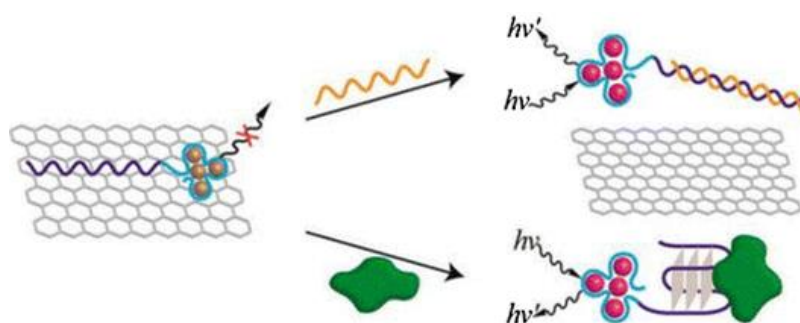


Figure 2-12: (AgNC)–GO hybrids and proteins using an aptamer-elongated DNA–AgNC–GO hybrid system as sensing matrices.²²¹

2.1.4 Chemical reactivity

The peculiar electronic properties of graphene, such as the combination of very high electronic mobilities and extraordinary strength, has boosted the efforts to explore the potential of graphene for a wide variety of applications. However, in order to fully exploit the potential of graphene, several fundamental limitations must be overcome. The absence of a gap as well as inertness to reaction, weakens the competitive strength of graphene in the field of semiconductors. Consequently, considerable efforts have been made to modify the structure of graphene and tailor the properties of interest.^{224,225,226}

Analogously to CNTs, the different approaches to the chemical modification of graphene (defect’s functionalization, covalent and non-covalent)

²²² C-W Liu, F. Xiong, H-Z. Jia, X-L. Wang, H. Cheng, Y-H. Sun, X-Z. Zhang, R-X. Zhuo and J Feng, *Biomacromolecules*, **2013**, *14*, 358.

²²³ N. Dubey, R. Bentini, I. Islam, T. Cao, A. H. Castro and V. Rosa, *Stem Cells Int.*, **2015**, *2015*, 804213.

²²⁴ Q. H. Wang and M. C. Hersam, *Nat. Chem.*, **2009**, *1*, 206.

²²⁵ (a) V. Georgakilas in “Functionalization of graphene”, John Wiley & Sons, 2014; (b) V. Georgakilas, M. Otyepka, A. B. Bourlinos, V. Chandra, N. Kim, K. C. Kemp, P. Hobza, R. Zboril and K. S. Kim, *Chem. Rev.*, **2012**, *112*, 6156. (c) T. Kuila, S. Bose, A. K. Mishra, P. Khanra, N. H. Kim, J. H. Lee, *Prog. Mater. Sci.*, **2012**, *57*, 1061.

²²⁶ S. P. Lonkar, Y. S. Deshmukh and A. A. Abdala, *Nano Res.*, **2015**, *8*, 1039.

endow graphene not only an improved solubility, but also new and better properties than the starting material (Figure 2-13).

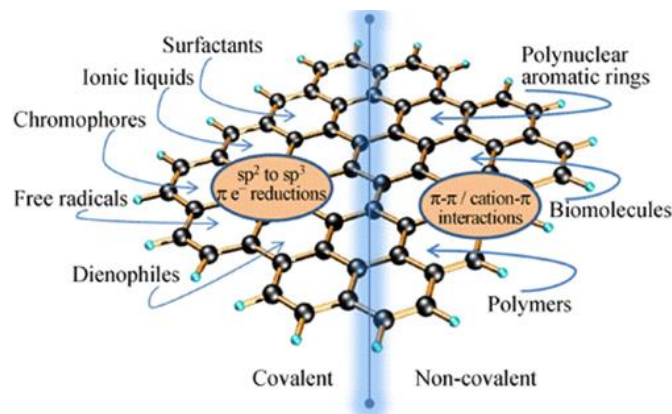


Figure 2-13. Schematic illustration of non-covalent and covalent functionalization of graphene.²²⁶

Covalent functionalization on the defects

Graphene oxide (GO) has been also widely used as a starting material for the synthesis of processable graphene. Graphene sheets with a high specific surface area tend to form irreversible agglomerates or even restack to form graphite through π - π stacking and van der Waals interactions if the sheets are not well separated from each other.²²⁷ As aforementioned, by the oxidation of graphene using strong oxidizing agents, oxygenated functionalities are introduced in the graphene structure which not only expand the layer separation, but also makes the material hydrophilic (meaning that it can be dispersed in water).

There are different methods for production of GO from natural graphite; the first well-known example was developed by the British chemist B. C. Brodie by adding potassium chlorate (KClO₃) to a slurry of graphite in fuming nitric acid (HNO₃). Nearly 60 years later, Hummers and Offeman developed an alternate oxidation method by reacting graphite with a mixture of potassium permanganate (KMnO₄) and concentrated sulfuric acid (H₂SO₄), achieving high levels of oxidation.¹⁹⁷ Though others have developed slightly modified versions, these methods comprise the primary routes for obtaining GO.

²²⁷ C. Shan, H. Yang, D. Han, Q. Zhang, A. Ivaska and L. Niu, *Langmuir*, **2009**, *25*, 12030.

The reactive oxygen functionalities in GO, such as carboxylic acid groups at their edges and epoxy and hydroxyl groups on the basal plane can be used to further modify GO by adding functionalities onto these groups.

A wide range of reactions have been performed on the carboxylic groups (Figure 2-14).²²⁸ The coupling reactions often require activation of the acid group using thionyl chloride (SOCl_2) as showed also in the case of CNTs.^{229,230} Subsequent addition of nucleophilic species, such as amines or hydroxyls, produce covalently attached functional groups to graphene oxide *via* the formation of amides or esters. Introduction of substituted amines is one of the most common methods of covalent functionalization, and the final products have been investigated for various applications in optoelectronics,²³⁰ biodevices,²³¹ drug-delivery vehicles,²³² and polymer composites.²³³

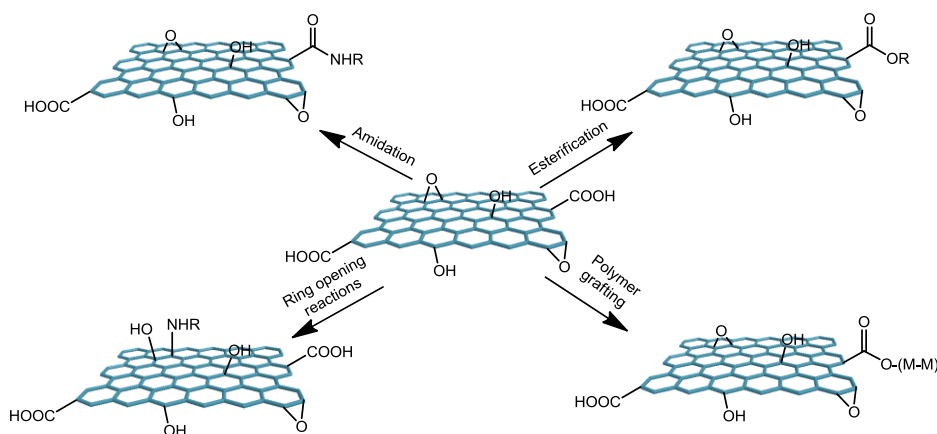


Figure 2-14. Strategies for covalent functionalization on the defects in GO.

As an example, porphyrin-functionalized primary amines and separately, fullerene-functionalized secondary amines have been attached to

²²⁸ D. R. Dreyer, S. Park, C. W. Bielawski and R. S. Ruoff, *Chem. Soc. Rev.*, **2010**, 39, 228.

²²⁹ Z.B. Liu, Y.F. Xu, X.Y. Zhang, X.L. Zhang, Y.S. Chen and J.G. Tian, *J. Phys. Chem. B*, **2009**, 113, 9681.

²³⁰ X. Zhang, Y. Huang, Y. Wang, Y. Ma, Z. Liu and Y. Chen, *Carbon*, **2009**, 47, 334.

²³¹ N. Mohanty and V. Berry, *Nano Lett.*, **2008**, 8, 4469.

²³² Z. Liu, J. T. Robinson, X. Sun and H. Dai, *J. Am. Chem. Soc.*, **2008**, 130, 10876.

²³³ L. M. Veca, F. Lu, M. J. Mezziani, L. Cao, P. Zhang, G. Qi, L. Qu, M. Shrestha and Y.-P. Sun, *Chem. Commun.*, **2009**, 2565.

graphene oxide (Figure 2-15),^{229,230,234} affording materials with useful nonlinear optical performance.

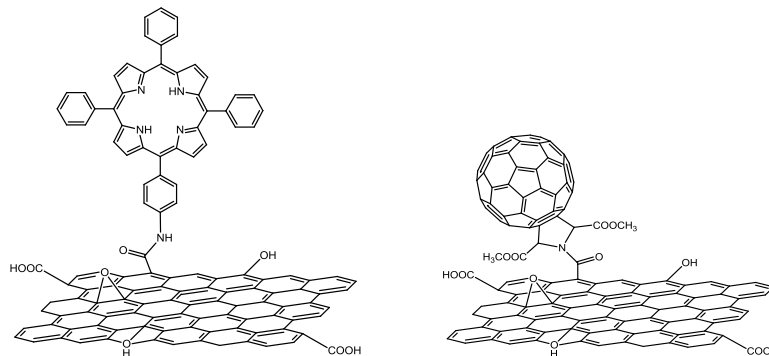


Figure 2-15. Functionalization of the carboxylic acid groups of graphene oxide through amidation reaction.²²²

Polymers have also been attached to the surface of graphene oxide through amine-functionalized GO (Figure 2-14).²³⁵

In addition to the carboxylic acids decorating the edges of graphene oxide, it contains also chemically reactive epoxy groups on its basal planes. The epoxy groups can be easily modified through ring-opening reactions (Figure 2-14). A likely mechanism for this reaction involves nucleophilic attack at the α -carbon by the amine. Wang *et al.*²³⁶ demonstrated the epoxide ring-opening reaction by the addition of octadecylamine to a dispersion of graphene oxide.

Covalent functionalization

Covalent functionalization of graphene allows the introduction of a wide variety of functional groups onto the graphene surface.^{237,238} In addition, covalent chemistry of graphene offers an effective pathway to the band structure modulation of this material, opening a substantial band gap on the zero-gap electronic band of pristine graphene.

²³⁴ Y. Xu, Z. Liu, X. Zhang, Y. Wang, J. Tian, Y. Huang, Y. Ma, X. Zhang and Y. Chen, *Adv. Mater.*, **2009**, *21*, 1.

²³⁵ Y. Yang, J. Wang, J. Zhang, J. Liu, X. Yang and H. Zhao, *Langmuir*, **2009**, *25*, 11808.

²³⁶ S. Wang, P. J. Chia, L. L. Chua, L. H. Zhao, R. Q. Png, S. Sivaramakrishnan, M. Zhou, R. G. S. Goh, R. H. Friend, A. T. S. Wee and P. K. H. Ho, *Adv. Mater.*, **2008**, *20*, 3440.

²³⁷ L. Liao, H. Peng and Z. Liu, *J. Am. Chem. Soc.* **2014**, *136*, 12194.

²³⁸ L. Rodriguez, M. A. Herranz and N. Martin, *Chem. Commun.* **2013**, *49*, 3721.

For the covalent functionalization of graphene, a covalent bond must be formed, which is accompanied by the rehybridization of C atoms from sp^2 to sp^3 . It can be achieved mainly through electrophilic substitution or cycloaddition reactions.^{225,239,240,241,242}

The grafting of **aryl radicals**, generated from the reduction of diazonium salts to the surface of graphene, is an example of electrophilic substitution. The obtained radical then attacks the sp^2 -hybridized graphene framework, forming new $C(sp^3)$ -aryl bonds (Figure 2-16).²⁴³

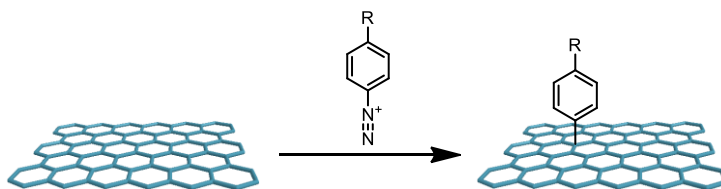


Figure 2-16. Aryl diazonium coupling on graphene.

The addition of aryl diazonium salts onto graphene was first introduced by Tour and co-workers, who performed the successful functionalization of graphene with chlorobenzene, nitrobenzene, methoxybenzene, and bromobenzene.²⁴⁴ Diazonium salts with many different functional groups have been also successfully grafted to graphene, including 4-nitrobenzene diazonium tetrafluoroborate (4-NBD), 4-bromobenzene tetrafluoroborate (4-BBD), 4-propargyloxybenzene diazonium tetrafluoroborate (4-PBD) and 4-tert-butylphenyldiazonium tetrafluoroborate (4-TBD).²⁴⁵ Tour *et al* described an example of diazonium salt chemistry allowing steric repulsion between modified graphene layers in order to avoid reaggregation.²⁴⁶ These chemically functionalized graphene sheets were more dispersible than pristine graphene.

²³⁹ S. Stankovich, D. A. Dikin, G. H. B. Dommett, K. M. Kohlhaas, E. J. Zimney, E. A. Stach, R. D. Piner, S. T. Nguyen, R. S. Ruoff, *Nature*, **2006**, *442*, 282.

²⁴⁰ Y. Xu, Z. Liu, X. Zhang, Y. Wang, J. Tian, Y. Huang, Y. Ma, X. Y. Zhang and Y. Chen, *Adv. Mater.* **2009**, *21*, 1275.

²⁴¹ H. Yang, C. Shan, F. Li, D. Han, Q. Zhang, L. Niu, *Chem. Commun.*, **2009**, 3880.

²⁴² A. Criado, M. Melchionna, S. Marchesan and M. Prato, *Angew. Chem. Int. Ed.* **2015**, *54*, 2.

²⁴³ D. Jiang, B. G. Sumpter, S. Dai, *J. Phys. Chem. B*, **2006**, *110*, 23628.

²⁴⁴ J. R. Lomeda, C. D. Doyle, D. V. Kosynkin, W. F. Hwang and J. M. Tour, *J. Am. Chem. Soc.*, **2008**, *130*, 16201.

²⁴⁵ L. C. G. Paulus, H. W. Quing and M. S. Strano, *Acc. Chem. Res.*, **2013**, *46*, 160.

²⁴⁶ Z. Sun, S. I. Kohama, Z. Zhang, J. R. Lomeda and J. M. Tour, *Nano Res.* **2010**, *3*, 117.

This methodology has also been utilized by Hirsch *et al.* who developed a wet chemical approach, in order to obtain graphene from graphite *via* reduction with sodium-potassium salt.²⁴⁷ Organic groups introduced through diazonium chemistry on graphene can also be exploited to further modification with more complex molecular entities such as biomolecules,²⁴⁸ porphyrins,²⁴⁹ phthalocyanines,²⁵⁰ etc... For example, the functionalization of graphene with a phthalocyanine through “click” chemistry on a previously arylated graphene was performed by Torres *et al.* (Figure 2-17).^{250b}

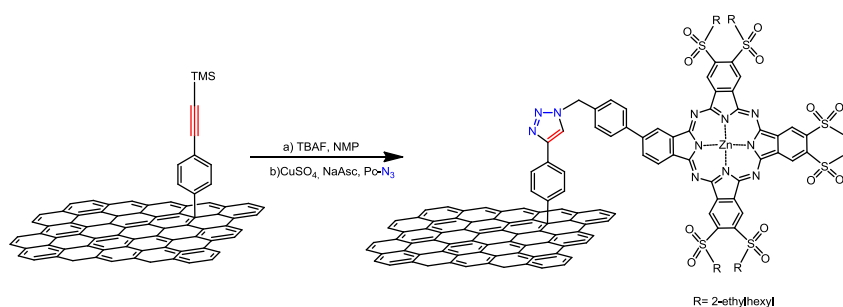


Figure 2-17. “Click” chemistry onto graphene modified through diazonium chemistry.^{250b}

Another common example of electrophilic substitution is the Friedel-Craft acylation.

A typical **Friedel-Crafts acylation reaction** goes through an acyl anion intermediate, catalyzed by the presence of a Lewis acid such as aluminum chloride (Figure 2-18).

²⁴⁷ J. M. Englert, C. Dotzer, G. Yang, M. Schmid, C. Papp, J. M. Gottfried, H-P. Steinrück, E. Spiecker, F. Hauke and A. Hirsch, *Nature Chemistry*, **2011**, 3, 279.

²⁴⁸ Q. H. Wang, Z. Jin, K. K. Kim, A. J. Hilmer, G. L. C. Paulus, C.-J. Shih, M.-H. Ham, J. D. Sanchez-Yamagishi, K. Watanabe, T. Taniguchi, J. Kong, P. Jarillo-Herrero and M. S. Strano, *Nat. Chem.* **2012**, 4, 72.

²⁴⁹ X. Zhang, L. Hou, A. Cnossen, A. C. Coleman, O. Ivashenko, P. Rudolf, B. J. van Wees, W. R. Browne and B. L. Feringa, *Chem. Eur. J.*, **2011**, 17, 8957.

²⁵⁰ (a) A. Stergiou, G. Pagona and N. Tagmatarchis, *Beilstein J. Nanotechnol.* **2014**, 5, 1580; (b) M. E. Ragoussi, G. Katsukis, A. Roth, J. Malig, G. de la Torre, D. M. Guldi and T. Torres, *J. Am. Chem. Soc.*, **2014**, 136, 4593.

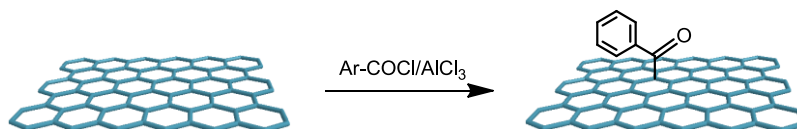


Figure 2-18. Friedel-Crafts acylation on graphene.

The acylation of graphene *via* Friedel-Crafts has been successfully demonstrated by Pumera *et al.*²⁵¹ Modification of graphene was achieved by a mild acylation technique with 4-aminobenzoic acid in the presence of polyphosphoric acid/phosphorous pentoxide (PPA/P₂O₅).

Graphene can be also covalently modified by the attachment of **single atoms** (Figure 2-19), including hydrogen, fluorine, chlorine and oxygen. These covalent modifications are very interesting because they are mostly reversible processes and allow for high functionalization levels. Sandeep *et. al.* carried out the functionalization of graphene with different halogen molecules.²⁵²

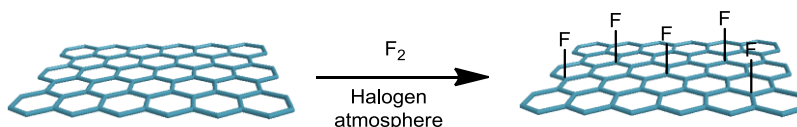


Figure 2-19. Halogenation of graphene.

The halogen molecules, being electron withdrawing in nature, induced distinct changes in the electronic states of graphene, which was manifested with a change in the spectroscopic signatures. More recently, Pumera *et. al.* developed the first scalable and simple bulk method for the preparation of halogenated (chlorine, bromine, and iodine) graphenes by thermal exfoliation in gaseous halogen atmospheres.²⁵³

²⁵¹ C. K. Chua and M. Pumera, *Chem. Asian J.*, **2012**, 7, 1009.

²⁵² S. Ghosh, S. R. K. C. Yamijala, S. K. Pati and C. N. R. Rao, *RSC Adv.*, **2012**, 2, 1181.

²⁵³ H. L. Poh, P. Simek, Z. Sofer and M. Pumera, *Chem. Eur. J.*, **2013**, 19, 2655.

Among the approaches to covalent functionalize the surface of graphene, cycloaddition reactions have been also successfully applied (Figure 2-20).^{254,255}

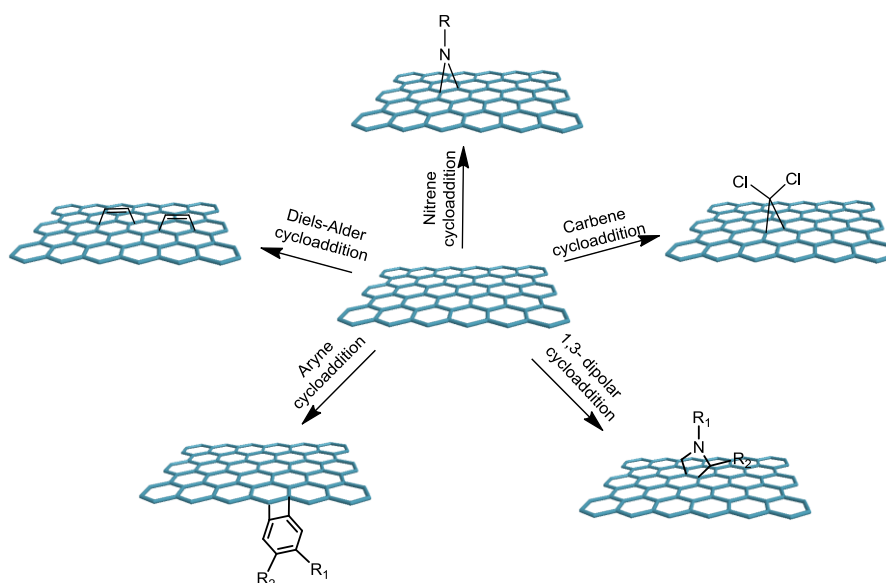


Figure 2-20. Functionalization of graphene by cycloaddition reactions.

The functionalization of graphene through [3+2] cycloaddition obtaining a five-membered ring can be achieved *via* a six-electron cycloaddition between a 1,3-dipole and a dipolarophile (graphene) (Figure 2-20). Azomethine ylide is one of the most common dienophiles that have been successfully applied in the functionalization of carbon nanostructures. After the successful production of graphene sheets from graphite dispersed in organic solvents, Georgakilas *et al.* showed that these graphene sheets could be modified with pyrrolidine rings *via* a 1,3-dipolar cycloaddition of azomethine ylides.^{254,256}

The flexibility of this reaction procedure makes it important because of the possibility to choose among several aldehydes or substituted α -amino acids as precursors, thus yielding a variety of desirable functional groups. In this

²⁵⁴ V. Georgakilas, A. B. Bourlinos, R. Zboril, T. A. Steriotis, P. Dallas, A. K. Stubos and C. Trapalisa, *Chem Commun*, **2010**, 46, 1766.

²⁵⁵ M. Quintana, K. Spyrou, M. Grzelczak, W. R. Browne, P. Rudolf and M. Prato, *ACS Nano*, **2010**, 4, 3527.

²⁵⁶ M. Quintana, E. Vazquez and M. Prato, *Acc. Chem. Res.* **2013**, 46, 138.

sense, Zhang *et al.* used tetraphenylporphyrin aldehyde (and the Pd analogue) and sarcosine as precursors, with the aim of decorating graphene sheets with tetraphenylporphyrin (TPP) or palladium-TPP.²⁵⁷ A novel nanohybrid composed of a bipyridine ruthenium complex covalently functionalized to graphene was synthesized by Xiao *et al.*²⁵⁸ through 1,3-dipolar cycloaddition of azomethine ylides. Guldi *et al.* also used this methodology for the covalent attachment of an electron-donor phthalocyanine to the basal plane of few layer graphene (Figure 2-21).²⁵⁹

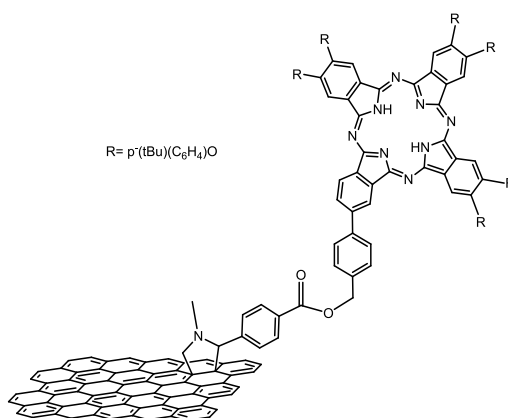


Figure 2-21. Graphene-Pc nanohybrid obtained through 1,3-dipolar cycloaddition.²⁵⁹

The **[2 + 1] cycloaddition** was one of the earliest used methods to functionalize the graphene sp^2 carbon lattice (Figure 2-20). There are generally two main approaches in this category, the cycloaddition towards the formation of cyclopropane or through the formation of aziridine rings.²⁶⁰

The cyclopropane adduct is achieved *via* dichlorocarbene insertion reaction, whereas the nitrene moiety is utilized as an intermediate towards the formation of an aziridine adduct.

²⁵⁷ X. Zhang, L. Hou, A. Cnossen, A. C. Coleman, O. Ivashenko, P. Rudolf, B. J. van Wees, W. R. Browne and B. L. Feringa, *Chem. Eur. J.*, **2011**, *17*, 8957.

²⁵⁸ B. Xiao, X. Wang, H. Huang, M. Zhu, P. Yang, Y. Wang and Y. Du, *J. Phys. Chem. C*, **2013**, *117*, 21303.

²⁵⁹ M. E. Ragoussi, J. Malig, G. Katsukis, B. Butz, E. Spiecker, G. de la Torre, T. Torres and D. M. Guldi, *Angew. Chem. Int. Ed.*, **2012**, *51*, 6421.

²⁶⁰ C. K. Chua and M. Pumera, *Chem. Soc. Rev.*, **2013**, *42*, 3222.

Chloroform, by reaction with a base, forms dichlorocarbene that can be transferred to organic layer by a phase transfer catalyst.²⁶¹ Such grafting of dichlorocarbene onto graphene, by utilizing a mixture of chloroform with sodium hydroxide and triethylbenzylammonium chloride as a phase transfer catalyst, was demonstrated by Pumera *et.al.*²⁶²

As aforementioned, the introduction of aziridine adduct onto the graphene sp^2 carbon network is usually achieved *via* a nitrene intermediate. Diazirines are three-membered heterocyclic rings that have a sp^3 carbon atom bonded to an azo group. Diazirines decompose upon heating or irradiation releasing molecular nitrogen and give rise to the electron-deficient species. The highly reactive species is capable of undergoing [2+1] cycloaddition reactions to C=C bonds.²⁶³ The addition of aziridine adducts through thermal photochemical activation techniques were carried out by Yan *et al.*^{264,265} Derivatives of perfluorophenylazide moieties containing long alkyl, ethylene oxide and perfluoroalkyl chains were grafted on exfoliated graphene to modify the solubility of the hybrid graphene materials in aqueous and organic solvents. Based on this methodology, Barron *et. al* carried out the addition of an amino acid side chain, phenylalanine, to modify the solubility of exfoliated graphene materials.²⁶⁶ To facilitate the attachment of biopolymers for their use in a thermoresponsive nanodevice, Fu *et al.* introduced cyclodextrin on the graphene surfaces using alkylazides.²⁶⁷ The resulting nanoconjugates were functionalized further with poly(*N*-isopropylacrylamide-co-vinylferrocene(II)) (PNIPAMFc) and ferrocene-modified hyperbranched polyglycerol (HPG-Fc).

The **[4 + 2] cycloaddition**, better known as the Diels–Alder cycloaddition, is the most famous pericyclic reaction in organic chemistry. The reaction proceeds in a single step *via* heat treatment giving rise to a six-membered ring (Figure 2-20). It involves the interaction between a diene (electron rich) and a dienophile (electron deficient). Haddon *et. al.* demonstrated

²⁶¹ J. Hine, *J. Am. Chem. Soc.* **1950**, 72, 2438.

²⁶² C. K. Chua, A. Ambrosi and M. Pumera, *Chem. Commun.*, **2012**, 48, 5376.

²⁶³ J. Brunner, H. Senn and F. M. Richards, *J. Biol. Chem.* **1980**, 255, 3313.

²⁶⁴ L. H. Liu, M. M. Lerner and M. Yan, *Nano Lett.*, **2010**, 10, 3754.

²⁶⁵ L. H. Liu, G. Zorn, D. G. Castner, R. Solanki, M. M. Lerner and M. Yan, *J. Mater. Chem.*, **2010**, 20, 5041.

²⁶⁶ T. A. Strom, E. P. Dillon, C. E. Hamilton and A. R. Barron, *Chem. Commun.*, **2010**, 46, 4097.

²⁶⁷ L. Q. Xu, Y. K. Yee, K. G. Neoh, E. T. Kang and G. D. Fu, *Polymer*, **2013**, 54, 2264.

the dual nature of graphene which acts as both a diene and a dienophile.^{268,269,270} For graphene as diene, the Diels–Alder reaction between it and a dienophile (tetracyanoethylene (TCNE)) proceeds at room temperature. The application of graphene as a dienophile was also demonstrated by cycloaddition with 9-methylanthracene and 2,3-dimethoxy-1,3-butadiene.²⁷¹

In the **[2+2] cycloaddition** reaction the interaction with the graphene sp² carbon network takes place through an aryne or benzyne intermediate (Figure 2-20). Zhong *et al.* described aryne cycloaddition to the graphene surface using 2-(trimethylsilyl)aryl triflate as a precursor. The reaction gave rise to the formation of a four-membered ring that connected the aromatic arene rings to the graphene surface.²⁷²

Non-Covalent functionalization

Graphene can also exhibit non-covalent binding (*via* π - π stacking or van der Waals interactions). In general, noncovalent chemistry is attractive because of the preservation of the conjugated π system. The noncovalent functionalization is based on weak interactions between graphene and a binding partner such as a surfactant. Noncovalent functionalization is achieved by polymer wrapping, adsorption of surfactants or small aromatic molecules, and interaction with porphyrins or biomolecules such as deoxyribonucleic acid (DNA) and peptides (Figure 2-22). As previously stated, this technique has been employed extensively in the surface modification of the sp² networks of CNTs.¹³⁰ Ongoing research shows that the same techniques can be applied with graphene using different kinds of organic modifiers.^{273,274,275}

²⁶⁸ S. Sarkar, E. Bekyarova, S. Niyogi and R. C. Haddon, *J. Am. Chem. Soc.*, **2011**, 133, 3324.

²⁶⁹ S. Sarkar, E. Bekyarova and R. C. Haddon, *Acc. Chem. Res.*, **2012**, 45, 673.

²⁷⁰ J.-M. Seo and J.-B. Baek, *Chem. Commun.*, **2014**, 50, 14651.

²⁷¹ E. Bekyarova, S. Sarkar, S. Niyogi, M. E. Itkis and R. C. Haddon, *J. Phys. D: Appl. Phys.*, **2012**, 45, 15.

²⁷² X. Zhong, J. Jin, S. Li, Z. Niu, W. Hu, R. Li and J. Ma, *Chem. Commun.* **2010**, 46, 7340.

²⁷³ H. Chang, G. Wang, A. Yang, X. Tao, X. Liu, and Y. Shen, *Adv. Funct. Mater.*, **2010**, 20, 2893.

²⁷⁴ C. Chen, W. Zhai, D. Lu, H. Zhang and W. Zheng, *Mater. Res. Bull.*, **2011**, 46, 583.

²⁷⁵ P. G. Campbell, M. D. Merrill, B. C. Wood, E. Montalvo, M. A. Worsley, T. F. Baumann and J. Biener, *J. Mater. Chem. A*, **2014**, 2, 17764.

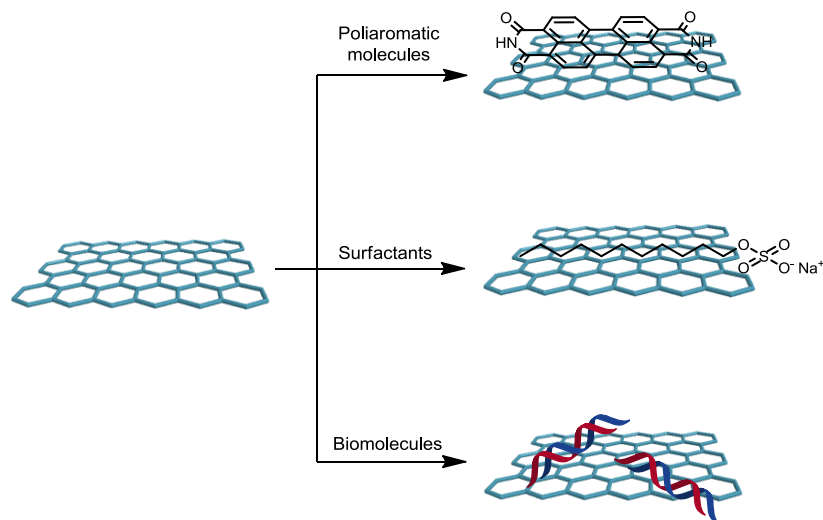


Figure 2-22. Strategies for non-covalent functionalization of graphene.

The first example of noncovalent functionalization of graphitic nanoplatelets was reported by Stankovich *et al.* by using poly(sodium 4-styrenesulfonate) (PSS).²⁷⁶ They obtained non-covalently functionalized graphitic nanoplatelets highly dispersible in water.

The utilization of polymers is probably, to the date, the method most commercially exploited. Their use not only leads to exfoliated layers, but also improve the mechanical properties of the material. Stable dispersion of reduced graphene in various organic solvents has been achieved *via* noncovalent functionalization with amine-terminated polymers.²⁷⁷ It was the first attempt to prepare functionalized graphene after reduction of GO. Liu *et al.* reported a modification technique for graphene by considering the π - π interaction between the π orbitals of graphene and poly(N-isopropylacrylamide) (PNIPAAM).²⁷⁸ In this sense, Pan *et al.* have prepared chemically converted graphene (CCG) sheets by grafting a thermo-responsive PNIPAAM *via click* chemistry.²⁷⁹ PNIPAAM

²⁷⁶ S. Stankovich, R. D. Piner, X. Chen, N. Wu, S. T. Nguyen, R. S. Ruoff, *J. Mater.Chem.*, **2006**, *16*, 155.

²⁷⁷ E. Y. Choi, T. H. Han, J. Hong, J. E. Kim, S. H. Lee, H. W. Kim and S. O. Kim, *J. Mater. Chem.*, **2010**, *20*, 1907.

²⁷⁸ J. Liu, W. Yang, L. Tao, D. Li, C. Boyer and T. P. Davis, *J. Polym. Sci. Part A Polym. Chem.*, **2010**, *48*, 425.

²⁷⁹ Y. Pan, H. Bao, N. G. Sahoo, T. Wu and L. Li, *Adv. Funct. Mater.*, **2011**, *21*, 2754.

modified graphene consist of about 50% polymer, which endows the sheets with a good dispersibility and stability in physiological solutions.

As reported for CNTs, polyaromatic systems are ideal candidates for the non-covalent functionalization of graphene (Figure 2-22). Kodali *et al.* reported non-covalently functionalized epitaxial graphene with pyrenebutanoic acid-succinimidyl ester (PYR-NHS),²⁸⁰ which can be prepared without disrupting graphene's electronic structure. Su *et al.* presented a unique approach to functionalize graphene sheets with pyrene and perylene diimide²⁸¹ as electronic donor and acceptor molecules, respectively. The resulting aqueous graphene dispersion yields single and double layer graphene sheets. A solar cell based on these functionalized graphene system showed an increase in conductivity. Zinc phthalocyanine (ZnPc) and sulfonated copper phthalocyanine (CuPc) complexes have been used for the surface modification of graphene through π - π interaction.^{282,283} Green *et al.* described the use of various pyrene derivatives to stabilize high concentrations of graphene in aqueous dispersions.²⁸⁴ More recently, Tagmatarchis *et al.* reported the attachment of a charged porphyrin salt to graphene through electrostatic interactions. Electronic communication is demonstrated through transient absorption spectroscopy (Figure 2-23).²⁸⁵

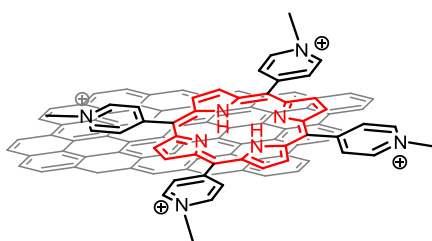


Figure 2-23. Porphyrin attached to graphene through non-covalent interactions.²⁸⁵

²⁸⁰ V. K. Kodali, J. Scrimgeour, S. Kim, J. H. Hankinson, K. M. Carroll, W. A. de Heer, C. Berger and J. E. Curtis, *Langmuir*, **2011**, 27, 863.

²⁸¹ Q. Su, S. P. Pang, V. Alijani, C. Li, X. L. Feng and K. Mullen, *Adv. Mater.*, **2009**, 21, 3191.

²⁸² J. Malig, N. Jux, D. Kiessling, J. J. Cid, P. Vazquez, T. Torres and D. M. Guldi, *Angew. Chem. Int. Ed.*, **2011**, 50, 3561.

²⁸³ A. Chunder, T. Pal, S. I. Khondaker and L. Zhai, *J. Phys. Chem. C*, **2010**, 114, 15129.

²⁸⁴ D. Parviz, S. Das, H. S. T. Ahmed, F. Irin, S. Bhattacharia and M. J. Green *ACS Nano*, **2012**, 6, 8857.

²⁸⁵ S. P. Economopoulos and N. Tagmatarchis, *J. Phys. Chem. C.*, **2015**, 119, 8046.

The non-covalent interaction of graphene with biomolecules is also an important issue in biomedical applications (Figure 2-22). Ren *et al.*²⁸⁶ showed that graphene sheets can be stably dispersed in water by hydrophilic interactions. The surface modified graphene are highly sensitive to a change in solution pH indicating its potential application in sensors, biology, medicine, nanoelectronics and other relevant areas. Huang *et al.* reported the non-covalent functionalized graphene with glucose oxidase as a promising candidate for the development of nanoelectronic biosensors.²⁸⁷ Noncovalent functionalization of graphene with single-stranded DNA (ssDNA) was obtained by chemical oxidation of graphite to GO, followed by hydrazine reduction in the presence of ssDNA.²⁸⁸

Adsorption of surfactants is also a well-known procedure for the non-covalent modification of graphene (Figure 2-22). Experiments concerning the use of surfactants to obtain the dispersion of graphene in water, yield individual graphene sheets, which are stabilized by non-covalent interactions with surfactants that show an extended conjugated π -system, such as sodium cholate (SC), sodium dodecyl sulfate (SDS) and sodium dodecylbenzenesulfonate (SBDS).¹⁹⁴ Chang *et al.* and Zeng *et al.* prepared SDBS-modified graphene.^{273,289} SDBS-functionalized graphene produces surfactant-wrapped graphene sheets which can be used as a biosensing material for the detection of hydrogen peroxide.

²⁸⁶ L. Ren, T. Liu, J. Guo, S. Guo, X. Wang and W. Wang, *Nanotechnology*, **2010**, *21*, 335701.

²⁸⁷ Y. Huang, X. Dong, Y. Shi, C. Ming Li, L. J. Li and P. Chen, *Nanoscale*, **2010**, *2*, 1485.

²⁸⁸ Y. Y. Liang, D. Q. Wu, X. L. Feng and K. Mullen, *Adv. Mater.*, **2009**, *21*, 1679.

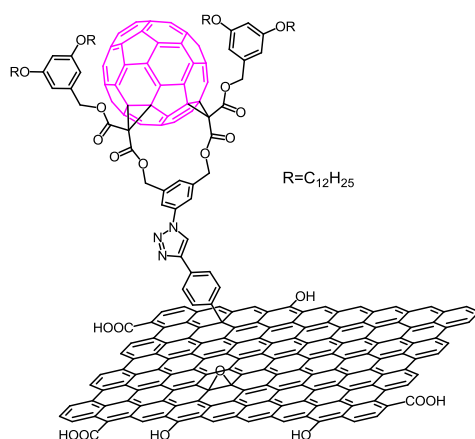
²⁸⁹ Q. Zeng, J. Cheng, L. Tang, X. Liu, Y. Liu, J. Li and J. Jiang, *Adv. Funct. Mater.*, **2010**, *20*, 3366.

2.2 Objectives

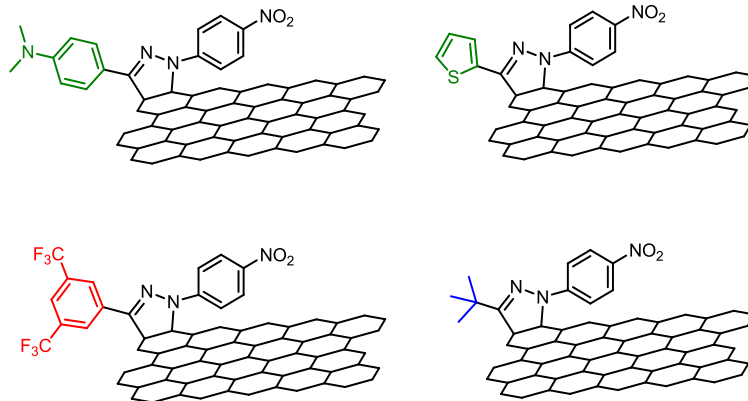
Considering the extraordinary structural, mechanical, and electronic properties of graphene, our aim in this chapter was focused on the covalent functionalization of the graphene surface with different electro-active moieties, and the study of the electronic and chemical properties of the resulting hybrid systems.

The specific aims in chapter 2 were as follows:

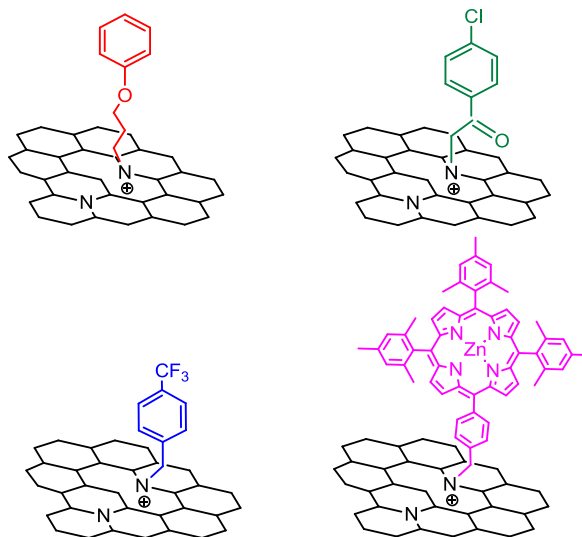
- a) Preparation of an all-carbon donor-acceptor hybrid combining graphene oxide (GO) and C_{60} .



- Full characterization of the nanoconjugate by analytical, spectroscopic, electrochemical and microscopic techniques (FTIR, TGA, XPS, Raman, cyclic voltammetry, AFM and HR-TEM)
 - Study of the of photoinduced electron transfer process from the GO acting as electron donor to the C_{60} (electron acceptor).
- b) Theoretical study on the viability and the reaction pathways of 1,3-dipolar cycloaddition of nitrile imines to graphene.
- Experimental verification of the functionalization of graphene using 1,3-dipolar cycloaddition of nitrile imines, to obtain pyrazoline substituted graphene hybrids bearing different electroactive species on the C atom of the pyrazoline ring.



- Full characterization of the nanoconjugates by analytical, spectroscopic and microscopic techniques (FTIR, TGA, XPS Raman, UV-vis, AFM and HR-TEM).
 - Work function measurements of the final hybrids compared to that of graphene, using ultraviolet photoelectron spectroscopy (UPS) and correlation between the work function and the different substituents.
- c) N-functionalization of N-doped graphene (NG) with different organic addends.



- Full characterization of the nanoconjugates by analytical, spectroscopic and microscopic techniques (TGA, XPS, FTIR, Raman, UV-vis-NIR, AFM, HR-TEM).
- Measurement of the optical band-gap of the final hybrids compared to that of (N)G. The mentioned band gaps were determined by using the Tauc plots of the modified Kubelka-Munk function.

2.3 Results and discussion

2.3.1 Synthesis of a nanoconjugate combining GO and C₆₀

Background

While individual graphene-platelets can be prepared by chemical vapor deposition (CVD) or mechanical “Scotch-tape” exfoliation from graphite, strong van der Waals interactions lead to reaggregation and poor solution processability. Unfortunately, attempts to control the solubility and dispersibility of graphene platelets by direct functionalization require aggressive conditions or hazardous reagents.²⁹⁰

As previously mentioned, to overcome these limitations, researchers have employed chemical oxidation to convert graphene to GO, sheets of sp² and sp³ carbon atoms containing different oxygen functional groups.^{291,228} The oxygenated groups in GO can strongly affect its electronic, mechanical, and electrochemical properties which explain the differences between GO and pristine graphene.²⁹²

In recent years, hybrid structures combining two different forms of carbon nanostructures have been prepared with the aim of generating multifunctional nanomaterials with enhanced properties.¹³⁶ Among them, several hybrids involving graphene and C₆₀ covalently linked have been reported. Chen *et al.*²³⁴ reported a facile preparation of a graphene-C₆₀ hybrid material *via* coupling reaction between GO and pyrrolidine fullerene. Through similar strategies, Chen *et al.* investigated the nonlinear optical properties of the graphene nanohybrid materials covalently functionalized with the fullerenes.²⁹³ Interestingly, such conjugates showed enhanced nonlinear optical performances when compared to their individual components. Zhang *et al.*²⁹⁴ inserted fullerene molecules in between graphene layers of graphene oxide through the Fisher esterification between the hydroxyl groups on graphite oxide and the carboxyl groups. The grafted fullerene facilitated the exfoliation of graphite oxide to monolayer graphene. In another example, GO was decorated with both

²⁹⁰ D. Yu, Y. Yang, M. Durstock, J. Baek and L. Dai, *ACS Nano* **2010**, *4*, 5633.

²⁹¹ K. Krishnamoorthya, M. Veerapandianb, K. Yunb and S.-J. Kim, *Carbon*, **2013**, *53*, 38.

²⁹² C. Gomez-Navarro, J. C. Meyer, R. S. Sundaram, A. Chuvilin, S. Kurasch, M. Burghard, K. Kern and U. Kaiser, *Nano Lett.* **2010**, *10*, 1144.

²⁹³ Z. B. Liu, Y. F. Xu, X. Y. Zhang, X. L. Zhang, Y. S. Chen and J. G. Tian, *J. Phys. Chem. B*, **2009**, *113*, 9681.

²⁹⁴ Y. Zhang, L. Ren, S. Wang, A. Marathe, J. Chaudhuri and G. Li, *J. Mater. Chem.*, **2011**, *21*, 5386.

C₆₀ and Zn(II)-phthalocyanines (ZnPc).²⁹⁵ Photophysical studies revealed the occurrence of photoinduced electron transfer (PET) from the ZnPc donor to the C₆₀ acceptor, suggesting that the GO scaffold was capable of mediating the electron transfer events involving the two other partners.

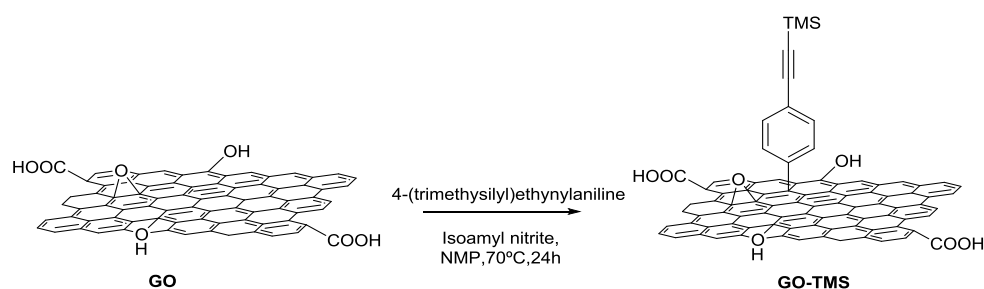
Recently, an ionic endohedral metallofullerene (Li⁺@C₆₀) with hydrophilic nature has been combined with GO to construct a donor-acceptor composite.²⁹⁶ They detected electron transfer from GO to the triplet excited state of Li⁺@C₆₀ by electron paramagnetic resonance spectroscopy, which markedly enhanced the photocurrent generation of the OTE/SnO₂ electrode loaded with GO-Li⁺@C₆₀ composites.

In the first part of this chapter, the synthesis and photophysical properties of a covalent GO-C₆₀ conjugate, in which GO behaves as an electron donor moiety, is presented.²⁹⁷

Synthesis

The starting GO was purchased from Nanoinnova Technologies, batch: GO.Z.10-1 (<http://www.nanoinnova.com>).

Functionalization of this material was firstly carried out with 4-(trimethylsilyl)ethynylaniline¹⁵¹ via aryl diazonium salt reaction in the presence of isoamyl nitrite, yielding GO-TMS (Scheme 2-1).



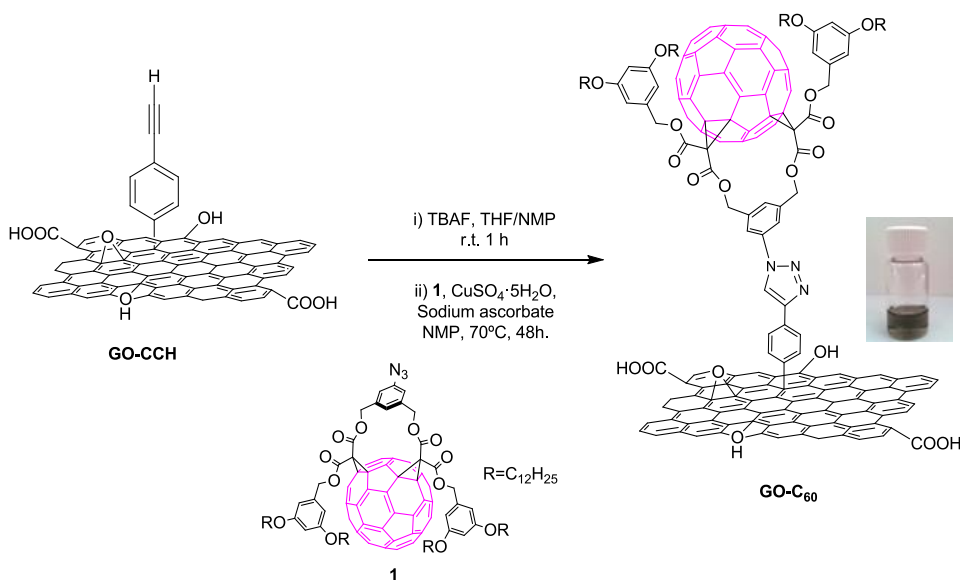
Scheme 2-1. Synthetic route for the arylation of GO.

²⁹⁵ S. K. Das, B. K. C. Chandra, K. Ohkubo, Y. Yamada, S. Fukuzumi and F. D'Souza, *Chem. Commun.*, **2013**, 49, 2013.

²⁹⁶ M. Supur, Y. Kawashima, K. Ohkubo, H. Sakai, T. Hasobeb and S. Fukuzumi, *PhysChemChemPhys.*, **2015**, 17, 15732.

²⁹⁷ M. Barrejón, M. Vizuete, M. J. Gómez-Escalonilla, J. L. G. Fierro, I. Berlanga, F. Zamora, G. Abellán, P. Atienzar, J.-F. Nierengarten, H. García and F. Langa, *Chem. Commun.*, **2014**, 50, 9053.

Subsequent cleavage of the TMS group using tetra-*n*-butylammonium fluoride (TBAF) gave GO modified with alkyne groups (**GO-CCH**). Finally, fullerene building block **1**¹⁴⁶ was grafted onto the modified GO scaffold using the Cu-catalysed alkyne-azide cycloaddition (CuAAC) reaction under the conditions optimized for the grafting of fullerene containing azide onto carbon nanohorns¹⁴⁶ (Scheme 2-2).



Scheme 2-2. Synthetic route for the preparation of **GO-C₆₀** nanoconjugate.

The resulting **GO-C₆₀** hybrid material formed stable suspensions in solvents such as DMF, NMP and CH₂Cl₂, owing to the four long alkyl chains per fullerene subunit.

The **GO-C₆₀** hybrid obtained was characterized in detail by Fourier-transformed infrared (FT-IR) spectroscopy, Raman spectroscopy, X-ray photoelectron spectroscopy (XPS), high-resolution transmission electron microscopy (HR-TEM) and atomic force microscopy (AFM).

Characterization

FTIR spectra of **GO-C₆₀** nanoensemble and its precursors are displayed in Figure 2-24. The typical bands in the range ~ 2925 and 2852 cm⁻¹ (attributed to C-H stretching vibrations) can be detected in the spectra of the final hybrid. Importantly, the characteristic signal of azide groups (2108 cm⁻¹) in fullerene

derivate **1** disappears for **GO-C₆₀**, confirming the successful functionalization of **GO-CCH** *via* the CuAAC reaction.

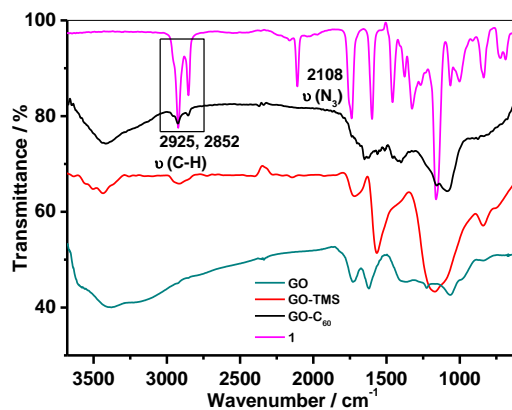


Figure 2-24. FT-IR spectra of GO (dark cyan), GO-TMS (red), **1** (magenta) and GO-C₆₀ (black) measured in KBr pellet.

The thermal behavior of GO-C₆₀ hybrid and starting GO were investigated by TGA under nitrogen atmosphere (Figure 2-25). The initial weight loss of GO (40%) observed between 40-270 °C was attributed to the decomposition of labile oxygen functional groups.²⁹⁸ For GO-C₆₀ an 18% weight loss was observed between 150-235 °C, whilst for azidefullerene **1** the thermal degradation only started at 290 °C. The difference observed between the azidefullerene **1** and GO-C₆₀ is thought to be due to the thermal decomposition of oxygen functionalities present on the GO-C₆₀ surface. Further differences were observed at higher temperatures, where the stability of the hybrid GO-C₆₀ is improved with respect to the starting materials. This increase in the thermal stability could be ascribed to the strong interactions of the final hybrid.

²⁹⁸ X. B. Fan, W. C. Peng, Y. Li, X. Y. Li, S. L. Wang, G. L. Zhang and F. B. Zhang, *Adv. Mater.*, **2008**, *20*, 4490.

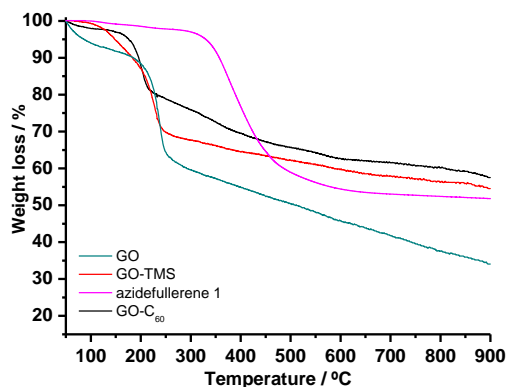


Figure 2-25: TGA curves of GO (dark cyan), GO-TMS (red line), GO-C₆₀ (black line) and azidefullerene (**1**) (magenta line), recorded under inert conditions.

Raman spectroscopy (532 nm laser excitation) of pristine GO showed an intense tangential mode (G band) at 1585 cm⁻¹ and the disordered-induced peak (D band) at 1356 cm⁻¹ (Figure 2-26). Both bands were also observed for GO-TMS, however the I_D/I_G ratio increased with respect to the starting GO (0.86 and 0.73 respectively) as a consequence of the formation of defects accompanied by the surface functionalization. The GO-C₆₀ spectrum showed the signatures of all the constituents: 1594 cm⁻¹ and 1355 cm⁻¹ corresponding to the GO sheet, together with the fingerprint of C₆₀ cage observed at 1486 cm⁻¹, assigned to the Ag(2) mode. It is worth noting that no further increase of I_D/I_G ratio was observed when going from GO-TMS to GO-C₆₀, thus confirming that the click reaction occurred on the triple bonds rather than directly onto the GO surface.

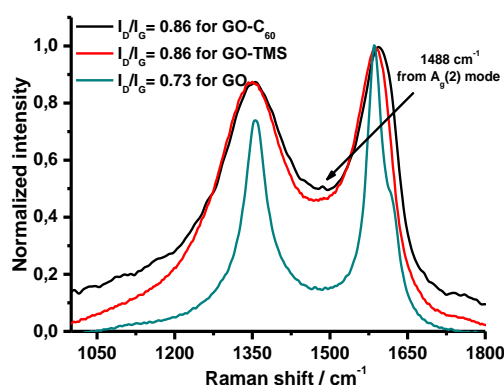


Figure 2-26. Raman spectra (532 nm) of the final hybrid (black) compared to that of GO (dark cyan) and GO-TMS (red).

The formation of **GO-C₆₀** was also evidenced by XPS. Quantitative data of the nanoconjugates compared to that of **GO** are presented in Table 2-1.

It is worth mentioning here that the incorporation of Si was observed for **GO-TMS** (0.4% Si atom), and after the *click* reaction, as expected, **GO-C₆₀** revealed the presence of nitrogen, which supported the successful anchorage of **1** on the graphene surface. Based on the nitrogen content measured by XPS, it was estimated that one fullerene was present per 161 carbon atoms.

Table 2-1 Surface atomic composition of the samples.

Sample	C (% at)	O (%at)	N (%at)	Si(%at)
GO	63.1	36.9	-	-
GO-TMS	67.3	32.3	-	0.4
GO-C₆₀	75.0	23.6	1.4	-
1	90.1	8.0	1.9	-

Figure 2-27 displays the C1s and O1s core-level peaks from starting **GO**. A detailed analysis of the deconvoluted high resolution C1s spectrum of **GO** showed the main component at 284.8 eV (sp²-C) and other minor components at 286.5 and 288.1 eV assigned to C-O, C=O and COO groups. Similarly, the high resolution O1s peak of **GO** was resolved into two components at 531.6 (O=C surface groups) and 532.8 eV (associated with the O-C bond) of almost the same intensity.

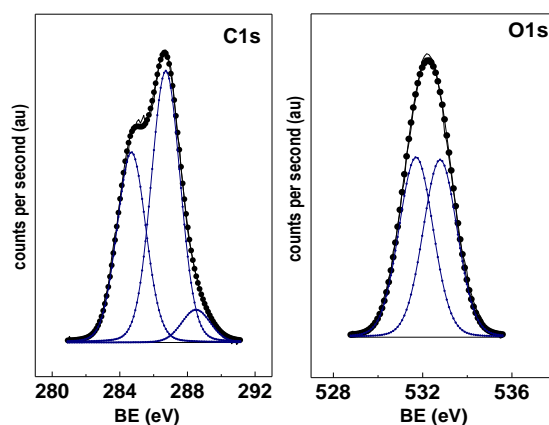


Figure 2-27. High resolution core level spectra of **GO**: C1s and O1s regions.

For **GO-C₆₀**, in addition to the aforementioned peaks, a new one was observed at 285.3 eV, corresponding to sp^3 bonded carbon atoms observed after functionalization (Figure 2-28).

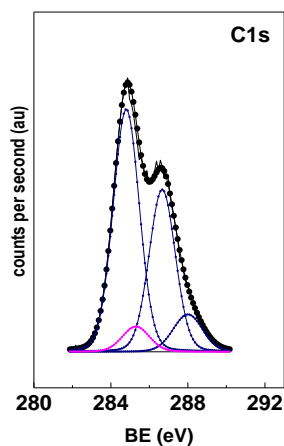


Figure 2-28. C1s core level spectra of **GO-C₆₀**.

The high-resolution N 1s spectrum (Figure 2-29, left) of **GO-C₆₀** displayed two components, (i) a major one at a binding energy of 399.9 eV, belonging to the two triazole N-atoms bound to C-atoms as nearest neighbors, and (ii) a minor one at 398.6 eV originating from the other remaining N-atom. In contrast only one component was observed at 400.2 eV for azide fullerene **1** (Figure 2-29, right). These observations unambiguously proved that the azide residue of fullerene **1** was no longer present, thus, confirming the formation of triazole rings during the reaction leading to **GO-C₆₀**.

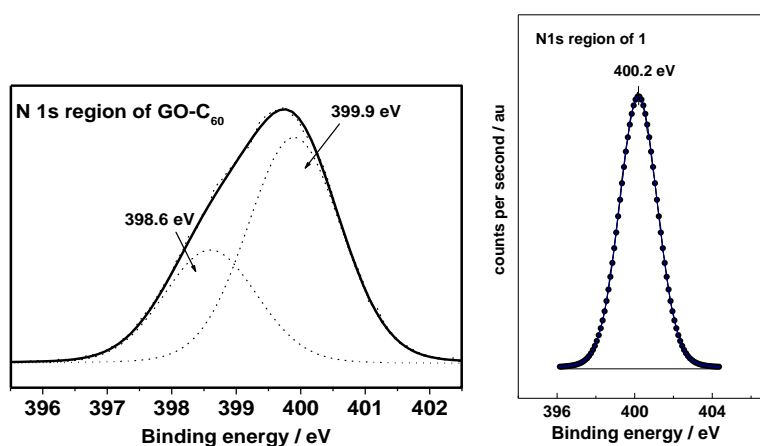


Figure 2-29. N 1s high resolution spectra of **GO-C₆₀** (left) and **1** (right).

HR-TEM gave information about the morphology of **GO-C₆₀** was constituted by large **GO** sheets with lateral dimensions of several microns (Figure 2-30). Importantly, electron diffraction in selected areas (SAED) revealed the characteristic graphitic hexagonal patterns. Moreover, the spherical structure of fullerene moieties grafted onto **GO** appeared as circles with an inner diameter of *ca.* 0.7 nm in perfect agreement with the size of C₆₀ units (insets of Fig. 2-30).¹⁴⁶

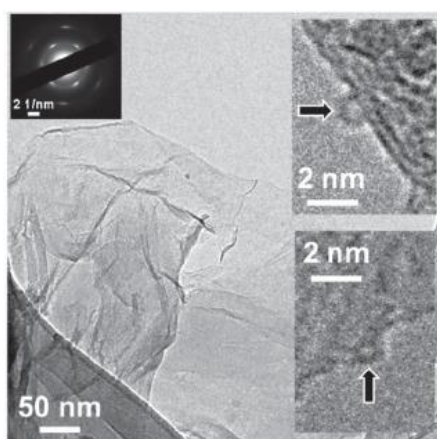


Figure 2-30. HR-TEM images of **GO-C₆₀** and its corresponding SAED pattern. Insets on the right show spherical C₆₀ units highlighted with arrows.

Additional structural data were obtained by AFM investigations. AFM revealed a layered material with typical heights in the range of 4-6 nm (Figure 2-31).

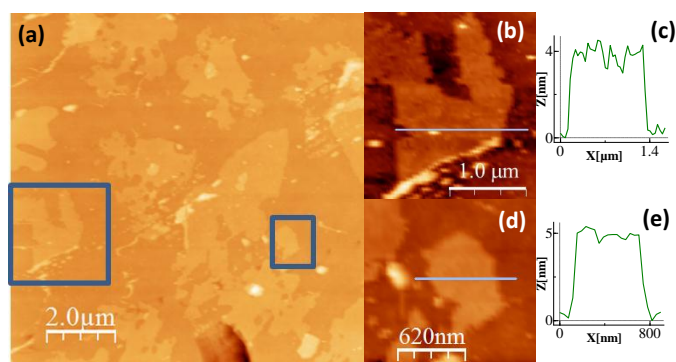


Figure 2-31. (a) AFM topography image of **GO-C₆₀** after 150 minutes of sonication and drop casting on SiO₂; (b) and (d) zoomed areas of (a) with their corresponding height profiles (c) and (e).

The images observed for **GO-C₆₀** were rather similar to those of the starting **GO** material, thus showing that the morphology was maintained during its functionalization (Figure 2-32).

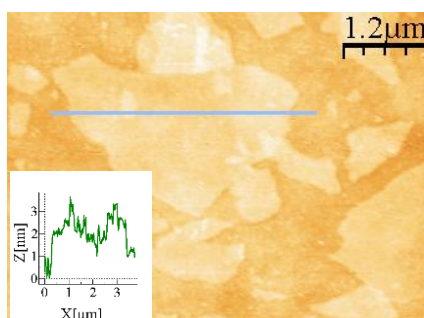


Figure 2-32. AFM image of **GO** deposited on SiO₂ and height profile (inset).

The electrochemical properties of the hybrid compound **GO-C₆₀** were studied by cyclic voltammetry (CV) in order to investigate the interactions between **GO** and **C₆₀** moieties in the **GO-C₆₀** hybrid (Figure 2-33).

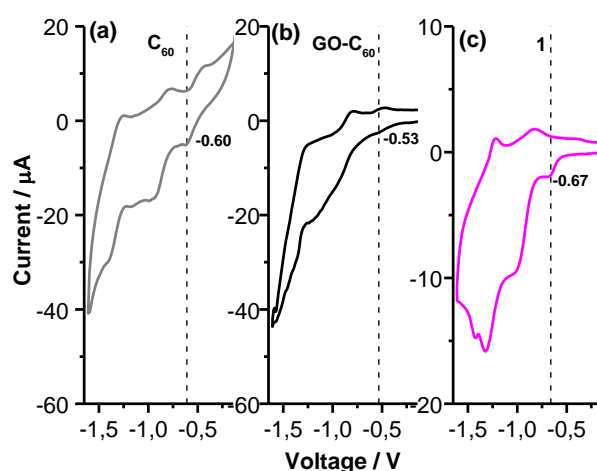


Figure 2-33. Cyclic voltammetry of A) **C₆₀**, B) **GO-C₆₀** and C) **1** film cast onto FTO electrode in a 0.05 M acetonitrile solution of TBABF₄. Scan rate of 50 mV/s.

For the sake of comparison, electrochemical measurements were also carried out for **C₆₀** and **1**. Cyclic voltammeteries, of **C₆₀** and the precursor azidefullerene **1**, showed the peak current of **C₆₀** reduction at -0.60 V and -0.67 V respectively. Interestingly, in the **GO-C₆₀** hybrid this reduction was observed at -0.53 V suggesting the existence of electronic communication between both

entities. A similar shift of the reduction potential was previously found in a CNH-C₆₀ hybrid prepared in our group.¹⁴⁶

One of the aims for the synthesis of the GO-C₆₀ conjugate was to demonstrate that the covalent linkage between both components favors excited state interactions between both carbon nanostructures. For this purpose, photophysical studies of the mentioned material were carried out in benzonitrile (PhCN).

As typically observed for fullerene derivatives, azide fullerene **1** exhibited a weak emission at *ca.* 720 nm ($\lambda_{\text{exc}} = 438$ nm) (Figure 2-34). As observed, this fluorescence signal was dramatically quenched in GO-C₆₀, suggesting the occurrence of excited-state interactions between the two forms of carbon in the nanoconjugate.

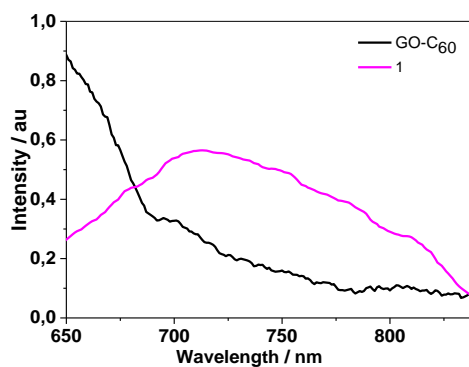


Figure 2-34. Fluorescence spectra of **1** (magenta) and GO-C₆₀ (black) recorded in PhCN ($\lambda_{\text{exc}} = 438$ nm).

In order to elucidate the quenching mechanism, laser flash photolysis experiments were carried out on GO-C₆₀ in PhCN solutions. These studies were carried out by Prof. Hermenegildo García, at the University of Valencia. The behavior of GO-C₆₀ was compared with compound **1** and starting GO.

Upon 355 nm nanosecond laser excitation of a PhCN solution of GO, a transient absorption spectrum characterized by a broad absorption band from 360 to 900 nm, having a residual low intensity from 1000 to 1200 nm in the NIR, was recorded (Figure 2-35 (a)). This transient absorption was attributed to electrons in the conduction band of GO as semiconductor, based on precedents in the literature and the signal quenching by N₂O.¹¹⁴ Figure 2-35 (b) shows transient absorption spectra of azide fullerene **1** obtained upon laser excitation at 355 nm in PhCN. Transient absorption bands at 450 and 710 nm decaying with

the same temporal profile in 8 μs were observed. These bands were attributed to the triplet excited states of **1** based on their quenching by oxygen and the known transient absorption of parent C_{60} that exhibits a $\lambda_{\text{max}} = 710 \text{ nm}$.²⁹⁹ It is worth mentioning that the transient absorption spectra of **GO** and **1** only exhibited a residual absorption in the NIR region from 800 to 1200 nm.

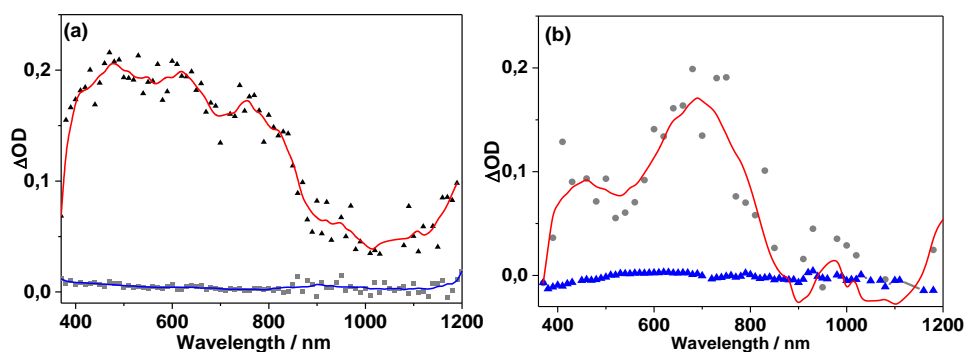


Figure 2-35. (a) Transient absorption spectra recorded at 0.1 (\blacktriangle) and 3.5 μs (\blacksquare) after 355 nm laser excitation of a N_2 -purged benzonitrile solution of **GO**. (b) Transient absorption spectra recorded at 0.1 (\bullet) and 8 μs (\blacktriangle) for fullerene derivative **1** dissolved in benzonitrile upon 355 nm laser excitation under N_2 purged solution.

The hybrid material **GO-C₆₀** was also studied through transient absorption spectroscopy. Laser excitation at 355 nm of a PhCN solution of **GO-C₆₀** also afforded a transient spectrum as shown in Figure 2-36. As observed, the transient absorption spectra have a continuous absorption from 360 to 900 nm, peaking at 820 nm, as well as a continuous band from 1000 to 1200 nm. While the continuous absorption of the transient absorption spectra of **GO-C₆₀** in the 400-800 nm region can be due to the combination of the spectra recorded for **GO** and the spectra of **1**, the most prominent feature is the intense NIR absorption, which was ascribed to the absorption of fullerene radical anions.³⁰⁰ Similar

²⁹⁹ (a) H. Imahori, D. M. Guldi, K. Tamaki, Y. Yoshida, C. Luo, Y. Sakata and S. Fukuzumi, *J. Am. Chem. Soc.* **2001**, *123*, 6617; (b) H. Imahori, Y. Sekiguchi, Y. Kashiwagi, T. Sato, Y. Araki, O. Ito, H. Yamada and S. Fukuzumi, *Chem. Eur. J.* **2004**, *10*, 3184; (c) D. M. Guldi, H. Imahori, K. Tamaki, Y. Kashiwagi, H. Yamada, Y. Sakata and S. J. Fukuzumi, *J. Phys. Chem. A* **2004**, *108*, 541.

³⁰⁰ Detection of the fullerene anion was not possible as it is faster than the detection limit of the instrument.

transient absorptions have been recently observed in the NIR region upon PET in a modified GO derivative bearing C₆₀ and ZnPc subunits.²⁹⁵

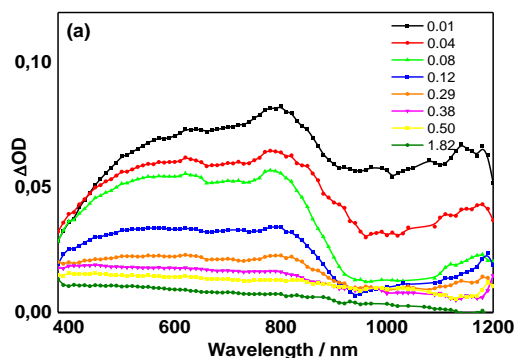


Figure 2-36. Transient absorption spectra of an N₂-purged benzonitrile solution of GO-C₆₀. Depicted spectral traces are from 0.01 to 1.82 ms after the laser pulse ($\lambda_{\text{exc}} = 355$ nm).

As showed in Figure 2-37, the temporal profile of the signals in the 360–900 nm zone was coincident, but the signal decay in the NIR region was slower indicating the presence of long-lived transient species, namely C₆₀[•]. GO was therefore acting as an electron donor. However the oxidized GO has no characteristic absorption bands³⁰¹ in the visible region and the formation of GO^{•+} was not monitored.

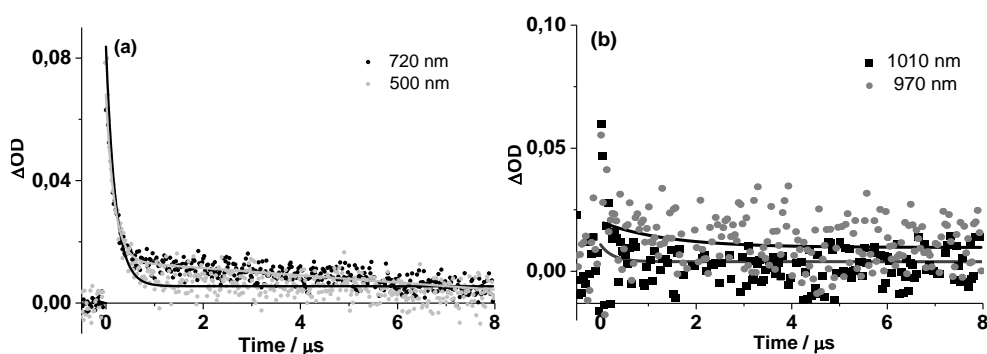


Figure 2-37. Signal decays monitored at 500, 720 nm (a) and 970 and 1010 nm (b) of an N₂ purged benzonitrile solution of GO-C₆₀.

³⁰¹ (a) S. Kaniyankandy, S. N. Achary, S. Rawalekar and H. N. Ghosh, *J. Phys. Chem. C*, **2011**, *115*, 19110; (b) J. Shang, L. Ma, J. Li, W. Ai, T. Yu and G. G. Gurzadyan, *Sci. Rep.*, **2012**, *2*, 792.

It is also worth noting that no transient absorption was observed in the NIR region during control experiments using compound **1** in the absence of GO.

To gain further insight into the species responsible for the NIR absorption of GO-C₆₀, we also performed bimolecular quenching experiments with mixtures of GO and C₆₀. Upon addition of increasing amounts of C₆₀ (in a proportion between 0 and 3 wt.%) quenching of the transient absorption recorded for GO from 360 to 900 nm was observed (Figures 2-38 and 2-39). Increasing the amounts of C₆₀ led to stronger quenching of the GO signal with the development of a peak at 720 nm (attributable to C₆₀ triplets formed presumably by direct excitation at 355 nm) together with the broad weak absorption from 900 to 1200 nm that can be assigned to C₆₀^{•-} radical anion³⁰² that would be generated by the quenching of GO transient. Overall the quenching of GO transient by C₆₀ indicated inhibition of GO signals, with the generation of low concentration of C₆₀^{•-}. It should be noted that control experiments using pure C₆₀ in benzonitrile showed the formation of C₆₀ triplets ($\lambda_{\text{max}} = 720 \text{ nm}$), without generation of C₆₀^{•-} that requires the presence of an electron donor.

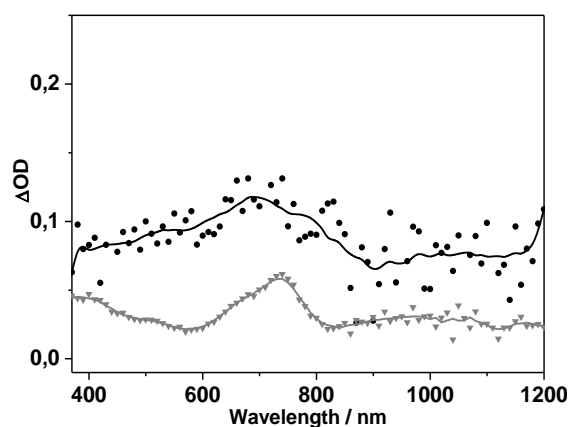


Figure 2-38. Transient spectra recorded at 0.1 (•) and 3.5 μs (▼) after 355 nm laser excitation of a N₂-purged benzonitrile solution of GO after adding 300 μL of a solution of 0.1 mg/mL of C₆₀.

³⁰² M. E. El-Khouly, Y. Araki, M. Fujitsuka and O. Ito, *PhysChemChemPhys*, **2002**, *4*, 3322.

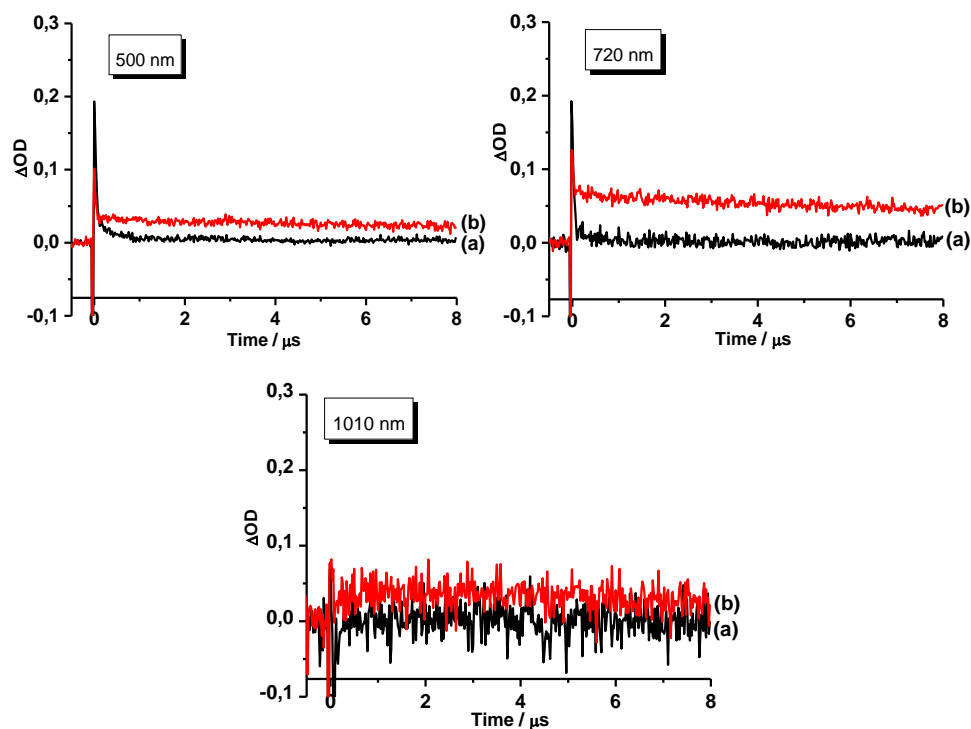


Figure 2-39. Signal decays monitored at 500, 720 and 1010 nm of an N_2 purged benzonitrile solution of GO before (a) and after (b) adding a solution of C_{60} .

Overall, comparison of the transient absorption spectra of $GO-C_{60}$ with that of mixtures of GO and C_{60} indicated similarities in the behavior with formation of $C_{60}^{\bullet-}$ radical anion, the differences being in the efficiency in the generation of these species that appear much larger for $GO-C_{60}$ than for mixtures of both components. In this regard there are precedents in the literature showing parallel behavior for modified carbon nanotubes having covalently attached electron acceptor quenchers with that of equivalent mixtures, except that the quenching effect is considerably more efficient when the two species are linked through a tether.²⁹⁹

2.3.2 Cycloaddition of nitrile imines to graphene.

Background

As aforementioned, graphene is currently considered one of the main candidates for applications in semiconductor electronics. Graphene is a zero band gap material, and its conductivity cannot be turned off electronically as in conventional semiconductor materials. For this reason, it is a critical issue in graphene-based nanoelectronic and optoelectronic devices to tune the band gap and the work function (WF) of graphene layers, while preserving its unique band structure, which will allow to be used in the semiconducting field for new low-dimensional nanoelectronic devices.^{303,304,305}

The WF (Φ) of any material can be defined as the energy required to remove an electron from the highest filled level in the Fermi distribution of a solid to vacuum. It is a fundamental electronic property of any material, and provides understanding of the relative position of the Fermi surface levels. It is well known that work function engineering is a powerful tool for tuning graphene electronic properties.³⁰⁶

In the past years, some attempts have been reported with the aim of modulating the work function of graphene by controlling the electronic structure.^{307,308,309} Among them, the interaction of graphene with different chemical species is the main approach utilized to get systems which fulfil the desired requirements in many of the potential applications of graphene-based devices. Chemical doping has been reported to be effective for tailoring the electrical properties of graphene and modulating the work function by charge transfer on the graphene sheet.³¹⁰

³⁰³ L. A. Chernozatonskii, D. G. Kvashnin, O. P. Kvashnina and N. A. Konstantinova, *J. Phys. Chem. C*, **2014**, *118*, 1318.

³⁰⁴ S. Bae, S. J. Kim, D. Shin, J.-H. Ahn and B. H. Hong, *Phys. Scr.*, **2012**, 014024.

³⁰⁵ T.-H. Han, Y. Lee, M.-R. Choi, S.-H. Woo, S.-H. Bae, B. H. Hong, J.-H. Ahn and T.-W. Lee, *Nat. Phonon*, **2012**, *6*, 105.

³⁰⁶ R. Garg, N. K. Dutta and N. R. Choudhury, *Nanomaterials*, **2014**, *4*, 267.

³⁰⁷ H.-J. Shin, W. M. Choi, D. Choi, G. H. Han, S.-M. Yoon, H.-K. Park, S.-W. Kim, Y. W. Jin, S. Y. Lee, J. M. Kim, J.-Y. Choi and Y. H. Lee, *J. Am. Chem. Soc.*, **2010**, *132*, 15603.

³⁰⁸ J. Park, W. H. Lee, S. Huh, S. H. Sim, S. B. Kim, K. Cho, B. H. Hong and K. S. Kim, *J. Phys. Chem. Lett.*, **2011**, *2*, 841 .

³⁰⁹ Y. Wang, S. W. Tong, X. F. Xu, B. Özyilmaz and K. P. Loh, *Adv. Mater.* **2011**, *23*, 1514. .

³¹⁰ K. C. Kwon, K. S. Choi and S. Y. Kim, *Adv. Funct. Mater.*, **2012**, *22*, 4724.

The first experimental demonstration of gap engineering was provided by Geim and *et al.*³¹¹ by completely hydrogenating graphene in an atomic hydrogen atmosphere to form a complete insulator, “graphane”.

On the other hand, cycloaddition reaction is a popular synthetic methodology for the surface modification of carbon nanostructures owing to the versatility of the reaction and the variety of functional groups that can be anchored through this method. Chemical modification of CNTs⁸⁵ and fullerenes⁸⁴ through 1,3-dipolar cycloaddition of azomethine ylides has been one of the most common methods employed to modify the electronic and chemical properties of these carbon allotropes.

In the case of graphene, examples of 1,3-dipolar cycloaddition of azomethine ylides have been also described,^{255,256,259} however, no examples of cycloaddition of less reactive dipoles as nitrile imines or nitrile oxides are available in the literature.

Our group has a wide experience in the preparation of pyrazoline derivatives through 1,3-dipolar cycloaddition of nitrile imines on different carbon nanoforms.^{89,312} It has been demonstrated that this is a good way to enhance the properties of these hybrids, making them attractive for many electronic applications.

In most cycloaddition reactions to [60]fullerene, the LUMO of the fullerene cage is shifted to higher values by around 0.15 eV due to the saturation of a double bond of the fullerene core. Nevertheless, we have previously demonstrated that, in the cycloaddition of nitrile imines to fullerenes, affording pyrazolinofullerenes, the LUMO of C₆₀ is not shifted to higher values due to the electron-acceptor character of the pyrazoline ring.^{89,312} In this way, cycloaddition of nitrile imines to graphene, if the reaction works, can be useful to modulate the band-gap in a different way than other cycloaddition reactions.

In the second part of this chapter, we present theoretical and experimental studies based on the modification of the band gap as well as the work function of graphene by the 1,3-cycloaddition reaction of nitrile imines,

³¹¹ D. C. Elias, R. R. Nair, T. M. G. Mohiuddin, S. V. Morozov, P. Blake, M. P. Halsall, A. C. Ferrari, D. W. Boukhvalov, M. I. Katsnelson, A. K. Geim and K. S. Novoselov, *Science*, **2009**, 323, 5914.

³¹² J. L. Delgado, N. Martín, P. de la Cruz and F. Langa, *Chem. Soc. Rev.*, **2011**, 40, 5253.

varying the nature of the electroactive species of the C atom anchored to the pyrazoline ring.

Computational studies

Computational chemistry is a powerful tool to understand and study various chemical aspects, among which stands the chemical reactivity. In this sense, an important fact of the Computational Chemistry is its ability to predict. This aspect is very important because this discipline can be used efficiently to design new experiments, which avoids some experimental studies that in case of graphene are expensive and complicated.

With this target in mind, the reactivity, regioselectivity and stereoselectivity of 1,3-dipolar cycloaddition of nitrilimines to graphene were studied by Dr. Pilar Prieto at University of Castilla-La Mancha (Ciudad Real) by means of density functional theory (DFT) calculations.³¹³ For the sake of comparison, also the cycloaddition of analogous azomethine ylides was studied.

Recently, some examples have been reported concerning computational calculations of different cycloadditions, such as Diels-Alder,³¹⁴ 1,3 dipolar,³¹⁵ [2+2]³¹⁶ and [2+1]³¹⁷ cycloadditions.

There are two ways to computationally study the graphene structure as infinite or finite form. Both can be studied, however, with *ab initio* methods with periodic boundary conditions, where the graphene is represented as a two dimensional superstructure repeated periodically.³¹⁸ In this work, graphene models as finite-size polybenzenoid (25 fused benzene rings) hydrocarbons with no considerations of defects were employed. Previous studies performed by

³¹³ (a) P. Hohenberg and W. Kohn, *Phys. Rev.*, **1964**, 136, 864; (b) W. Kohn and L. J. Sham, *Phys. Rev.*, **1965**, 140, 1133.

³¹⁴ (a) Y. Cao, S. Osuna, Y. Liang, R. C. Haddon and K. N. Houk, *J. Am. Chem. Soc.* **2013**, 135, 17643; (b) P. A. Denis, *Chem. Eur. J.* **2013**, 15719.

³¹⁵ (a) Y. Cao and K. N. Houk, *J. Mater. Chem.*, **2011**, 21, 1503; (b) Y. Yuan, P. Chen, X. Ren and H. Wang, *ChemPhysChem*, **2012**, 13, 741; (c) P. A. Denis and F. Iribarne, *Chem. Phys. Lett.* **2012**, 550, 111.

³¹⁶ P. A. Denis and F. J. Iribarne, *Mat. Chem.* **2012**, 22, 5470.

³¹⁷ I. K. Petrushenko, *Monatsh. Chem.* **2014**, 145, 891.

³¹⁸ H. W. Shih, M. N. Vander Wal, R. L. Grange and D. W. C. MacMillan, *J. Am. Chem. Soc.*, **2012**, 134, 13600.

Houk *et al.*^{314a} indicated that polyacenes possess an open-shell singlet ground state.³¹⁹

All the calculations were performed with Gaussian 09³²⁰ using (U)M06-2X level of theory³²¹ and 6-31G(d) as basis set.³²² This method has been reported to provide excellent energetics values for cycloadditions reactions.³²³ All stationary points were characterized by harmonic analysis and the relative energies included the zero-point vibrational energy (ZPVE) corrections.

As it was explained before, there are two known forms of graphene depending on the nature of its edges, *zigzag* or *armchair*. In this study we considered both models: model 1 terminates with *zigzag* edges and model 2 has *armchair* edges (Figure 2-40).

³¹⁹ M. Bendikov, H. M. Doung, K. Starkey, K. N. Houk, E. A. Carter and F. Wuld, *J. Am. Chem. Soc.* **2004**, *126*, 7416.

³²⁰ Gaussian 09, Revision D.1, M. J. Frisch, G. W. Trucks, H. B. Schlegel, G. E. Scuseria, M. A. Robb, J. R. Cheeseman, G. Scalmani, V. Barone, B. Mennucci, G. A. Petersson, H. Nakatsuji, M. Caricato, X. Li, X. H. P. Hratchian, A. F. Izmaylov, J. Bloino, G. Zheng, J. L. Sonnenberg, M. Hada, M. Ehara, K. Toyota, R. Fukuda, J. Hasegawa, M. Ishida, T. Nakajima, Y. Honda, O. Kitao, H. Nakai, T. Vreven, Jr. J. A. Montgomery, J. E. Peralta, F. Ogliaro, M. Bearpark, J. J. Heyd, E. Brothers, K. N. Kudin, V. N. Staroverov, R. Kobayashi, J. Normand, K. Raghavachari, A. Rendell, A. J. C. Burant, S. S. Iyengar, S. J. Tomasi, M. Cossi, N. Rega, N. J. Millam, M. Klene, J. E. Knox, J. B. Cross, V. Bakken, C. Adamo, J. Jaramillo, R. Gomperts, R. E. Stratmann, O. Yazyev, O. A. J. Austin, R. Cammi, C. Pomelli, J. W. Ochterski, R. L. Martin, K. Morokuma, V. G. Zakrzewski, G. A. Voth, P. Salvador, J. J. Dannenberg, S. Dapprich, A. D. Daniels, O. Farkas, J. B. Foresman, J. V. Ortiz, J. Cioslowski and D. J. Fox, *Gaussian, Inc., Wallingford CT*, **2009**.

³²¹ (a) Y. Zhao and D. G. Truhlar, *Theor. Chem. Acc.* **2008**, *120*, 215; (b) Y. Zhao and D. G. Truhlar, *Acc. Chem. Res.* **2008**, *41*, 157.

³²² (a) R. Ditchfield, W. J. Hehre and J. A. Pople, *J. Chem. Phys.*, **1971**, *54*, 724.; (b) W. J. Hehre, R. Ditchfield and J. A. Pople, *J. Chem. Phys.*, **1972**, *56*, 2257; (c) P. C. Hariharan and J. A. Pople, *Theor. Chim. Acta*, 1973, **28**, 213-222; (d) P. C. Hariharan and J. A. Pople, *Mol. Phys.*, **1974**, *27*, 209.; (e) M. S. Gordon, *Chem. Phys. Lett.*, **1980**, *76*, 163.

³²³ Y. Lan, L. F. Zou, Y. Cao and K. N. Houk, *Phys. Chem. Chem. Phys.*, **2008**, *10*, 6615.

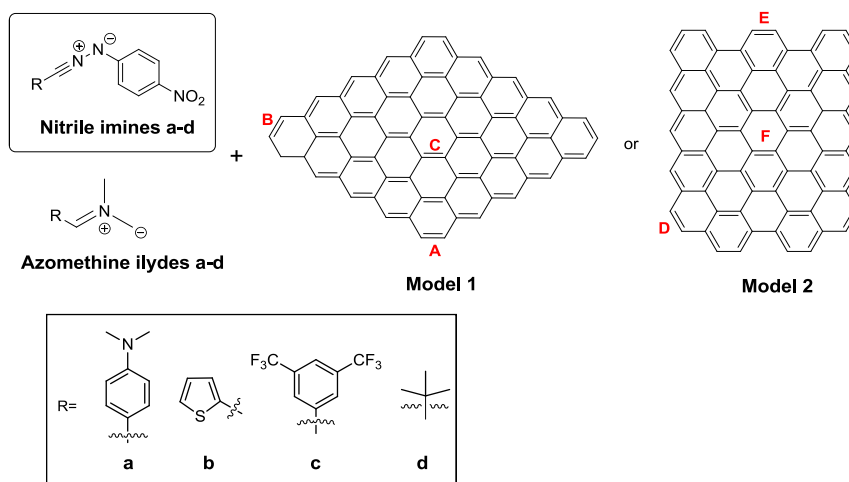


Figure 2-40: Two possible models considered for the theoretical calculations: model 1 (*zigzag*) and model 2 (*armchair*).

Firstly, the reactant's structures were optimized and the energy values of the frontier molecular orbitals as well as the band gap were calculated. All the outcomes are collected in Table 2-2 and Table 2-3. The energy band gap values are referenced to the graphene sheet model 2 because it was demonstrated computationally that it is 28.67 kcal/mol more stable than model 1.^{314a}

Table 2-2. Energy values (eV) of frontier molecular orbitals and energy band gap (eV) in gas-phase computed at (U)M06-2X/6-31G(d) for nitrile imines a-d.

Sample	HOMO (eV)	LUMO (eV)	Band gap (LUMO _{graphene} - HOMO _{dipole})	Band gap (LUMO _{dipole} - HOMO _{graphene})
Nitrile imine a	-6.49	-0.91	3.45	3.64
Nitrile imine b	-7.00	-1.60	3.97	2.95
Nitrile imine c	-7.27	-2.09	4.23	2.45
Nitrile imine d	-6.48	-0.91	3.45	3.64

Table 2-3. Energy values (eV) of frontier molecular orbitals and energy band gap (eV) in gas-phase computed at (U)M06-2X/6-31G(d) for azomethyne ylides a-d.

Sample	HOMO (eV)	LUMO (eV)	Band gap (LUMO _{graphene} -HOMO _{dipole})	Band gap (LUMO _{dipole} -HOMO _{graphene})
Azomethine ylide a	-5.25	-1.29	2.21	3.26
Azomethine ylide b	-5.70	-1.89	2.66	2.65
Azomethine ylide c	-6.27	-2.28	3.19	2.26
Azomethine ylide d	-5.79	-1.06	2.76	3.47

As observed, the band gap values obtained for the azomethine ylides were smaller than that of the analogous nitrile imines, indicating higher reactivity of the former in the cycloaddition reaction as reported in the literature.^{225b}

These findings also showed that the most favourable interaction was LUMO dipole-HOMO graphene in the case of the nitrile imines and HOMO graphene-LUMO dipole for the azomethine ylides.

Secondly, the transition states were studied. For this purpose all the reaction paths were computed taking as example the nitrile imine **d** (R= tert-butyl), since this is the most simple nitrile imine with no electron-donating or electron-withdrawing effects (see Figure 2-40).

Six possible attacks, denoted as **A**, **B**, **C**, **D**, **E** and **F** (Figure 2-40) were taken into consideration for the study. For each of them, we considered two possible regioisomers and within each both possible stereoisomers, denoted as: subscript 1 is employed for graphene model 1, subscript 2 is employed for graphene model 2; r1, nitro group right, r2, nitro group left, c1 nitro group ahead, c2, nitro group behind. Hence, the four possible approaches (except for functionalization in the positions **C** and **F**, in the centre of the sheet) were denoted as r1c1, r1c2, r2c1, r2c2, being r1c1, r2c1 and r1c2, r2c2 enantiomers. The outcomes were collected in Table 2-4.

Table 2-4: Transition State (TS) structure, Activation Energies (ΔE_a , kcal/mol), Reaction Energies (ΔE_{rxn} , kcal/mol) computed at the (U)M06-2X/6-31G(d).

Entry	TS	ΔE_a	ΔE_{rxn}
1	A ₁ -r1c1	10.2	-47.5
2	A ₁ -r1c2	3.5	-42.1
3	A ₂ -r2c1	10.2	-47.5
4	A ₂ -r2c2	3.6	-38.2
5	B ₁ -r1c1	15.1	-30.6
6	B ₁ -r1c2	9.7	-23.5
7	B ₂ -r2c1	14.9	-30.4
8	B ₂ -r2c2	9.5	-23.6
9	C	27.5	17.2
10	D ₁ -r1c1	10.6	-44.1
11	D ₁ -r1c2	4.6	-33.5
12	D ₂ -r2c1	11.9	-44.2
13	D ₂ -r2c2	5.7	-29.6
14	E ₁ -r1c1	18.8	-11.2
15	E ₁ -r1c2	9.1	-12.6
16	E ₂ -r2c1	18.4	-20.2
17	E ₂ -r2c2	9.1	-9.1
18	F	38.8	6.7

The data clearly evidenced that the attack on the central positions **C** and **F** (Figure 2-40) was both kinetically (27.5 and 38.8 kcal/mol) and thermodynamically (17.2 and 6.7 kcal/mol) disfavoured (Table 2-3, entries 9 and 18). On the contrary, reactions on the corner and the edges bonds (**A**, **B**, **D** and **E**, Figure 2-40) would be favoured kinetically and thermodynamically. It is noteworthy to mention that c2 attacks are always the kinetically favoured, due to an π - π interaction between the nitrobenzene ring and the graphene sheet, which leads to the stabilization of the transition state. Taking into account the previous assumptions, the four possible stereoisomers and regioisomers resulting from the attack on the most favourable positions (**A** and **D**) are showed in Figure 2-41.

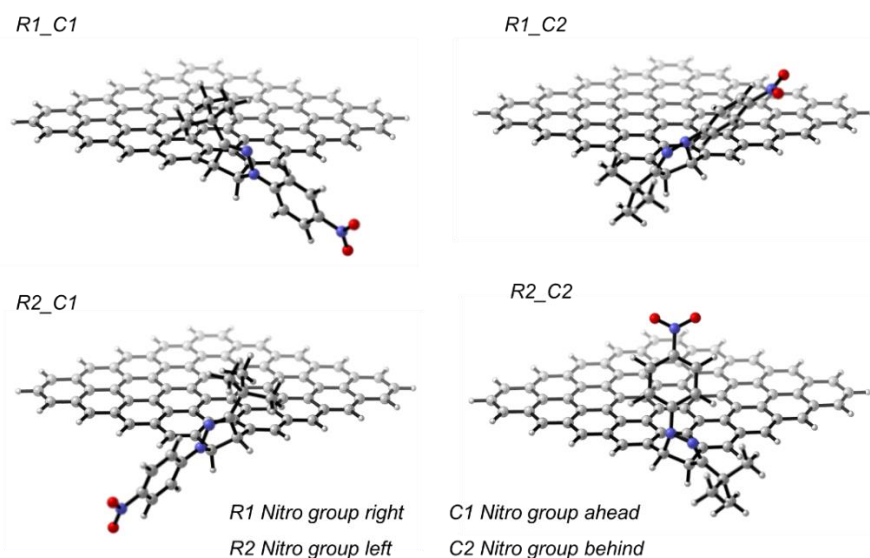


Figure 2-41. Possible stereoisomers and regioisomers resulting from the attack on the most favourable position after the 1,3-dipolar cycloaddition of nitrile imines to graphene.

Based on the results, it can be concluded that among all the positions, the most reactive, both kinetically and thermodynamically, are **A** and **D**. In addition, considering that graphene model 2 (armchair) is 28 kcal/mol more stable than the model 1,^{314a} position **D** (in the corner) would be the most favoured.

Synthesis and characterization

Once confirmed the viability of the reaction through computational studies we proceeded with the experimental studies.

Exfoliated graphene (**EG**) was obtained from graphite following the process described by Coleman *et al.*¹⁸⁷ For the exfoliation process, graphite flakes (100 mg) were dispersed in NMP (100 mL) and sonicated at a low-power by using an Elmasonic P 300 H sonicator bath (37 KHz). In order to exclude the effect of temperature and to avoid the degradation of the solvent due to an increase of the bath water during sonication, a cooling system was connected to the bath sonicator performing the process at 20 °C. The dispersion was centrifuged at 500 rpm for 45 minutes, the supernatant was decanted and stored in solution.

In order to study the number of layers obtained after the exfoliation process, Raman studies were performed. The main difference between the Raman features of single layer graphene (SLG) and graphite is the 2D band. The 2D band corresponding to SLG is a sharp and symmetric peak while that of graphite can be fitted into 2 peaks. The shape and position of the 2D band change from one to four layers since it is very sensitive to the stacking order of the graphene sheets along the c axis. The 2D band in bilayer, three and four layers graphene can be resolved into two or more components. In our case, the 2D band can be deconvoluted into three bands (Lorentzian-shaped peaks) (Figure 2-42), which is characteristic of the Raman spectra of few layer graphenes (less than five layers) as previously reported.³²⁴ Unfortunately, the differences in this band between two and few layers of graphene are not unambiguous; nevertheless we can also make use of the G band intensity which increases almost linearly as the graphene thickness increases.³²⁵ The intensity ratio of 2D band to G band (I_{2D}/I_G) decrease as the number of graphene layers increase. For bilayer graphene $I_{2D}/I_G \approx 1-2$ and less than 1 for three or more layers. In our case, the ratio I_{2D}/I_G is approximately ~ 0.5 indicating that we have a three-four layers graphene.

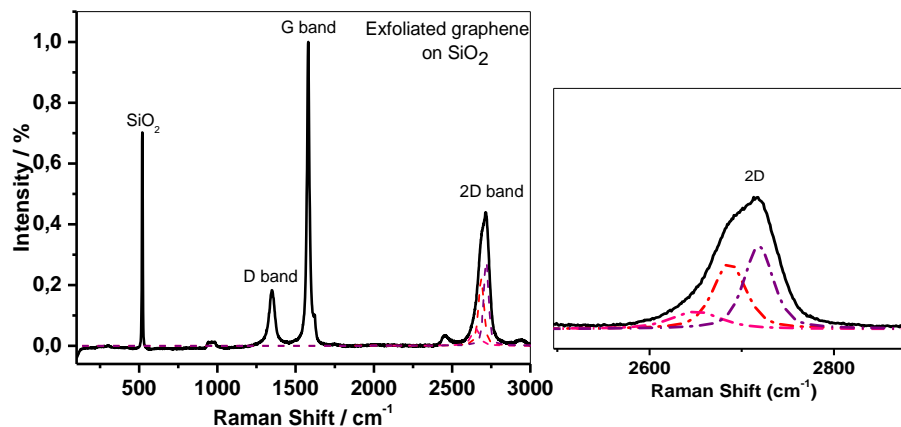


Figure 2-42. Raman spectrum of few layers graphene on SiO₂ (left) and enlarged 2D band region formed by three Lorentzian peaks (right). The spectrum was obtained using the 532 nm (2.33 eV) laser excitation energy.

³²⁴ A. C. Ferrari, J. C. Meyer, V. Scardaci, C. Casiraghi, M. Lazzeri, F. Mauri, S. Piscanec, D. Jiang, K. S. Novoselov, S. Roth and A. K. Geim, *Phys. Rev. Lett.*, **2006**, 97, 187401.

³²⁵ Y. Y. Wang, Z. H. Ni, T. Yu, H. M. Wang, Y. H. Wu, W. Chen, A. T. S. Wee and Z. X. Shen, *J. Phys. Chem. C*, **2008**, 112, 10637.

To confirm this findings, AFM measurement were performed by drop-casting the solutions resulting from the exfoliation process onto SiO₂ surfaces. (Figure 2-43).

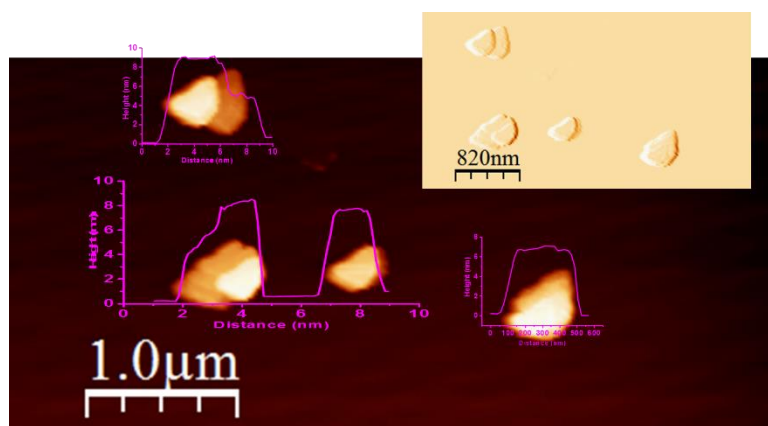
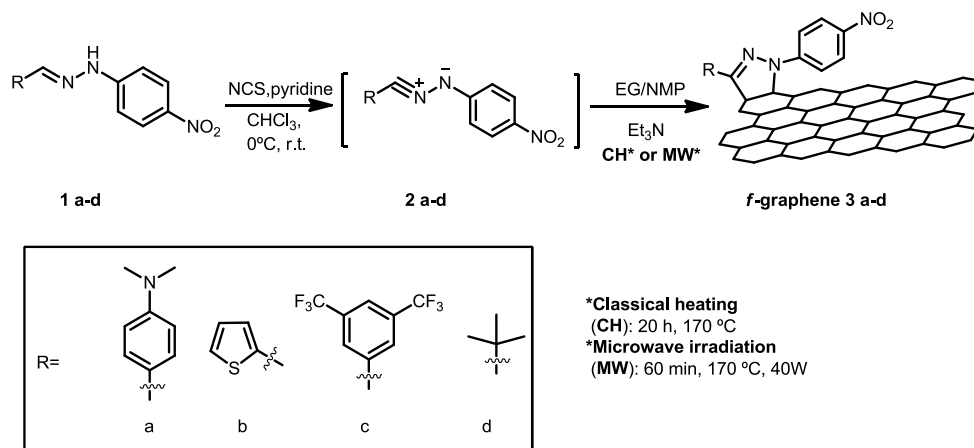


Figure 2-43: AFM image of EG solution deposited on SiO₂.

Figure 2-43 shows a structure with several height levels (terraces) suggesting that what we observe is, in fact, the result of the collapse of two exfoliated layers, that is, the dispersed graphene easily tend to aggregate during the deposition process. AFM images of graphene (EG) revealed therefore the presence of few layers graphene with an average height of *ca.* 4 nm, and AFM step heights of 4 nm and 8 nm in the overlapped regions.

Next, the preparation of the pyrazoline graphene based materials *f-graphene 3a-d* was performed (Scheme 2-3). For this purpose, nitrile imines were used as dipoles (**2a-d**) and were generated *in situ* from the corresponding hydrazones^{71,312} **1a-d** and *N*-chlorosuccinimide (NCS) in the presence of Et₃N. Thereafter, the dipoles were allowed to react with EG.

The reaction was performed in the first place under classical heating (CH) for 20 hours at 170 °C. However, a low degree of functionalization was proved by TGA through this approach. With this in mind, the reactions were performed now under microwave (MW) irradiation. For this purpose a CEM focused microwave reactor model Discover was used, and the procedure was carried out in a closed quartz tube with controlled pressure, at the same temperature (170 °C), in 60 minutes and with an irradiation power of 40 W, reaching pressures not higher than 5 psi. By using this methodology, higher functionalization degrees at the same time that reduced reaction times were achieved.



Scheme 2-3. Synthetic procedure for the preparation of pyrazoline graphene derivatives **3a-d** under classical heating (CH) or microwave irradiation (MW).

The structural and thermal properties of all graphene-based nanohybrids (*f-graphene 3a-d*) were fully investigated by FTIR, XPS, TGA and Raman spectroscopy. AFM and HR-TEM studies were performed as well for morphological characterization.

Evidence for the 1,3-dipolar cycloaddition onto the surface of graphene was firstly achieved by comparing the TGA curves of EG with those of the *functionalized* graphene materials. Figure 2-44 displays the TGA profiles of EG (black line) and *f-graphene 3a-d*, prepared under both heating approaches: CH (blue line) and MW (red line). The weight loss observed for EG (2.6%) is attributed to the defects caused by sonication,^{187a} which are also evident in the Raman spectra (from the D/G band ratio) (Figure 2-45).

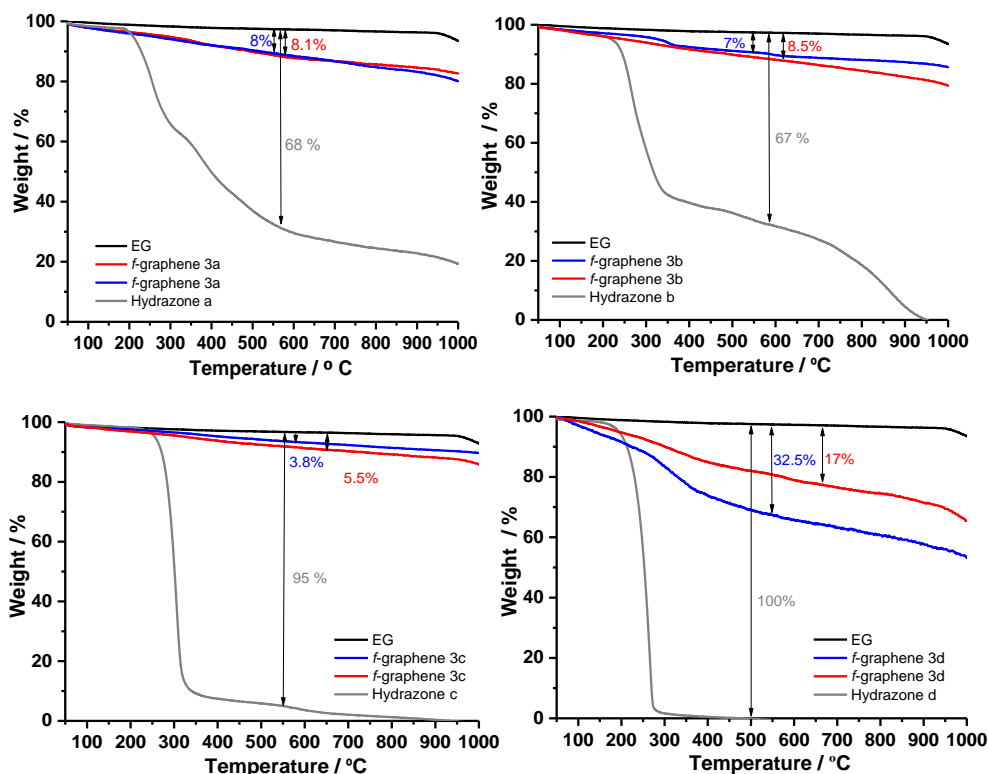


Figure 2-44. TGA curves recorded at 10° C/min under N₂ of EG (black) and *f*-graphene 3a-d. The curves in blue represents the hybrids prepared under CH and in red the curves prepared under MW irradiation.

Under classical heating, all *functionalized* graphene derivatives showed an additional [8.6% (**3a**), 7% (**3b**), 3.8% (**3c**) and 32.5% (**3d**)] weight loss in the temperature range 250-550°C due to the thermal decomposition of the covalent grafted organic groups on graphene. On the basis of these values, the number of graphene carbon atoms per pyrazoline unit is ~ 261 (**3a**), 290 (**3b**), 803 (**3c**) and 55 (**3d**) respectively (Table 2-5). It is remarkable that in the case of nanoconjugate **3c** (Table 2-5) higher degree of functionalization was detected in the material produced under MW irradiation (red line) in comparison with the same *functionalized* graphene obtained under CH (blue line), as expected according to the literature.⁹⁴ On the contrary, the functional group coverage obtained under MW irradiation is almost half for *f*-graphene **3d** when compared to CH, which could be attributed to the lower absorption of MW irradiation by this hydrazone due to its lower dipolar moment. For the other two cases (*f*-graphene **3a-b**), similar functionalization degrees were observed under both heating methods.

Table 2-5. Comparative study of the degree of functionalization of *f-graphene* **3a-d**.

Sample	TGA weight loss (%) ^a		C atoms/organic group	
	Classical heating	Microwave irradiation	Classical heating	Microwave irradiation
3a	8.6	8.1	261	279
3b	7	8.5	290	231
3c	3.8	5.5	803	551
3d	32.5	17	55	102

^aTGA results show relative weight loss.

Additional support concerning the covalent functionalization arose from Raman spectroscopy (532 nm excitation, from powdered samples) (Figure 2-45). As observed, the two most intense features in the **EG** spectra are the G band (sp² carbons) at around 1580 cm⁻¹ and the two-phonon 2D band at around 2700 cm⁻¹. In addition, we can detect also a weak D band due to the defects at the edges of the graphene plane together with a shoulder around 1600 cm⁻¹ on the G band (called D') as a signal of few-layer graphene, which is a defect-related band and not found in graphite.³²⁶ The ratio in the intensities between D and G band (I_D/I_G) has been used to quantify the density of defects in graphene.³²⁷ In this sense, while exfoliated graphene (**EG**) has an I_D/I_G of 0.05, *f-graphene* **3a-d** display higher intensity ratios (see Table 2-6), which is indicative of the success of the covalent functionalization.

³²⁶ (a) A. Eckmann, A. Felten, A. Mishchenko, L. Britnell, R. Krupke, K. S. Novoselov and C. Casiraghi, *Nano Lett.*, **2012**, *12*, 3925; (b) A. C. Ferrari and D. M Basko, *Nat. Nanotechnol.*, **2013**, *8*, 235.

³²⁷ (a) L. G. Cancado, A. Jorio, E. H. Martins Ferreira, F. Stavale, C. A. Achete, R. B. Capaz, M. V. O. Moutinho, A. Lombardo, T. S. Kulmala and A. C. Ferrari, *Nano Lett.*, **2011**, *11*, 3190; (b) D. Graf, F. Molitor, K. Ensslin, C. Stampfer, A. Jungen, C. Hierold and L. Wirtz, *Nano Lett.*, **2007**, *7*, 238.

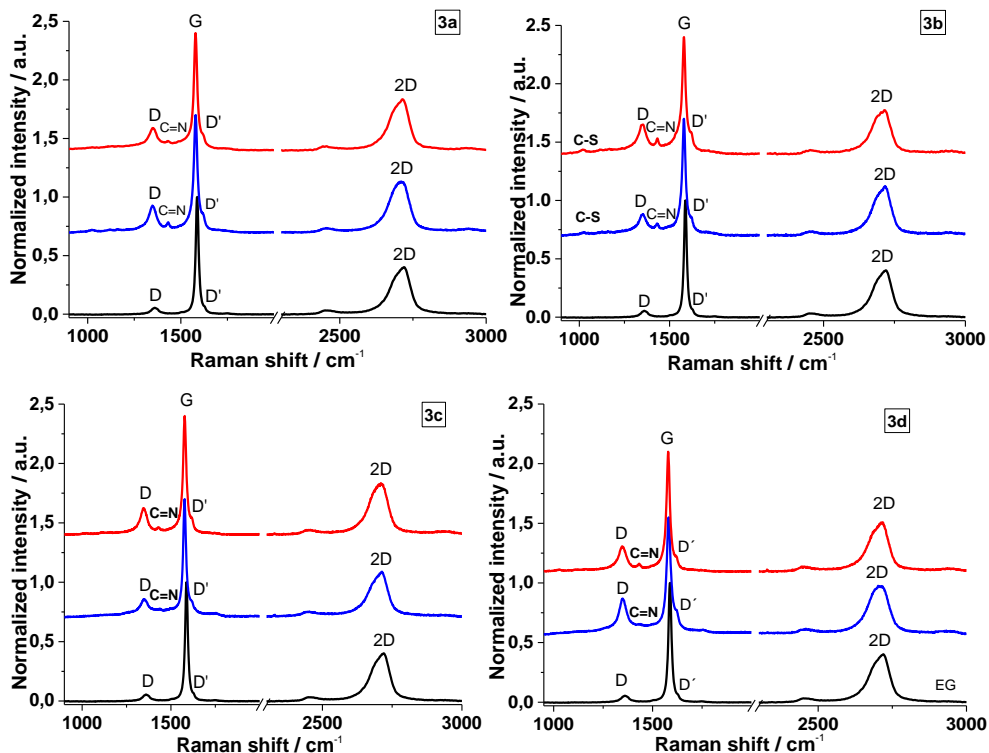


Figure 2-45. Raman spectra of *f*-graphenes **3a-d** compared with EG (in black). The curves *in blue* represents the hybrids prepared under CH and *in red* under MW. $\lambda_{\text{exc}} = 532 \text{ nm}$.

Table 2-6. Comparative of I_D/I_G ratio for *f*-graphene **3a-d**.

Samples	I_D/I_G	
	Classical	Microwave
3a	0.22	0.18
3b	0.17	0.24
3c	0.15	0.21
3d	0.32	0.20
EG	0.05	

In addition the ratio of the *D* and *G* band intensities (I_D/I_G), is inversely proportional to the crystallite size of the sample (L_a), which gives information about the presence of defects in the sample.^{328,329} A general expression that gives

³²⁸ F. Tuinstra and J. L. Koenig, *J. Chem. Phys.*, **1970**, *53*, 1126.

³²⁹ F. Tuinstra and J. L. Koenig, *J. Compos. Mater.*, **1970**, *4*, 492.

the L_a crystallite size from the intensity ratio (I_D/I_G) by using any laser line in the visible range can be found in the literature³³⁰ and is given by the equation [4]:

$$L_a \text{ (nm)} = (2.4 \times 10^{-10})\lambda_l^4 (I_D/I_G)^{-1} \quad [4]$$

where λ_l is the excitation laser energy in eV.

By applying the equation showed above the value of L_a observed for **EG** is $L_a = 384$ nm. Considering L_a as an average interdefects distance, the large value obtained is indicative of the high quality of the starting material. The mentioned decrease approximately by one-third after the functionalization process (average $L_a \sim 100$ nm) as a consequence of the presence of the pyrazolino groups on the surface.

On the other hand, in the Raman spectra of all *functionalized* samples, we observed a peak (C=N) at approximately 1430 cm^{-1} which confirmed the formation of the pyrazole ring onto the exfoliated graphene material.¹¹³ Also, in the case of thiophene-derivative **3b** the peak at $\sim 1020 \text{ cm}^{-1}$ corresponding to C-S aromatic vibration can be observed and the NO_2 band, which overlaps with the G band is observed at around 1590 cm^{-1} .

It is also important noting the shift observed in the G band to lower frequencies ($\sim 8 \text{ cm}^{-1}$), evidencing the n-doping of the material.^{160,168,331} As an example, we can observe in Figure 2-46 the G band for the sample **f-graphene 3d**, in which the mentioned shift is clearly evidenced. The shifts for the rest of *functionalized* graphene derivatives are showed in Table 2-7.

³³⁰ L. G. Cançado, K. Takai, T. Enoki, M. Endo, Y. A. Kim, H. Mizusaki, A. Jorio, L. N. Coelho, R. Magalhães-Paniago and M. A. Pimenta, *Appl. Phys. Lett.*, **2006**, *88*, 163106.

³³¹ V. Straub, A. Gallego, G. de la Torre, T. W. Chamberlain, A. N. Khlobystov, T. Torres and D. M. Guldi, *Faraday Discuss.*, **2014**, *173*, 233.

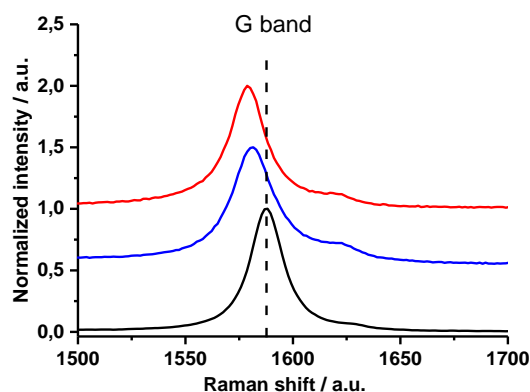


Figure 2-46. G-band region ($\lambda_{\text{exc}} = 532 \text{ nm}$) of EG (black line) in comparison with the nano hybrid **3d** (blue line, applying classical heating and red line under microwave irradiation).

Table 2-7. G band shifts of *f*-graphene **3a-d** derivatives compared to EG.

Samples	G band shift (cm ⁻¹)	
	Classical heating	Microwave irradiation
3a	1579	1579
3b	1580	1579
3c	1577	1577
3d	1581	1580
EG	1587	

The XP survey spectra of all graphene derivate samples (*f*-graphene **3a-d**) and its counterparts (graphite, EG and hydrazones **1a-b**) were recorded to identify the chemical composition of the surfaces.

The survey spectrum, as well as the C1s and O1s spectra of the raw graphite and exfoliated graphene (EG) samples are shown in Figure 2-47 and Figure 2-48, respectively. Following the assignment by Boehm¹⁵⁶ and Stankovich,³³² the C1s core-level spectra of both samples (raw graphite and EG) exhibit a dominant peak at 284.8 eV due to the sp² C-atoms of the graphene structure. In the case of graphite, it is possible to observe the π - π^* plasmon component at about 291.3 eV. In addition, the component at 286.2 eV, assigned to C-OH, and the components at 287.7 and 289.3 eV assigned to C=O and -

³³² S. Stankovich, D. A. Dikin, R. D. Piner, K. A. Kohlhaas, A. Kleinhammes, Y. Jia, Y. Wu, S. T. Nguyen and R. S. Ruoff, *Carbon*, **2007**, *45*, 1558.

COOH species, respectively, were found in the graphite sample.³³³ Similarly, the O1s emission was curve-resolved with two components related to the oxygen-containing functional groups (Figures 2-47 (c)). The minor component at 532.1 eV corresponds to O=C surface groups whereas the major one at 533.8 eV associated to the O-C bonds.²⁹⁷ The same components with almost the same binding energies were found for EG (Figure 2-48).

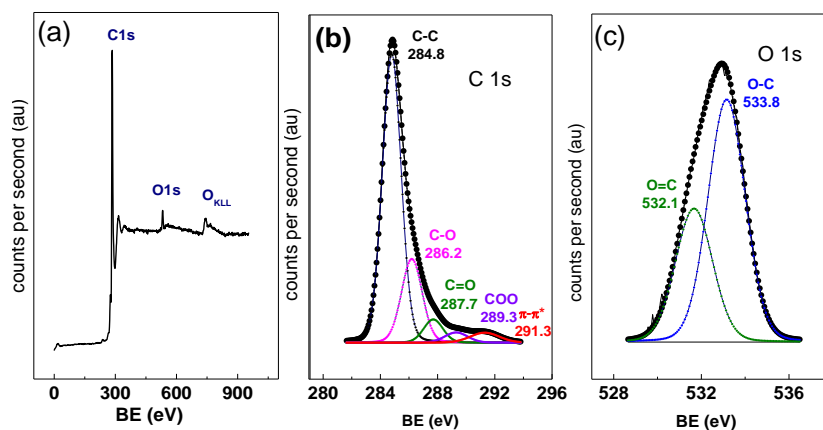


Figure 2-47. (a) Survey, (b) C1s and (c) O1s core-level spectra of graphite.

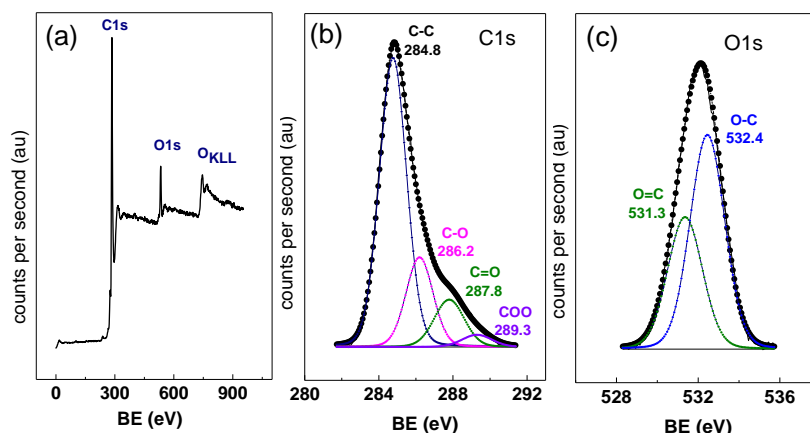


Figure 2-48. (a) Survey, (b) C1s and (c) O1s core-level spectra of EG.

C and O surface composition was also computed for both samples (graphite and EG) and the values are reported in Table 2-8. As expected, after

³³³ E. Del Canto, K. Flavin, D. Movia, C. Navio, C. Bittencourt and S. Giordani, *Chem. Mater.*, **2011**, *23*, 67.

liquid exfoliation, the O-content of the raw graphite 2.4% O atom increased slightly to 2.8% O atom for EG.¹⁸⁸

Table 2-8. Elemental content of graphite and EG.

Sample	C (% at)	O (%at)
Graphite	97.6	2.4
EG	97.2	2.8

Furthermore, high-resolution C1s, O1s and N1s core-level spectra as well as S2p for **3b** or F1s for **3c**, were recorded and the corresponding binding energies (prepared under classical heating and microwave irradiation) are summarized in Tables 2-8 and 2-9.

Table 2-9. Binding energies (eV) and percentages (%) in brackets for *f-graphene 3a-d* and its precursors under CH.

Sample	C 1s							O1s		N1s		F1s	S2p
	C sp ²	C sp ³	C-O	C=O	COO	C-F	C-N	O=C	O-C	C=N C-N	NO ₂	F-C	S-C
EG	284.8 (65)	-	286.2 (20)	287.8 (12)	289.3 (3)	-	-	531.3 (38)	532.4 (62)	-	-		
1a	284.8 (66)	285.2 (16)	-	-	-	-	286.1 (18)	-	532.1	399.4 (50) 400.4 (24)	405.9 (26)		
1b	284.8 (90)	-	286.2 (10)	-	-	-	-		532.0	399.9 (66)	406.1 (34)		164.0
1c	284.8 (58)	-	-	287.8 (12)	-	292.7 (5)	286.2 (25)		532.0	400.3(67)	406.5 (33)	688.4	
1d	284.8 (68)	285.3 (13)	-	-	-		286.2 (19)		532.0	400.1 (67)	406.2 (33)		
3a	284.8 (81)	285.3 (2)	286.3 (14)	287.7 (2)	289.3 (1)		-	531.8 (33)	533.2 (67)	399.4 (25) 400.4 (50)	407.1 (25)		
3b	284.8 (75)		286.3 (16)	287.7 (6)	289.3 (3)			531.9 (34)	533.2 (66)	400.4 (67)	407.1 (33)		164.0
3c	284.8 (71)	285.3 (2)	286.3 (18)	287.7 (7)	289.3 (2)			531.8 (33)	533.1 (67)	400.4 (67)	407.0 (33)	688.4	
3d	284.8 (75)	285.2 (6)	286.3 (12)	287.7 (4)	289.2 (3)			531.6 (20)	532.9 (80)	400.0 (67)	406.0 (33)		

Table 2-10. Binding energies (eV) and percentages (%) in brackets for *f-graphene 3a-d* and its precursors under MW irradiation.

Sample	C1s							O1s		N1s		F1s	S2p
	C _{sp²}	C _{sp³}	C-O	C=O	COO	C-F	C-N	O=C	O-C	C=N C-N	NO ₂	F-C	S-C
EG	284.8 (65)	-	286.2 (20)	287.8 (12)	289.3 (3)	-	-	531.3 (38)	532.4 (62)	-	-		
1a	284.8 (66)	285.2 (16)	-	-	-	-	286.1(18)	-	532.1	399.4 (50) 400.4 (24)	405.9 (26)		
1b	284.8 (90)	-	286.2 (10)	-	-	-	-		532.0	399.9 (66)	406.1 (34)		164.0
1c	284.8 (58)	-	-	287.8 (12)	-	292.7 (5)	286.2(25)		532.0	400.3(67)	406.5 (33)	688.4	
1d	284.8 (68)	285.3 (13)	-	-	-		286.2(19)		532.0	400.1 (67)	406.2 (33)		
3a	284.8 (62)	285.3 (3)	286.3 (24)	287.7 (8)	289.2 (3)		-	531.7 (46)	533.9 (54)	399.9 (69)	407.5 (31)		
3b	284.8 (70)		286.2 (23)	287.7 (7)				531.3 (25)	532.7 (75)	400.0 (75)	407.4 (25)		164.1
3c	284.8 (64)		286.3 (25)	287.7 (9)	289.3 (2)			531.9 (36)	533.4 (64)	399.9 (67)	407.0 (33)	688.4	
3d	284.8 (68)	285.2 (2)	286.2 (21)	287.7 (9)				531.7 (36)	533.2 (64)	400.0 (67)	407.4 (33)		

For *f-graphene 3a* (prepared under classical heating), in addition to C1s and O1s spectra, a minor N1s emission was observed (Figure 2-49 (a)). Considering the high-resolution N1s core level spectrum, three nitrogen species must contribute as components to the spectrum: two peaks at 399.4 and 400.4 eV (for the pyrazoline ring and that for the *N,N*-dimethyl-anilinyll group, respectively) and a third component at ~ 406 eV (which can be assigned to the NO₂ group)³³⁴; the intensities of the two latter very similar and almost one half of the former.

As a consequence of resonance, the electron density on both N-atoms of the pyrazoline ring was the same, only one N1s component was recorded whose intensity was twofold than that of C-N and C-NO₂ bonds. All these findings unambiguously confirmed the molecular anchorage of the pyrazoline moiety on graphene sheets.

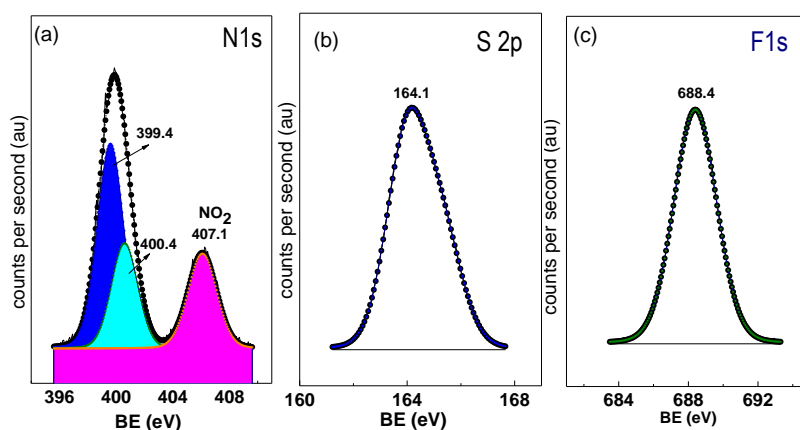


Figure 2-49. XPS high-resolution spectrum of (a) N1s region of *f-graphene 3a* (b) S2p region of *f-graphene 3b* and (c) F1s region of *f-graphene 3c*.

Functionalization is also effective for *f-graphene 3b*. This sample (prepared under MW irradiation) showed, in addition to C1s and O1s peaks of graphene substrate, the S2p one at a binding energy of about 164.1 eV which is characteristic of C-S bonds in thiophene based structures³³⁵ (Figure 2-49 (b))

³³⁴ (a) P. Allongue, M. Delamar, B. Desbat, O. Fagebaume, R. Hitmi, J. Pinson and J. M. Saveant, *J. Am. Chem. Soc.*, **1997**, *119*, 201; (b) A. Sinitskii, A. Dimiev, D. A. Corley, A. A. Fursina, D. V. Kosynkin and J. M. Tour, *ACS Nano*, **2010**, *4*, 1949.

³³⁵ T. Nomoto, S. Yagi, G. Kutluk, K. Soda, E. Hashimoto and M. Taniguchi, *J. Surface Anal.* **2005**, *12*, 238.

together with the N1s line (see Table 2-8 and Table 2-9) whose components show binding energies and intensities similar to that found in sample ***f*-graphene 3a**.

Similarly, photoelectron spectra of sample ***f*-graphene 3c** were recorded. In addition to the C1s and O1s peaks coming from the graphene substrate, the N1s and F1s emissions of the anchored pyrazoline moiety are observed (see Table 2-8 and Table 2-9). Figure 2-49 (c) shows the F1s peak at a binding energy of 688.4 eV (in both cases, for CH and MW irradiation) which in conjunction with the observation of an additional C1s component at 292.7 eV (see Table 2-8 and Table 2-9) are conclusive of the strong C-F covalent bonding.³³⁶

Surprisingly, in all the samples (Table 2-8 and Table 2-9) the binding energy of the N1s peak appears at higher binding energies (~ 407 eV) when compared with the values observed in the literature (~ 405.8 eV).³³⁴ Such binding energy differences have been attributed to the orientation of -NO₂ group with respect to the graphene surface.³³⁷

Something important to mention here is that the experimental and theoretical expected values of N/S and F/N atom ratio for ***f*-graphene 3b** and ***f*-graphene 3c** derivatives (prepared under CH or MW) are almost the same (Table 2-11), corroborating again the covalent anchoring of the pyrazoline moiety on the graphene sheets.

Table 2-11. Comparative study of surface atomic composition of *functionalized* graphene samples ***f*-graphene 3a-d**, prepared under CH and MW irradiation.

Sample	C (%at)		O (%at)		N (%at)		S (%at)		F (%at)	
	CH	MW	CH	MW	CH	MW	CH	MW	CH	MW
3a	95.5	95.6	4.1	3.9	0.4	0.5	-	-	-	-
3b	95.4	96.1	4.2	3.5	0.3	0.3	0.1	0.1	-	-
3c	95.4	95.5	4.0	3.6	0.2	0.3	-	-	0.4	0.6
3d	96.2	95.8	3.1	3.8	0.7	0.4	-	-	-	-

The anchoring of the pyrazoline ring onto the EG surface was also verified by FTIR spectroscopy (Figure 2-50). Due to the formation of the pyrazoline rings, the NH bond stretching at 3250-3100 cm⁻¹ corresponding to the hydrazono group disappears in the spectra corresponding to the *functionalized*

³³⁶ H. Touhara and F. Okino, *Carbon*, **2000**, *38*, 241.

³³⁷ G. Yang, H. Hu, Y. Zhou, Y. Hu, H. Huang, F. Nie and W. Shi, *Sci. Rep.* **2012**, *2*, 698.

samples **3a-d**, and a new peak corresponding to the C=N bond appears (C=N band $\sim 1460\text{ cm}^{-1}$).

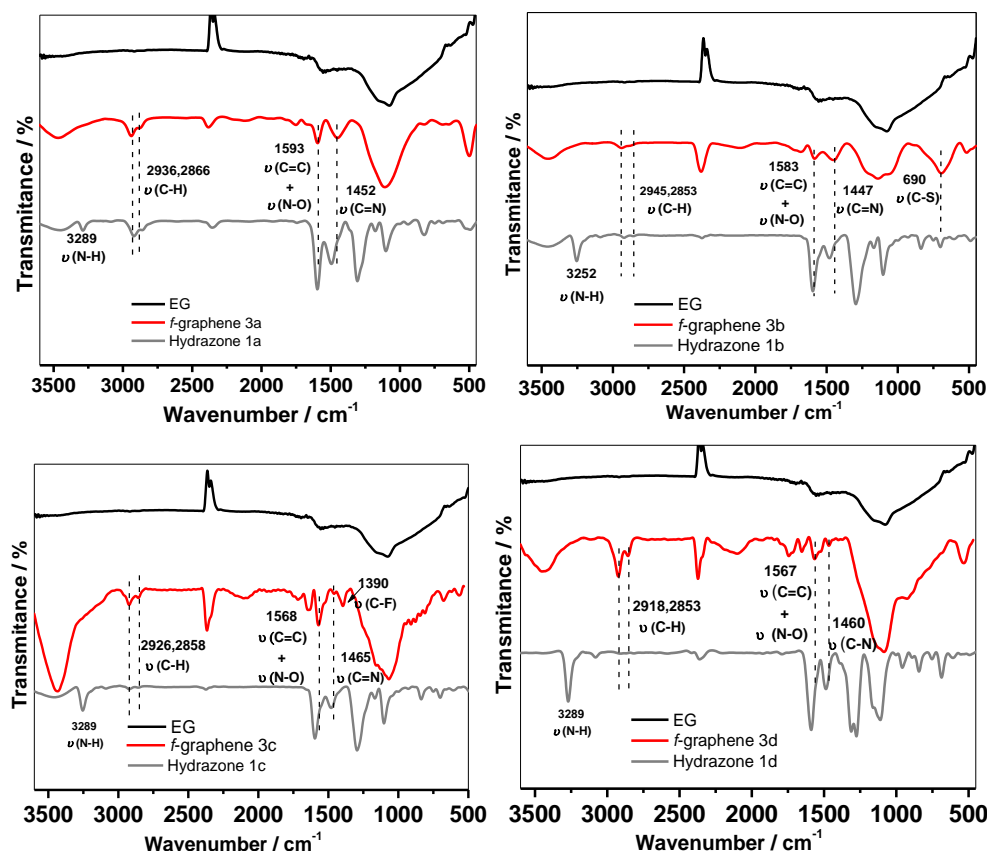


Figure 2-50. FTIR spectra of the hybrids *f-graphene 3a-d* compared to the corresponding hydrazones **1a-d**.

The presence of NO_2 groups on the EG surface is also identified since the spectra corresponding to *f-graphene 3a-d* exhibits the band at around 1580 cm^{-1} , which fall within the range of the symmetric mode of the NO_2 group. The C=C band at around 1600 cm^{-1} overlaps with the NO_2 groups. Finally, the aliphatic C-H stretching mode located around 2900 cm^{-1} are also observed.

To further characterize the *functionalized* graphene nanohybrids, morphological studies were performed. For this purpose, the functionalized samples (1 mg mL^{-1}) were sonicated (frequency: 37 kHz ; power 380 W) in milli-Q water for 90 minutes; then samples were prepared by dropcast method on SiO_2 surfaces. AFM images of graphene (EG) were again performed, revealing

once more the presence of overlapped few layers graphene with an average height of *ca.* 4 nm (Figure 2-51). Due to the small heights of the pyrazoline rings no differences were observed in the height profiles after functionalization. As example, Figure 2-52 displays the AFM image of *f-graphene 3b*.

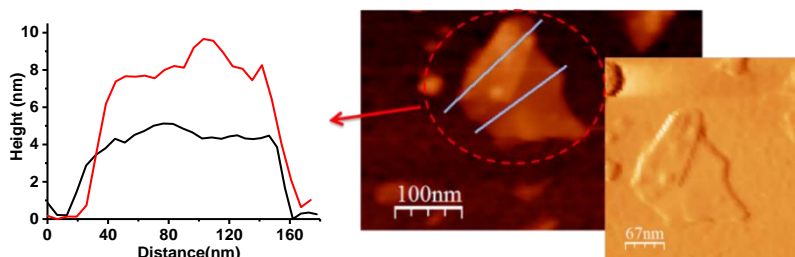


Figure 2-51. Atomic force microscope images of EG deposited onto SiO₂ surface.

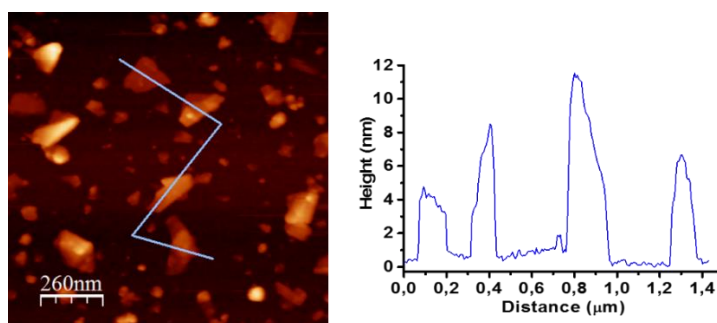


Figure 2-52. AFM image of sample *f-graphene 3b*. The height profile is taken along the solid line.

In order to gain some insight on the microstructure of the samples, HRTEM experiments were performed on selected samples *f-graphene 3c* and *f-graphene 3d* (Figure 2-53). A suspension in DMF of the samples *f-graphene 3c*, *f-graphene 3d*, as well as the pristine graphene EG, were drop casted onto a lacey carbon grid and desiccated at 75°C under vacuum. The study of the pristine exfoliated graphene in DMF exhibited the presence of some aggregates of graphene platelets of several hundreds of nanometers in lateral dimensions.

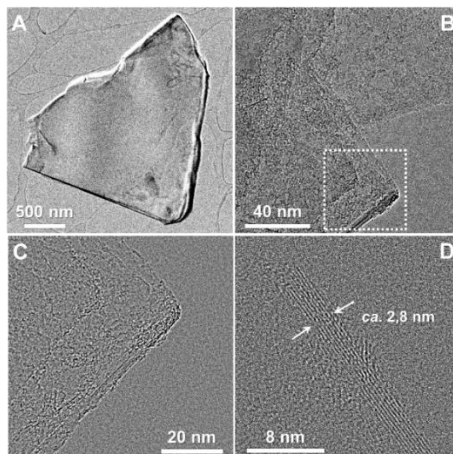


Figure 2-53. A) TEM image of an exfoliated graphitic flake. B) Higher magnification showing the thin terraces. C) Zoom in showing the area marked in (B). D) HRTEM highlighting the few-layers structure of the exfoliated graphene, with a thickness of *ca.* 2,8 nm, in excellent accordance with AFM analysis.

Figures 2-53 B and C show the presence of a residual amorphous contribution probably arising from hydrocarbon contamination and/or DMF solvent, as recently reported by Kaiser and co-workers.³³⁸ A detailed inspection of some of the thinnest flakes revealed that the aggregates consists of highly crystalline few layers graphene showing in average less than 5 nm in thickness, in excellent accordance with the AFM studies. Indeed, Figure 2-53 D exhibit the characteristic fringes with a thickness of *ca.* 2,8 nm, consisting of approximately 8 graphene layers.

Figures 2-54 A-C show the HRTEM study of functionalized sample *f-graphene 3d* (*tert*-butyl derivative). Figure 2-54 A confirms the aggregated structure consisting on few-layers graphene after the functionalization process. Interestingly, a higher magnification of the thinnest flakes revealed the typical crystalline hexagonal lattice, as well as the contribution of some amorphous moieties, that can be related with the presence of the pyrazolines and/or some physisorbed organic solvent residues.

³³⁸ G. Algara-Siller, O. Lehtinen, A. Turchanin and U. Kaiser, *Appl. Phys. Lett.*, **2014**, *104*, 153115.

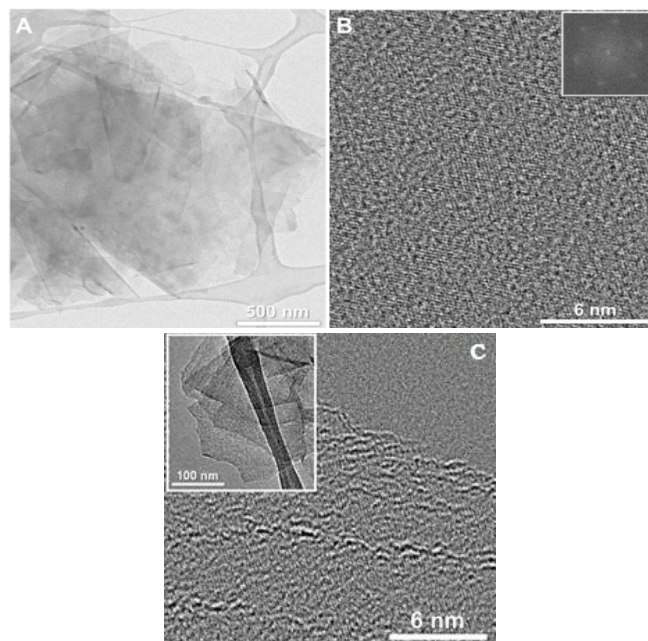


Figure 2-54. A) Low magnification of functionalized sample *f-graphene 3d* deposited onto a holey carbon TEM grid. B) HRTEM (300kV) image of a functionalized graphene sheet showing that the crystal lattice retains its hexagonal pattern. C) HRTEM image of the edge of a flake of sample *f-graphene 3d*, in which one can clearly distinguish the terraces composed of different numbers of graphene layers.

On the other hand, the analysis of the functionalized sample *f-graphene 3c* revealed a markedly different morphology consisting on aggregates of smaller flakes, highlighting the influence of the fluoroalkyl groups (Figure 2-55).

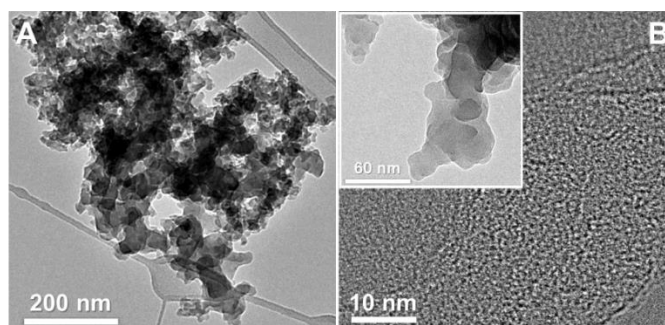


Figure 2-55. A) TEM image of an agglomerate of graphitic flakes of sample *f-graphene 3c* on a holey carbon grid; the sample seems to consist on aggregates

of few-layer graphene terraces with scrolled edges. B) HRTEM image showing some of the thinnest flakes with the presence of an amorphous contribution in the same way that sample **f-graphene 3d**.

Finally, Ultraviolet Photoelectron Spectroscopy (UPS) was used to study the work function (WF) of the final nanoconjugates compared to that of the starting EG.

The work function is the energy required to remove an electron from the highest filled level in the Fermi distribution of a solid, to the vacuum.

In semiconductor materials the valence bands and conduction bands are separated by the band gap (E_g). In Figure 2-56 we can observe a schematic energy diagram of an n-type semiconductor. In metals, work function and ionization energy are the same, however, in a nondegenerate semiconductor (having a moderate doping level), the Fermi level is located within the band gap, which means the work function is now different from the ionization energy (energy difference between valence bands maximum (VBM) and vacuum level).

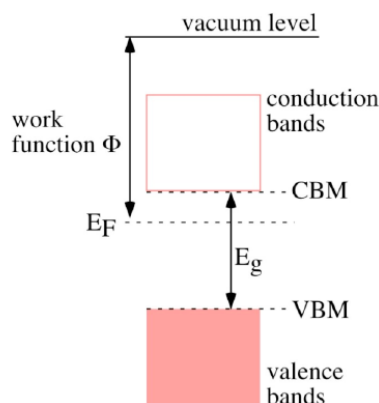
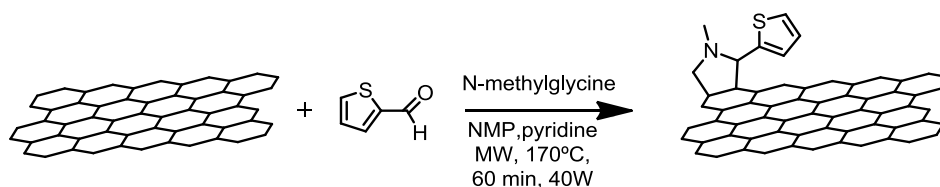


Figure 2-56. Schematic energy diagram of a semiconductor.³³⁹

UPS measures the kinetic energy spectra of photoelectrons emitted by molecules which have absorbed photons (see Annexe: *Experimental Techniques Section*). Functionalization of graphene leads to changes in its electronic structure. The type and concentration of such functionalities have a decisive influence on the WF of graphene.

³³⁹ Tutorial on Work Function by Dr. Rudy Schlaf.

With the aim of comparing the work function values of the final pyrazoline graphene derivatives with an analogous pyrrolidine graphene derivative, the following nanoconjugate was synthesized:



Scheme 2-4: Synthetic procedure for the preparation of the pyrrolidine graphene derivative (*f*-graphene pyr).

The successful formation of *f*-graphene was confirmed by TGA (Figure 2-57). At 550 °C the weight loss observed for the new hybrid was approximately 39%, which corresponds to the presence of 1 group each 34 carbon atoms. This is in agreement with the results obtained from the theoretical studies, which confirmed the higher reactivity of the azomethine ylides in cycloaddition reactions to graphene.

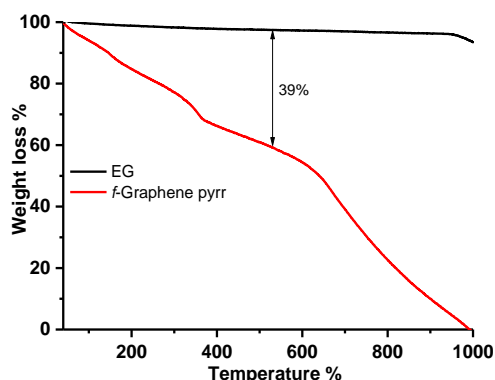


Figure 2-57: TGA curves for EG (black) and they hybrid *f*-graphene pyr (red) under nitrogen atmosphere.

Once the hybrid *f*-graphene pyr was synthesized we proceeded to perform the measurements of the work function for each derivative.

Work function measurements were performed by evaluating the secondary electron-cut off in ultraviolet photoemission spectroscopy (UPS). Figure 2-58 shows the obtained UPS spectra for all the hybrids compared to that of EG.

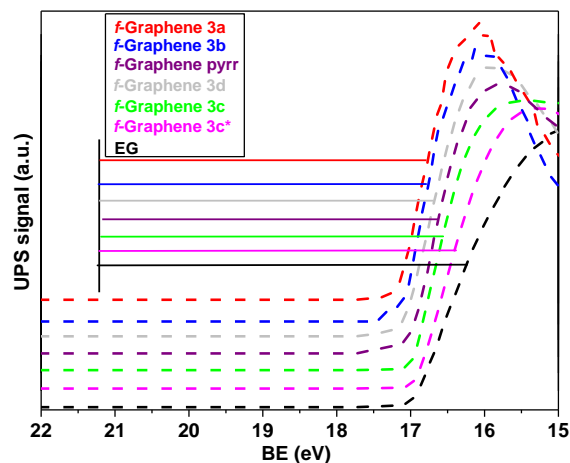


Figure 2.58: UPS spectra of *f*-graphene 3a-d compared to that of *f*-graphene pyrr and EG.

First, we compared the pyrazolino graphene hybrids bearing different substituents (*f*-graphene 3a-d); secondly, a comparison with an analogous *f*-graphene pyrr previously synthesized was accomplished. Finally, to observe the influence of the degree of functionalization in the WF, *f*-graphene 3c and *f*-graphene 3c* showing the same substituent but different functional group coverage (one group each 803 carbon atoms and one group each 551 carbon atoms, respectively) were employed.

In this study, the UPS spectra were measured with He I radiation ($h\nu = 21.21$ eV, where “ $h\nu$ ” is the energy of the incident photons). The work function (WF) was determined by the equation [5]:

$$WF = h\nu - (BE_{\text{cutoff}} - BE_{\text{Fermi}}) \quad [5]$$

where BE_{cutoff} is the binding energy of the secondary electron cutoff and BE_{Fermi} in our case is “0 eV” since the energy scales were calibrated through the measure of a gold foil reference in such a way that the Fermi level was located at 0 eV binding energy. According to this, the WF of EG was $WF = 21.21 - 16.24 = 4.97$ eV. The same procedure was employed for the rest of samples.

The UPS spectra (figure 2-58) indicated that the secondary electron cutoff shifted gradually to higher binding energies as the graphene surface was functionalized. This means that the WF of EG gradually decreased after its surface modification.

From these results, the WF obtained for **EG** and the final hybrids are summarized in Table 2-12.

Table 2-12: Values of the WF for all the nanoconjugates.

Sample	Work Function (WF, eV)
EG	4.97
<i>f</i> -graphene 3a	4.45
<i>f</i> -graphene 3b	4.46
<i>f</i> -graphene pyrrolydine	4.59
<i>f</i> -graphene 3d	4.54
<i>f</i> -graphene 3c	4.82
<i>f</i> -graphene 3c*	4.64

*Higher degree of functionalization

From the data observed in Table 2-12 the following findings can be drawn:

- Work function of graphene can be easily tuned by chemical functionalization.
- Electron-withdrawing substituents (**3c** with R=(bistrifluoromethyl) phenyl) decrease the work function in a lower degree than electron-donating substituents (the lowest values for WF are observed for R=(dimethylamino)phenyl (**3a**) and R= thiophene (**3b**) which show electron-donating behaviour).
- UPS data observed in Table 2-12 show that the WF of **EG** decreased from 4.97 eV to 4.82 eV (C atoms/organic group = 803) and then decreased to 4.64 eV for the most functionalized sample (C atoms/organic group = 551). From this findings we can state that the WF decrease when increasing the the functional group coverage.

From the previous results it is important to remark the succes in the modification of the work function of graphene which has been demonstrated by UPS. This effect of WF modulation has proved to be very useful in employing graphene for electronic applications such as electrodes,

field effect transistors, photovoltaic cells, etc... therefore, this work opens up new possibilities to engineer the electrical properties of graphene.

2.3.3 N-functionalization of N-doped graphene (N)G

Background

Controlling the electronic properties of graphene has attracted growing and intense interest in recent years, with the aim of modulating the response of graphene materials. In this regard, chemical doping appears as an obvious method for tuning graphene's properties.³⁴⁰ Two means are known to chemically dope graphene: (1) functionalization on the graphene surface or (2) substitutional doping, which introduces heteroatoms into the carbon lattice. Both of these methods can modulate the electronic properties of graphene. Heteroatom doping of graphene results in the disruption of the ideal sp² carbon lattice, thus inducing significant changes of the local electronic density and chemical reactivity.³⁴¹ Among various possible dopants (e.g. B, N, S and P), N-doping has been the most widely reported due to the facile doping process and the effective modulation of the electronic properties while maintaining high electrical conductivity.^{342,343}

Concerning the preparation of heteroatom-doped graphene, the most used procedure consists in introducing the dopant element during the arch discharge process, carried out in an atmosphere that contains the dopant element, such as N, P, B or another element. However, an alternative procedure for the preparation of doped graphene, has involved the pyrolysis of a natural biopolymer containing the doping element in its composition. In this regard, chitosan, which acts as a source of carbon and nitrogen, has been used for the preparation of few layers thick N-doped G [(N)G] films and powders (from 0.4 to 7 wt %) by pyrolysis under moderate temperatures (800-1200 °C).^{344,345} Three common bonding configurations are usually obtained when introducing nitrogen into the carbon lattice: pyridinic N, pyrrolic N and quaternary or graphitic N. Pyridinic N and quaternary N are sp² hybridized and pyrrolic N is

³⁴⁰ S. Navalón, A. Dhakshinamoorthy, M. Álvaro and H. García, *Chem. Rev.*, **2014**, *114*, 6179.

³⁴¹ H. Wang, T. Maiyalagan and X. Wang, *ACS Catal.*, **2012**, *2*, 781.

³⁴² D. Wai, Y. Liu, Y. Wang, H. Zhang, L. Huang and G. Yu, *Nano Lett.*, **2009**, *9*, 1752.

³⁴³ W. J. Lee, U. N. Maiti, J. M. Lee, J. Lim, T. H. Han and S. O. Kim, *Chem. Commun*, **2014**, *50*, 6818.

³⁴⁴ A. Primo, P. Atienzar, E. Sánchez, J. M. Delgado and H. García, *Chem. Commun*, **2012**, *48*, 9254.

³⁴⁵ A. Primo, E. Sánchez, J. M. Delgado and H. García, *Carbon*, **2014**, *68*, 777.

sp³ hybridized. Among these configurations, the quaternary N and pyridinic N are the most common types.^{340,346}

The electron-rich nature of nitrogen induces a n-type semiconducting effect and the Fermi level is shifted above the Dirac point,^{347,348} thus, the band gap between the valence and the conduction band will be opened. In summary, doping converts graphene from gapless structure to semiconductor, and this effect should increase with the doping concentration, that is, the band gap continues to grow with increasing doping concentrations.³⁴⁷

Therefore, as mentioned above, N-doping has been demonstrated to provide the possibility of tuning the band gap of graphene which makes these doped materials great candidates for applications in electronic devices.^{349,350,351}

Compared to heteroatom doping of graphene, its chemical functionalization using techniques such as alkylation are based on standard organic reactions, through which a wide spectrum of functional groups can be anchored onto its surface. In principle, doped graphene could also be modified by specific reactions at the dopant heteroatom through different routes depending on the nucleophilic or electrophilic nature of the dopant element.³⁴⁰

Phase transfer catalysis (PTC) is a versatile method to promote organic reactions between immiscible solutions due to the action of catalytic amounts of phase transfer agents, facilitating interface transfer of species.³⁵²

On the other hand, as stated before, microwave (MW) irradiation is another methodology which has been extensively used for carrying out chemical reactions over the past thirty years and presents several advantages, which result from the rapid heating throughout the materials.^{71,353,354,355}

³⁴⁶ X. Wang, G. Sun, P. Routh, D-H Kim, W. Huang and P. Chen, *Chem. Soc. Rev.*, **2014**, *43*, 7067.

³⁴⁷ M. Wu, C. Cao and J. Jiang, *Nanotechnology*, **2010**, *21*, 505202.

³⁴⁸ P. Rani and V.K. Jindal, *RSC Adv.*, **2013**, *3*, 802.

³⁴⁹ M. Latorre-Sanchez, A. Primo, P. Atienzar, A. Forneli and H. García, *Small*, **2015**, *11*, 970.

³⁵⁰ M. Gupta, N. Gaur, P. Kumar, S. Singh, N. K. Jaiswal and P. N. Kondekar, *Phys. Lett. A*, **2015**, *379*, 710.

³⁵¹ H. S. Kim, H. S. Kim, S. S. Kim and Y. H. Kim, *Nanoscale*, **2014**, *6*, 14911.

³⁵² S. Shirakawa and K. Maruoka, *Angew. Chem. Int. Ed.*, **2013**, *52*, 4312.

³⁵³ K. C. Oliver Kappe, *Angew. Chem. Int. Ed.*, **2004**, *43*, 6250.

³⁵⁴ F. Langa and P. de la Cruz, *Microwaves in organic synthesis; "Application of Microwave Irradiation in Carbon Nanostructures, chapter 22"* Wiley-VCH, **2013**.

³⁵⁵ G. Keglevich, A. Grün and E. Bálint, *Curr. Org. Synth.*, **2013**, *10*, 751.

In the last part of this chapter, an efficient method to synthesize **(N)G** sheets bearing organic addends anchored to the N pyridinic sites by combination of PTC and MW irradiation techniques is reported.

Synthesis

(N)G was prepared in the group of Prof. Hermenegildo García at University of Valencia. For this purpose, chitosan (Aldrich, low molecular weight) previously purified from insoluble residues was pyrolyzed under Ar atmosphere at 900°C for 6 h (Figure 2-59).³⁴⁴ The turbostratic graphitic residue was sonicated at 700 W for 1 h to obtain dispersed **(N)G** in water. The nitrogen content of the sample determined by elemental combustion chemical analysis was 6.65 wt%.

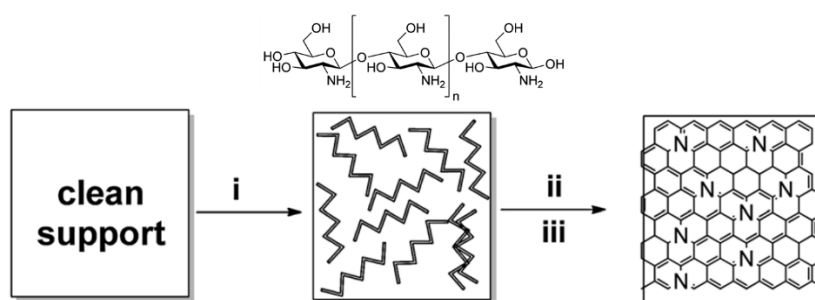


Figure 2-59: Pictorial illustration of the preparation procedure of N-doped graphene films by (i) spin coating of chitosan, followed by (ii) annealing at 200 °C for 2 h and (iii) calcination at 900 C°.³⁴⁴

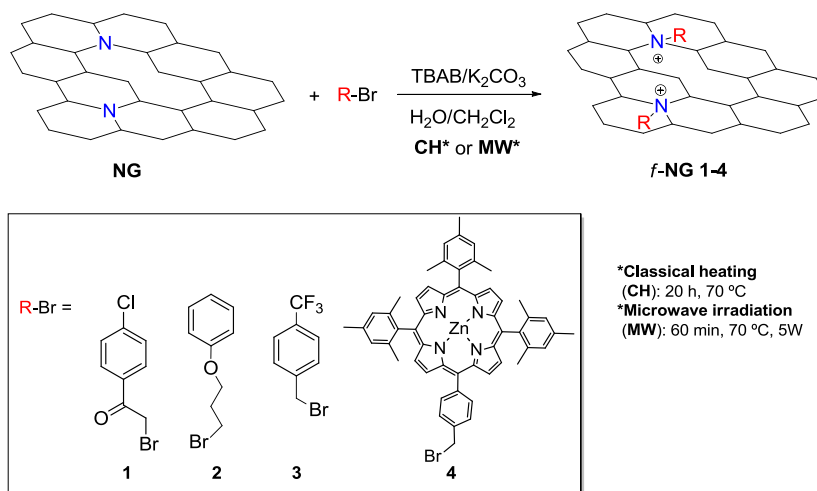
Subsequently, covalent N-functionalization of **(N)G** suspensions with different bromide derivatives (see Scheme 2-5) was performed. For this purpose, bromide derivatives **1-3** were purchased from commercial suppliers while the porphyrin-Br **4** was synthesized according to the procedure described in the literature.³⁵⁶

Initially, PTC conditions and classical heating (CH) were applied. For this purpose, N-alkylation reaction of **(N)G** was carried out at 70 °C for 20 hours in the presence of tetra-*n*-butylammonium bromide (TBAB) as phase transfer catalyst and potassium carbonate (K₂CO₃) as base, affording functionalized graphene *f*-**NG 1-4**. The resulting materials were thoroughly washed with

³⁵⁶ J. S. Lindsey, H. C. Hsu and I. C. Schreiman, *Tetrahedron Lett.*, **1986**, 24, 4969.

different solvents to remove any remaining salt and unreacted bromide derivatives.

However, hybrids *f*-NG 1-4 obtained under classical heating showed a low degree of functionalization according to TGA. For this reason, the reactions were performed under MW irradiation, reducing through this approach the reaction time from 20 hours to 60 minutes. In this case, the reactions were carried out in a CEM microwave reactor in a closed quartz tube under pressure control. Finally, as a control experiment, the N-alkylation reaction on (N)G was also performed with the bromide derivative 1 under MW irradiation, in the absence of the phase transfer catalyst (TBAB).



Scheme 2-5. Synthetic procedure for the preparation of the (N)G derivatives.

In order to provide evidence of (N)G functionalization different techniques were used, such as TGA, XPS, FTIR, Raman spectroscopy, UV-vis as well as AFM and TEM measurements provided information about the sample topography.

Characterization

TGA analysis of all the samples afforded evidence of the successful covalent functionalization of (N)G. Figure 2-60 shows the TGA thermograms of (N)G together with those of N-alkylated graphene (N)G samples. For (N)G, a gradual weight loss starting at approximately 200 °C was observed, which can be ascribed to the decomposition of labile oxygen-containing groups present in the material.

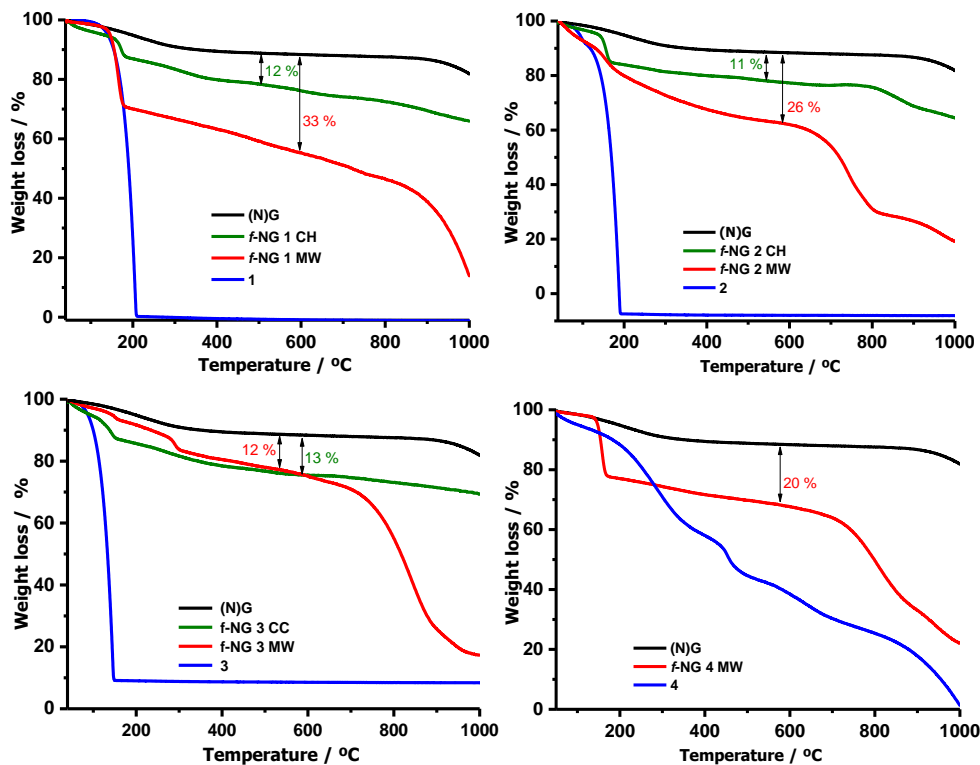


Figure 2-60. TGA curves for (N)G (black), hybrids obtained under CH (green), hybrids obtained under MW irradiation (red) and bromide derivatives (blue).

At 600 °C *f*-NG 1 obtained by classical heating (CH) showed an additional weight loss of 12%, which can be attributed to the decomposition of the addend attached to (N)G, based on the TGA profile of the *p*-chlorophenacyl bromide 1. Taking this into account, the number of groups attached to the basal plane of graphene was estimated 1 per 6.2 nitrogen or 93 carbon atoms. In the case of the thermogram obtained for the N-alkylation with the *p*-chlorophenacyl bromide 1 under MW irradiation, the additional weight loss observed for *f*-NG 1 at 600 °C was approximately 33%, which corresponds to the presence of 1 group per 2.2 nitrogen atoms or 34 carbon atoms.

TGA analysis of the hybrid obtained from the control experiment (without PTC) was also performed. As observed in Figure 2-61, the thermogravimetric profile of *f*-NG 1 control, showed a weight loss of 23%, indicating that the degree of functionalization was proportionally lower than that of *f*-NG 1 obtained in the presence of PTC (33%).

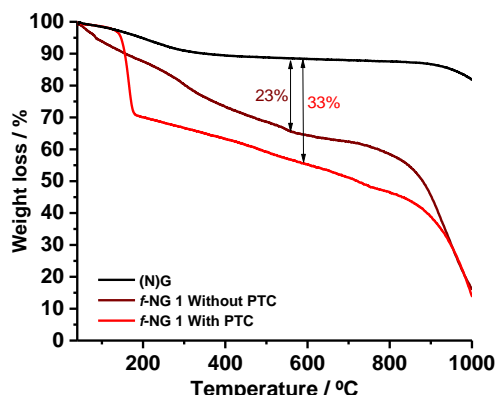


Figure 2-61. TGA curves for (N)G (black) and hybrid 1 obtained under microwave irradiation without phase transfer catalyst (brown) and with phase transfer catalyst (red).

Weight losses corresponding to the rest of (N)G hybrids 1-4 bearing different groups (Scheme 2-5) are summarized in Table 2-13.

Table 2-13. Comparative study of the degree of functionalization under classical heating (CH) and microwave (MW) irradiation.

Sample	TGA weight loss (%)		Functional group coverage ^a	
	CH	MW	CH	MW
<i>f</i> -NG 1	12.22	33.12	93	34
<i>f</i> -NG 2	11.07	26.37	90	38
<i>f</i> -NG 3	12.89	13.24	91	88
<i>f</i> -NG 4	-	20	-	295

^aNumber of carbon atoms per functional group

As deduced from the data indicated in Table 2-13, reactions performed under MW irradiation not only reduced significantly the reaction times but also gave rise to materials with higher degrees of functionalization respecting to classical heating.

The covalent anchoring of the functional groups on the (N)G surface was also established by XPS (Table 2-14).

Table 2-14. Surface atomic composition of *functionalized (N)G* samples **1-4**, prepared under MW irradiation, compared with its precursor **(N)G**.

Sample	C (%at)	O (%at)	N (%at)	X (%at)	Zn (%at)
(N)G	96.0	3.6	0.6	-	-
<i>f</i> -NG 1	93.7	4.6	0.7	1.0	-
<i>f</i> -NG 2	92.8	6.6	0.6	-	-
<i>f</i> -NG 3	93.2	4.0	0.7	2.0	-
<i>f</i> -NG 4	94.3	3.6	1.8	-	0.3

In Table 2-14 the presence of all expected atoms in *modified (N)G* materials (**1-4**) is observed, demonstrating that N-graphene derivatized as expected. These data unambiguously prove that the bromide derivatives have been attached to the surface of **(N)G** leading to the formation of *f*-NG **1-4**.

Something important to mention here is that the atomic percentage of N determined by XPS is much lower than the value determined by chemical analysis. It is important noting that elemental quantification by XPS is not completely accurate, since it only provides analysis of the surface layers (up to *ca.* 3 nm) of powders. In this sense, N atoms could not be homogeneously distributed between the surface and the bulk when **(N)G** is analyzed as dry powders.

The corresponding binding energies and the relative fractions of the components are summarized in Table 2-15.

Table 2-15. Binding energies (eV) and percentages (%) in brackets of core-levels of *f*-NG 1-4 (prepared under MW irradiation) and its precursor (N)G.

	C1s	O1s	N1s	F1s	Cl2p	Zn2p
NG	284.8 (62)		398.7 (25)			
	286.4 (27)	531.6 (35)	399.8 (54)	-	-	
	288.6 (11)	532.9 (65)	401.3 (21)			
<i>f</i> -NG 1	284.8 (64)		398.6 (26)			
	286.6 (27)	531.1 (60)	399.8 (48)	-	200.0	
	288.9 (9)	532.9 (40)	401.4 (26)			
<i>f</i> -NG 2	284.8 (65)		398.7 (34)			
	286.6 (29)	531.3 (73)	399.8 (38)	-	-	
	288.9 (6)	532.8 (27)	401.4 (28)			
<i>f</i> -NG 3	284.8 (62)		398.7 (29)			
	286.5 (30)	530.9 (27)	399.8 (41)	688.0	-	
	288.4 (8)	532.7 (73)	401.2 (30)			
<i>f</i> -NG 4	284.8 (67)		398.7 (35)			
	286.5 (26)	530.9 (19)	399.8 (40)	-	-	1021.7
	288.9 (7)	532.8 (81)	401.3 (25)			

For the (N)G substrate its C1s core-level spectrum (Table 2-15) was satisfactorily curve-resolved with three components being the most intense peak, at 284.8 eV, assigned to sp² C-atoms of the graphene structure. The component at 286.4 eV is often assigned to C-OH and C-N bonds and the components at 288.6 eV to C=O bonds.¹⁵⁶ Similarly, the O1s emission of this sample was curve-resolved with two components: the less intense component at 531.6 eV corresponds to O=C surface groups whereas the most intense one at 532.9 eV arises from O-C bonds.³¹ The high-resolution of the N1s peak was resolved into three components and the respective binding energies appeared at

398.7 eV, 399.8 eV and 401.3 eV. These are associated to pyridinic, pyrrolic and quaternary N in graphite respectively (Figure 2-62).³⁵⁷

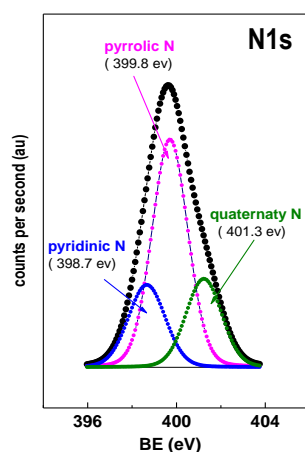


Figure 2-62. N1s core-level spectra of (N)G.

Something important to remark here was the slight increase observed in the amount of quaternary N content (see Table 2-15), which evidenced that the anchoring took place on the N atoms rather than directly on the carbon lattice.

As expected, functionalization of the N-doped surface with the bromide derivatives **1** and **3** (*f*-NG **1** and *f*-NG **3**) also led to the appearance of Cl2p and F1s emissions, respectively (Figure 2-63 (a) and (b)). The binding energies of Cl2p at 200.9 eV and of F1s at 688.1 eV are indicative of the presence of Cl-C³⁵⁸ and F-C³⁵⁹ covalent bonds respectively, which verified the anchorage of **1** and **3** functionalization agents. Finally, the XPS spectra of *f*-NG **4** sample displayed the Zn2p3/2 peak with binding energies close to that of the respective bulk porphyrin (Figure 2-63 (c)).³⁶⁰

³⁵⁷ W. J. Gammon, O. Kraft, A.C. Reilly and B.C. Holloway, *Carbon*, **2003**, *41*, 1917.

³⁵⁸ L. J. Webb and N. S. Lewis, *J. Phys. Chem. B*, **2003**, *107*, 5404.

³⁵⁹ E. P. Dillon, C. A. Crouse and A. R. Barron, *ACS Nano*, **2008**, *2*, 156.

³⁶⁰ K. H. L. Ho, L. Rivier, B. Jusselme, P. Jégou, A. Filoramo and S. Campidelli, *Chem. Commun.*, **2010**, *46*, 8731.

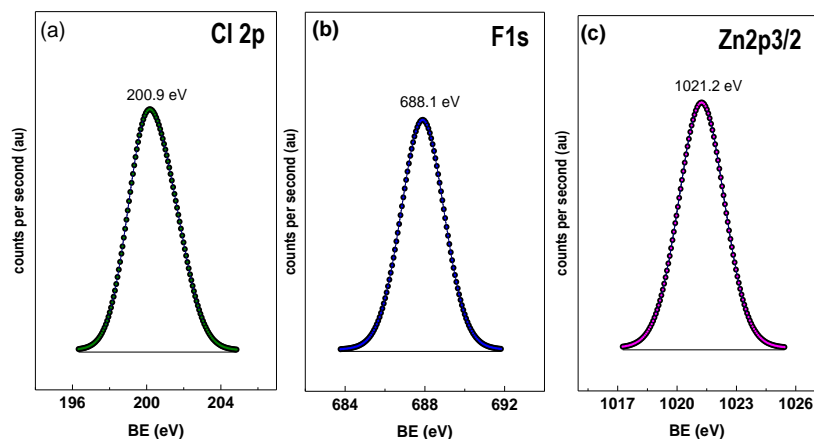


Figure 2-63. XPS high-resolution spectrum of (a) Cl 1s region of *f*-NG 1 and (b) F 1s is region of *f*-NG 3 and (c) Zn2p_{3/2} region of *f*-NG 4.

FTIR confirmed also the successful formation of the hybrids *f*-NG 1-4 (Figure 2-64). The FTIR spectrum of (N)G was almost featureless, however the FTIR spectra of the final hybrids showed peaks at approximately 1630 and 1400 cm^{-1} , characteristic of the C=O and C-N stretching vibration modes, respectively. In addition, for *f*-NG 1 a new band appeared at 699 cm^{-1} which is attributable to the C-Cl stretching mode. It is also important noting the presence of the characteristic C-N bonds from the porphyrin at 1385 cm^{-1} in the hybrid *f*-NG 4, confirming that 4 was successfully grafted onto graphene. Finally, the effective anchorage of the bromide derivatives was further confirmed by the increase of the aliphatic C-H stretching bands around 2900 cm^{-1} .

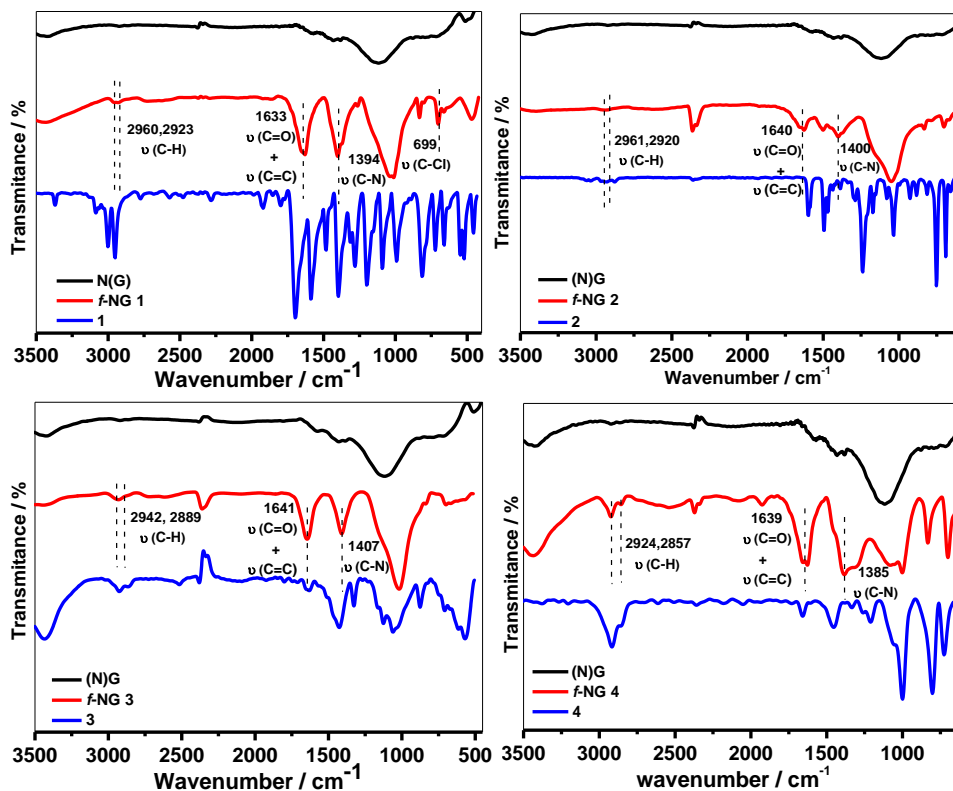


Figure 2-64. FT-IR spectra of (N)G compared to that of the final hybrids obtained under MW irradiation.

Raman spectra were not useful to prove the success of the N-functionalization due to the general distortion of the bands observed for all the hybrids (Figure 2-65). In addition, the D band in the starting material (N)G, showed already a high intensity, indicating a high density of defects within the hybrid structure. This is in concordance with the low crystallite size obtained for these samples; according to the equation [4] described in the previous section ($L_a \sim 20$ nm).³⁶¹ This high intensity of the D band could be attributed to the N content of the sample (a higher N content implies a higher number of defects, higher I_D/I_G).³⁴⁵ In this regard, previous studies have demonstrated that the

³⁶¹ Z. H. Ni, L. A. Ponomarenko, R. R. Nair, R. Yang, S. Anissimova, I. V. Grigorieva, F. Schedin, P. Blake, Z. X. Shen, E. H. Hill, K. S. Novoselov and A. K. Geim, *Nano Lett.*, **2010**, *10*, 3868.

Raman bands get broader and the 2D band disappear when increasing the doping concentration.³⁶²

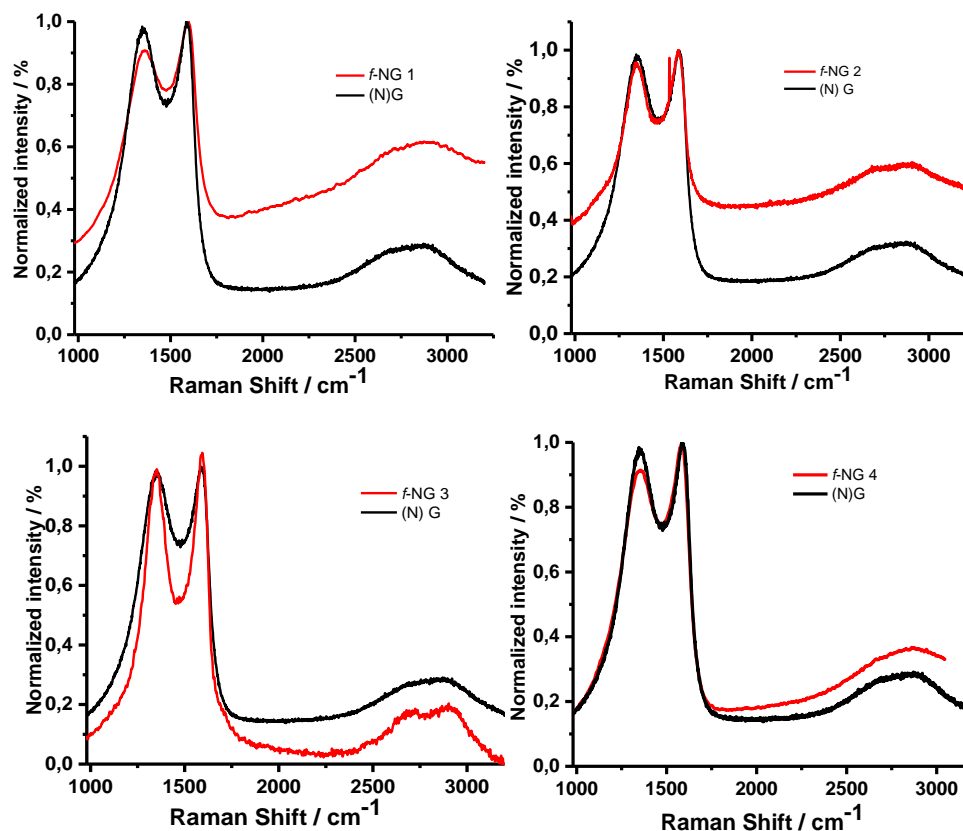


Figure 2-65. Raman spectra of (N)G compared to that of the final hybrids obtained under MW irradiation.

In addition, no differences were observed between the Raman spectra of the starting (N)G and those corresponding to the functionalized hybrids, indicating that N-functionalization did not have any influence in the density of defects of the graphene sheet.

The ^1H NMR spectrum of *f*-NG 1 recorded in CDCl_3 is presented in Figure 2-66. As observed, it was possible to record the signals corresponding to

³⁶² C. Chang, S. Kataria, C. Kuo, A. Ganguly, B. Wang, J. Hwang, K. Huang, W. Yang, S. Wang, C. Chuang, C. Huang, W. Pong, K. Song, S. Chang, J. Guo, Y. Tai, M. Tsujimoto, S. Isoda, C. Chen, L. Chen and K-H Chen, *ACS Nano*, **2013**, *7*, 1333.

the *p*-chlorophenacyl units in the aromatic region as well as the singlet of the methylene group appearing at 5.30 ppm. This chemical shift was different from that of the *p*-chlorophenacyl bromide used as reagent (4.42 ppm) and was about 1.3 ppm upfield with respect to the value reported for N-(*p*-chlorophenacyl)pyridinium, a structurally close analog of the subunits present in *f*-NG **1**, which is 6.66 ppm. This strong upfield shift would be compatible with the influence that the anisotropy of the π -cloud of graphene exerts on this CH₂ group.

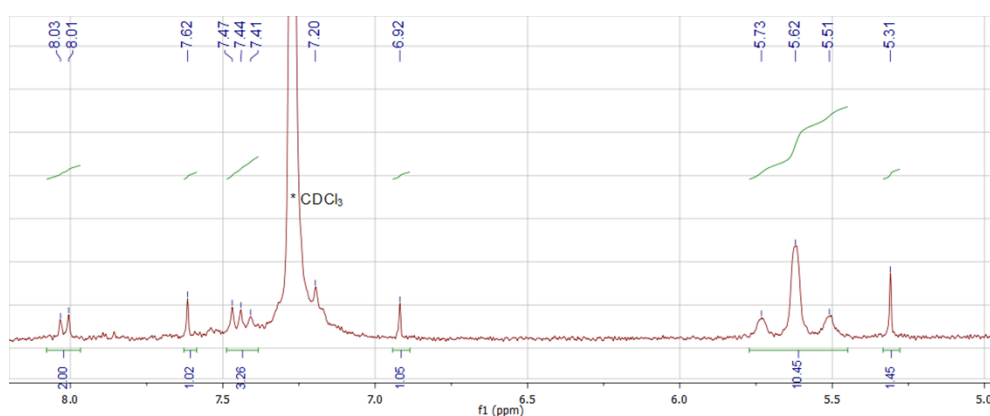


Figure 2-66. Expansion of the ¹H-NMR spectrum recorded for *f*-NG **1** in CDCl₃.

The UV-vis absorption spectra for (N)G showed the dominant absorbance peak around 200 nm, which was ascribed to π - π^* transition of the aromatic C–C bonds, and a shoulder at 280 nm, associated with n- π^* transition of C=O bonds (Figure 2-67).³⁶³ For *f*-NG **1**, a new peak was observed at around 230 nm which could be attributed to the anchored addend, since its absorption spectrum shows a sharp peak at around this wavelength. For *f*-NG **2** and *f*-NG **3** no helpful information was obtained from the UV-vis spectra, since the peaks corresponding to the addends fell just with the dominant absorbance peak from (N)G.

³⁶³ T. V. Cuong, V. H. Pham, Q. T. Tran, S. H. Hahn, J. S. Chung, E. W. Shin and E. J. Kim, *Mater. Lett.*, **2010**, *64*, 399.

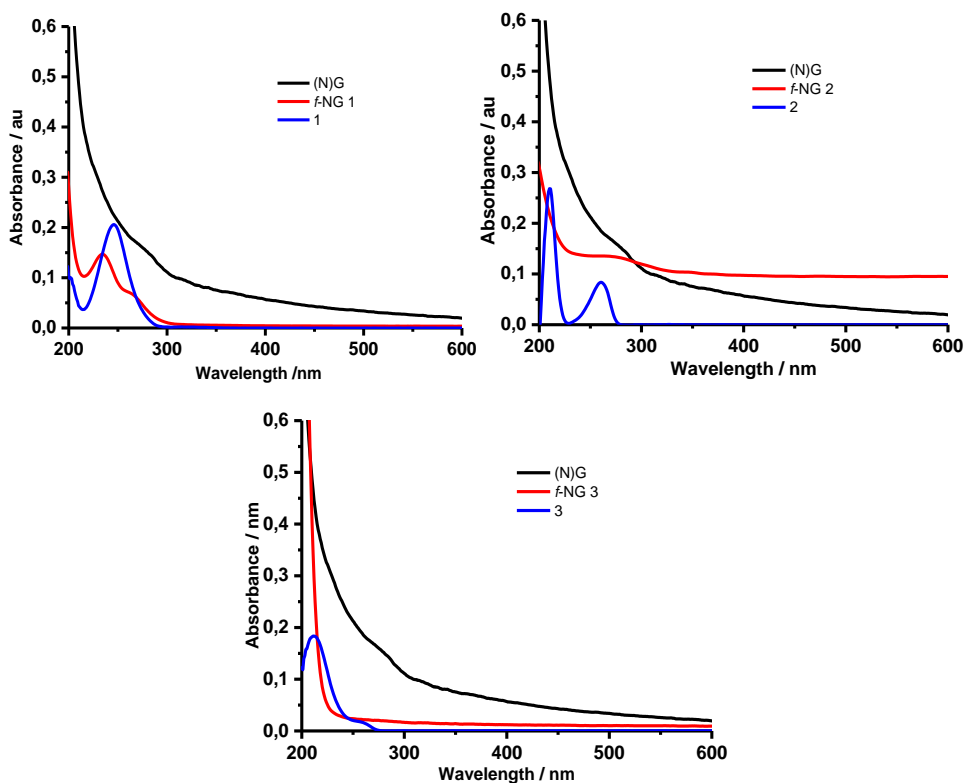


Figure 2-67. UV-visible absorption spectra (recorded in water) of the starting (N)G compared to the final hybrids *f*-NG 1-3.

However, for *f*-NG 4 (Figure 2-68 (a)), the UV-vis spectrum showed a new absorption peak at 428 nm, which is attributable to the π - π^* transition of the porphyrin unit. As observed, this peak was bathochromically shifted by 4 nm with respect to the bromide derivative 4, which suggested the existence of electronic interactions between porphyrins and the basal plane of (N)G.

In order to prove the excited-state interactions between the porphyrin and graphene, fluorescence spectra of the hybrid *f*-NG 4 and its precursor 4 were compared (Figure 2-68 (b)). Both solutions were prepared in THF optically matched at the selected excitation wavelength and their emission spectra were acquired. Upon excitation of 4 at the Soret band (426 nm), a fluorescence emission was observed at 494 nm. A weaker fluorescence emission was observed when the hybrid *f*-NG 4 was excited at the same wavelength. The calculated quenching efficiency was around 40%, suggesting the existence of photoinduced electron transfer from the porphyrin 4 to (N)G.

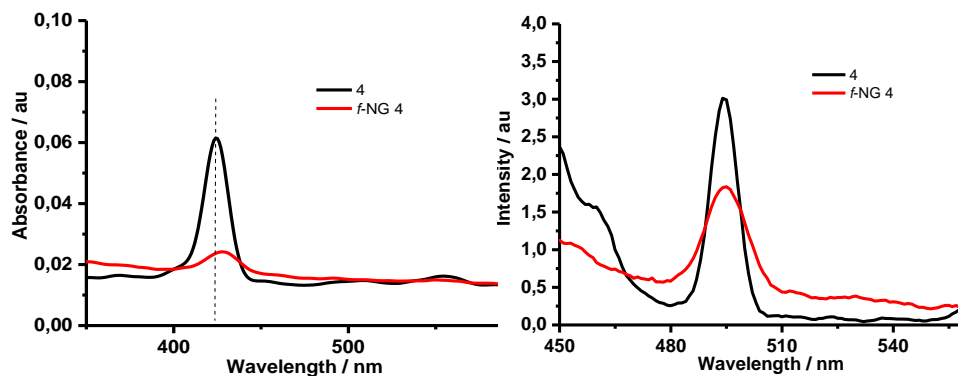


Figure 2-68. (a) UV-visible absorption spectrum of *f*-NG 4 and 4 and (b) fluorescence emission spectrum of *f*-NG 4 and 4 upon excitation at 426 nm in THF.

Additional information about the structural features of the samples was obtained from AFM images. Figure 2-69 shows two AFM topography images corresponding to (N)G and *f*-NG 4. The AFM images revealed the presence of large graphene sheets with sizes ranging between 200 and 600 μm and few layer graphene flakes with an average height of *ca.* 1.5 nm, which correspond to approximately four layer thick structures.³⁶⁴ In addition, it might be possible that the thickness of (N)G could be somewhat larger than that of pristine graphene sheets. Anyway, this thickness clearly evidenced the strongly exfoliated character of the sample. Further, the isolated layers showed polygonal shapes which are very characteristic in graphene samples. It is worth mentioning that when comparing the images from the starting (N)G (top panel) and *f*-NG 4 (bottom panel), the last showed brightened zones whose height fits quite well with the distance calculated through semiempirical methods for the porphyrin unit (~ 1.5 nm). This observation suggest as well the presence of the porphyrin attached to the basal plane of graphene.

³⁶⁴ Y. K. Koh, M-H Bae, D. G. Cahill and E. Pop, *ACS Nano*, **2011**, 5, 269.

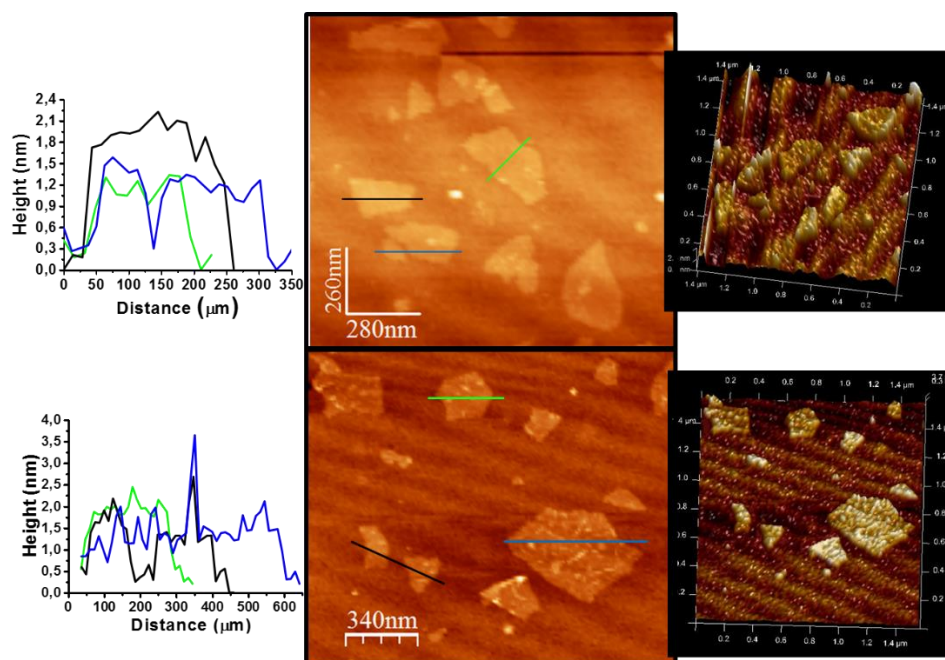


Figure 2-69. AFM image of **(N)G** on SiO₂-coated Si wafers and 3D image on the right side (top panel). AFM image of *f*-**NG 4** and 3D image on the right side (bottom panel).

TEM was performed in order to obtain detailed views of the morphology as well and analyze the possible crystal structure. TEM images obtained for **(N)G** and *f*-**NG 4** are shown in Figure 2-70. **(N)G** exhibited wrinkled paper-like morphology (Figure 2-70 (a)). Magnified images revealed the presence of few-layers thick graphene with a detailed crystalline structure (Figure 2-70 (b)). The selected area electron diffraction (SAED) pattern given in Figure 2-70 (c) further supported the high crystallinity of **(N)G**, showing a symmetric hexagonal diffraction pattern, which is ascribed to a typical diffraction pattern of graphite.^{365,366} As observed for *f*-**NG 4**, chemical modification induced morphological changes on the surface (Figure 2-70 (d) and 2-70 (e)), and the crystalline structure was disrupted after functionalization with the porphyrin unit **4** (Figure 2-70 (e)). This decrease of the crystallinity was further confirmed

³⁶⁵ A. Reina, X. Jia, J. Ho, D. Nezich, H. Son, V. Bulovic, M. S. Dresselhaus and J. Kong, *Nano Lett.*, **2009**, *9*, 30.

³⁶⁶ C. T. Pan, J. A. Hinks, Q. M. Ramasse, G. Greaves, U. Bangert, S. E. Donnelly and S. J. Haigh, *Sci. Rep.*, **2014**, *4*, 6334.

by the SAED pattern (Figure 2-70 (f)) that showed ring-like diffraction spots, probably due to structure distortion caused by intercalation of porphyrin into its graphitic planes.³⁶⁷

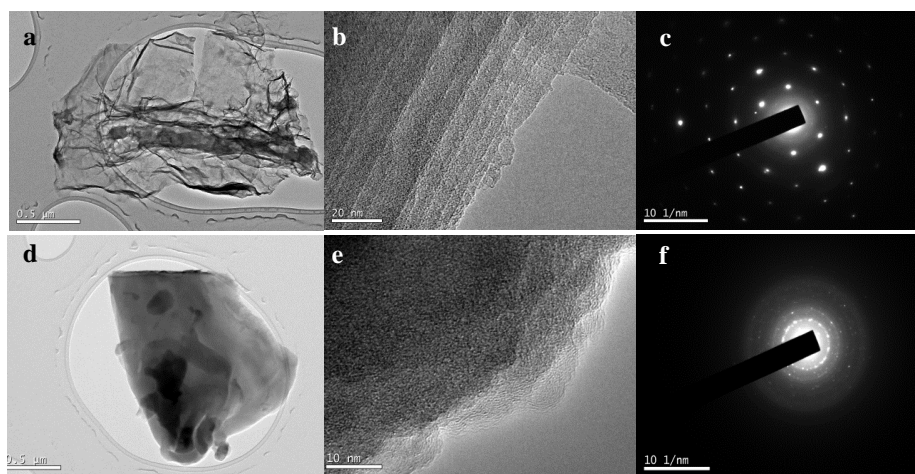


Figure 2-70. (a,b)TEM images of (N)G at different magnifications and (c) corresponding SAED pattern and (d, e) TEM images of *f*-NG 4 at different magnifications and (f) corresponding SAED pattern.

Finally, assuming the materials to be semiconductors, a plot of the Kubelka-Munk function³⁶⁸ vs. $h\nu$ afforded the band gap energies. The optical band gaps of the new hybrids were determined using the Tauc plot³⁶⁹ of the modified Kubelka-Munk function with a linear extrapolation (Figure 2-71). By extracting the corresponding onset energies from the spectra, the effective band gap energies of (N)G modified with different addends were found to be 4.12 eV for (N)G, and 3.35 eV, 3.50 eV, 3.20 eV and 3.79 eV for *f*-NG 1-4 respectively (see Table 2-16). The variation of the band gap after N-functionalization in these materials could be attributed to the disruption of graphene sublattices and the changes in the electronic density at the N atoms. From these results we can confirm that the higher decrease in the band gap was observed for the group containing electron-withdrawing CF₃ substituents (*f*-NG 3; Eg= 3.20), while the

³⁶⁷ Y-F. Lu, S-T. Lo, J-C. Lin, W. Zhang, J-Y. Lu, F-H. Liu, C-M. Tseng, Y-H. Lee, C-T. Liang and L-J. Li, *ACS Nano*, **2013**, 7, 6522.

³⁶⁸ Diffuse reflectance- Theory and applications, **2011**, Pike Technologies, <http://www.piketech.com/files/pdfs/DiffuseAN611.pdf>

³⁶⁹ J. Tauc, R. Grigorovici, A. Vancu, *Phys. Status Solidi*, **1966**, 15, 627.

lower decrease was observed for the most electron donating addend, that is, the Zn-porphyrin (*f*-NG 4; $E_g=3.79$ eV).

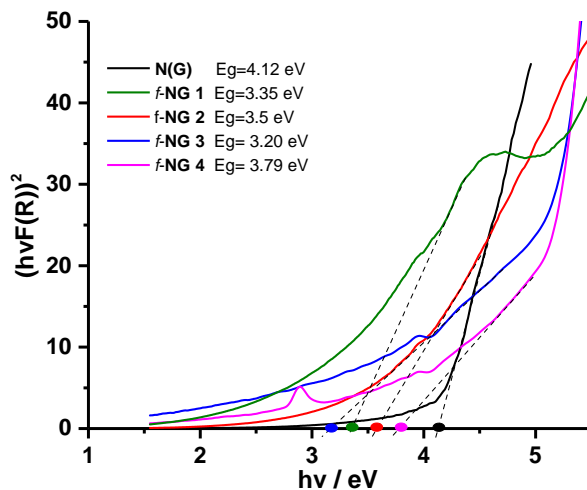
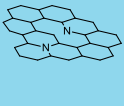
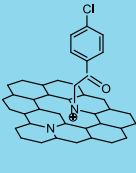
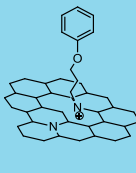
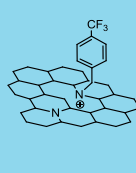
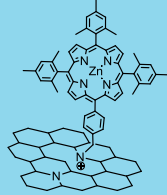


Figure 2-71. Tauc plots to determine the optical band gap of (N)G compared to that of *f*-NG 1-4.

Table 2-16. Optical band gaps obtained for EG and *f*-NG 1-4.

Sample					
	(N)G	<i>f</i> -NG 1	<i>f</i> -NG 2	<i>f</i> -NG 3	<i>f</i> -NG 4
Optical band gap (eV)	4.12	3.35	3.50	3.20	3.79

From the previous results we can remark that the electronic properties of graphene are affected by the attachment of functional groups onto its surface. Since band gap engineering is one of the high priority goals in the development

of graphene electronics, the experimental influence of optical band gap as a function of the substituent on the N atoms appears as a new method to tune the electronic properties of graphenic materials for future applications.

2.4 Conclusions

Based on the previous findings, the following conclusions can be drawn:

In the first part of the chapter a new nanoconjugate which combines two nanoforms of carbon (**GO** and **C₆₀**) is synthesized through CuAAC chemistry. The successful formation of the mentioned nano hybrid was proven by XPS, FTIR and Raman spectroscopies as well as TGA, AFM and HRTEM. Electronic communication between both nanoforms was confirmed by electrochemical studies, which showed an anodic shift of 70 mV. Finally, laser flash photolysis experiments evidenced the existence of photoinduced electron-transfer.

In the second part of the chapter, a comparative study of the cycloaddition of different nitrile imines to graphene is performed. Comparison with an analogous azomethine ylide is also accomplished. Firstly, DFT calculations confirmed the viability of the reaction being the most favorable approach, both kinetically and thermodynamically, the attack on the edges of the sheet. Secondly, experimental studies were carried out and the success of the cycloaddition reaction was confirmed by TGA, Raman spectroscopy, XPS, FTIR, AFM and HRTEM.

Finally, UPS measurements demonstrated that tuning of the work function (WF) of graphene can be achieved by chemical functionalization. The presence of electron-withdrawing substituents exerted a higher influence on the resulting WF. In addition, it was demonstrated that the functionalization degree also affects the electronic properties of the material, showing a lower value of WF those hybrids with higher functional group coverage.

In the third part of this chapter, the *N*-functionalization of *N*-doped graphene with different organic addends was performed. The best results in terms of yields and reaction times were obtained under PTC conditions in combination with microwave irradiation. The successful formation of the final hybrids was confirmed by TGA, XPS, FTIR, Raman spectroscopy, AFM and HRTEM.

Finally, to gain insight into the electronic behavior of the functionalized (**N**)**G** hybrids, the optical band gaps were determined from the optical absorption spectra. For this purpose, the Kubelka Munk function and Tauc plots were employed. The results revealed a change in the optical band gap which depended on the alkylation agent employed.

2.5 Experimental section

- **Materials**

Organic solvents used in this work were purchased from commercial suppliers and use as received.

Graphene Oxide (GO) was purchased from Nanoinnova Technologies (www.nanoinnova.com) Batch: GO.Z.10-1.

Exfoliated graphene (EG) was obtained from TIMCAL graphite (TIMREX KS15, $\rho = 2.255$ g/cc, particle size = 8.0 μm , specific surface = 12 m^2/g , ashes $\leq 0.100\%$, interlamellar distance = 0.3354-0.3359 nm).

The concentration was estimated from the absorbance at 660 nm by using the extinction coefficient of graphene ($\alpha = 3620$ $\text{mL mg}^{-1} \text{m}^{-1}$) previously determined by Coleman.³⁷⁰ According to the Lambert-Beer law the graphene concentrations were calculated as follows:

$$A(660\text{nm}) = \alpha \cdot C_G \cdot l$$

where A is graphene's absorbance at 660 nm, α is the absorption coefficient, l is the cell length and C_G the graphene concentration.

N-doped graphene (N)G was obtained by pyrolysis of chitosan beads at 900 °C for 6 h under an inert atmosphere. Sample sonication was carried out by using an Elmasonic P 300 H sonicator bath (37 KHz) without prior treatment.

Instrumentation

FTIR spectra were measured using a Fourier Transform IR spectrometer (Avatar 370), in KBr pellets. The spectral range was 4000-400 cm^{-1} .

Raman spectra were acquired on a Renishaw inVia Raman microscope at room temperature, using 532 nm excitation source. The laser power at the sample was 10 mW and the exposure time for sample measurement was 10 seconds at varying numbers of accumulations. The laser spot was focused on the sample surface using a long working distance 50 \times objective. Raman spectra were collected on numerous spots on the sample and recorded with a Peltier cooled CCD camera. The intensity ratio I_D/I_G was obtained by taking the peak intensities following any baseline corrections. The data were collected and analyzed with Renishaw Wire and Origin software.

³⁷⁰ J. N. Coleman, *Acc. Chem. Res.*, **2013**, *46*, 14.

TGA was performed using a TGA/DSC Linea Excellent instrument by Mettler-Toledo, collected under inert atmosphere of nitrogen. The sample (~ 0.5 mg) was introduced inside a platinum crucible and equilibrated at 40 °C followed by a 10 °C min⁻¹ ramp between 40 and 1000 °C. The weight changes were recorded as a function of temperature.

UV-vis spectra in the visible region were measured by using a Shimadzu UV 3600 spectrometer in quartz cuvettes with a path length of 1 cm.

Fluorescence experiments were recorded on a Cary Eclipse fluorescence spectrofluorometer.

XPS were acquired with a Escalab 200R (Vacuum Generators, Ltd., UK) spectrometer provided with a hemispherical electron analyser and a MgK α (h ν = 1254.6 eV) X-ray source. The spectra were acquired in the constant analyser energy mode at 200 eV pass energy for survey spectra and between 20-50 eV pass energy. High resolution spectra envelopes were obtained by curve fitting synthetic peak components using the software “XPS peak”. The raw data were used with no preliminary smoothing. Symmetric Gaussian-Lorentzian (90%G-10%L) lines were used to approximate the line shapes of the fitting components. Atomic ratios were computed from experimental intensity ratios and normalized by atomic sensitivity factors.

AFM images for **GO-C₆₀** (first part of the chapter) were acquired in dynamic mode using a Nanotec Electronic system. Olympus cantilevers were used with a nominal force constant of 0.75 Nm⁻¹ and a resonance frequency of 70 kHz. The images were processed using WSxM (freely downloadable scanning probe microscopy software from (www.nanotec.es) operating at room temperature in ambient air conditions.

AFM images for **pyrazolino graphene based materials** and **(N)G derivatives** (second and third part of the chapter) were acquired in tapping mode using a Multimode V8.10 (Veeco Instruments Inc., Santa Barbara, USA) with a NanoScope V controller (Digital Instruments, Santa Barbara, USA). The cantilevers (RTESP from Bruker Probes) were silicon cantilevers with a resonance frequency of 300 kHz and a nominal force constant of 40 Nm⁻¹. The functionalized samples (1 mg mL⁻¹) were sonicated (frequency: 37 kHz; power 380 W) in milli-Q water for 90 minutes, then samples were prepared by dropcast method on SiO₂ surfaces. The images were processed using WSxM (freely

downloadable scanning probe microscopy software from www.nanotec.es) operating at room temperature in ambient air conditions.

HRTEM images for GO-C₆₀ (first part of the chapter) were carried out on a JEM-2010 microscope (JEOL, Japan) operating at 200 kV. Samples were prepared by drop casting a sonicated suspension of the sample in ethanol on a carbon-coated copper grid. The digital analysis of the HRTEM micrographs was done using DigitalMicrograph™ 1.80.70 by Gatan.

HRTEM images for pyrazolino graphene based materials (second part of the chapter) were performed using a CM300 UltraTWIN (Philips, Netherlands), equipped with a LaB6 filament and a nominal point resolution of 1.7 Å at the Scherzer defocus. The microscope was operated at an acceleration voltage of 300 kV. TEM images were recorded with a charged coupled device camera (TVIPS, Germany), which has an image size of 2048 × 2048 pixels. TEM samples were prepared by drop casting a sonicated suspension of the sample in ethanol/DMF onto Cu grids coated with a holey carbon film layer. The free available software ImageJ (version 1.48r) was used for image analysis.

HRTEM images for (N)G derivatives (last part of the chapter) were performed on a JEOL 2100 microscope operating at 200 kV. The N-graphene samples were dispersed in acetone and sonicated for 15 minutes. The resulting suspension was dropped onto a holey carbon copper grid, and the solvent was allowed to evaporate.

Electrochemical characterization was performed using a three electrode standard configuration with a platinum wire as counter electrode and Ag/AgCl sat. as reference electrode in a 0.05 M TBABF₄ (tetra-*n*-butylammonium tetrafluoroborate) as electrolyte. A FTO conducting glass substrate coated by a thin film of C₆₀, **1** or GO-C₆₀ in CH₂Cl₂ deposited by drop casting was used as a working electrode. The solution was purged with N₂ for at least 30 min before measurements. Scan rate of 50 mV/s. These electrodes were connected to an AMEL 7050 potentiostat that allows scanning the voltage while measuring the current.

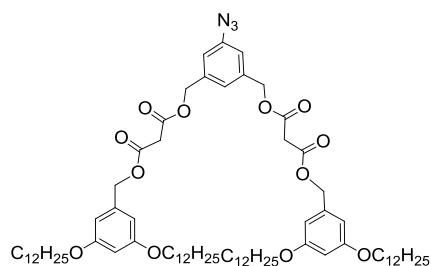
Laser flash photolysis experiments were carried out using the third (355 nm) harmonic of a Q-switched Nd:YAG laser (Spectron Laser Systems, UK; pulse width *ca.* 9 ns and 35 mJ pulse⁻¹). The signal from the monochromator/photomultiplier detection system was captured by a Tektronix

TDS640A digitizer and transferred to a PC that controlled the experiment and provided suitable processing and data storage capabilities.

Ultraviolet photoelectron spectroscopy (UPS) studies were performed in a Thermo Scientific Multilab 2000 spectrometer fitted with a He(I) and He(II) UV source with a photon flux $>1.5 \times 10^{12} \text{ s}^{-1}$ and a 110 mm mean radius hemispherical sector analyzer. The binding energy scale was corrected through the Fermi level of a gold foil in thermal and electrical contact with the sample surfaces.

2.4.1 Synthesis of organic compounds

Precursor bis-malonate¹⁴⁶

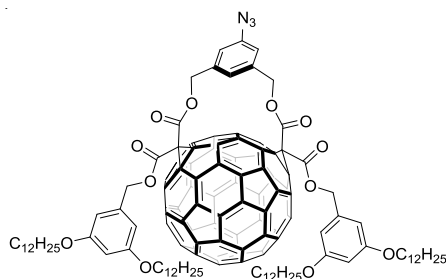


N,N'-dicyclohexylcarbodiimide (DCC) (3.02 g, 14.8 mmol) was added to a solution of [3,5-bis(dodecyloxy)phenyl]methyl hydrogen propanedioate (7.84 g, 14.8 mmol), 5-azido-1,3-resorcinol (1.00 g, 5.90 mmol), hydroxybenzotriazol (HOBT) (160 mg, 1.18 mmol) and dimethylaminopyridine (DMAP) (290 mg, 2.36 mmol) in CH_2Cl_2 (250 mL) at 0°C . After 1 hour, the mixture was allowed to warm slowly to room temperature and was then stirred for 3 days at this temperature. The resulting mixture was filtered and evaporated. Column chromatography (SiO_2 , CH_2Cl_2 /cyclohexane 8:2) gave the desired product (5.80 g, 81%) as a yellow oil that was used in the next step without further purification.

$^1\text{H NMR}$ (CDCl_3 , 300 MHz, δ / ppm): 7.06 (s, 1H), 6.95 (s, 2H), 6.46 (d, $J = 2$ Hz, 4H), 6.39 (t, $J = 2$ Hz, 2H), 5.14 (s, 4H), 5.09 (s, 4H), 3.91 (t, $J = 7$ Hz, 8H), 3.94 (s, 4H), 1.79-1.71 (m, 8H), 1.45-1.38 (m, 8H), 1.35-1.27 (m, 64H), 0.88 (t, $J = 7$ Hz, 12H).

$^{13}\text{C NMR}$ (CDCl_3 , 75 MHz, δ / ppm): 166.08, 166.06, 160.5, 140.9, 137.7, 137.1, 123.7, 118.3, 106.5, 101.2, 68.1, 67.3, 66.2, 41.4, 31.9, 29.68, 29.65, 29.62, 29.60, 29.42, 29.36, 29.27, 26.1, 22.7, 14.1.

Fullerene building block 1¹⁴⁶



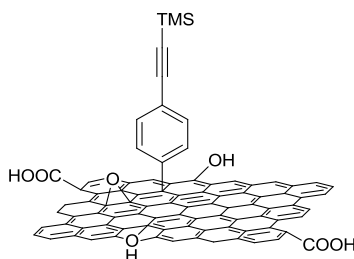
1,8-diazabicyclo[5.4.0]undec-7-ene (DBU) (0.54 mL, 3.62 mmol) was added to a stirred solution of C₆₀ (570 mg, 0.79 mmol), I₂ (500 mg, 1.97 mmol) and the bis-malonate derivative described above (1.00 g, 0.79 mmol) in toluene (570 mL) at room temperature. The resulting solution was stirred for 12 hours under Argon, then filtered through a short plug of SiO₂ (CH₂Cl₂) and evaporated. Column chromatography (SiO₂, hexane/ CH₂Cl₂ 1:1) gave **1** (652 mg, 42%) as a brown glassy product.

¹H NMR (CDCl₃, 300 MHz, δ / ppm): 7.31 (s, 1H), 6.93 (s, 2H), 6.50 (d, J = 2 Hz, 4H), 6.39 (t, J = 2 Hz, 2H), 5.78 (d, J = 13 Hz, 2H), 5.36 (d, J = 12 Hz, 2H), 5.26 (d, J = 12 Hz, 2H), 5.04 (d, J = 13 Hz, 2H), 3.88 (t, J = 7 Hz, 8H), 1.79-1.70 (m, 8H), 1.45-1.38 (t, 8H), 1.35-1.29 (m, 64H), 0.91 (t, J = 7 Hz, 12H).

¹³C NMR (CDCl₃, 75 MHz, δ / ppm): 162.6, 162.5, 160.5, 148.6, 147.52, 147.49, 147.37, 146.1, 145.78, 145.76, 145.71, 145.6, 145.4, 145.2, 145.0, 144.9, 144.7, 144.3, 144.2, 144.0, 143.8, 143.6, 143.2, 142.7, 142.3, 141.2, 141.1, 140.6, 140.0, 138.8, 137.9, 136.6, 136.2, 135.9, 134.3, 119.6, 116.9, 107.2, 101.6, 70.6, 68.7, 68.2, 66.9, 66.8, 48.9, 31.9, 29.73, 29.69, 29.67, 29.5, 29.4, 29.3, 26.1, 22.3, 14.2.

2.4.2 Synthesis of nanoconjugates

Preparation of GO-TMS



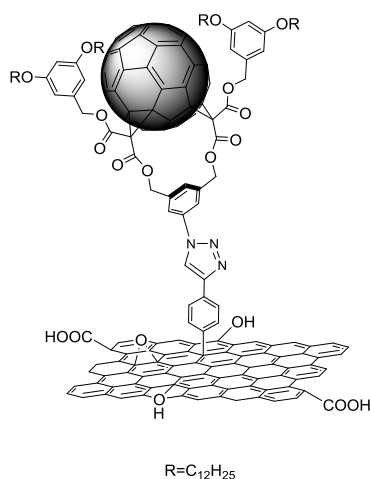
A suspension of graphene oxide (**GO**) (30 mg) and 4-(trimethylsilyl)ethynylaniline (2 equiv, 5 mmol) in NMP (80 mL) was first sonicated for 30 minutes and then isoamyl nitrite (2.4 equiv, 6 mmol) was added. The reaction mixture was stirred at 70 °C for 48 h under Ar. After cooling to room temperature, the suspension was filtered on a PTFE membrane (Millipore, 0.1 μ m pore) and the black solid was washed several times with DMF and then with CH₂Cl₂ to give the desired product **GO-TMS** as a black solid.

IR (KBr) ν , cm⁻¹: 2925, 2852 (C-H stretching mode), 1722 (C=O stretching mode), 1620 (C-H in plane stretching mode) and 2144 (C \equiv C stretching mode).

Raman: $I_D/I_G = 0.86$.

XPS (% atomic): C = 67.3, O = 32.3, Si = 0.4

Preparation of GO-C₆₀



To a suspension of **GO-TMS** (20 mg) in NMP (50 mL) at 0 °C a solution of tetra-*n*-butylammonium fluoride (TBAF, 1M in THF) (5 mL) was added. The reaction mixture was stirred at room temperature for 2 h under Ar and then filtered on a PTFE membrane (Millipore, 0.1 μm pore). The deprotected modified **GO-CCH** was then washed several times with DMF and then, with CH₂Cl₂, suspended in NMP (50 mL) and used directly for the next step; a suspension of **GO-CCH** (20 mg) in NMP (100 mL) was sonicated for 5 min and then were added, **1** in THF (24 mg, 14.88 μmol), CuSO₄ · 5H₂O (4 mg, 15.5 μmol) and sodium ascorbate (29.5 mg, 148.8 μmol). The reaction mixture was stirred at 70 °C for 48 hours under Ar and then filtered on a PTFE membrane (Millipore, 0.1 μm pore). In order to remove the catalyst and unreacted **1**, the black solid was sonicated and washed with a DMF/water mixture (v/v: 1/4) then a DMF/THF mixture (v/v: 1/4). These operations were repeated two times and the modified graphene oxide was finally washed with THF and CH₂Cl₂ to afford **GO-C₆₀** as a black solid.

IR (KBr) ν , cm⁻¹: 2925, 2852 (C-H stretching mode), 1732 (C=O stretching mode), 1629 (C-H in plane stretching mode).

XPS (% atomic): C = 76, O = 23.6, N = 1.4

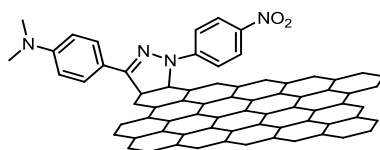
General procedure for the synthesis of graphene-pyrazolines under classical heating.

Pyridine (0.5 mL) was added to a solution of the appropriate hydrazone (0.10 mmol) in dry CH₃Cl (15 mL) under argon and the mixture was cooled to 0°C. NCS (0.42 mmol, 56 mg) was then added and the mixture was stirred for 30 min. Thereafter, CH₃Cl was evaporated under vacuum and then a solution of exfoliated graphene (EG) in NMP (80 mL) and Et₃N (2 mL) were added and the resulting solution was heated at 170 °C under argon for 6 days. The crude product was separated by centrifugation, decanted, and then washed several times with methanol and CH₂Cl₂.

General procedure for the synthesis of graphene-pyrazolines under microwave irradiation.

Pyridine (0.5 mL) was added to a solution of the appropriate hydrazone (0.10 mmol) in dry CH₃Cl (15 mL) under argon and the mixture was cooled to 0°C. NCS (0.42 mmol, 56 mg) was then added and the mixture was stirred for 30 min. Thereafter, CH₃Cl was evaporated under vacuum and then a solution of exfoliated graphene (EG) in NMP (80 mL) and Et₃N (2 mL) were added and the mixture was subjected to microwave irradiation (40 W, 170 °C, 60 min). The crude product was separated by centrifugation, decanted, and then washed several times with methanol and CH₂Cl₂.

1'-(4-nitrophenyl)-3'-(4-dimethylamino)phenyl-pyrazolino[4',5'] graphene (*f*-graphene 3a)



According to the general procedure, pyridine (0.5 mL), 3'-(4-dimethylamino)phenyl-1'-(4-nitrophenyl) hydrazone (28 mg, 0.10 mmol), NCS (56 mg, 0.42 mmol), exfoliated graphene in NMP (80 mL) and Et₃N (2 mL) gave the desired product.

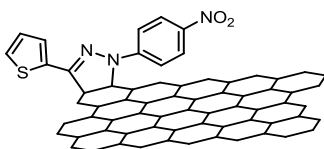
IR (KBr) ν , cm⁻¹: 2936, 2866 (C-H stretching mode), 1593 (C-H in plane stretching mode), 1452 (C=N stretching mode).

TGA: Weight loss and temperature of desorption: 8.1%, 550 °C.

Raman: I_D/I_G = CH: 0.22; MW: 0.18

XPS (% atomic): CH: C= 95.5, O= 4.1, N= 0.4; MW: C = 95.6, O = 3.9, N = 0.5.

1'-(4-nitrophenyl)-3'-thienyl-pyrazolino[4',5']graphene (f-graphene 3b)



According to the general procedure, pyridine (0.5 mL), 3'-thiophene-1'-(4-nitrophenyl)hydrazide (25 mg, 0.10 mmol), NCS (56 mg, 0.42 mmol), exfoliated graphene in NMP (80 mL) and Et₃N (2 mL) gave the desired product.

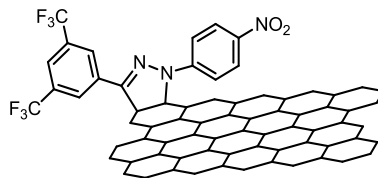
IR (KBr) ν , cm⁻¹: 2945, 2853 (C-H stretching mode), 1583 (C-H in plane stretching mode), 1447 (C=N stretching mode), 690 (C-S stretching mode).

TGA: Weight loss and temperature of desorption: 8.5%, 550 °C.

Raman: I_D/I_G = CH: 0.17; MW: 0.24

XPS (% atomic): CH: C=95.4, O= 4.2, N= 0.3, S=0.1; MW: C = 96.1, O = 3.5, N = 0.3, S = 0.1.

1'-(4-nitrophenyl)-3'-(3,5-bis(trifluoromethyl)phenyl)-pyrazolino [4',5']graphene (f-graphene 3c)



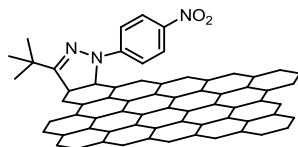
According to the general procedure, pyridine (0.5 mL), 3'-(3,5-bis(trifluoromethyl)phenyl)-1'-(4-nitrophenyl)hydrazide (37 mg, 0.10 mmol), NCS (56 mg, 0.42 mmol), exfoliated graphene in NMP (80 mL) and Et₃N (2 mL) gave the desired product.

IR (KBr) ν , cm⁻¹: 2926, 2858 (C-H stretching mode), 1568 (C-H in plane stretching mode), 1465 (C=N stretching mode), 1390 (C-F stretching mode).

TGA: Weight loss and temperature of desorption: 5.5%, 550 °C.

Raman: I_D/I_G = CH: 0.15; MW: 0.21.

XPS (% atomic): CH: C= 95.4, O=4.0, N= 0.2, F= 0.4; MW: C = 95.5, O = 3.6, N = 0.3, F = 0.6.

1'-(4-nitrophenyl)-3'-tert-butyl-pyrazolino[4',5']graphene (*f*-graphene 3d)

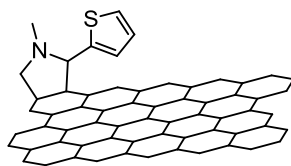
According to the general procedure, pyridine (0.5 mL), 3'-tert-butyl-1'-(4-nitrophenyl)hydrazone (22 mg, 0.10 mmol), NCS (56 mg, 0.42 mmol), exfoliated graphene in NMP (80 mL) and Et₃N (2 mL) gave the desired product.

IR (KBr) ν , cm⁻¹: 2918, 2863 (C-H stretching mode), 1567 (C-H in plane stretching mode), 1460 (C=N stretching mode).

TGA: Weight loss and temperature of desorption: 17%, 550 °C.

Raman: I_D/I_G = CH: 0.32; MW: 0.20

XPS (% atomic): CH: C = 96.2, O = 3.1, N = 0.7; MW: C = 95.8, O = 3.8, N = 0.4.

N-methyl-2'-thienylpyrrolidino[4',5']graphene (*f*-graphene pyr)

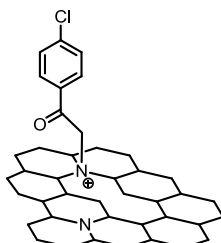
70 mL of the graphene dispersion in NMP (7.13 mg) together with sarcosine (48 mg, 0.54 mmol) and 2-thiophenecarboxaldehyde (60 mg, 0.54 mmol) were irradiated for 1 h at 40 W and 170 °C. The mixture was then brought to room temperature. Separation by centrifugation and washing with MeOH and CH₂Cl₂ afforded the desired product.

TGA: Weight loss and temperature of desorption: 39%, 550 °C.

Raman: I_D/I_G = 0.16

General procedure for the N-alkylation of (N)G under classical heating (CH)

To a suspension of (N)G (4 mg) in water (100 mL), potassium carbonate (CO₃K₂) (2 equiv), tetra-*n*-butylammonium bromide (TBAB) (4 equiv) and the corresponding bromide derivative dissolved in 5 mL of dichloromethane (CH₂Cl₂) were added. The reaction was stirred for 20 h at 70 °C. The solvent was evaporated under reduced pressure and the crude product was then washed several times with methanol and CH₂Cl₂.

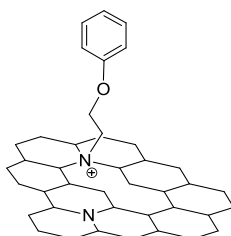
Synthesis of *f*-NG 1 (CH)

According to the general procedure, (**N**)**G** (4 mg), CO_3K_2 (69.1 mg, 0.5 mmol), TBAB (322.5 mg, 1 mmol) and 2-Bromo-4'-chloroacetophenone **1** (584 mg, 2.5 mmol) afforded the final product.

IR (KBr) ν , cm^{-1} : 2960, 2923 (C-H stretching mode), 1633 (C=O stretching mode) 1624 (C-H in plane stretching mode), 1394 (C=N stretching mode), 699 (C-Cl stretching mode).

TGA: Weight loss and temperature of desorption: 12.2%, 600 °C.

XPS (% atomic): C = 93.7, O = 4.6, N = 0.7, Cl = 1.0.

Synthesis of *f*-NG 2 (CH)

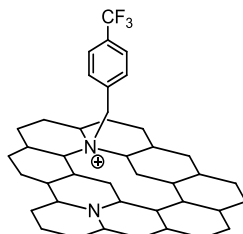
According to the general procedure, (**N**)**G** (4 mg), CO_3K_2 (69.1 mg, 0.5 mmol), TBAB (322.5 mg, 1 mmol) and 3-phenoxypropyl bromide **2** (538 mg, 2.5 mmol) afforded the final product.

IR (KBr) ν , cm^{-1} : 2961, 2920 (C-H stretching mode), 1640 (C=O stretching mode) 1624 (C-H in plane stretching mode), 1400 (C=N stretching mode).

TGA: Weight loss and temperature of desorption: 11.1%, 600 °C.

XPS (% atomic): C = 92.8, O = 6.6, N = 0.6.

Synthesis of *f*-NG 3 (CH)



According to the general procedure, **(N)G** (4 mg), CO_3K_2 (69.1 mg, 0.5 mmol), TBAB (322.5 mg, 1 mmol) and 4-(trifluoromethyl)-benzyl bromide **3** (598 mg, 2.5 mmol) afforded the final product.

IR (KBr) ν , cm^{-1} : 2942, 2889 (C-H stretching mode), 1641 (C=O stretching mode) 1624 (C-H in plane stretching mode), 1407 (C=N stretching mode).

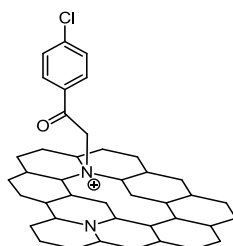
TGA: Weight loss and temperature of desorption: 12.9%, 600 °C.

XPS (% atomic): C = 93.2, O = 4.0, N = 0.7, F = 2.0.

General procedure for the N-alkylation of **(N)G** under microwave irradiation (MW)

To a suspension of **(N)G** (4.7 mg) in water (80 mL), CO_3K_2 (2 equiv), TBAB (4 equiv) and the corresponding bromide derivative dissolved in 5 mL of CH_2Cl_2 were added. Single-mode microwave irradiation (5W) was applied for 60 min at 70 °C. The reaction was then allowed to reach room temperature, and the crude product was separated by centrifugation, decanted, and then washed several times with methanol and CH_2Cl_2 .

Synthesis of *f*-NG **1** (MW)



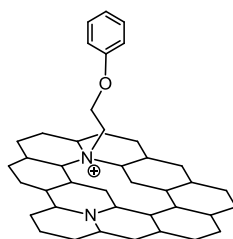
According to the general procedure, **(N)G** (4.7 mg), CO_3K_2 (110 mg, 0.8 mmol), TBAB (516 mg, 1.6 mmol) and 2-Bromo-4'-chloroacetophenone **1** (918 mg, 3.93 mmol) afforded the final product.

IR (KBr) ν , cm^{-1} : 2960, 2923 (C-H stretching mode), 1633 (C=O stretching mode) 1624 (C-H in plane stretching mode), 1394 (C=N stretching mode), 699 (C-Cl stretching mode).

TGA: Weight loss and temperature of desorption: 33.1%, 600 °C.

XPS (% atomic): C = 93.7, O = 4.6, N = 0.7, Cl = 1.0.

Synthesis of *f*-NG 2 (MW)



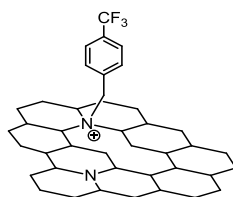
According to the general procedure, (**N**)**G** (4.7 mg), CO_3K_2 (110 mg, 0.8 mmol), TBAB (516 mg, 1.6 mmol) and 3-phenoxypropyl bromide **2** (0.62 mL, 3.94 mmol) afforded the final product.

IR (KBr) ν , cm^{-1} : 2961, 2920 (C-H stretching mode), 1640 (C=O stretching mode) 1624 (C-H in plane stretching mode), 1400 (C=N stretching mode).

TGA: Weight loss and temperature of desorption: 26.4%, 600 °C.

XPS (% atomic): C = 92.8, O = 6.6, N = 0.6.

Synthesis of *f*-NG 3 (MW)



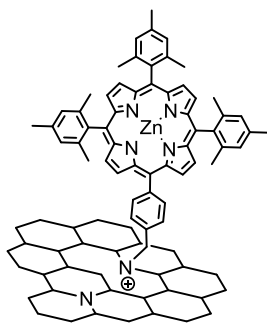
According to the general procedure, (**N**)**G** (4.7 mg), CO_3K_2 (110 mg, 0.8 mmol), TBAB (516 mg, 1.6 mmol) and 4-(trifluoromethyl) benzyl bromide **3** (940 mg, 3.94 mmol) afforded the final product.

IR (KBr) ν , cm^{-1} : 2942, 2889 (C-H stretching mode), 1641 (C=O stretching mode) 1624 (C-H in plane stretching mode), 1407 (C=N stretching mode).

TGA: Weight loss and temperature of desorption: 13.2%, 600 °C.

XPS (% atomic): C = 93.2, O = 4.0, N = 0.7, F = 2.0.

Synthesis of *f*-NG 4 (MW)



According to the general procedure, **(N)G** (3.4 mg), CO_3K_2 (55 mg, 0.4 mmol), TBAB (258 mg, 0.8 mmol) and 5-*p*-(bromomethyl) phenyl)-10,15,20 trimesitylporphyrinate Zn (II) **4** (372.4 mg, 0.42 mmol) afforded the final product.

IR (KBr) ν , cm^{-1} : 2924, 2857 (C-H stretching mode), 1639 (C-H in plane stretching mode), 1460 (C=N stretching mode), 1385 (porphyrin C=N stretching mode), 994 (porphyrin Zn-N stretching mode).

TGA: Weight loss and temperature of desorption: 20%, 600 °C.

XPS (% atomic): C = 94.3, O = 3.6, N = 1.8, Zn = 0.3.

ANNEXE: EXPERIMENTAL TECHNIQUES

In order to lighten the comprehension of the techniques mentioned in this work, a brief description about the fundamentals of the techniques used to explore the chemical and structural characteristics of carbon nanostructures is provided in this section. The chemical and structural information obtained from each technique is discussed, as well as their strengths and limitations.

Fourier transform infrared spectroscopy (FTIR)

Infrared spectroscopy (FTIR) can identify organic or inorganic functional groups on carbon nanostructures by measuring characteristic vibrational modes. FTIR takes advantage of the fact that each chemical bond in a molecule vibrates at different energy depending on its nature, so by means of energy they can be identified. However, IR does not provide a quantitative measure of functional group concentrations, and peaks use to be hard to distinguish from background features. Normally, IR spectra are recorded as absorbance or transmittance as a function of frequency, and either solid, liquid or gaseous samples can be measured. In this work, IR spectra were taken using a Fourier Transform IR spectrometer (Avatar 370) using powdered samples diluted in KBr pellets.

Raman spectroscopy

Raman spectroscopy, which is based on the inelastic scattering of monochromatic light, is a significant technique that is used to study the vibrational and rotational excitations of a molecular system³⁷¹; it is highly sensitive to carbon derivatives and able to provide a wealth of information about their structure. In Raman spectroscopy, vibrational modes are identified by measuring the energy of scattered photons generated from a sample exposed to intense laser light. Frequency of the reemitted photons is shifted up or down in comparison with original monochromatic frequency, which is called the “*Raman effect*”. This shift provides information about vibrational, rotational and other low frequency transitions in molecules. Raman spectroscopy can be used to study solid, liquid and gaseous samples and it is particularly well suited to molecular morphology characterization of carbon materials. Finally, a single

³⁷¹ M. S. Dresselhaus, A. Jorio, M. Hofmann, G. Dresselhaus and R. Saito *Nano Letters* **2010** *10*, 751.

laser cannot probe the entire sample because Raman scattering is observed only when probing laser is in resonance with an electronic transition in the CNT.

For sp^2 nanocarbons such as graphene and carbon nanotubes Raman spectroscopy can give information about crystallite size, the presence of sp^2 - sp^3 hybridization and the introduction of chemical impurities, number of graphene layers, nanotube diameter, chirality, curvature, and finally the metallic *vs* semiconducting behavior.

There are several characteristic bands that provide important information:

- RBM

A series of bands appearing at the low frequency end of the spectrum known as Radial Breathing Mode (RBM)(Figure 1). The RBM bands are unique to CNTs and as their name suggests, correspond to the expansion and contraction of the tubes. The frequency of these bands can be correlated to the diameter, chirality (n,m) and nature (metallic or semiconducting) of carbon nanotubes and they can provide important information on their aggregation state. The RBM bands are useful to calculate the diameter in Carbon Nanotubes following the equation [1]:

$$(\omega_{\text{RBM}}) = 218.2/dt + 19.6 \text{ cm}^{-1} \quad [1]$$

where dt is the diameter of the nanotube (in nm).

In the case of DWCNTs, it is possible to observe both, the peaks corresponding to the inner and outer walls, which are thus less bandwidth.³⁷²

³⁷² F. Villalpando-Paez, H. Son, D. Nezich, Y. P. Hsieh, J. Kong, Y. A. Kim, D. Shimamoto, H. Muramatsu, T. Hayashi, M. Endo, M. Terrones, and M. S. Dresselhaus, *Nano Letters* **2008**, *8*, 3879.

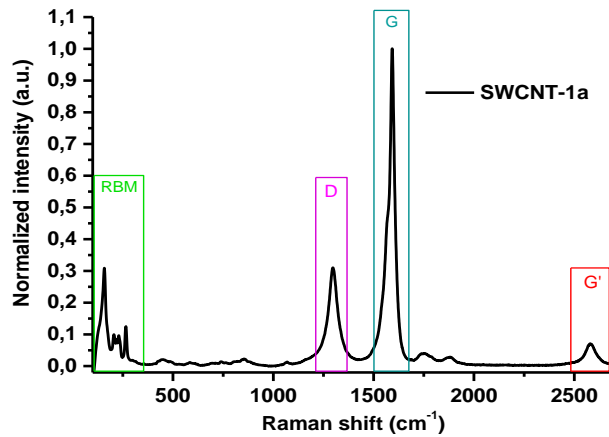


Figure 1. Raman spectrum of SWCNTs.³⁷³

- G-BAND

The stretching of the C-C bond in graphitic materials gives rise to the so-called G-band Raman feature which is common to all sp^2 carbon systems. It is a doubly degenerate phonon mode (E_{2g} symmetry) due to the bond stretching of all pairs of sp^2 atoms in both rings and chains. Curvature effects, such as occur in carbon nanotubes, give rise to multiple peaks in the G-band spectrum for a SWCNT. This curvature dependence generates a diameter dependence, thus making the G band a probe also for the tube diameter.

The most important aspect of the G-band is the shape which depends on whether the nanotube is semiconducting or metallic, allowing readily distinguishing between both types. (Figure 2).

³⁷³ Ref cruzada carbon maria

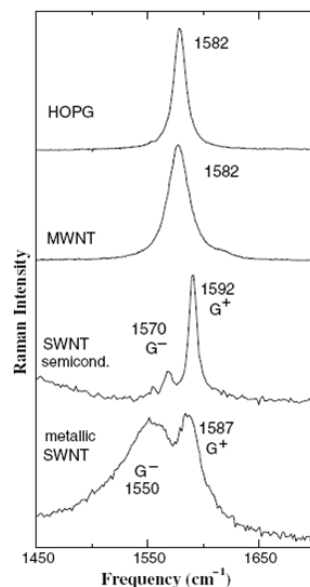


Figure 2. G-band for highly ordered pyrolytic graphite (HOPG), MWNT bundles, one isolated semiconducting SWCNT and one isolated metallic SWCNT.³⁷⁴

This band can be decomposed into 2 components, the lower frequency component associated with vibrations along the circumferential direction (G^-), at around 1570 cm^{-1} and the higher frequency component, (G^+), at around 1590 cm^{-1} , attributed to vibrations along G direction of the nanotube axis and is independent of the diameter and the chiral angle. Also, this component is sensitive to charge transfer processes, finding a shift to higher frequencies (up-shift) with dopants or acceptor impurities or toward lower frequencies (down-shift) with electron donors.¹⁶⁸

- D-BAND

The D band originates from a hybridized vibrational mode associated with graphene edges and it indicates the presence of some disorder in the graphene structure. This band is often referred to as the disorder band and its intensity relative to that of the G band is often used as a measure of the quality with nanotubes. The relative intensity of D to G (I_D/I_G) provides information about the in plane crystallite size or the degree of disorder. Finally, this intensity

³⁷⁴ A. Jorio, M. A. Pimenta, A. G. S. Filho, R. Saito, G. Dresselhaus, and M. S. Dresselhaus, *New J. Phys.*, **2003**, *5*, 139.

ratio can be used as an indicator of the degree of functionalization in carbon nanostructures.

- G' OR 2D BAND

All kinds of sp^2 carbon materials exhibit a strong peak in the range 2500 - 2800 cm^{-1} in the Raman spectra. Combined with the G-band, this spectrum is a Raman signature of graphitic sp^2 materials. 2D-band is a second-order two-phonon process and exhibits a strong frequency dependence on the excitation laser energy. The 2D band can be used to determine the number of layers of graphene since in multi-layer graphene, the shape of 2D band is pretty much different from that in the single-layer graphene (Figure 3).³⁷⁵

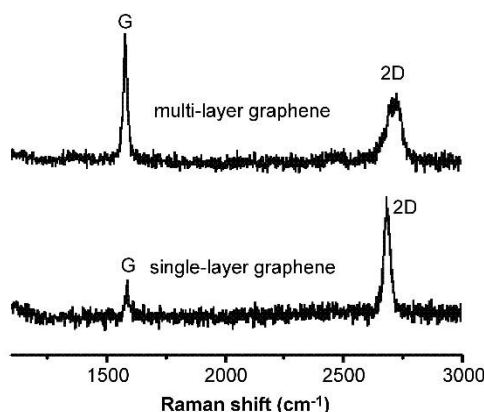


Figure 3. Raman spectrum of pristine single layer compared to that of multilayer.³⁷⁶

Thermogravimetric Analysis (TGA)

TGA measures the decrease in sample mass as a function of annealing temperature. It allows to determine the decomposition temperature or range of stabilities of a substance under air, nitrogen or other environments. Because carbon nanostructures generally have higher decomposition temperatures than absorbed molecules, TGA can be used to estimate the presence and

³⁷⁵ C. Ferrari, J. C. Meyer, V. Scardaci, C. Casiraghi, M. Lazzeri, F. Mauri, S. Piscanec, D. Jiang, K. S. Novoselov, and S. Roth, A. K. Geim, *Phys. Rev. Lett.*, **2006**, 97, 187401.

³⁷⁶ Z. Yan, A. R. Barron, Characterization of Graphene by Raman Spectroscopy <http://cnx.org/contents/f06226c5-c2a4-4798-9c75-b016acea73cd@2/Characterization-of-Graphene-b>

concentration of organic molecules attached to CNTs sidewalls or to the basal plane of graphene, in other words, provide information about the functionalization degree (Figure 4).

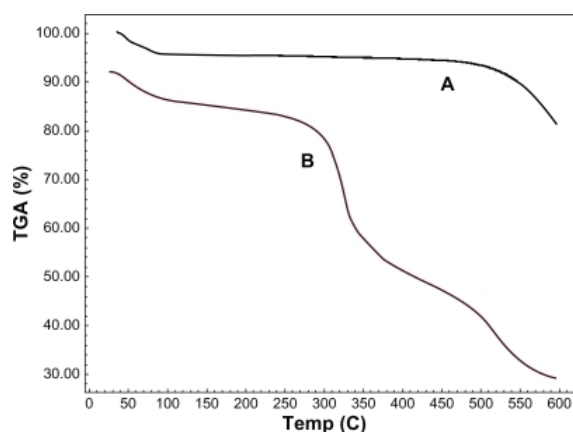


Figure 4. Thermogravimetric analysis (TGA) graphs of a) non-functionalized single-walled carbon nanotube and b) functionalized single-walled carbon nanotube.³⁷⁷

TGA and Raman spectroscopy are complementary techniques when studying carbon nanostructures, since the weight loss used to be in concordance with the I_D/I_G ratio.

X-Ray photoelectron spectroscopy (XPS)

XPS measures the surface composition from the top 10 nm of a sample by determining the binding energy of photoelectrons ejected when carbon nanostructures are irradiated with X-Rays. This allows the elemental composition of the surface to be quantified. The binding energy expressed in eV is used to determine the elements, the electronic state and type of hybridization by comparison with tabulated values.

For example, the C1s high resolution spectrum (Figure 5) from a sample with high concentration of sp^2 carbon will have a broad, asymmetric tail towards higher binding energy due to the presence of oxygen functionalities in the sample. Carbon allotropes typically have C-C, C-O-C and O-C=O components.

³⁷⁷ N. Hadidi, F. Kobarfard, N. Nafissi-Varcheh and R. Aboofazeli, *Int. J. Nanomedicine*, **2011**, *6*, 737.

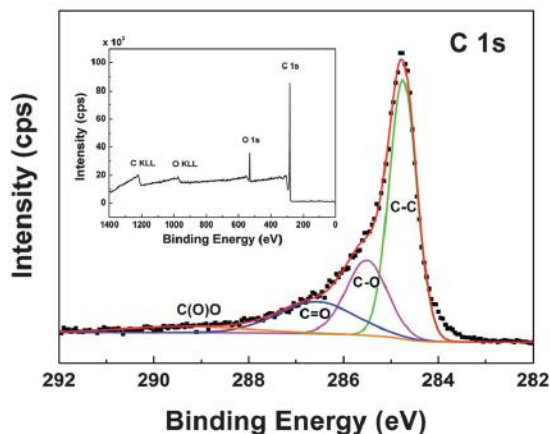


Figure 5. Typical C1s spectrum for a graphene sample.

After functionalization, when the concentration of sp^3 -bonded carbon increase, the C1s peak will have a more symmetric shape and will also be slightly shifted to higher binding energy.

How does XPS work?

A surface is irradiated with X-Rays in an ultrahigh vacuum. When an x-ray photon hits and transfers this energy to a core-level electron, it is emitted from its initial state with a kinetic energy dependent on the incident X-ray and binding energy of the atomic orbital from which it originated (Figure 6). The energy and intensity of the emitted photoelectrons are analysed to identify and determine the concentrations of the elements present. The photoemission process is very fast and it can be described through the equation [2]:

$$BE = h\nu - KE \quad [2]$$

Where BE is the electron binding energy, $h\nu$ is the characteristic energy of the X-Ray source and KE the kinetic energy from the ejected photoelectron.

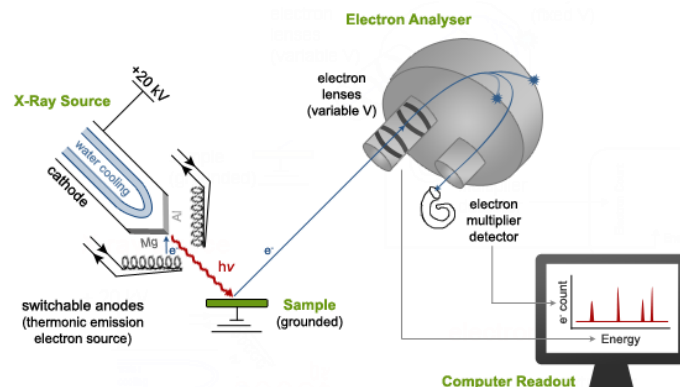


Figure 6. Representation for the XPS emission process

In a typical experiment, the sample is fitted inside a UHV chamber and irradiated with the X-ray source which produces photons capable of de-bound electrons for the surface of sample (top 1-10 nm of the sample). Those photoelectrons pass through the electron focusing system and arrive to the spectrometer, in which a hemispherical capacitor defines the path energy of the electrons and measures the kinetic energy of the photoelectron. This kinetic energy is finally measured in the detector and transduced by a computer programme.

Atomic force microscopy (AFM)

Atomic force microscopy (AFM) is a technique used to characterize surfaces at extremely high resolution. The deflection of a microfabricated cantilever with a sharp tip is measured by reflecting a laser beam off the backside of the cantilever while it is scanning over the surface of the sample (Figure 7). A tip is brought into close proximity with the sample to be analyzed. There are two basic modes in which structural images can be acquired. In contact mode, the tip remains in contact with the sample/substrate, or tapping mode, the tip is placed in contact with the surface to provide high resolution and then it is lifted off the surface to avoid dragging the tip across the surface. Tapping mode overcomes problems associated with friction, adhesion, electrostatic forces, and other difficulties that conventional AFM scanning methods present. This enables tapping mode to image soft, fragile, and adhesive surfaces without damaging them while work under contact mode allows the damage to occur.

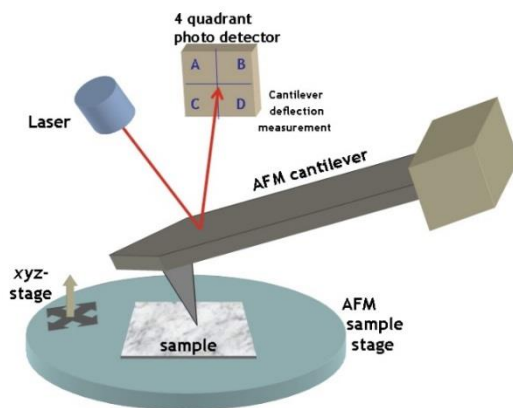


Figure 7. Typical AFM setup.

In carbon nanostructures, AFM allows to obtain three-dimensional images of the nanomaterials providing specific information about the sample's topography (Figure 8).

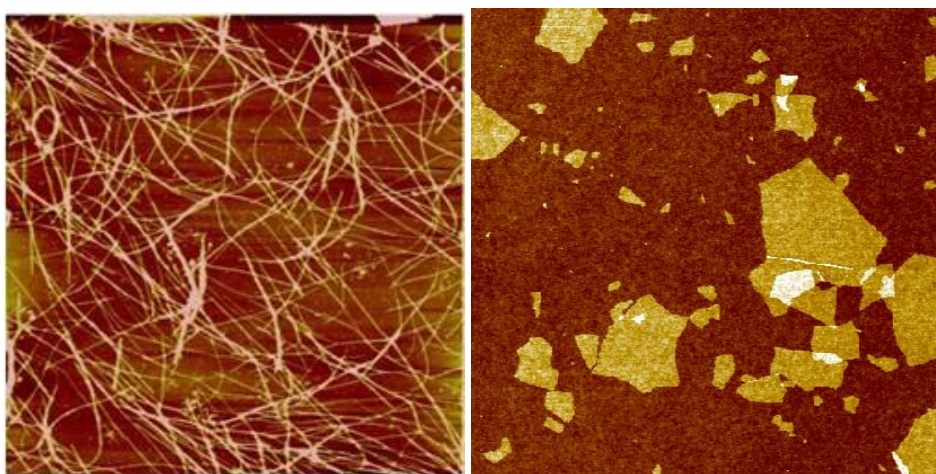


Figure 8. AFM images of SWCNTs (left)³⁷⁸ and few-layered graphene (right).³⁷⁹

Transmission electron microscopy (TEM)

The transmission electron microscope uses a high energy electron beam transmitted through a very thin sample to image and analyze the microstructure

³⁷⁸ <http://unidym.net/technology/>

³⁷⁹ <http://www.graphene.it/sol-go-4/>

of materials with atomic scale resolution. The image is magnified and focused onto an imaging device (i.e. fluorescent screen, photographic film or CCD camera). TEM can be used to study the growth of layers, their composition and defects in carbon nanostructures.

High resolution transmission electron microscopes (HR-TEM) can identify the defects in the carbon nanotube structures and can differentiate between different types of carbon nanotubes (zig-zag, armchair, chiral, etc) (Figure 9). In the case of graphene, it is a useful technique to determine the thickness and crystallinity of the material. As a result of the important information that TEM provides (which may not be available from other characterization techniques), it has become the most important technique for the study of carbon nanomaterials.

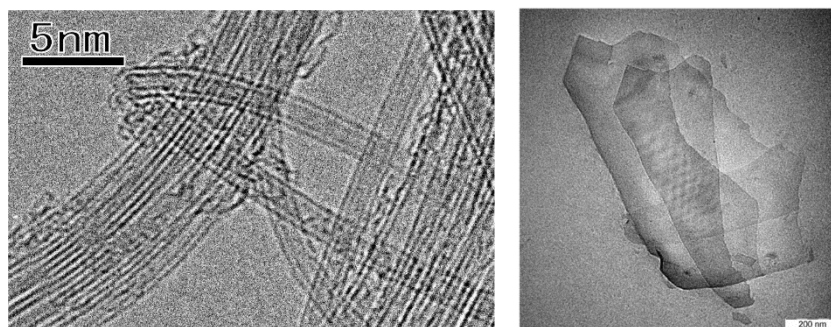


Figure 9. TEM images of DWCNTs (left)³⁸⁰ and few-layered graphene (right).³⁸¹

UV-vis-NIR absorption spectroscopy

UV-vis-NIR absorption spectroscopy has proven to be a powerful tool in SWCNT characterization, giving wide information related to the physical and electronic properties of the SWCNT sample accessible through a readily available and inexpensive technique.

In absorption spectroscopy, the optical transitions of the SWCNTs are observed, which arise from so-called van Hove singularities. The electronic structure of a SWCNT is unique for every (n, m) kind of nanotube. Accordingly,

³⁸⁰ <http://www.wakayama-u.ac.jp/~kisoda/int/indexen.html>

³⁸¹ B. W. Chieng, N. A. Ibrahim, W. M. Z. Wan Yunus, M. Z. Hussein and V. S. Giita Silverajah, *Int. J. Mol. Sci.*, **2012**, *13*, 10920.

absorption spectroscopy yields very valuable information of the composition of the nanotube sample.

A typical absorption of SWCNTs dispersed in an aqueous solution of SDBS is presented in Figure 10a. In the UV/Vis region, the transitions of metallic SWCNTs are observed, while the semiconducting nanotubes are observed in the Vis and NIR region. Each peak in the spectrum corresponds to a specific SWCNT. The (7, 5)-SWCNT is pointed out as an example.³⁸²

The effects of surface functionalization will result in loss in van Hove singularities (Figure 10b). Side wall functionalization leads to alteration of the electronic structure as a result of the conversion of sp^2 hybridized carbon to sp^3 hybridization.³⁸³

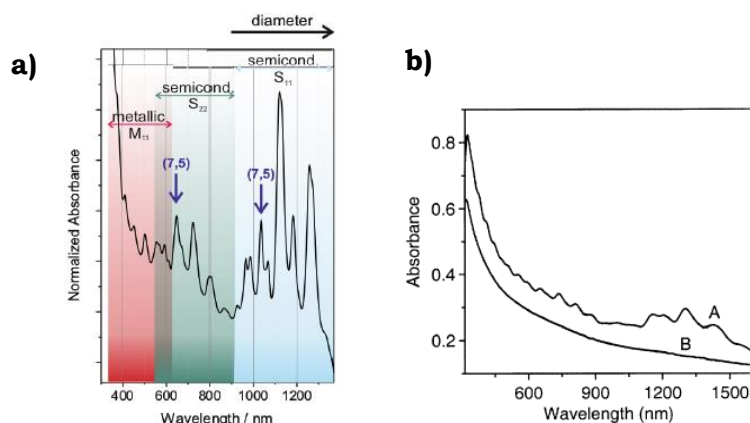


Figure 10. Typical absorption spectrum of a mixture of SWCNTs dispersed in an aqueous solution of SBDS (left) and UV-vis-NIR absorption spectra before (A) and after (B) functionalization (right).

When talking about graphene samples, the most characteristic peak appears normally around ~ 230 nm and is ascribed to the $\pi \rightarrow \pi^*$ transition of aromatics C-C bonds. A shoulder is also observed around ~ 295 nm when oxygenated functional groups are present. This technique allows studying the modification of the graphene sheets since the inclusion or removal of dopants

³⁸² C. Backes, Noncovalent functionalization of carbon nanotubes: Fundamental aspects of dispersion and separation in water. (Springer, 2012).

³⁸³ J. L. Bahr and J. M. Tour, *J. Mater. Chem.* **2002**, *12*, 1952.

normally cause the shift of these characteristic peaks or the appearance of a new one (Figure 11).

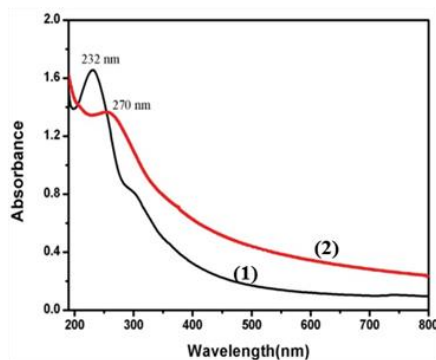


Figure 11. UV-vis spectra of graphene (1) and functionalized graphene (2).³⁸⁴

Fluorescence spectroscopy

Fluorescence is a process involving the emission of light from any substance in the excited states. Generally speaking, fluorescence is the emission of electromagnetic radiation (light) by the substance that has absorbed radiation of a different wavelength. Its absorption and emission is illustrated in the Jablonski diagram (Figure 12), a chromophore is excited to higher electronic and vibrational state from ground state after excitation. The excited molecules can relax to lower vibrational state due to the vibrational relaxation and, then further return to the ground state in the form of fluorescence emission.

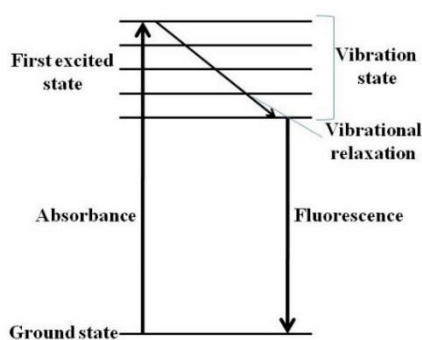


Figure 12. Jablonski diagram of fluorescence.

³⁸⁴ P. Huang, C. Xu, J. Lin, C. Wang, X. Wang, C. Zhang, X. Zhou, S. Guo, D. Cui, *Theranostics*, **2011**, *1*, 240.

This luminescence process has enormous scientific value because of the detailed information that spectral positions and intensities can reveal about a sample's electronic structure. In addition, it permits the sensitive qualitative and quantitative analysis of specific substances in complex mixtures.

Under an applied electric current or light irradiation, excited electrons and holes (positively charged locations where electrons are missing) are created, and carbon nanotubes emit near-infrared light. In this process, excited electrons and holes form bound states called excitons, and a photon is emitted due to the recombination of an electron and a hole during this process. Electronic states of SWCNTs are delocalized along the axis of the nanotube. Because SWCNTs are formed in a variety of discrete structures having distinct diameters and chiralities, a corresponding variety of π -electron band structures and excitations are found in mixtures of nanotubes. Such samples show photoluminescence in the near-infrared, with emission features evident at wavelengths from approximately 900 to 1600 nm. Fluorescence spectroscopy is therefore a powerful tool since fluorescence is mapped from excitonic band gap transitions allowing precise the (n, m) nanotube species.

When talking about graphene, no emission is observed. This can be readily understood from the absence of a band gap. Thus, photoluminescence has only been reported in oxidized graphene, where the electronic structure has been modified and longer lived states may be present. When the surface of graphene or the sidewall of the nanotube is functionalized with a chromophore, the last absorbs the light and emits a fluorescence signal. This signal can be quenched as a result of a variety of processes such as energy transfer, electron transfer, excited-state reactions etc... between the chromophore and the carbon nanostructure. Fluorescence intensity is proportional to the concentration of species, its absorption cross-section (or absorptivity) at the excitation wavelength, and its fluorescence quantum yield.

Transient-absorption spectroscopy (TAS)

TAS measures the absorbance at a particular wavelength or range of wavelengths of a sample as a function of time after excitation by light.³⁸⁵ This allows us to follow the evolution of molecular, aggregate or material systems on the ground and excited states as a function of femtosecond to nanosecond time

³⁸⁵ R. Berera, R. V. Grondelle and J. T. M. Kennis, *Photosynthesis Research*, **2009**, *101*, 105.

delays. In transient absorption spectroscopy, a fraction of the molecules is promoted to an electronically excited state by means of an excitation. A weak probe pulse is sent through the sample with a delay τ with respect to the pump pulse (Figure 13). A difference absorption spectrum is then calculated, *i.e.*, the absorption spectrum of the excited sample *minus* the absorption spectrum of the sample in the ground state (ΔD).

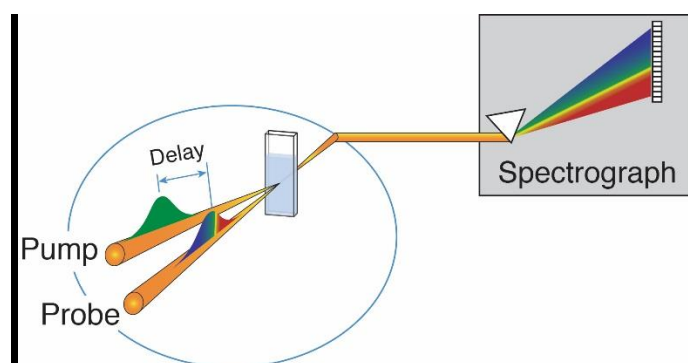


Figure 12. Schematic depiction of the transient absorption principle.

By changing the time delay between the pump and the probe, we can track the dynamics of the electrons in the molecule as a function of time obtaining information about the processes that occur in the system such as excited-state energy migration, electron and/or proton transfer processes, isomerization, and intersystem crossing.

In general, the spectrum contains contributions from various processes:

- 1) The first contribution is by ground-state bleach. As a fraction of the molecules has been promoted to the excited state through the action of the pump pulse, the number of molecules in the ground state has been decreased. Hence, the ground-state absorption in the excited sample is less than that in the non-excited sample. Consequently, a negative signal is observed in the wavelength region of ground state absorption.
- 2) The second contribution is by stimulated emission. For a two-level system, the Einstein coefficients for absorption from the ground to the excited state (A_{12}) and stimulated emission from the excited to the ground state (A_{21}) are identical. Thus, upon population of the excited state, stimulated emission to the ground state will occur when the probe pulse passes through the excited volume.

3) The third contribution is provided by excited-state absorption. Upon excitation with the pump beam, optically allowed transitions from the excited (populated) states of a chromophore to higher excited states may exist in certain wavelength regions, and absorption of the probe pulse at these wavelengths will occur. Consequently, a positive signal is observed in the wavelength region of excited-state absorption.

4) A fourth possible contribution to the DA spectrum is given by product absorption. After excitation of the photochemical system, reactions may occur that result in a transient or a long-lived molecular state, such as triplet states, charge-separated states, and isomerized states. The absorption of such a (transient) product will appear as a positive signal in the DA spectrum. A ground-state bleach will be observed at the wavelengths where the chromophore on which the product state resides has a ground-state absorption.

Ultraviolet photoelectron spectroscopy (UPS)

UPS is a method used to probe the occupied DOS of the near surface of a material. In this technique, UV photons of energy $h\nu$ are created in a continuous discharge source by applying a high voltage to a gas to cause breakdown. The photons are then targeted onto the sample under investigation. These photons will liberate electrons with sufficient energy, from the sample and into the vacuum where their kinetic energies may be analysed to gain an idea of their energy origin in the density of states. The resulting spectrum reflects the electronic structure of the sample providing information on the density of states, the occupation of states, and the work function.

As an example, in Figure 13 is showed a typical UPS spectrum of a gold sample. The spectrum is calibrated in a way that the Fermi level is located at 0 eV binding energy. To the right, at low binding energies (0-10 eV) the valence bands structures of Au are visible. The strong peaks correspond to the d-bands of Au, which have a high density of states and are fairly narrow. Then there is the high binding energy cutoff (or "secondary edge"), where the spectrum ends. Electrons close to the edge are the slowest electrons of the spectrum (right at the edge they have a kinetic energy of zero after leaving the sample surface, i.e. they had barely enough energy to overcome the work function of the material). Since we know the binding energy of the electrons right at the secondary edge, we can determine the work function, which is just the difference between the energy of the UV photons (21.21 eV for He I radiation) and the binding energy of the

secondary edge (15.9 eV in the case of Au). From Figure 3 it follows that the investigated Au surface has a work function of $\Phi_{\text{Au}} = 21.21 \text{ eV} - 15.9 \text{ eV} = 5.3 \text{ eV}$.

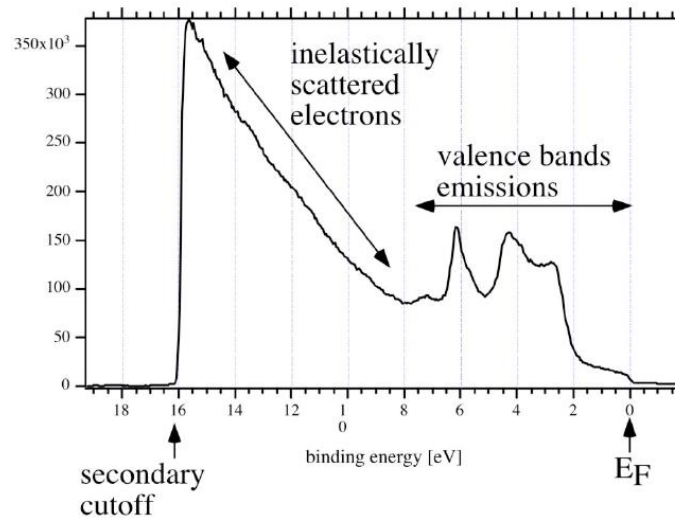


Figure 13. UP-spectrum of Au surface.

List of publications arising from this thesis

1. "Covalent functionalization of N-doped graphene by N-functionalization". **Barrejón M.**, Primo A., Gómez-Escalonilla M. J., Fierro J. L. G., García H., Langa F. *Chem. Commun.* **2015** (in press) DOI: 10.1039/C5CC06285C.
2. "Peripheral versus Axial Substituted Phthalocyanine-Double- Walled Carbon Nanotube Hybrids as Light Harvesting Systems". Arellano L. M., Martín-Gómis L., Gobeze H. B., **Barrejón M.**, Molina D., Gómez-Escalonilla M. J., Fierro J. L. G., Zhang M., Yudasaka M. Iijima S., D'Souza, F., Langa F., Sastre A. *J. Mater. Chem. C.* **2015**, 3, 10215-10224
3. "Application to the determination of adiponectin cytokine in serum". Ojeda I., **Barrejón M.**, Arellano L. M., González-Cortés A., Yáñez-Sedeño P., Langa F., Pingarrón M. (2015): *Biosensors and Bioelectronics.* **2015**, 74, 24-29.
4. "Covalent Decoration onto the Outer Walls of Double Wall Carbon Nanotubes with Perylenediimides: Synthesis, Characterization and Photoinduced Electron Transfer" **Barrejón M.**, Pla. S., Berlanga. I., Gómez-Escalonilla M.J., Martín-Gómis L., Fierro J. L. G., Zhang M., Yudasaka M., Iijima S., Gobeze. H. B., D'Souza F., Sastre A., Langa F. *J. Mater. Chem. C.* **2015**, 3, 4960-4969.
5. "A photoresponsive graphene oxide-C₆₀ conjugate" **Barrejón M.**, Vizuite. M., Gómez-Escalonilla M. J., Fierro J. L. G., Atienzar P., Nierengarten J-F., García H., Langa F. (2014):. *Chem. Commun.* **2014**, 50, 9053-9055.
6. "Endohedral and Exohedral Hybrids involving Fullerenes and Carbon Nanotubes" Langa F., Gómez-Escalonilla M. J., Vizuite M., **Barrejón M.** *Nanoscale.* **2012**, 4, 4370-4381.
7. "Hybrids involving Fullerenes and Carbon Nanotubes" in *Handbook of Carbon Nanomaterials*, Vol. 4, pp. 217-243. **2012**. World Scientific Publishing (ISBN: 13 978-981-4401-41-8). Vizuite M., **Barrejón M.**, Gómez-Escalonilla M. J., Langa F.

8. "Synthesis, Characterization and Photoinduced Charge Separation of Carbon Nanohorn-Oligothiénylenevinylene Hybrids". Vizúete M., Gómez-Escalonilla M.J., **Barrejón M.**, Fierro J. L. G., Zhang M., Yudasaka M., Iijima S., Atienzar P., García H., Langa F. (2015). Submitted to Physical Chemistry Chemical Physics.
9. "All-carbon based SWCNT-C60 donor-acceptor nanoensembles separated by poly(phenylene ethynylene) spacers: Synthesis, characterization and excited state charge transfer interactions" Barrejón, M., Gobeze, H. B., Gómez-Escalonilla, M. J., Fierro, J. L. G., Zhang, M., Yudasaka, M., Iijima, S., D'Souza, F. and Langa, F. (2015). Manuscript in preparation.